2016

JOURNAL OF CENTRAL EUROPEAN GREEN INNOVATION

4 (4)

Eszterházy Károly Egyetem

HUNGARY

Editorial Office / Szerkesztőség
Líceum Kiadó
3300 Eger, Eszterházy tér 1.

Publisher / Kiadó
Líceum Kiadó
3300 Eger, Eszterházy tér 1.

Responsible Publisher / Felelős kiadó
Liptai Kálmán, rektor

HU ISSN 2064-3004

2016

ELŐSZÓ

Az Eszterházy Károly Egyetem kiemelt figyelmet fordít kutatási eredményeinek, valamint innovációinak a megismertetésére mind szélesebb körben konferenciák, workshopok, nyomtatott és elektronikus folyóiratok formájában egyaránt.

Ez utóbbi megvalósításához nyújt lehetőséget az intézmény számára a TÁMOP-4.2.3-12/1/1KONV-2012-0047 „Kutatási eredmények és innovációk disszeminációja az energetikai biomassza (zöldenergia) termelés, átalakítás, hasznosítás a vidékfejlesztés és a környezeti fenntarthatóság terén a Zöld Magyarországért" program, melynek keretében útnak indítjuk a „**Journal of Central European Green Innovation (JCEGI)**" című elektronikus folyóiratot.

Az intézményben folyó széles körű kutatások egyik kiemelt iránya a fizika, azon belül is a femtoszkópia. Több mint egy évtizeddel ezelőtt, 2005-ben Workshop on Particle Correlations and Femtoscopy (WPCF) elnevezéssel új konferencia sorozat indult, amelynek célja a mikrométer milliomod része ezredrészén, a femtométer hossztartományban történő távolságmérések szakterülete, a femtoszkópia éves fejlődésének áttekintése. A X. jubileumi konferencia megrendezésére a gyöngyösi Károly Róbert Főiskola, a Magyar Tudományos Akadémia Wigner Fizikai Kutatóközpontja és az Eötvös Lóránd Tudományegyetem csapata nyerte el a jogot, így a jubileumi, 10. WPCF konferenciának a Károly Róbert Főiskola adott otthont 2014. augusztus 25-29. között. A rendezvénynek 85 résztvevője volt, 73 előadás hangzott el, 37 doktorandusz jött el a világ 23 országából, 5 nap alatt 4 világrész femtoszkópiai eredményeit tekintve át.

Jelen kötetben a konferencia legérdekesebb eredményeit közöljük. Részletesebb konferencia összefoglaló tanulmányt pedig a JCEGI korábbi kötetében (JCEGI, 2(4) pp. 183-187 (2014)) talál az olvasó.

A WPCF 2014 konferencia szervezése elektronikusan történt, így a rendezvény teljes anyaga (beleértve a résztvevők listáját, az előadások anyagait, illetve a konferenciakötet elektronikus archivumát) megtalálható a konferencia honlapján:

https://indico.cern.ch/e/wpcf2014

A WPCF 2014 konferenciakiadványt szerkesztette:

Csanád M. (tudományos titkár) Csörgő T. (elnök) Novák T. (társelnök)
A szerkesztők

A WPCF2014 KONRENECIA TÁMOGATÓI

Ezúton is szeretnénk köszönetet mondani támogatóinknak a segítségnyújtásukért, mely nagyban hozzájárult ahhoz, hogy a WPCF 2014 egy valóban sikeres, inspiráló és hasznos konferencia legyen. Külön szeretnénk köszönetet mondani az alábbiaknak

- Academia Humana Foundation, Budapest, Magyarország;
- Berze Secondary/Middle School, and Berze Science Club Gyöngyös, Magyarország;
- CERN, Genf, Svájc;
- Eötvös University, Budapest, Hungary;
- Hungarian Academy of Sciences, Budapest, Magyarország;
- Károly Róbert College, Gyöngyös, Magyarország;
- OTKA, Budapest, Magyarország;
- Rubik Studio, Budapest, Magyarország;
- TÁMOP 4.1.1.C-12/1/KONV-2012-0001 "KEZEK – Észak-Magyarország felsőoktatási intézményeinek együttműködése"
- TÁMOP-4.1.1.C-12/1/KONV - 2012-0012 "Zöld Energia Felsőoktatási Együttműködés"
- TÁMOP-4.2.3-12/1/1KONV-2012-0047 „Kutatási eredmények és innovációk disszeminációja…”
- Széchenyi 2020 fund by the Europan Union and the Government of Hungary;
- US Department of Energy, USA;
- MTA Wigner Fizikai Kutatóközpont, Budapest, Magyarország;
- anonim magánvállalkozások Gyöngyös környékéről, Magyarország;
- anonim magánszemélyek Gyöngyös környékéről, Magyarország.

Ez a lista a konferenciakötet zárásakor készült.

INTRODUCTION

Eszterházy Károly University pays special attention to disseminate its research results and innovations increasingly as widely as possible in conferences and workshops as well as in print and electronic journals.

The implementation of the latter by the institution is aided by the TÁMOP-4.2.3-12/1/1KONV-2012-0047 program "dissemination of research results and innovations in the field of biomass energy (green energy) production, transformation and utilization in the field of rural development and environmental sustainability for a Green Hungary" in the framework of which the electronic version of the "**Journal of Central European Green Innovation**" will be launched.

One of the key directions of the wide range of research at the institution is physics, within it femtoscopy. More than ten years ago, in 2005, a new series of international Workshop on Particle Correlations and Femtoscopy (WPCF) conferences was initiated and started, with the aim of overviewing the annual developments in femtoscopy, the science of measuring length scales in the range of a femtometer, corresponding to a thousandth part of a millionth part of a micrometer or 10-15 m. The 10th, anniversary conference was organized by a consortium of the Wigner Research Centre for Physics (Wigner RCP), the Eötvös University (ELTE), both located in Budapest and by the Károly Róbert College (KRF), located in Gyöngyös. Hungary. The Károly Róbert College of Gyöngyös provided the site for the anniversary, 10th WPCF meeting in the period of August 25-29, 2014.

In the present publication of JCEGI the most interesting results of the conference are published. A more detailed conference summary can be found in the former edition of this electronic journal. (JCEGI, 2(4) pp. 189-194 (2014))

WPCF 2014 was organized mainly electronically, and the conference materials (including the full list of participants, archive of the talks and electronic archive of the proceedings) is archived and availabe from the home page of WPCF 2014 at

https://indico.cern.ch/e/wpcf2014

The proceedings of WPCF 2014 was edited by:

M. Csanád (Scientific Secretary) T. Csörgő (Chair) T. Novák (Co-Chair)
The Editors

SUPPORTERS OF WPCF2014

We would like to sincerely thank for the various contributions from our supporters that helped us to organize WPCF 2014 as a gateway to knowledge and to create an inspiring and useful, successful meeting in Gyöngyös, Hungary. In particular, we would like to express our gratitude to:

- Academia Humana Foundation, Budapest, Hungary;
- Berze Secondary/Middle School, and Berze Science Club Gyöngyös, Hungary;
- CERN, Geneva, Switzerland;
- Eötvös University, Budapest, Hungary;
- Hungarian Academy of Sciences, Budapest, Hungary;
- Károly Róbert College, Gyöngyös, Hungary;
- OTKA, Hungarian National Science Fund, Budapest, Hungary
- Rubik Studio, Budapest, Hungary;
- TÁMOP 4.1.1.C-12/1/KONV-2012-0001 "KEZEK – Észak-Magyarország felsőoktatási intézményeinek együttműködése"
- TÁMOP-4.1.1.C-12/1/KONV - 2012-0012 "Zöld Energia Felsőoktatási Együttműködés"
- TÁMOP-4.2.3-12/1/1KONV-2012-0047 „Kutatási eredmények és innovációk disszeminációja…”
- Széchenyi 2020 fund by the Europan Union and the Government of Hungary;
- US Department of Energy, USA;
- Wigner Research Centre, Hungarian Academy of Sciences, Budapest, Hungary;
- an anonymous private company from Gyöngyös region, Hungary;
- some anonymous private persons from Gyöngyös region, Hungary.

This is the full list of WPCF2014 supporters and patrons, at the time of finalizing the proceedings of the conference.

TARTALOMJEGYZÉK / TABLE OF CONTENTS

TANULMÁNYOK – SCIENTIFIC PAPERS

Finite size of hadrons and Bose-Einstein correlations

Andrzej Bialas

M. Smoluchowski Institute of Physics,
Jagellonian University, PL-30-059 Krakow

Abstract

In this presentation I report on the results of the paper we published recently together with Kacper Zalewski [1]. It exploits the consequences of the observation that the hadrons, being the composite objects, cannot be produced too close to each other and thus must be correlated in space-time. One of these consequences, which we discuss here, is that the correlation function need not be larger than 1 (as is necessary if the space-time correlations are absent). Since the data from LEP [2, 3] and from LHC [4] do show that the correlation function falls below 1, the particles must be correlated and we show that our observation does explain this unexpected effect.

In absence of correlations between produced hadrons, the Bose-Einstein correlation function between momenta of two identical particles

$$C(p_1,p_2)=\frac{N(p_1,p_2)}{N(p1)N(p2)} \tag{1}$$

is given by [5]

$$C(p_1,p_2)=\frac{\tilde{w}(P_{12};Q)\tilde{w}(P_{12};-Q)}{w(p_1)w(p_2)}=1+\frac{|\tilde{w}(P_{12};Q)|^2}{w(p_1)w(p_2)}\geq 1 \tag{2}$$

where $w(p,x)$ is the single-particle "distribution" (Wigner function) and

$$\tilde{w}(P_{12};Q)=\int dx e^{iQx}w(P_{12};x);\qquad w(p)=\int dx w(p;x), \tag{3}$$

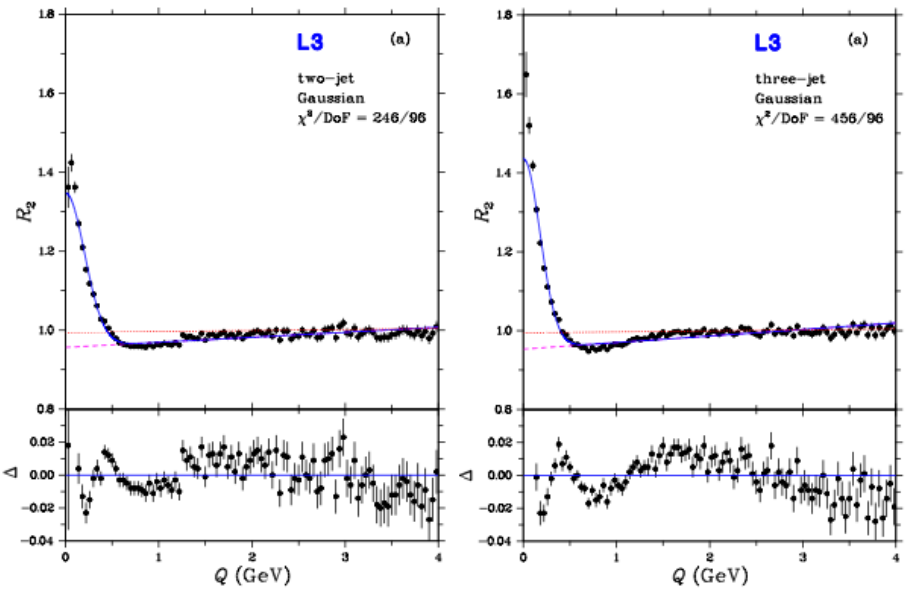

Figure 1: L3 data for two-jet and three-jet events.

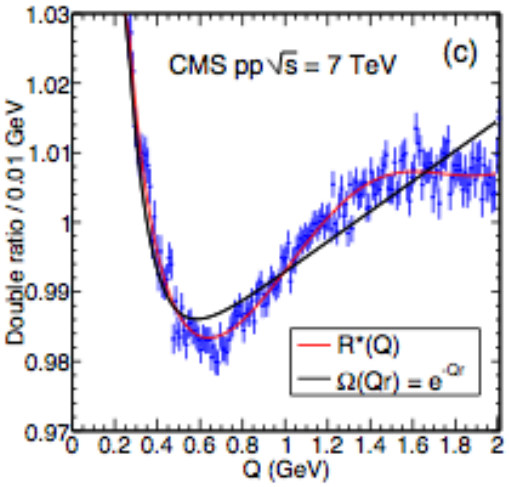

Figure 2: Two-pion correlation function from CMS (pp at 7 TeV)

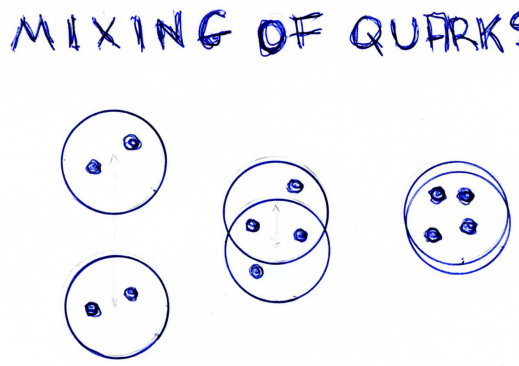

Figure 3: Illustration of the excluded volume effect.

$P_{12} = (p_1 + p_2)/2$; $Q = p1 - p2$.

In Fig. 1 the data from L3 collaboration and in Fig. 2 the data from CMS collaboration are shown. They clearly indicate that the correlation function $C(q)$ takes values below 1, contrary to the Eq. (2)

These data show that particles must be correlated and we claim that the correlations responsible for this effect are caused by the composite nature of hadrons. Indeed, since hadrons are composite, they cannot be produced too close to each other because in this case *they are not hadrons anymore* but rather a mixture of the hadronic constituents. This is illustrated in Fig. 3.

Since the HBT experiment measures the quantum interference between the wave functions of hadrons, it cannot see hadrons which are too close to each other. Consequently the "source function" $W(P12; P12; x1; x2)$ must vanish at x_1 close to x_2 and thus can be written as

$$w(P, x) = e^{-|\vec{x}|^2/R^2} e^{-t^2/\tau^2} f(P)$$

$$W(P_{12}; P_{12}; x_1; x_2) = w(P_{12}; x_1) w(P_{12}; x_2)[1 - D(x_1 - x_2)]. \tag{4}$$

where the cut-off function $D(x1 - x2)$ equal 1 and $(x1 - x2)$ (below, say, 1 fm) and vanishes at larger distances.

Thus the HBT correlation function becomes:

$$C(p_1, p_2) = 1 + \frac{|\tilde{w}(P_{12}; Q)|^2}{w(p_1) w(p_2)} - C_{corr}(p_1, p_2); \tag{5}$$

$$C_{corr} = \frac{\int dx_1 dx_2 e^{i(x_1 - x_2)Q} w(P_{12}; x_1) w(P_{12}; x_2) D(x_1 - x_2)}{w(p_1) w(p_2)}$$

One sees that the contribution from the part responsible for space-time correlation is negative. Moreover, since it obtains contribution from a small region of space-time, its dependence on Q is much less steep than that of the uncorrelated part. Consequently, at Q large enough $C(P12; Q)$may easily fall below one.

For illustration, take $D(x_1 - x_2) = \Theta[r_{cut}^2 - |\vec{x}_1 - \vec{x}_2|^2 - (t_1 - t_2)^2]$; The result is shown in Fig. 4 where one sees that, indeed, $C(Q)$ is smaller than 1 at Q larger than 400 MeV.

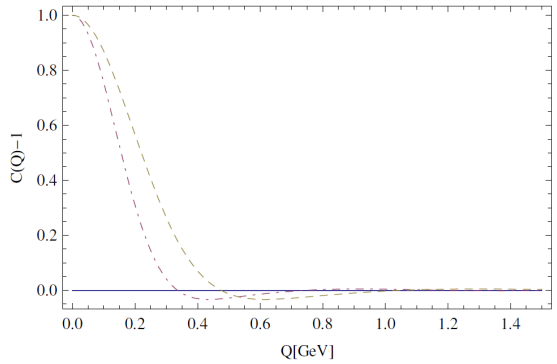

Figure 4: Oscillating two-pion correlation function. $R = r_{cut} = \tau = 1$ fm.

In conclusion, the presented qualitative argument shows that the observed falling of the HBT correlation function below one at large Q is not accidental but re ects the fundamental fact that hadrons are NOT POINT-LIKE. Therefore this region of Q^2 deserves special attention in data analysis. It seems that the effect simply MUST BE THERE and the real experimental challenge is to determine its position and its size. Precise measurements may allow to determine the distance at which the hadron structure is affected by its neighbors and thus also the density at which the hadron gas starts melting into quarks and gluons.

More serious calculations, as well as a detailed comparison with data are clearly needed and are in progress (together with W.Florkowski) [6]. The preliminary results indicate that the effect significantly depends on the orientation of Q. This points to interest in separate measurements in *side*, *out* and *long* directions.

References

[1] A.Bialas and K.Zalewski, Phys. Lett. B727 (2013) 182.

[2] M. Acchiari et al. [L3 coll.] Phys. Lett. B458 (1999) 517;
P.Achard et al. [L3 coll.], Eur. Phys.J. C71 (2011) 1648.

[3] G.Abbiendi et al. [OPAL coll.], Eur. Phys. J. C16 (2000) 423;
P.Abreu et al. [DELPHI coll.] Ohys. Lett. B471 (2000) 460;
A.Heister et al. [ALEPH coll.] Eur. Phys. J. C36 (2004) 460.

[4] V.Khachatryan et al. [CMS coll.], JEHP 1105 (2011) 029;
L.Perroni, PoS (WPCF2011) 015. 4

[5] See, e.g., M. A. Lisa, S. Pratt, R. Soltz and U. Wiedemann, Ann. Rev. Nucl. Part. Sci. 55, 357 (2005).

[6] A.Bialas, W.Florkowski and K.Zalewski, J. Phys. G: Nucl.Part.Phys. 42 (2015) 045001 and to be published.

Event geometrical anisotropy and fluctuation viewed by HBT interferometry

Takafumi Niida

University of Tsukuba
1-1-1 Tennoudai, Tsukuba, Ibaraki 305-8571, Japan

Abstract

Azimuthal angle dependence of the pion source radii was measured applying the event shape selection at the PHENIX experiment. The measured final source eccentricity is found to be enhanced when selecting events with higher magnitude of the second-order flow vector, as well as the elliptic flow coefficient v_2. The spatial twist of the particle-emitting source was also explored using a transport model. Results indicate a possible twisted source in the final state due to the initial longitudinal fluctuations.

1 Introduction

Higher-order flow coefficients v_n are useful observables to constrain the properties of the quark-gluon plasma, such as a shear viscosity over entropy density ratio, in heavy ion collisions [1, 2]. The v_n are found to largely fluctuate in each event even if the collision centrality is fixed [3], which is due to the initial spatial fluctuation of participating nucleons. To control such event-by-event initial fluctuations, the event shape engineering was suggested [4]. The event shape engineering can be performed by selecting the magnitude of the event flow vector Q_2:

$$\begin{aligned} Q_2 &= \sqrt{q_{2,x}^2 + q_{2,y}^2}/\sqrt{M}, \\ q_{2,x} &= \sum_i w_i \cos(2\phi_i), \quad q_{2,y} = \sum_i w_i \sin(2\phi_i), \end{aligned} \tag{1}$$

where M is the particle multiplicity, ϕ_i is the azimuthal angle of particles, and w_i is a weight for particle i. The magnitude of Q_2 is proportional to the strength of event-by-event v_2 and also reflects the resolution of the second order event plane. This technique could allow us to test the effect of the initial geometry on the final state distribution of emitted particles, which help to understand the medium response through the system evolution.

The event shape engineering focuses on the fluctuations in the transverse plane. It is naturally considered that there would be the fluctuations not only in the transverse plane but also in the longitudinal direction. The presence of such fluctuations could cause a twisted source along the longitudinal direction [5]. The number of participants going to the forward and backward directions would be different, and therefore participant planes might also be different. As a result, the event plane angle in the final state could be different between the forward and backward angles. Thus the initial spatial twist may survive in the final state as well as a twisted flow [8, 9].

In this proceedings, we present results on HBT measurements using charged pions and applying the event shape engineering technique for Au+Au collisions at $\sqrt{s_{NN}}$=200 GeV recorded with the PHENIX experiment. Also, we examine the possibility of a spatially twisted source in the final state using HBT interferometry in AMPT model.

2 The event shape engineering at the PHENIX

The flow vector was determined by the Reaction Plane Detector (RXN, $1 < |\eta| < 2.8$). In our analysis, the w_i in Eq. (2) reflects the multiplicity or energy measured in a segment i of the RXN and M is $\sum w_i$. The tracking for charged particles was performed by the Drift Chamber and the Pad Chamber, and the particle identification was done by the electromagnetic calorimeter, where they have the acceptance of $|\eta| < 0.35$ and $|\phi| < \pi/2$ in the west and east central arms.

The measured Q_2 distributions were fitted with the Bessel-Gaussian function [4], and then the events were classified with the magnitude of Q_2. Figure 1 shows charged hadron v_2 for the higher 20% and the lower 30% Q_2 events. Results without Q_2 selection are also plotted for the comparison. The effect of Q_2 selection

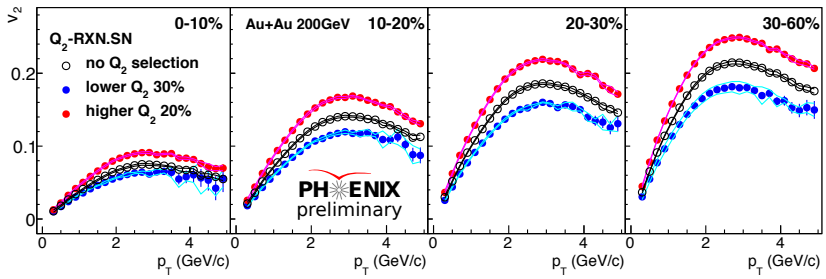

Figure 1: Charged hadron v_2 as a function of p_{T} for four centrally bins with and without the Q_2 selection in Au+Au 200 GeV collisions. The lower and higher Q_2 events were selected.

on the v_2 is clearly observed, that is, the higher (lower) Q_2 enhances (decreases)

the strength of v_2 compared to the v_2 without the Q_2 selection.

Then the Q_2 selection was applied to the HBT measurements using charged pion pairs. In the HBT analysis, pion pairs were analyzed with the out-side-long parameterization [10, 11] in the longitudinally co-moving system. The effect of the event plane resolution was also corrected for both cases with and without Q_2 selection. Figure 2(left) shows the extracted pion HBT radii, $R_{\rm s}^2$ and $R_{\rm o}^2$, as a function of azimuthal pair angle ϕ relative to the second-order event plane Ψ_2. Results show that the higher Q_2 selection increases the oscillation strength compared to the case without Q_2 selection.

These oscillations of HBT radii are supposed to be sensitive to the final source eccentricity at freeze-out, $\varepsilon_{\rm final}$. Blast-wave studies suggest that the quantity of $2R_{\rm s,2}^2/R_{\rm s,0}$ would be a good probe of $\varepsilon_{\rm final}$ in the limit of $k_{\rm T}=0$, where $k_{\rm T}$ denotes a mean transverse momentum of pairs. The oscillation amplitudes of $R_{\rm s}^2$ and $R_{\rm o}^2$ in a form of the final eccentricity are plotted as a function of the number of participants calculated by Glauber model in Fig. 2(right). The higher Q_2 selection enhances the measured $\varepsilon_{\rm final}$ as well as v_2. It could be originating from a larger initial eccentricity, although there should be a bias from selecting the larger v_2 events because the radii modulations also depend on the anisotropy in the momentum space [6, 7].

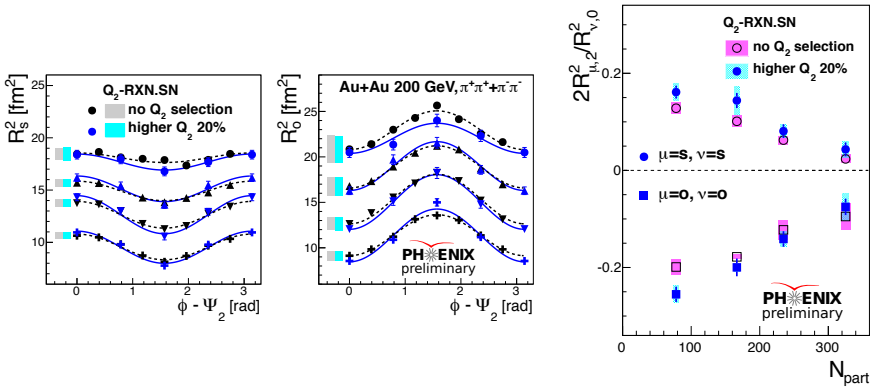

Figure 2: (Left and center) Azimuthal angle dependence of $R_{\rm s}^2$ and $R_{\rm o}^2$ relative to Ψ_2. (Right) $2^{\rm nd}$-order azimuthal oscillation on R_s^2 and R_o^2. In both panels, results with and without higher Q_2 selection are shown.

3 Study on the event twist effect

The data of Pb+Pb 2.76 TeV collisions simulated using a Multi Phase Transport Model (AMPT, v2.25 with string melting) were used for the study on the twist effect of the particle-emitting source in the final state. The impact parameter was fixed to 8 fm. For the HBT study, the interference effect between two identical particles, $1+\cos(\Delta\mathbf{r}\cdot\Delta\mathbf{p})$, was calculated and weighted to the relative pair momentum distributions. Then the correlation functions were reconstructed by taking a ratio of the distributions with and without the weight. Also, all charged pions were allowed to make a pair with each other including $\pi^+\pi^-$ to increase the statistics (the consistency between results for positive and negative pairs was checked). The event plane was determined using particles in $4<|\eta|<6$, where particles were

divided into two sub-groups. A set of forward and backward event planes ($\Psi_2^{\rm F}, \Psi_2^{\rm B}$) were used for the event cut which requires finite difference between $\Psi_2^{\rm F}$ and $\Psi_2^{\rm B}$ as a event twist selection, whereas the other set of event planes was used for a reference angle of azimuthal HBT measurements. The effect of the event plane resolution was not taken into account in this study, assuming the resolution hardly affects the phase of the radii oscillations but the magnitude of the oscillations.

Figure 3 shows $R_{\rm s}^2$, $R_{\rm o}^2$, and $R_{\rm os}^2$ as a function of azimuthal pair angle relative to the $\Psi_2^{\rm B}$ ($\Delta\phi$) for four η regions, where $(\Psi_2^{\rm B} - \Psi_2^{\rm F}) > 0.6$ was required. The oscillations of the HBT radii measured in $\eta > 0$ are shifted to the direction of $\Delta\phi < 0$, which is the direction of $\Psi_2^{\rm F}$ in the current event cut. This phase shift can be understood to be a possible twist effect in the final source distribution. The radii oscillations measured in $\eta < 0$ have no phase shift because the negative η is closer to the backward angle used for a reference of the HBT measurement and therefore the twist effect is supposed to be small. Figure 4 shows all the extracted radii parameters measured with respect to Ψ_2^B and Ψ_2^F with the event cut of $(\Psi_2^B - \Psi_2^F) > 0.6$. The phase shift can be seen in the transverse radii (not in the longitudinal radii including the cross terms) when comparing the results for Ψ_2^B and Ψ_2^F in the same η region. It indicates the twist of the event plane angles in the backward and forward angles. These oscillations were fitted with the following functions:

$$R_\mu^2(\Delta\phi) = R_{\mu,0}^2 + 2R_{\mu,2}^2\cos(2\Delta\phi + \alpha) \ \ (\text{for } \mu = o, s), \tag{2}$$

$$R_\mu^2(\Delta\phi) = R_{\mu,0}^2 + 2R_{\mu,2}^2\sin(2\Delta\phi + \alpha) \ \ (\text{for } \mu = os), \tag{3}$$

to extract the magnitude of the phase shift (α). The phase shift parameter α obtained from the results with respect to $\Psi_2^{\rm F}$ and $\Psi_2^{\rm B}$ is plotted as a function of η in Fig. 4. The α increases going from backward to forward angle in all cases. The variation of α in the η dependence is comparable to the difference between results relative to $\Psi_2^{\rm F}$ and $\Psi_2^{\rm B}$ at the same η. The finite slope in the η dependence of α indicates the twisted source in the final state due to the initial longitudinal fluctuations, as well as the twisted event plane and flow as discussed in Ref. [8, 9]. In this study, the effect of the event plane resolution is assumed to be negligible, but there should be an uncertainty derived from the event cut of $(\Psi_2^{\rm B} - \Psi_2^{\rm F})$ and their finite event plane resolutions.

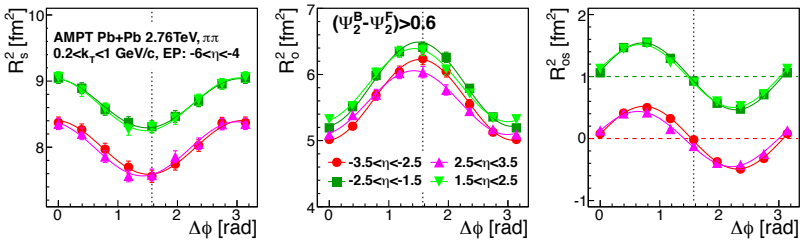

Figure 3: Azimuthal angle dependence of $R_{\rm s}^2$, $R_{\rm o}^2$, and R_{os}^2 relative to the backward Ψ_2 with the event cut of $(\Psi_2^{\rm B} - \Psi_2^{\rm F}) > 0.6$, where the dashed lines show $R_{\rm os}^2 = 0$ and the dotted lines show $\Delta\phi = \pi/2$.

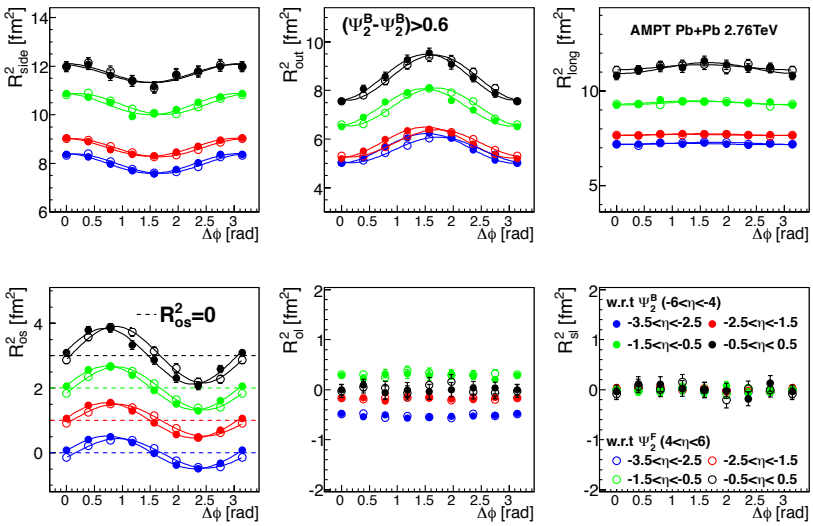

Figure 4: Azimuthal angle dependence of the radii parameters relative to the backward and forward Ψ_2 with the event cut of $(\Psi_2^{\rm B} - \Psi_2^{\rm F}) > 0.6$, where the dashed lines show $R^2_{\rm os} = 0$.

4 Summary

We presented the results of HBT measurements using the event shape engineering for Au+Au collisions at $\sqrt{s_{\rm NN}} = 200$ GeV at the PHENIX experiment. We found that the higher Q_2 selection enhances the measured final source eccentricity as well as v_2. Although the model comparison is needed to disentangle both spatial and dynamical effects on the HBT radii, this study would clarify the relation between the initial and final source eccentricities and constrain better the system dynamics.

We also studied the event twist effect using AMPT model. When selecting events with finite difference between forward and backward event plane angles, the oscillations of HBT radii are shifted in the phase and the phase shift increases with η. The results indicate a possible twisted source in the final state preserving the initial twist due to the longitudinal fluctuations. This effect might be measured in experiments at RHIC and the LHC.

Both techniques could be useful to probe and control initial fluctuations in transverse plane and longitudinal directions, as well as to study the response of the system to the space-time evolution.

References

[1] A. Adare *et al.* (PHENIX Collaboration), Phys. Rev. Lett. **107**, 252301 (2011).

[2] C. Gale, S. Jeon, B. Schenke, P. Tribedy, and R. Venugopalan, Phys. Rev. Lett. **100**, 012302 (2013).

[3] G. Aad *et al.* (ATLAS Collaboration), JHEP **11** (2013) 183.

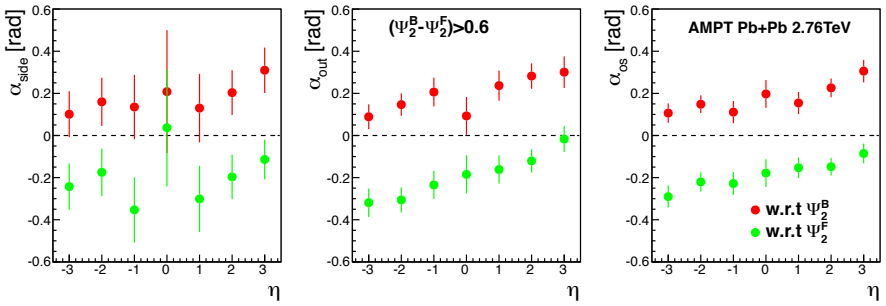

Figure 5: Phase shift parameters α obtained from the $R_{\rm s}^2$, $R_{\rm o}^2$, and $R_{\rm os}$ as a function of η. Results measured with respect to forward and backward event planes ($\Psi_2^{\rm F}$, $\Psi_2^{\rm B}$) are shown, with the event cut of $(\Psi_2^{\rm B} - \Psi_2^{\rm F}) > 0.6$.

[4] J. Schukraft, A. Timmins, and S. A. Voloshin, Phys. Lett. B **719**, 394 (2013).

[5] P. Bożek, W. Broniowski, and J. Moreira, Phys. Rev. C **83**, 034911 (2011).

[6] F. Retière and M. A. Lisa, Phys. Rev. C **70**, 044907 (2004).

[7] C. J. Plumberg, C. Shen, and U. Heinz, Phys. Rev. C **88**, 044914 (2013).

[8] J. Jia and P. Huo, Phys. Rev. C **90**, 034915 (2014).

[9] J. Jia and P. Huo, Phys. Rev. C **90**, 034905 (2014).

[10] S. Pratt, Phys. Rev. D **33**, 72 (1986).

[11] G. Bertsch, M. Gong, and M. Tohyama, Phys. Rev. C **37**, 1896 (1988).

Multiplicity, Jet, and Transverse Mass dependence of Bose-Einstein Correlations in e^+e^-- Annihilation*

Wesley J. Metzger[1],

[1]IMAPP, Radboud University, 6525 AJ Nijmegen, The Netherlands

Abstract

Bose-Einstein correlations of pairs of identical charged pions produced in hadronic Z decays are analyzed for both two- and three-jet events. A parametrization suggested by the τ-model is used to investigate the dependence of the Bose-Einstein correlation function on track multiplicity, number of jets, and transverse momentum.

1 Introduction

After a brief review of relevant previous results, new *preliminary* results are presented on the dependence of the Bose-Einstein correlation function on track and jet multiplicity and transverse momentum, using a parametrization which has been found [1] to describe well Bose-Einstein correlations (BEC) in hadronic Z decay, namely that of the τ-model [2, 3],

1.1 Review

The Bose-Einstein correlation function, R_2, is usually parametrized as

$$R_2 = \gamma \left[1 + \lambda \exp\left(-(rQ)^2\right)\right](1 + \epsilon Q)\,, \tag{1}$$

*This talk was also given at *XLIV International Symposium on Multiparticle Dynamics*, Bologna, 8–12 September 2014.

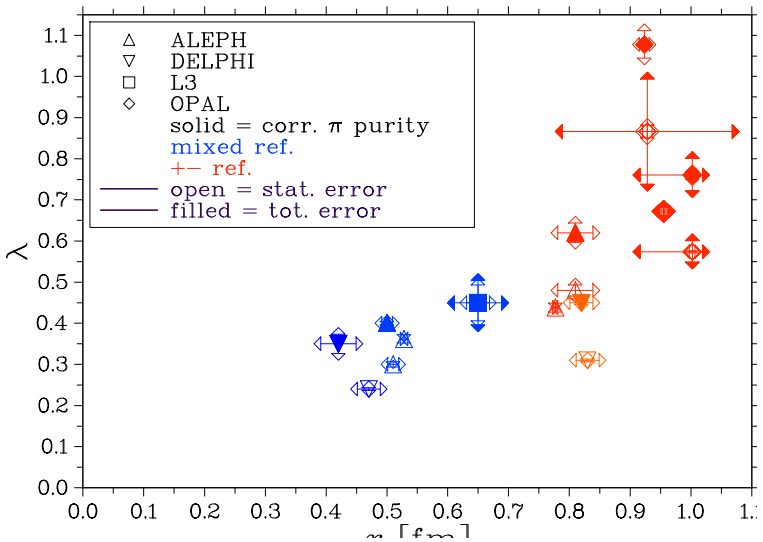

Figure 1: λ and r at $\sqrt{s} = M_{\mathrm{Z}}$ found in the LEP experiments [4–10].

and is measured by $R_2(Q) = \rho(Q)/\rho_0(Q)$, where $\rho(Q)$ is the density of identical boson pairs with invariant four-momentum difference $Q = \sqrt{-(p_1 - p_2)^2}$ and $\rho_0(Q)$ is the similar density in an artificially constructed reference sample, which should differ from the data only in that it does not contain BEC.

Dependence on the reference sample Two methods were frequently used at LEP to construct ρ_0: unlike-sign pion pairs from the same event, and like-sign pairs from different events. The latter method is generally referred to as mixed events. However, it must be pointed out that the observed values of the parameters r and λ depend to a great extent on which reference sample is used. This is clearly seen in Fig. 1 where the values of λ and r found for charged-pion pairs from hadronic Z decays by the LEP experiments ALEPH [4, 5], DELPHI [6], L3 [7] and OPAL [8–10] are displayed. Solid points are corrected for pion purity; open points are not. This correction increases the value of λ but has little effect on the value of r. All of the results with $r > 0.7$ fm were obtained using an unlike-sign reference sample, while those with smaller r were obtained with a mixed reference sample. The choice of reference sample clearly has a large effect on the observed values of λ and r. In comparing results we must therefore be sure that the reference samples used are comparable.

Dependence on the particle mass It has been suggested, on several grounds [17], that r should depend on the particle mass as $r \propto 1/\sqrt{m}$. Values of r found at LEP for various types of particle are shown in Fig. 2. Comparing only results using the same type of reference sample (in this case mixed), we see no evidence for a $1/\sqrt{m}$ dependence. Rather, the data suggest one value of r for mesons and a smaller value for baryons. The value for baryons, about 0.1 fm, seems very small, since the size of a proton is an order of magnitude greater. If true it is telling us something unexpected about the mechanism of baryon production.

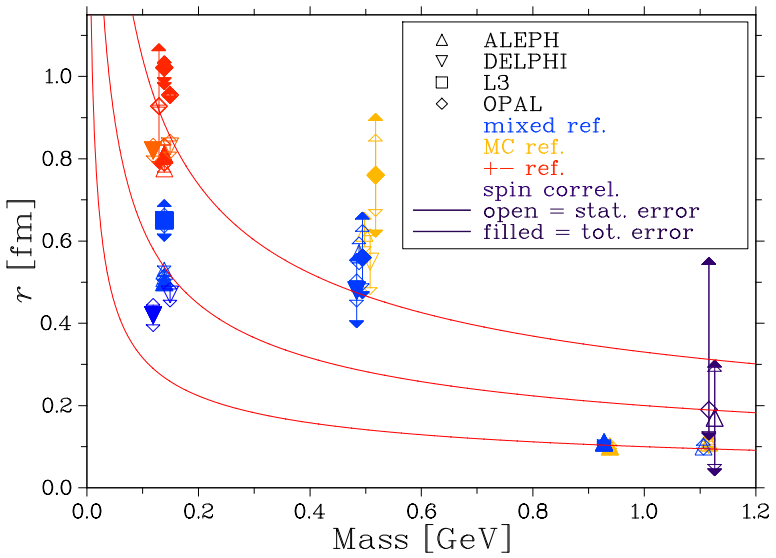

Figure 2: Dependence of r on the mass of the particle as determined at $\sqrt{s} = M_{\mathrm{Z}}$ from 2-particle BEC for charged pions [4–10], charged kaons [11,12] and neutral kaons [11,13,14] and from Fermi-Dirac correlations for protons [13] and lambdas [15,16]. The curves illustrate a $1/\sqrt{m}$ dependence.

Dependence on the transverse mass However, r has been observed to depend on the transverse mass of the particle pair, [18, 19] as is shown in Fig. 3.

Dependence on particle and jet multiplicity The OPAL collaboration has studied the dependence of r and λ on the charged track multiplicity and on the number of jets [9]. They used an opposite-sign reference sample, which necessitated the exclusion of regions of Q where R_2 was too strongly affected by resonances in the reference sample. To describe the long-range correlations they introduced a quadratic term resulting in

$$R_2(Q) = \gamma \left[1 + \lambda \exp\left(-(rQ)^2\right)\right] \left(1 + \epsilon Q + \delta Q^2\right) \ . \tag{2}$$

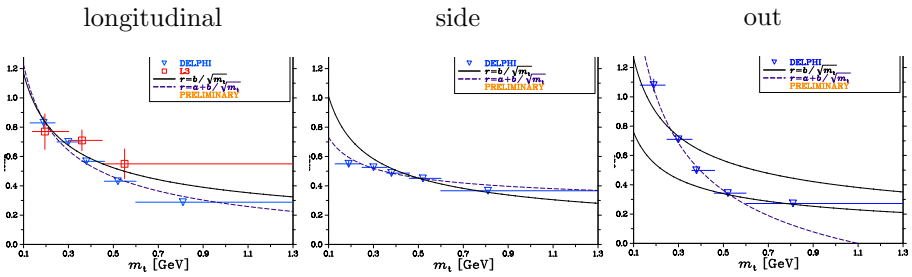

Figure 3: The transverse mass dependence of the components of r in the LCMS from Refs. 18, 19.

They observed a linear rise of r with charged track multiplicity as well as an increase of r with the number of jets. The behavior of λ was the opposite. However, when only two-jet (or only three-jet) events were selected, r was approximately independent of multiplicity.

1.2 τ-model

However, the "classic" parametrization of Eq. (1) is found to be inadequate, even when it is generalized to allow for a Lévy distribution of the source:

$$R_2 = \gamma \left[1 + \lambda \exp\left(-\left(rQ\right)^{\alpha}\right)\right] \left(1 + \epsilon Q\right) , \quad 0 < \alpha \leq 2 \tag{3}$$

This was not realized for a long time because the correlation function was only plotted up to $Q = 2\,\mathrm{GeV}$ or less. In Ref. 1 Q was plotted to $4\,\mathrm{GeV}$, and it became apparent that there is a region of anti-correlation ($R_2 < 1$) extending from about $Q = 0.5$ to $1.5\,\mathrm{GeV}$. This anti-correlation, as well as the BEC correlation are well described by the τ-model.

In the τ-model R_2 is found to depend not only on Q, but also on quantities a_1 and a_2. For two-jet events $a = 1/m_{\mathrm{t}}$, where $m_{\mathrm{t}} = \sqrt{m^2 + p_{\mathrm{t}}^2}$ is the transverse mass of a particle). Parameters of the model are the parameters of the Lévy distribution which describes the proper time of particle emission: α, the index of stability of the Lévy distribution; a width parameter $\Delta\tau$; and the proper time τ_0 at which particle production begins.

We shall use a simplified parametrization [1] where τ_0 is assumed to be zero and a_1 and a_2 are combined with $\Delta\tau$ to form an effective radius R:

$$R_2(Q) = \gamma \left[1 + \lambda \cos\left(\left(R_{\mathrm{a}}Q\right)^{2\alpha}\right) \exp\left(-\left(RQ\right)^{2\alpha}\right)\right] \left(1 + \epsilon Q\right) , \tag{4a}$$

$$R_{\mathrm{a}}^{2\alpha} = \tan\left(\frac{\alpha\pi}{2}\right) R^{2\alpha} . \tag{4b}$$

Note that the difference between the parametrizations of Eqs. (3) and 4 is the presence of the $\cos$ term, which accounts for the description of the anti-correlation. The parameter R describes the BEC peak, and R_{a} describes the anti-correlation region. While one might have had the insight to add, *ad hoc*, a $\cos$ term to Eq. (3), it is the τ-model which predicts a relationship, Eq. (4b), between R and R_{a}.

A fit of Eq. (4) to L3 two-jet events is shown in Fig. 4, from which it is seen that the τ-model describes both the BEC peak and the anti-correlation region quite well. Also the three-jet data is well described [1], which is perhaps surprizing since the τ-model is inspired by a picture of fragmentation of a single string.

It must also be pointed out that the τ-model has its shortcomings: The τ-model predicts that R_2 depends on the two-particle momentum difference only through Q, not through components of Q. However, this is found not to be the case [1]. Nevertheless, regardless of the validity of the τ-model, Eq. (4) provides a good description of the data. Accordingly, we shall use it in the following.

Since the results on the dependence of the BEC parameters on particle and jet multiplicities and on transverse mass mentioned in Sect. 1.1 were obtained using the classic Gaussian parametrization, Eq. (1), and since this parametrization has been shown to be inadequate, in the rest of this paper we investigate these properties using the τ-model parametrization, Eq. (4). The results are *preliminary*.

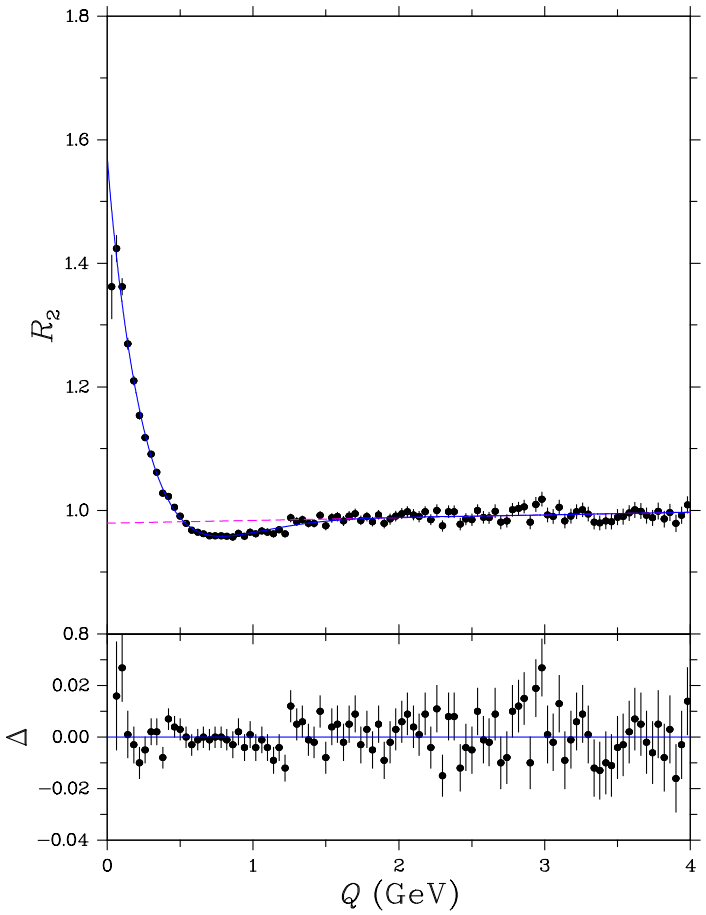

Figure 4: The Bose-Einstein correlation function R_2 for two-jet events. The curve corresponds to the fit of Eq. (4). Also plotted is Δ, the difference between the fit and the data. The dashed line represents the long-range part of the fit, *i.e.*, $\gamma(1 + \epsilon Q)$. The figure is taken from Ref. 1.

1.3 l3 Data

The data were collected by the L3 detector at an e^+e^- center-of-mass energy of $\sqrt{s} \simeq 91.2\,\mathrm{GeV}$. Approximately 36 million like-sign pairs of well-measured charged tracks from about 0.8 million hadronic Z decays are used. This data sample is identical to that of Ref. 1.

The same event mixing technique is used to construct ρ_0 as in Ref. 1.

Using the JADE algorithm, events can be classified according to the number of jets. The number of jets in a particular event depends on the jet resolution parameter of the algorithm, y_{cut}. We define y_{23}^{J} as that value of y_{cut} at which the number of jets in the event changes from two to three. Small y_{23} corresponds to narrow two-jet events, large y_{23} to events with three or more well-separated jets.

2 New *Preliminary* Results

The parameters of the Bose-Einstein correlation function have been found to depend on charged multiplicity, the number of jets, and the transverse mass. However these quantities are related. Both the charged particle multiplicity and the transverse mass increase rapidly with the number of jets. This is seen in Fig. 5, where the average transverse mass and the average charged multiplicity are plotted *vs.* y_{23}^{J}. In the following we investigate the dependence of R and λ on these three quantities.

An unfortunate property of the τ-model parameterization, Eq. (4), is that the estimates of α and R from fits tend to be highly correlated. Therefore, to stabilize the fits, α is fixed to the value 0.44, which corresponds to the value obtained in a fit to all events.

While we show only the results using the JADE jet algorithm, we have also performed the same analysis using the Durham algorithm. It is found to lead to the same conclusions.

2.1 Dependence of R and λ on track and jet multiplicities

The dependence of R and λ on the detected charge multiplicity,[1] is shown in Figs. 6 and 7, respectively, for two- and three-jet events as well as for all events.

For all events R is seen to increase linearly with the multiplicity, as was observed for R by OPAL. However, the same linear increase is also seen for two- and three-jet events, with R for three-jet events and for all events being approximately equal and R for two-jet events shifted lower by about a 0.5 fm. This contrasts with the OPAL observation of little dependence of r on multiplicity for two- and three-jet events.

For all events, as well as for two- and three-jet events, λ decreases with multiplicity, the rate of decrease becoming less for high multiplicity. It is higher for three-jet events than for two-jet events, with the values for all events lying in between. This contrasts with the OPAL observation that λ was higher for two-jet events, as well as the OPAL observation that the decrease of λ with multiplicity is linear.

[1] The charge multiplicity is approximately given by $N_{\mathrm{ch}} \approx 1.7 N_{\mathrm{ch}}^{\mathrm{det}}$.

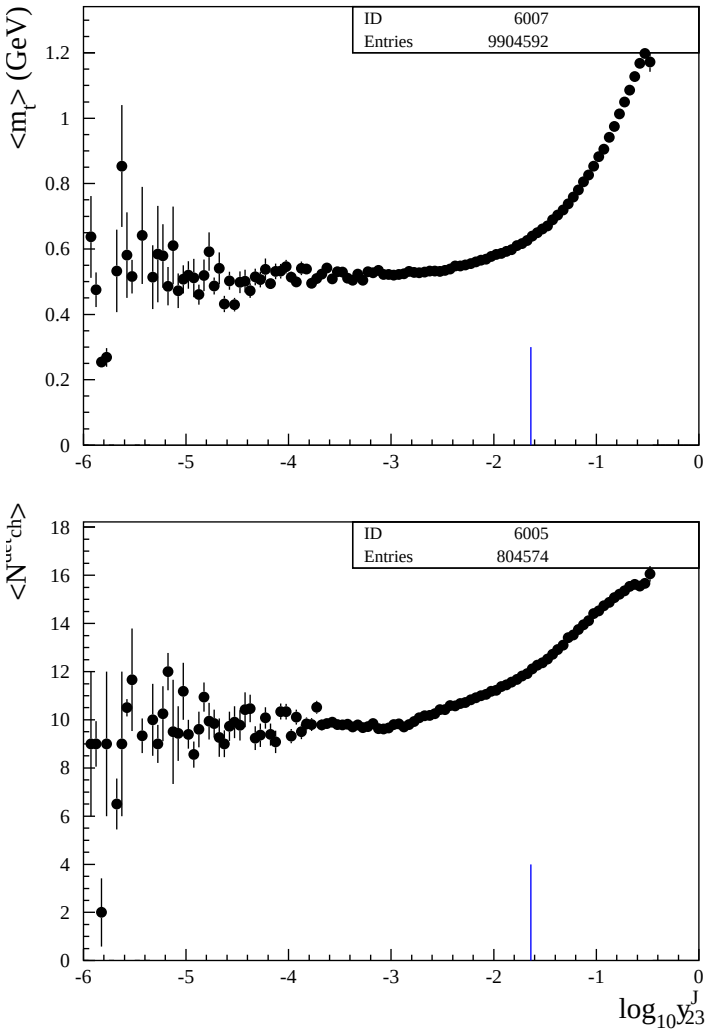

Figure 5: The average transverse mass and the average charged multiplicity as function of y_{23}^{J}. The short vertical line at $\log_{10} y_{23}^{\mathrm{J}} = -1.638$ corresponds to the cut used to define 2- and 3-jet events.

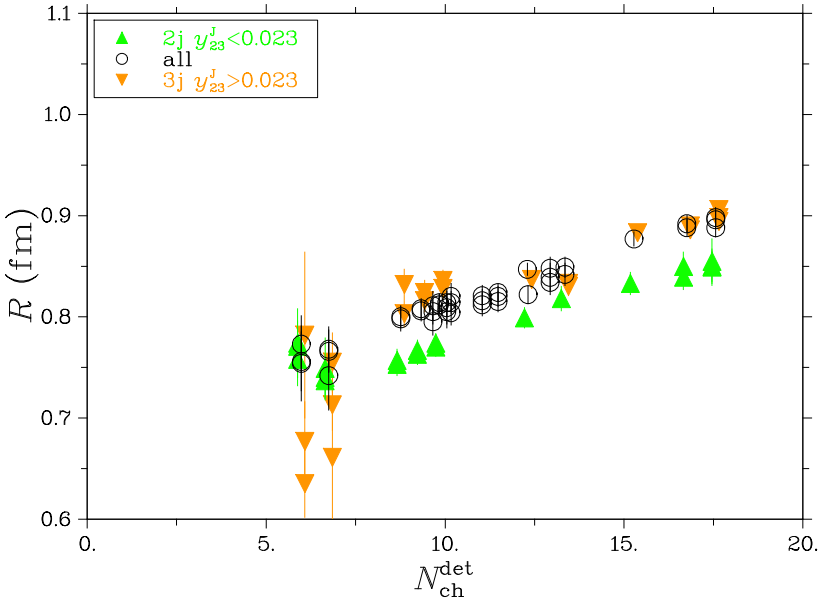

Figure 6: R obtained in fits of Eq. (4) as function of detected charged multiplicity for two-jet events ($y_{23}^{\rm J} < 0.23$), for three-jet events ($y_{23}^{\rm J} > 0.23$), and all events

2.2 Dependence of R and λ on trasverse mass and jet multiplicity

The dependence of R and λ on track multiplicity is shown in Figs. 8 and 9, respectively, for various selections on the transverse momentum, $p_{\rm t}$, (or, equvilantly, $m_{\rm t}$) of the tracks. For two-jet events both R and λ are slightly higher when both tracks have $p_{\rm t} < 0.5$ GeV than when only one track is required to have so small a $p_{\rm t}$. For three-jet events the same may be true, but the statistical significance is less; the difference decreases with multiplicity. When neither track has $p_{\rm t} < 0.5$ GeV, the values of both R and λ are much lower for both two- and three-jet events. In all cases both R and λ increase with multiplicity, and the values for two-jet events are roughly equal to those for three-jet events.

3 Conclusions

The dependence of R and λ for the τ-model parametrization is different from that of r and λ found by OPAL for the usual Gaussian parametrization. However, it is unclear how much the differences depend on the use of different reference samples and how much on the parametrization used.

Multiplicity, number of jets, and transverse mass all affect the values of R and λ in the τ-model parametrization, Eq. (4).

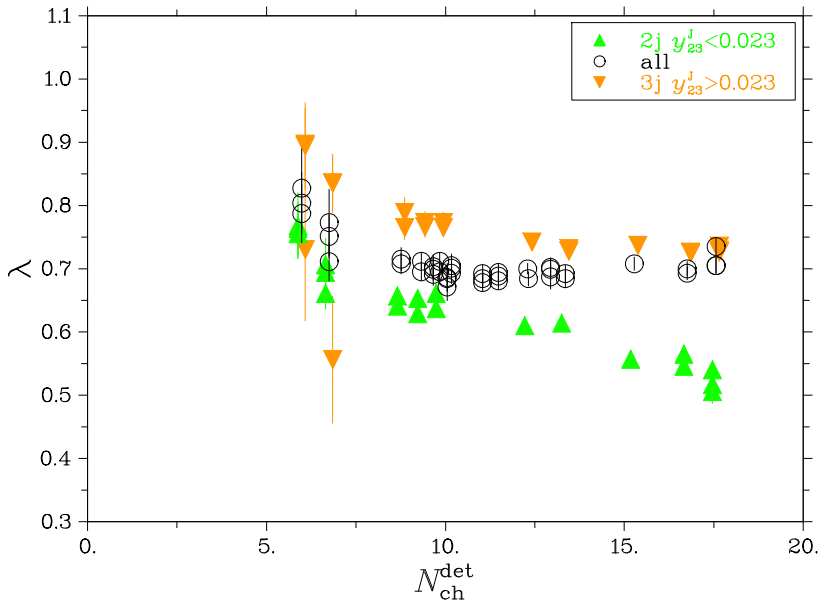

Figure 7: λ obtained in fits of Eq. (4) as function of detected charged multiplicity for two-jet events ($y_{23}^{\mathrm{J}} < 0.23$), for three-jet events ($y_{23}^{\mathrm{J}} > 0.23$), and all events

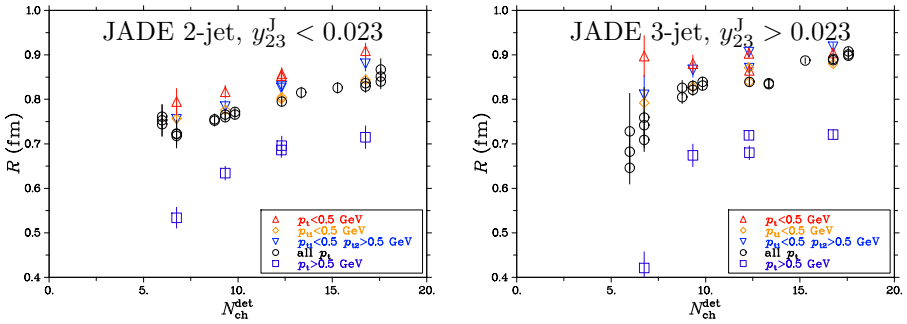

Figure 8: R obtained in fits of Eq. (4) as function of detected charged multiplicity (left) for two-jet events ($y_{23}^{\mathrm{J}} < 0.23$) and (right) for three-jet events ($y_{23}^{\mathrm{J}} > 0.23$) with the following selections on p_{t}: $\triangle$ both tracks having $p_{\mathrm{t}} < 0.5$ GeV; $\diamond$ at least one track having $p_{\mathrm{t}} < 0.5$ GeV; $\triangledown$ one track with $p_{\mathrm{t}} < 0.5$ GeV and one with $p_{\mathrm{t}} > 0.5$ GeV; $\circ$ all tracks; $\square$ both tracks having $p_{\mathrm{t}} > 0.5$ GeV. Note that $p_{\mathrm{t}} = 0.5$ GeV corresponds to $m_{\mathrm{t}} = 0.52$ GeV.

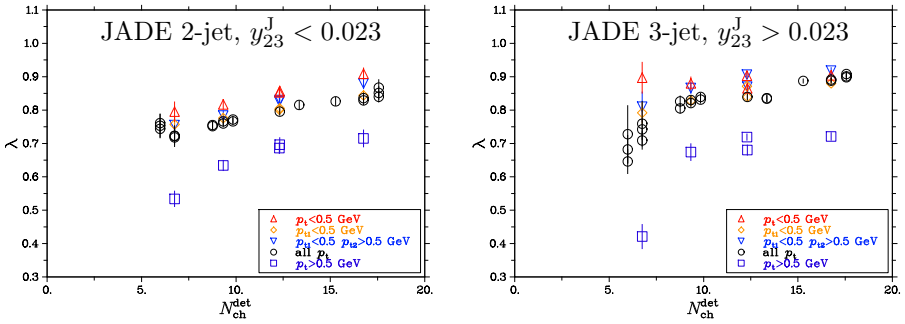

Figure 9: λ obtained in fits of Eq. (4) as function of detected charged multiplicity (left) for two-jet events ($y_{23}^{J} < 0.23$) and (right) for three-jet events ($y_{23}^{J} > 0.23$) with the following selections on p_t: $\triangle$ both tracks having $p_t < 0.5$ GeV; $\diamond$ at least one track having $p_t < 0.5$ GeV; $\triangledown$ one track with $p_t < 0.5$ GeV and one with $p_t > 0.5$ GeV; $\circ$ all tracks; $\square$ both tracks having $p_t > 0.5$ GeV. Note that $p_t = 0.5$ GeV corresponds to $m_t = 0.52$ GeV.

References

[1] L3 Collab. P. Achard *et al.*, Eur. Phys. J. **C71** (2011) 1–25, 10.1140/epjc/s10052-011-1648-8.

[2] T. Csörgő and J. Zimányi, Nucl. Phys. **A517** (1990) 588–598.

[3] T. Csörgő, W. Kittel, W.J. Metzger, and T. Novák, Phys. Lett. **B663** (2008) 214–216.

[4] ALEPH Collab. D. Decamp *et al.*, Z. Phys. **C54** (1992) 75–85.

[5] ALEPH Collab. A. Heister *et al.*, Eur. Phys. J. **C36** (2004) 147–159.

[6] DELPHI Collab. P. Abreu *et al.*, Phys. Lett. **B286** (1992) 201–210.

[7] L3 Collab. P. Achard *et al.*, Phys. Lett. **B540** (2002) 185–198.

[8] OPAL Collab. P.D. Acton *et al.*, Phys. Lett. **B267** (1991) 143–153.

[9] OPAL Collab. G. Alexander *et al.*, Z. Phys. **C72** (1996) 389–398.

[10] OPAL Collab. G. Abbiendi *et al.*, Eur. Phys. J. **C16** (2000) 423–433.

[11] DELPHI Collab. P. Abreu *et al.*, Phys. Lett. **B379** (1996) 330–340.

[12] OPAL Collab. G. Abbiendi *et al.*, Eur. Phys. J. **C21** (2001) 23–32.

[13] ALEPH Collab. S. Schael *et al.*, Phys. Lett. **B611** (2005) 66–80.

[14] OPAL Collab. R. Akers *et al.*, Z. Phys. **C67** (1995) 389–401.

[15] ALEPH Collab. R. Barate *et al.*, Phys. Lett. **B475** (2000) 395–406.

[16] OPAL Collab. G. Alexander *et al.*, Phys. Lett. **B384** (1996) 377–387.

[17] Gideon Alexander, Rep. Prog. Phys. **66** (2003) 481–522.

[18] B. Lörstad and O.G. Smirnova, in Proc. 7$^{\rm th}$ Int. Workshop on Multiparticle Production "Correlations and Fluctuations", ed. R.C. Hwa *et al.*, (World Scientific, Singapore, 1997), p. 42.

[19] J.A. van Dalen, in Proc. 8$^{\rm th}$ Int. Workshop on Multiparticle Production "Correlations and Fluctuations '98: From QCD to Particle Interferometry", ed. T. Csörgő *et al.*, (World Scientific, Singapore, 1999), p. 37.

Femtoscopy with identified hadrons in pp, pPb, and peripheral PbPb collisions in CMS

F. Siklér[1] for the CMS Collaboration

[1]Wigner RCP, Budapest, Hungary

Abstract

Short range correlations of identified charged hadrons in pp ($\sqrt{s}$ = 0.9, 2.76, and 7 TeV), pPb ($\sqrt{s_{\mathrm{NN}}}$ = 5.02 TeV), and peripheral PbPb collisions ($\sqrt{s_{\mathrm{NN}}}$ = 2.76 TeV) are studied with the CMS detector at the LHC. Charged pions, kaons, and protons at low p_{T} and in laboratory pseudorapidity $|\eta| < 1$ are identified via their energy loss in the silicon tracker. The two-particle correlation functions show effects of quantum statistics, Coulomb interaction, and also indicate the role of multi-body resonance decays and mini-jets. The characteristics of the one-, two-, and three-dimensional correlation functions are studied as a function of pair momentum and the charged-particle multiplicity of the event. The extracted radii are in the range 1-5 fm, reaching highest values for very high multiplicity pPb, also for similar multiplicity PbPb collisions, and decrease with increasing k_{T}. The dependence of radii on multiplicity and k_{T} largely factorizes and appears to be insensitive to the type of the colliding system and center-of-mass energy.

1 Introduction

Measurements of the correlation between hadrons emitted in high energy collisions of nucleons and nuclei can be used to study the spatial extent and shape of the created system. The characteristic radii, the homogeneity lengths, of the particle emitting source can be extracted with reasonable precision [1]. The topic of quantum correlations was well researched in the past by the CMS Collaboration [2, 3] using unidentified charged hadrons produced in $\sqrt{s}$ = 0.9, 2.36, and 7 TeV pp

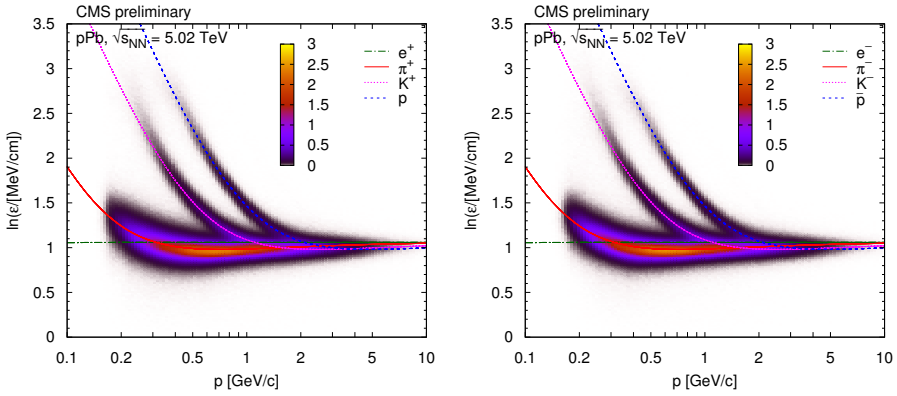

Figure 1: The distribution of $\ln \varepsilon$ as a function of total momentum p, for positively (left) and negatively (right) charged particles, in case of pPb collisions at $\sqrt{s_{\mathrm{NN}}} =$ 5.02 TeV. Here ε is the most probable energy loss rate at a reference path length $l_0 = 450$ μm. The z scale is shown in arbitrary units and is linear. The curves show the expected $\ln \varepsilon$ for electrons, pions, kaons, and protons (full theoretical calculation, Eq. (30.11) in Ref. [8]).

collisions. Those studies only included one-dimensional fits (q_{inv}) of the correlation function. Our aim was to look for effects present in pp, pPb, and PbPb interactions using the same analysis methods, producing results as a function of the transverse pair momentum k_{T} and of the fully corrected charged-particle multiplicity N_{tracks} (in $|\eta| < 2.4$) of the event. In addition, not only charged pions, but also charged kaons are studied. All details of the analysis are given in Ref. [4].

2 Data analysis

The analysis methods (event selection, reconstruction of charged particles in the silicon tracker, finding interaction vertices, treatment of pile-up) are identical to the ones used in the previous CMS papers on the spectra of identified charged hadrons produced in $\sqrt{s} = 0.9$, 2.76, and 7 TeV pp [5] and $\sqrt{s_{\mathrm{NN}}} = 5.02$ TeV pPb collisions [6]. A detailed description of the CMS (Compact Muon Solenoid) detector can be found in Ref. [7].

For the present study 8.97, 9.62, and 6.20 M minimum bias events are used from pp collisions at $\sqrt{s} = 0.9$ TeV, 2.76 TeV, and 7 TeV, respectively, while 8.95 M minimum bias events are available from pPb collisions at $\sqrt{s_{\mathrm{NN}}} = 2.76$ TeV. The data samples are completed by 3.07 M peripheral (60–100%) PbPb events, where 100% corresponds to fully peripheral, 0% means fully central (head-on) collision. The centrality percentages for PbPb are determined via measuring the sum of the energies in the forward calorimeters.

The multiplicity of reconstructed tracks, N_{rec}, is obtained in the region $|\eta| <$ 2.4. Over the range $0 < N_{\mathrm{rec}} < 240$, the events were divided into 24 classes, a region that is well covered by the 60–100% centrality PbPb collisions. To facilitate comparisons with models, the corresponding corrected charged particle multiplicity N_{tracks} in the same acceptance of $|\eta| < 2.4$ is also determined.

The reconstruction of charged particles in CMS is bounded by the acceptance of

the tracker and by the decreasing tracking efficiency at low momentum. Particle-by-particle identification using specific ionization is possible in the momentum range $p < 0.15$ GeV/c for electrons, $p < 1.15$ GeV/c for pions and kaons, and $p < 2.00$ GeV/c for protons (Fig. 1). In view of the (η, p_{T}) regions where pions, kaons, and protons can all be identified, only particles in the band $-1 < \eta < 1$ (in the laboratory frame) were used for this measurement. In this analysis a very high purity ($> 99.5\%$) particle identification is required, ensuring that less than 1% of the examined particle pairs would be fake.

2.1 Correlations

The pair distributions are binned in the number of reconstructed charged particles N_{rec} of the event, in the transverse pair momentum $k_{\mathsf{T}} = |\mathbf{p_{T,1}} + \mathbf{p_{T,2}}|/2$, and also in the relative momentum $(\mathbf{q})$ variables in the longitudinally co-moving system of the pair. One-dimensional ($q_{\mathsf{inv}} = |\mathbf{q}|$), two-dimensional $(q_{\mathsf{l}}, q_{\mathsf{t}})$, and three-dimensional $(q_{\mathsf{l}}, q_{\mathsf{o}}, q_{\mathsf{s}})$ analyses are performed. Here q_{o} is the component of $\mathbf{q_t}$ parallel to $\mathbf{k_T}$, q_{s} is the component of $\mathbf{q_t}$ perpendicular to $\mathbf{k_T}$.

The construction of the $\mathbf{q}$ distribution for the "signal" pairs is straightforward: all valid particle pairs from the same event are taken and the corresponding histograms are filled. There are several choices for the construction of the background. We considered the following three prescriptions:

- particles from the actual event are paired with particles from some given number of, in our case 25, preceding events ("event mixing"); only events belonging to the same multiplicity (N_{rec}) class are mixed;
- particles from the actual event are paired, the laboratory momentum vector of the second particle is rotated around the beam axis by 90 degrees ("rotated");
- particles from the actual event are paired, but the laboratory momentum vector of the second particle is negated ("mirrored").

Based on the goodness-of-fit distributions the event mixing prescription was used while the rotated and mirrored versions, which give worse or much worse χ^2/ndf values, were employed in the estimation of the systematic uncertainty.

The measured two-particle correlation function $C_2(\mathbf{q})$ is the ratio of signal and background distributions

$$C_2(\mathbf{q}) = \frac{N_{\mathsf{signal}}(\mathbf{q})}{N_{\mathsf{bckgnd}}(\mathbf{q})}, \tag{1}$$

where the background is normalized such that it has the same integral as the signal distribution. The quantum correlation function C_{BE}, part of C_2, is the Fourier transform of the source density distribution $f(\mathbf{r})$. There are several possible functional forms that are commonly used to fit C_{BE} present in the data: Gaussian $(1 + \lambda \exp\left[-(qR)^2/(\hbar c)^2\right])$ and exponential parametrizations $(1+\lambda \exp\left[-(|q|R)/(\hbar c)\right])$, and a mixture of those in higher dimensions. (The denominator $\hbar c = 0.197$ GeV fm is usually omitted from the formulas, we will also do that in the following.) Factorized forms are particularly popular, such as $\exp(-q_{\mathsf{l}}^2 R_l^2 - q_{\mathsf{o}}^2 R_o^2 - q_{\mathsf{s}}^2 R_s^2)$ or $\exp(-q_{\mathsf{l}} R_l - q_{\mathsf{o}} R_o - q_{\mathsf{s}} R_s)$ with some theoretical motivation. (Here q_{o} is the component of the transverse relative momentum $\mathbf{q_t}$ parallel to $\mathbf{k_T}$, while q_{s} is the component of $\mathbf{q_t}$ perpendicular to $\mathbf{k_T}$.) The fit parameters are usually interpreted as

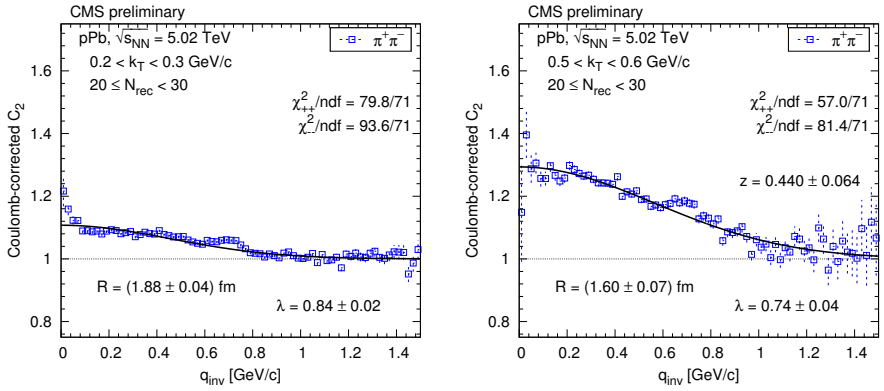

Figure 2: Contribution of clusters (mini-jets and multi-body decays of resonances) to the measured Coulomb-corrected correlation function of $\pi^+\pi^-$ (open squares) for some selected k_{T} bins, $20 \leq N_{\mathrm{rec}} < 30$, in case of pPb interactions at $\sqrt{s_{\mathrm{NN}}} =$ 5.02 TeV. The solid curves show the result of the Gaussian fit.

chaoticity λ, and characteristic radii R, the homogeneity lengths, of the particle emitting source.

As will be shown in Sec. 3, the exponential parametrization does a very good job in describing all our data. It corresponds to the Cauchy (Lorentz) type source distribution $f(r) = R/(2\pi^2\left[r^2 + (R/2)^2\right]^2)$. Theoretical studies show that for the class of stable distributions, with index of stability $0 < \alpha \leq 2$, the Bose-Einstein correlation function has a stretched exponential shape [9, 10]. The exponential correlation function implies $\alpha = 1$. (The Gaussian would correspond to the special case of $\alpha = 2$.) The forms used for the fits are

$$C_{\mathrm{BE}}(q_{\mathrm{inv}}) = 1 + \lambda \exp\left[-q_{\mathrm{inv}}R\right], \tag{2}$$

$$C_{\mathrm{BE}}(q_{\mathrm{l}}, q_{\mathrm{t}}) = 1 + \lambda \exp\left[-\sqrt{(q_l R_l)^2 + (q_t R_t)^2}\right], \tag{3}$$

$$C_{\mathrm{BE}}(q_{\mathrm{l}}, q_{\mathrm{o}}, q_{\mathrm{s}}) = 1 + \lambda \exp\left[-\sqrt{(q_l R_l)^2 + (q_o R_o)^2 + (q_s R_s)^2}\right], \tag{4}$$

meaning that the system in multi-dimensions is an ellipsoid with differing radii R_l, R_t, or R_l, R_o, and R_s.

2.2 Coulomb interaction

After the removal of the trivial phase space effects (ratio of signal and background distributions), one of the most important source of correlations is the mutual Coulomb interaction of the emitted charged particles. The effect of the Coulomb interaction is taken into account by the factor K, the squared average of the relative wave function Ψ, as $K(q_{\mathrm{inv}}) = \int d^3\mathbf{r}\ f(\mathbf{r})\ |\Psi(\mathbf{k}, \mathbf{r})|^2$, where $f(\mathbf{r})$ is the source intensity discussed above. For pointlike source, $f(\mathbf{r}) = \delta(\mathbf{r})$, and we get the Gamow factor $G(\eta) = |\Psi(0)|^2 = 2\pi\eta/[\exp(2\pi\eta) - 1]$, where $\eta = \pm\alpha m/q_{\mathrm{inv}}$ is the Landau parameter, α is the fine-structure constant, m is the mass of the particle. The positive sign should be used for repulsion, and the negative is for attraction.

For an extended source, a more elaborate treatment is needed [11, 12]. The use of the Bowler-Sinyukov formula [13, 14] is popular. Our data on unlike-sign

correlation functions show that while the Gamow factor might give a reasonable description of the Coulomb interaction for pions, it is clearly not enough for kaons. In the q range studied in this analysis $\eta \ll 1$ applies. The absolute square of confluent hypergeometric function of the first kind F, present in Ψ, can be well approximated as $|F|^2 \approx 1+2\eta\,\mathrm{Si}(x)$ where Si is the sine integral function. Furthermore, for Cauchy type source functions the factor K is nicely described by the formula $K(q_{\mathrm{inv}}) = G(\eta)\,[1 + \pi\eta q_{\mathrm{inv}}R/(1.26 + q_{\mathrm{inv}}R)]$. In the last step we substituted $q_{\mathrm{inv}} = 2k$. The factor π in the approximation comes from the fact that for large kr arguments $\mathrm{Si}(kr) \to \pi/2$. Otherwise it is a simple but faithful approximation of the result of a numerical calculation, with deviations less than 0.5%.

2.3 Clusters: mini-jets, multi-body decays of resonances

The measured unlike-sign correlation functions show contributions from various resonances. The seen resonances include the $\mathrm{K}^0_{\mathrm{S}}$, the $\rho(770)$, the $\mathrm{f}_0(980)$, the $\mathrm{f}_2(1270)$ decaying to $\pi^+\pi^-$, and the $\phi(1020)$ decaying to $\mathrm{K}^+\mathrm{K}^-$. Also, $\mathrm{e}^+\mathrm{e}^-$ pairs from γ conversions, when misidentified as pion pairs, can appear as a very low q_{inv} peak in the $\pi^+\pi^-$ spectrum. With increasing N_{rec} values the effect of resonances diminishes, since their contribution is quickly exceeded by the combinatorics of unrelated particles.

Nevertheless, the Coulomb-corrected unlike-sign correlation functions are not always close to unity at low q_{inv}, but show a Gaussian-like hump (Fig. 2). That structure has a varying amplitude but a stable scale (σ of the corresponding Gaussian) of about 0.4 GeV/c. This feature is often related to particles emitted inside low momentum mini-jets, but can be also attributed to the effect of multi-body decays of resonances. In the following we will refer to those possibilities as fragmentation of clusters, or cluster contribution. We have fitted the one-dimensional unlike-sign correlation functions with a $(N_{\mathrm{rec}}, k_{\mathrm{T}})$-dependent Gaussian parametrization [4].

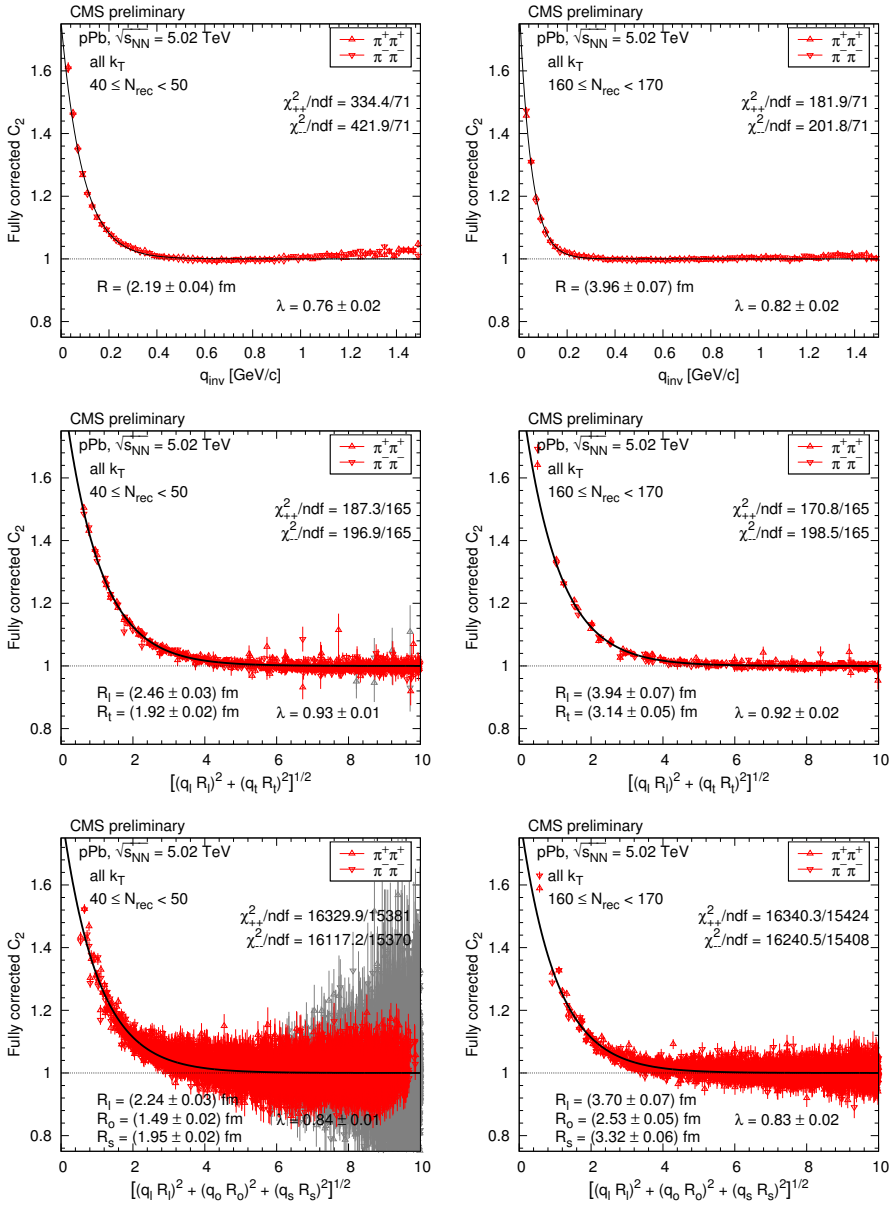

Figure 3: The like-sign correlation function of pions (red triangles) corrected for Coulomb interaction and cluster contribution (mini-jets and multi-body resonance decays) as a function of q_{inv} or the combined momentum, in some selected N_{rec} bins for all k_{T}. The solid curves indicate fits with the exponential Bose-Einstein parametrization.

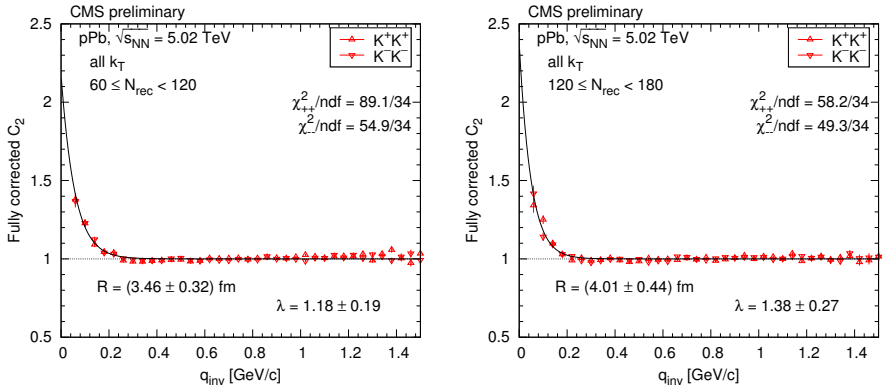

Figure 4: The like-sign correlation function of kaons (red triangles) corrected for Coulomb interaction and cluster contribution (mini-jets and multi-body resonance decays) as a function of q_{inv}, in some selected N_{rec} bins for all k_{T}. The solid curves indicate fits with the Bose-Einstein parametrization.

The cluster contribution can be also extracted in the case of like-sign correlation function, if the momentum scale of the Bose-Einstein correlation and that of the cluster contribution ($\approx$0.4 GeV/c) are different enough. An important element in both mini-jet and multi-body resonance decays is the conservation of electric charge that results in a stronger correlation for unlike-sign pairs than for like-sign pairs. Hence the cluster contribution is expected to be also present for like-sign pairs, with similar shape but a somewhat smaller amplitude. The form of the cluster-related contribution obtained from unlike-sign pairs, but now multiplied by the extracted relative amplitude z, is used to fit the like-sign correlations. A selection of correlation functions and fits are shown in Figs. 3 and 4.

In the case of two and three dimensions the measured unlike-sign correlation functions show that instead of q_{inv}, the length of the weighted sum of $\mathbf{q}$ components is a better common variable.

3 Results

The systematic uncertainties are dominated by two sources: the dependence of the final results on the way the background distribution is constructed, and the uncertainties of the amplitude z of the cluster contribution for like-sign pairs with respect to those for unlike-sign ones.

The characteristics of the extracted one- and two-dimensional correlation functions as a function of the transverse pair momentum k_{T} and of the charged-particle multiplicity N_{tracks} (in the range $|\eta| < 2.4$ in the laboratory frame) of the event are presented here. Three-dimensional results are detailed in Ref. [4]. In all the following plots (Figs. 5–8), the results of positively and negatively charged hadrons are averaged. For clarity, values and uncertainties of the neighboring N_{tracks} bins were averaged two by two, and only the averages are plotted. The central values of radii and chaoticity parameter λ are given by markers. The statistical uncertainties are indicated by vertical error bars, the combined systematic uncertainties (choice of background method; uncertainty of the relative amplitude z of the cluster contribution; low q exclusion) are given by open boxes. Unless indicated, the lines are

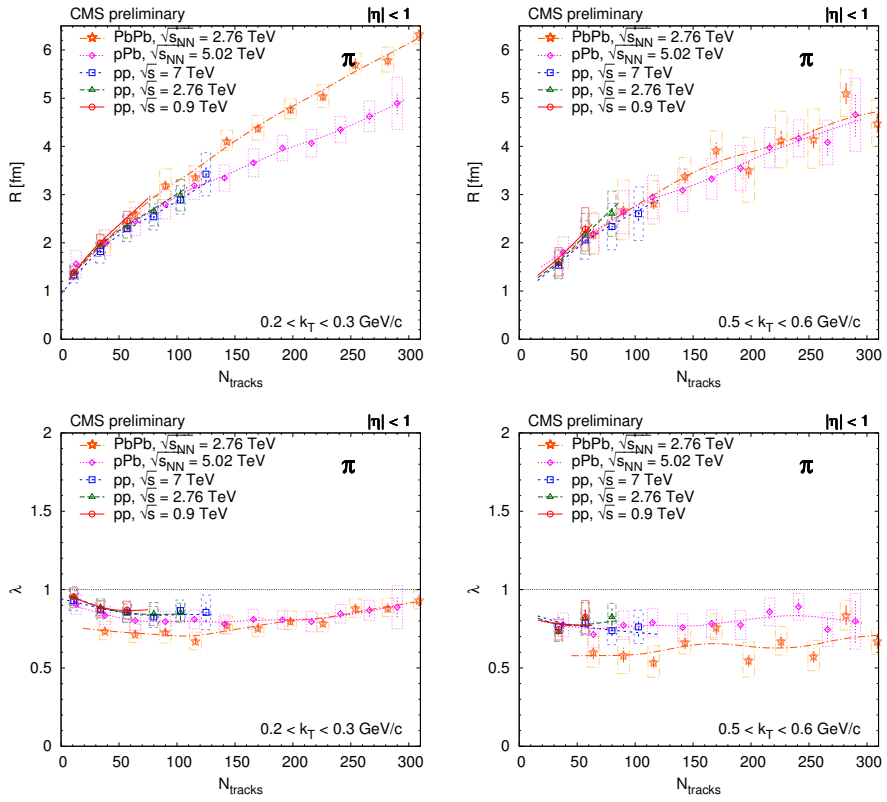

Figure 5: N_{tracks} dependence of the one-dimensional pion radius (top) and the one-dimensional pion chaoticity parameter (bottom), shown here for several k_{T} bins, for all studied reactions. Lines are drawn to guide the eye.

drawn to guide the eye (cubic splines whose coefficients are found by weighing the data points with the inverse of their squared statistical uncertainty).

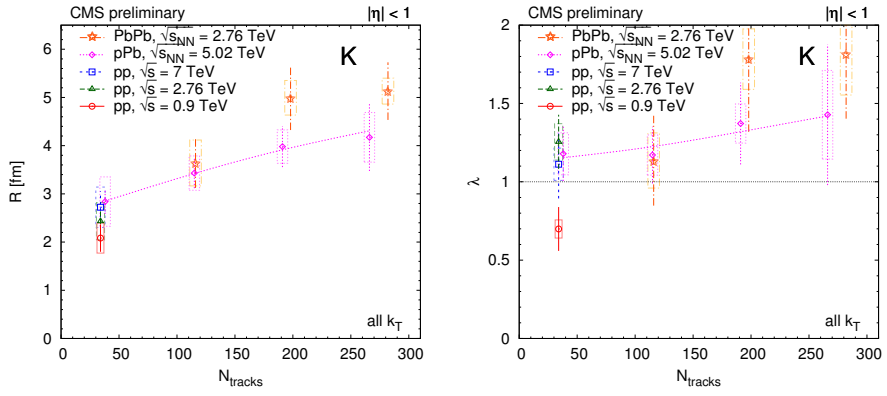

Figure 6: N_{tracks} dependence of the one-dimensional kaon radius (left) and chaoticity parameter (right). Lines are drawn to guide the eye.

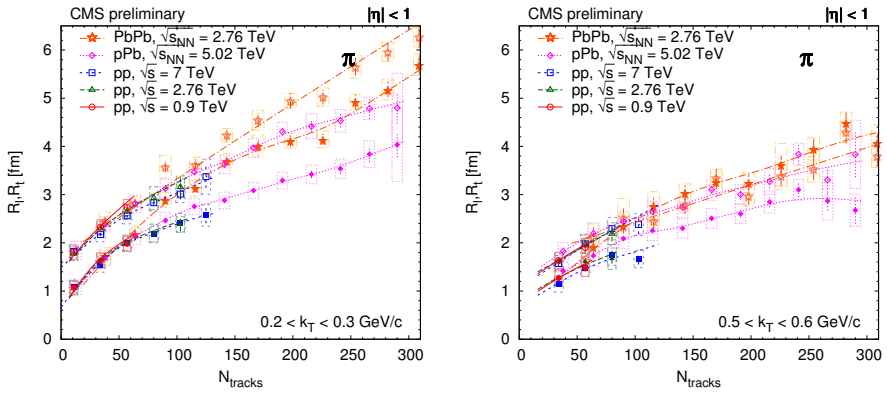

Figure 7: N_{tracks} dependence of the two-dimensional pion radii (R_l – open symbols, R_t – closed symbols), shown here for several k_{T} bins, for all studied reactions. Lines are drawn to guide the eye.

The extracted exponential radii for pions increase with increasing N_{tracks} for all systems and center-of-mass energies studied, for one, two, and three dimensions alike. Their values are in the range 1–5 fm, reaching highest values for very high multiplicity pPb, also for similar multiplicity PbPb collisions. The N_{tracks} dependence of R_l and R_t is similar for pp and pPb in all k_{T} bins, and that similarity also applies to peripheral PbPb if $k_{\text{T}} > 0.4$ GeV/c. In general there is an ordering, $R_l > R_t$, and $R_l > R_s > R_o$, thus the pp and pPb source is elongated in the beam direction. In the case of peripheral PbPb the source is quite symmetric, and shows a slightly different N_{tracks} dependence, with largest differences for R_t and R_o, while there is a good agreement for R_l and R_s. The most visible divergence between pp, pPb and PbPb is seen in R_o that could point to the differing lifetime of the created systems in those collisions.

The kaon radii also show some increase with N_{tracks}, although its magnitude is smaller than that for pions. Longer lived resonances and rescattering may play a role here.

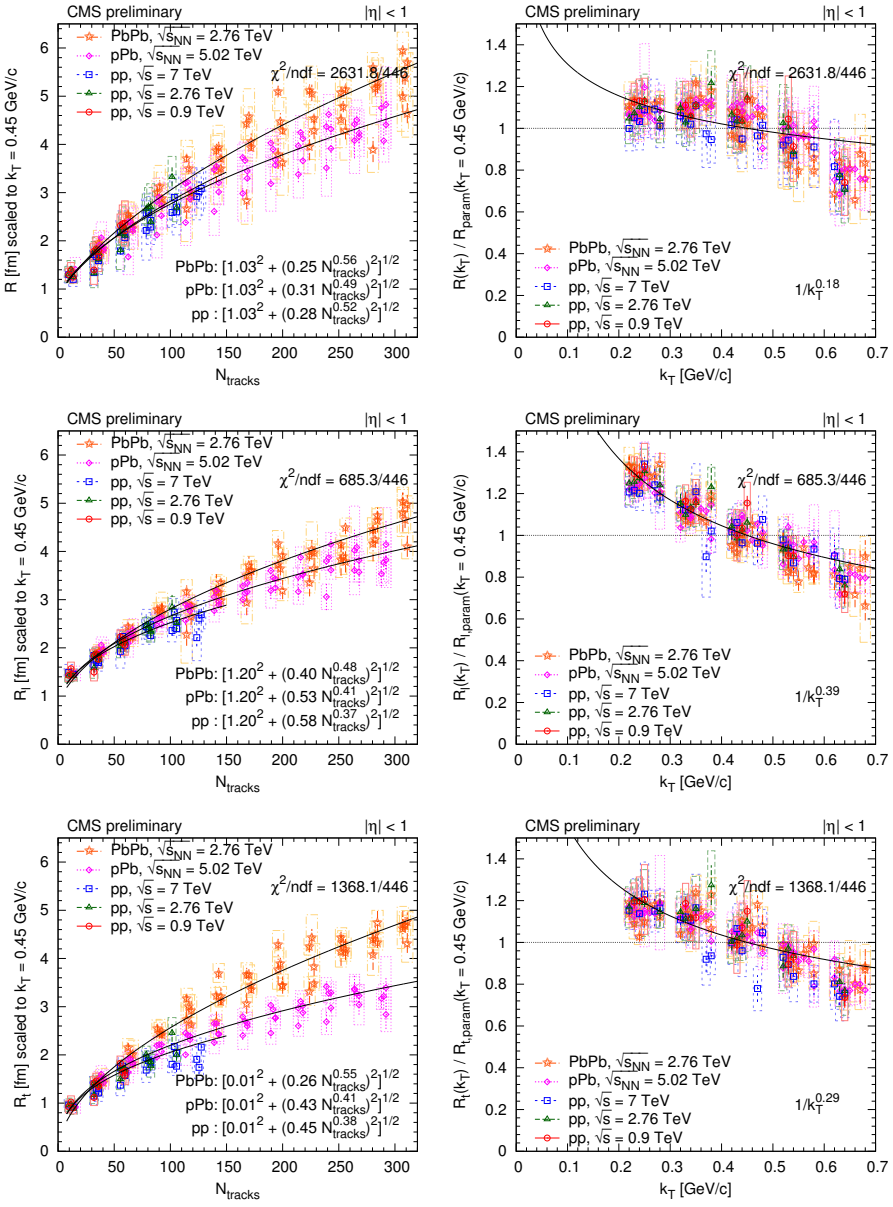

Figure 8: Left: radius parameters as a function of N_{tracks} scaled to $k_{\text{T}} = 0.45$ GeV/c with help of the parametrization R_{param} (Eq. (5)). Right: ratio of the radius parameter and the value of the parametrization R_{param} (Eq. (5)) at $k_{\text{T}} = 0.45$ GeV/c as a function k_{T}. (Points were shifted to left and to right with respect to the center of the k_{T} bin for better visibility.) Upper row: R from the one-dimensional (q_{inv}) analysis. Middle row: R_l from the two-dimensional ($q_{\text{l}}, q_{\text{t}}$) analysis. Bottom row: R_t from the two-dimensional ($q_{\text{l}}, q_{\text{t}}$) analysis. Fit results are indicated in the figures, for details see text.

3.1 Scaling

The extracted radii are in the range 1–5 fm, reaching highest values for very high multiplicity pPb, also for similar multiplicity PbPb collisions, and decrease with increasing k_{T}. By fitting the radii with a product of two independent functions of N_{tracks} and k_{T}, the dependences on multiplicity and pair momentum appear to factorize. In some cases the radii are less sensitive to the type of the colliding system and center-of-mass energy. Radius parameters as a function of N_{tracks} at $k_{\mathrm{T}} = 0.45$ GeV$/c$ are shown in the left column of Fig. 8. We have also fitted and plotted the following R_{param} functions

$$R_{\mathrm{param}}(N_{\mathrm{tracks}}, k_{\mathrm{T}}) = \left[a^2 + (bN_{\mathrm{tracks}}^{\beta})^2\right]^{1/2} \cdot (0.2 \text{ GeV}/c/k_{\mathrm{T}})^{\gamma}\,, \tag{5}$$

where the minimal radius a and the exponents γ of k_{T} are kept the same for a given radius component, for all collision types. This choice of parametrization is based on previous results [15]. The minimal radius can be connected to the size of the proton, while the power-law dependence on N_{tracks} is often attributed to the freeze-out density of hadrons. The ratio of radius parameter and the value of the above parametrization at $k_{\mathrm{T}} = 0.45$ GeV$/c$ as a function k_{T} is shown in the right column of Fig. 8.

4 Conclusions

The similarities observed in the N_{tracks} dependence may point to a common critical hadron density in pp, pPb, and peripheral PbPb collisions, since the present correlation technique measures the characteristic size of the system near the time of the last interactions.

Acknowledgments

This work was supported by the Hungarian Scientific Research Fund (K 109703), and the Swiss National Science Foundation (SCOPES 152601).

References

[1] B. Erazmus, R. Lednicky, L. Martin, D. Nouais, and J. Pluta, "Nuclear interferometry from low-energy to ultrarelativistic nucleus-nucleus collisions." SUBATECH-96-03, 1996.

[2] CMS Collaboration, "Measurement of Bose-Einstein correlations with first CMS data," Phys. Rev. Lett. 105 (2010) 032001, arXiv:1005.3294 [hep-ex].

[3] CMS Collaboration, "Measurement of Bose-Einstein Correlations in pp Collisions at $\sqrt{s} = 0.9$ and 7 TeV," JHEP 05 (2011) 029, arXiv:1101.3518 [hep-ex].

[4] CMS Collaboration, "Femtoscopy with identified charged hadrons in pp, pPb, and peripheral PbPb collisions at LHC energies," CMS PAS HIN-14-013 (2014) .

[5] CMS Collaboration, "Study of the inclusive production of charged pions, kaons, and protons in pp collisions at $\sqrt{s} = 0.9$, 2.76, and 7 TeV," Eur. Phys. J. C 72 (2012) 2164, arXiv:1207.4724 [hep-ex].

[6] CMS Collaboration, "Study of the production of charged pions, kaons, and protons in pPb collisions at $\sqrt{s_{NN}} =$ 5.02 TeV," Eur. Phys. J. C 74 (2014) 2847, arXiv:1307.3442 [hep-ex].

[7] CMS Collaboration, "The CMS experiment at the CERN LHC," JINST 3 (2008) S08004.

[8] Particle Data Group, J. Beringer, *et al.*, "Review of Particle Physics," Phys. Rev. D 86 (2012) 010001.

[9] T. Csörgő, S. Hegyi, and W. Zajc, "Bose-Einstein correlations for Levy stable source distributions," Eur. Phys. J. C 36 (2004) 67–78, arXiv:nucl-th/0310042 [nucl-th].

[10] T. Csörgő, S. Hegyi, and W. Zajc, "Stable Bose-Einstein correlations," arXiv:nucl-th/0402035 [nucl-th].

[11] S. Pratt, "Coherence and Coulomb effects on pion interferometry," Phys. Rev. D 33 (1986) 72.

[12] M. Biyajima and T. Mizoguchi, "Coulomb wave function correction to Bose-Einstein correlations." SULDP-1994-9, 1994.

[13] M. Bowler, "Coulomb corrections to Bose-Einstein correlations have been greatly exaggerated," Phys. Lett. B 270 (1991) 69–74.

[14] Y. Sinyukov, R. Lednicky, S. Akkelin, J. Pluta, and B. Erazmus, "Coulomb corrections for interferometry analysis of expanding hadron systems," Phys. Lett. B 432 (1998) 248–257.

[15] M. Lisa, "Femtoscopy in heavy ion collisions: Wherefore, whence, and whither?," AIP Conf. Proc. 828 (2006) 226–237, arXiv:nucl-ex/0512008 [nucl-ex].

Higher order anisotropies in hydrodynamics

M. Csanád, A. Szabó, S. Lökös, A. Bagoly,

Eötvös University, Pázmány P. s. 1/a, 1117 Budapest, Hungary

Abstract

In the last years it has been revealed that if measuring relative to higher order event planes Ψ_n, higher order flow coefficients v_n for $n > 2$ can be measured. It also turned out that Bose-Einstein (HBT) correlation radii also show 3rd order oscillations if measured versus the third order event plane Ψ_3. In this paper we investigate how these observables can be described via analytic hydro solutions and hydro parameterizations. We also investigate the time evolution of asymmetry coefficients and the mixing of velocity field asymmetries and density asymmetries.

1 Introduction

In relativistic heavy ion collisions, an expanding and cooling medium is created, usually referred to as the strongly interacting quark gluon plasma. Hydrodynamics provides a tool to investigate the time evolution of this medium, and exact analytic models are particularly useful in this regards. Usually spherical, axial or ellipsoidal symmetry is assumed in these solutions, as these are simple to handle and represent geometries that yield realistic results for many soft observables. However, event-by-event fluctuating nuclear distributions yield event-by-event fluctuating initial conditions, and thus higher order azimuthal asymmetries arise. In order to describe these one has to utilize higher order asymmetries in hydro as well. This was successfully done in numerical calculations, see for example [1, 2].

In this paper we discuss the first exact analytic solutions [3] of relativistic hydrodynamics that assume higher order asymmetries and thus give realistic higher order flow coefficients. We also discuss possible extensions of this approach, by analyzing

the time evolution of the asymmetries in a numerical approach, and by investigating the effect of spatial versus momentum space anisotropies.

2 Multipole solutions and higher order anisotropies

The first 1+3D relativistic solution with ellipsoidal geometry was discovered in Ref. [4]. In this solution the thermodynamic quantities at a given proper-time τ are constant on the surfaces of an expanding ellipsoid, defined by the s scale variable

$$s = \frac{r_x^2}{X^2} + \frac{r_y^2}{Y^2} + \frac{r_z^2}{Z^2}, \tag{1}$$

where r_x,r_y,r_z are the spatial coordinates, while X, Y, Z are the time-dependent axes of the ellipsoid. The velocity profile as a function of space-time coordinates x^μ is given in form of a 3D Hubble flow, i.e. $u^\mu = x^\mu/\tau$. With these, $u^\mu \partial_\mu s = 0$ holds (if the expansion of the axes is linear in time). In Ref. [4] it was already indicated, that more complicated scale variables can also be written up (with $u^\mu \partial_\mu s = 0$ still holding). In Ref. [3] we showed that this solution can indeed be extended to multipole symmetries with a generalized scale variable

$$s = \frac{r^N}{R^N} \left(1 + \epsilon \cos(N\phi)\right) \tag{2}$$

With the s given in Eq. (2), the new solutions can be given in cylindrical coordinates (r, ϕ, z) as:

$$s = \sum_N \frac{r^N}{R^N} \left(1 + \epsilon_N \cos(N(\phi - \psi_N))\right) + \frac{z^N}{R^N} \tag{3}$$

$$n = n_f \left(\frac{\tau_f}{\tau}\right)^3 \nu(s) \tag{4}$$

$$T = T_f \left(\frac{\tau_f}{\tau}\right)^{3/\kappa} \frac{1}{\nu(s)} \tag{5}$$

$$p = p_f \left(\frac{\tau_f}{\tau}\right)^{3+3/\kappa} \tag{6}$$

and u^μ still representing a Hubble-flow, as in the original paper of Ref. [4]. In the formula for s, ψ_N being the Nth order reaction planes (which cancel from the observables). This way we get new solutions with almost arbitrary shaped initial distributions, see Fig. 1. It is important to note here that however, the initial state fluctuation in the observed collision is present through the orientation of the Nth order reaction planes and the strength of higher order asymmetries, the event plane orientation itself does not affect the measured quantities. Thus if every v_N is measured relatively to the Nth order reaction plane, then the (event-through-event) averaged value of v_N will correspond to an average n-pole anisotropy ϵ_N.

We also calculated hadronic observables from the above solution (see details of the freeze-out scenario in Ref [3] or Ref. [5]. A comparison to PHENIX data on higher order harmonics measured in 200 GeV Au+Au collisions [6] is shown in Fig. 2. Fit parameters of the model are ϵ_N (for $N = 2, 3, 4$), u_t and b (T_0 and τ_0 was fixed to values given from spectra and HBT comparisons of a similar model, as described in Refs. [3, 5]).

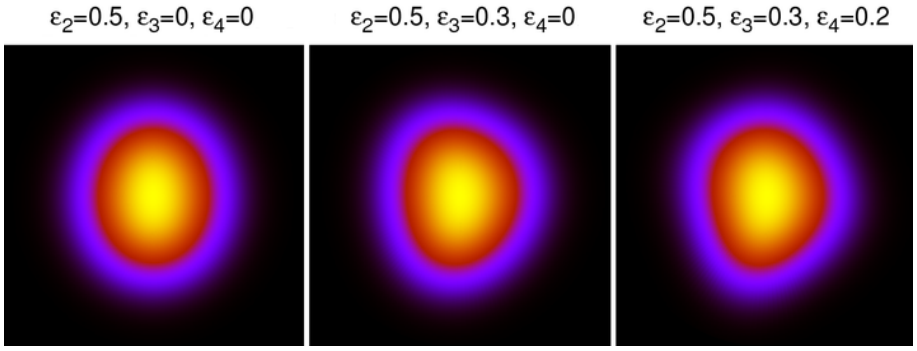

Figure 1: Heat map of s values in the transverse plane, with multiple superimposed symmetries. The more ϵ_N components are included, the more asymmetric the shape gets.

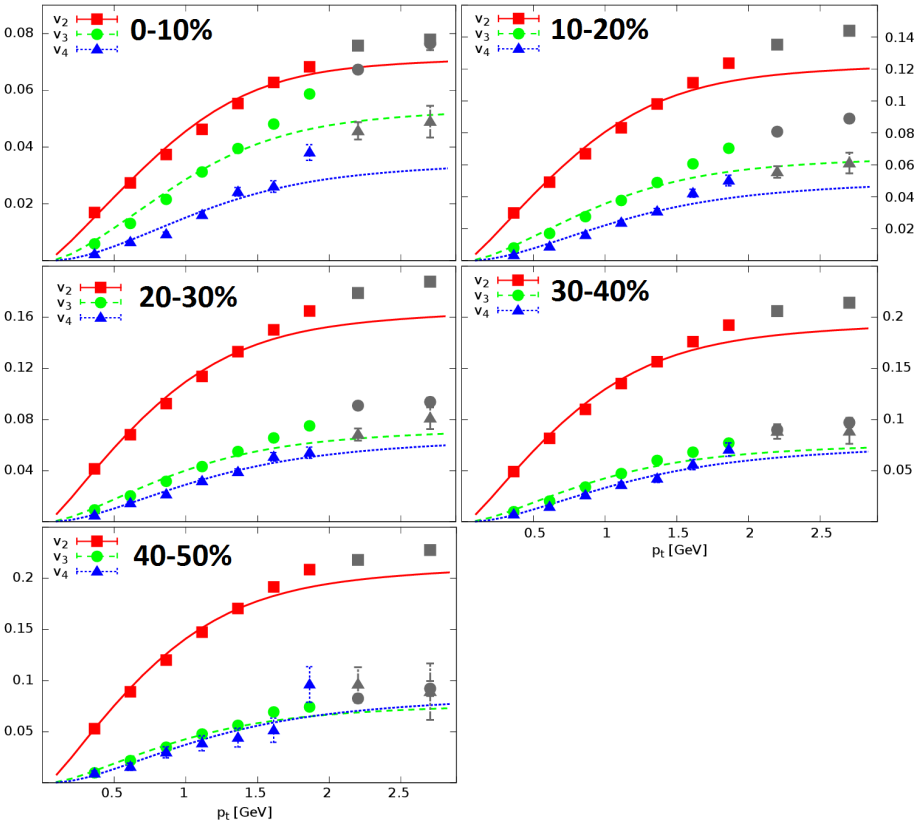

Figure 2: Fits to PHENIX 200 GeV Au+Au data [6] in 5 centrality bins. Fit parameters are summarized in Ref. [3]

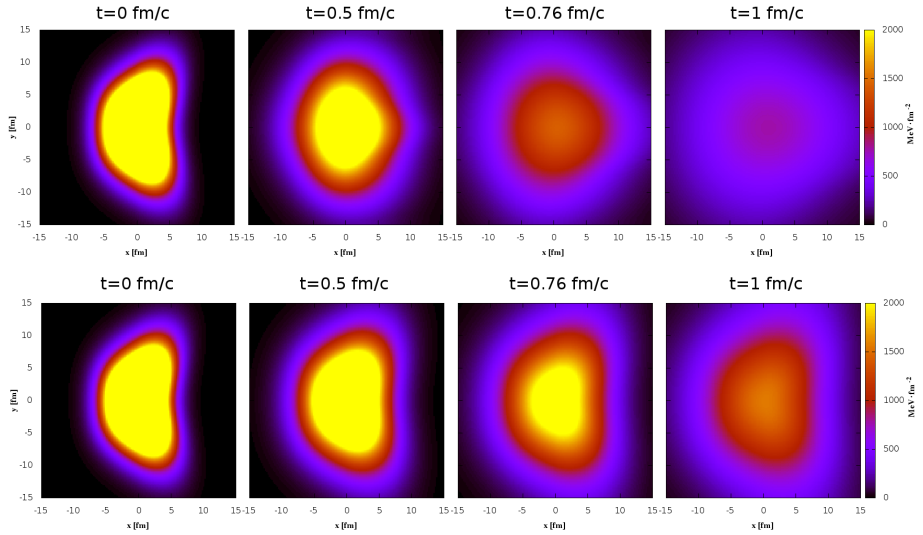

Figure 3: Time evolution of energy density. Top row shows viscosity free case, the bottom row with $\mu = 10\text{MeV} \cdot \text{fm}$ viscosity.

3 Time evolution of the anisotropies

In the above described solution, the anisotropies don't change over time - due to the lack of pressure gradients and the Hubble-flow. In a numerical framework, we investigated how the introduction of pressure gradients, various speeds of sound and viscosity coefficients influence the time evolution of the asymmetries, when starting from an initial condition that is very similar to one described by know analytic solutions – except in pressure, where we used a pressure profile similar to the density profile given in usual Hubble-expansion models [4, 3]. We used a multi-stage predictor-corrector method outlined in Ref. [7]. This is a finite volume scheme, where the initial flux is a weighted average of the Lax-Friedrichs and Lax-Wendroff fluxes, called GFORCE. This flux is used to make a new prediction on the grid points, which is used to get a better flux approximation. This procedure is repeated for a number of times, as described e.g. in Ref. [7]. This multi-stage flux gives results that are comparable to those of the Godunov method. We tested our method with known analytic solutions given in Refs. [8, 4, 3]. We analyzed both non-relativistic and relativistic hydrodynamics, and arrived at similar conclusions.

Fig. 3 shows the result of a nonrelativistic calculation of the time evolution of the energy density. If we assume a small amount of viscosity, it makes the flow itself and thus the disappearance of asymmetries slower. The time evolution of the asymmetries themselves is shown in Fig. 4. In this figure we also see the effect of speed of sound in this nonrelativistic calculation: the reduction of speed of sound makes the asymmetries disappear slower – due to the reduction of the speed of sound waves. A similar effect is seen in case of a relativistic calculation, as shown in Fig. 5: the increase of $\kappa = c_s^{-2}$ makes the disappearance of asymmetries slower. It is important to see that this also slows down the speed of cooling, which means the system will freeze out latter.

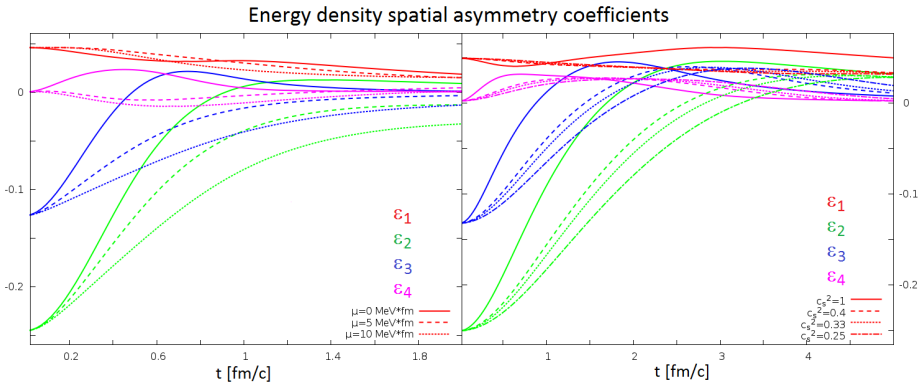

Figure 4: The time evolution of the asymmetry coefficients $\epsilon_{1,2,3,4}$ in the energy density, as modified by a small amount of viscosity (left plot) and the change in speed of sound (right plot).

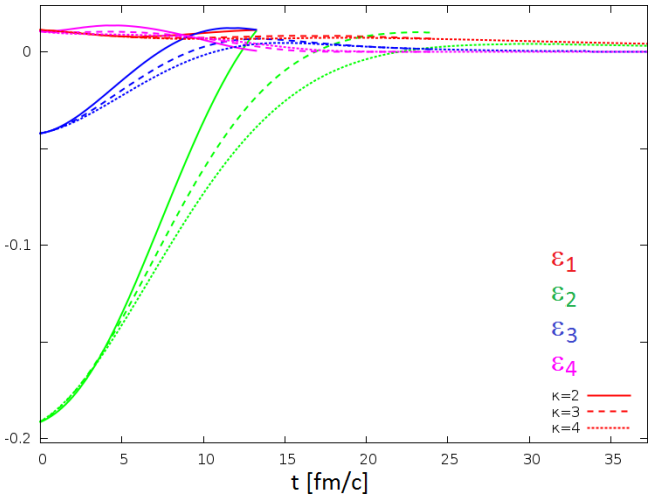

Figure 5: The time evolution of the asymmetry coefficients in the energy density in a relativistic calculation, as modified by the change in $\kappa = c_s^{-2}$ (right plot).

4 Anisotropy mixing

It is important to see that there may be asymmetries in both momentum space (i.e. in the velocity field) and in density (i.e. in energy density or pressure), and both influence the measured anisotropies. To investigate this effect, we created a multipole version of the Buda-Lund model [9], with a scale variable given in Eq. 3, but we introduced a multipole flow field as well. We start from a "flow potential" Φ, which gives us the flow:

$$\mathbf{v} = (\partial_x \Phi, \partial_y \Phi, \partial_z \Phi). \tag{7}$$

The flow field at a given time is spherically symmetric if $\Phi = \frac{r^2}{2H}$ with H being a Hubble-coefficient at that given time. Elliptical symmetry is obtained with $\Phi = \frac{r^2}{2H}(1 + \chi_2 \cos(2\varphi))$, while

$$\Phi = \frac{r^2}{2H}(1 + \chi_2 \cos(2\varphi)) + \frac{r^3}{3H^2}\chi_3 \cos(3\varphi)) \tag{8}$$

represents a triangular perturbation of the elliptical flow. Of course the various anisotropies can have various event planes (symmetry planes), but the specific angle of these does not enter into the results. Inspired by Ref. [10], we analyzed how $\chi_{2,3}$ and $\epsilon_{2,3}$ influence flow coefficients v_2 and v_3 – see results in Fig. 6. Compared to the spatial anisotropy, velocity field anisotropy has a much larger effect on elliptic and triangular flow coefficients.

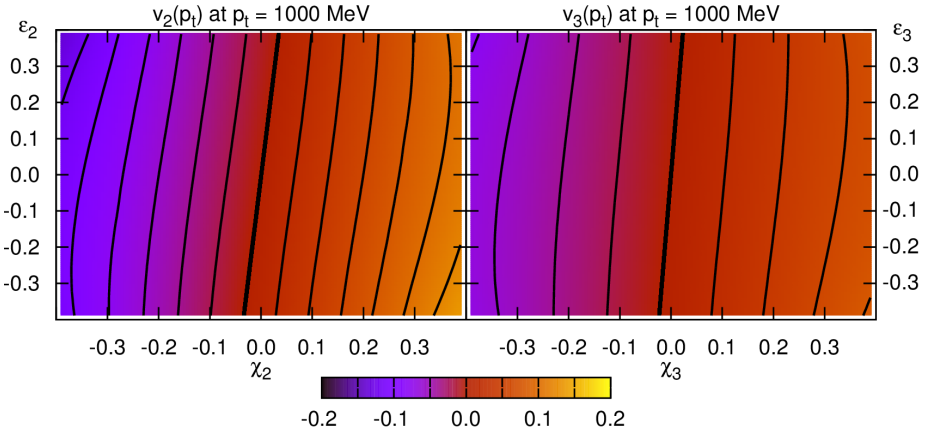

Figure 6: Dependence of flow anisotropy coefficients $v_{2,3}$ on asymmetry parameters $\chi_{2,3}$ and $\epsilon_{2,3}$. Velocity field asymmetry has a stronger influence on flow coefficients.

5 Summary and acknowledgments

In this paper we showed an extension of the scope of analytic relativistic hydrodynamics to higher order azimuthal asymmetries, compatible with realistic (event-by-event fluctuating) geometries. Higher order flow observables were calculated from this model, and are found to be compatible with data. In the analytic model,

anisotropy parameters were independent of time, thus we investigated their time evolution in a numerical framework, developed for this purpose. We also investigated how velocity- and density-field anisotropies "mix", in the framework of a multipole Buda-Lund model. We are thankful to Tamás Csörgõ and Márton Nagy for useful discussions with respect to this project. We thank the WPCF community and the WPCF 2014 organizers, in particular the local hosts, Tamás Novák and Tamás Csörgõ, for the possibility to present this work. We also thankfully acknowledge the support of the OTKA grant NK 101438.

References

[1] R. Chatterjee, D. K. Srivastava, and T. Renk arXiv:1401.7464 [hep-ph].

[2] L. Yan and J.-Y. Ollitrault *Phys.Lett.* **B744** (2015) 82–87, arXiv:1502.02502 [nucl-th].

[3] M. Csanád and A. Szabó *Phys.Rev.* **C90** no. 5, (2014) 054911, arXiv:1405.3877 [nucl-th].

[4] T. Csörgő, L. P. Csernai, Y. Hama, and T. Kodama *Heavy Ion Phys.* **A21** (2004) 73–84, nucl-th/0306004.

[5] M. Csanád and M. Vargyas *Eur. Phys. J.* **A44** (2010) 473–478, arXiv:0909.4842 [nucl-th].

[6] A. Adare *et al. Phys.Rev.Lett.* **107** (2011) 252301, arXiv:1105.3928 [nucl-ex].

[7] E. F. Toro and V. A. Titarev *J. Comp. Phys.* **216** (2016) 403–429.

[8] T. Csörgő, S. V. Akkelin, Y. Hama, B. Lukács, and Y. M. Sinyukov *Phys. Rev.* **C67** (2003) 034904, hep-ph/0108067.

[9] M. Csanád, T. Csörgő, and B. Lörstad *Nucl. Phys.* **A742** (2004) 80–94, nucl-th/0310040.

[10] M. Csanád, B. Tomásik, and T. Csörgő *Eur. Phys. J. A* **37** (2008) 111–119, arXiv:0801.4434 [nucl-th].

Collision Geometry and Flow in Uranium+Uranium Collisions

Andy Goldschmidt[1], Zhi Qiu[1,2], Chun Shen[1,3], Ulrich Heinz[1]

[1]Department of Physics, The Ohio State University, Columbus, OH 43210, USA
[2]Google Inc., Mountain View, CA 94043, USA
[3]Department of Physics, McGill University, Montreal, Quebec H3A 0G4, Canada

Abstract

Using event-by-event viscous fluid dynamics to evolve fluctuating initial density profiles from the Monte-Carlo Glauber model for U+U collisions, we report a "knee"-like structure in the elliptic flow as a function of collision centrality, located near 0.5% centrality as measured by the final charged multiplicity. This knee is due to the preferential selection of tip-on-tip collision geometries by a high-multiplicity trigger. Such a knee structure is not seen in the STAR data. This rules out the two-component MC-Glauber model for initial energy and entropy production. An enrichment of tip-tip configurations by triggering solely on high-multiplicity in the U+U collisions thus does not work. On the other hand, using the Zero Degree Calorimeters (ZDCs) coupled with event-shape engineering, we identify the selection purity of body-body and tip-tip events in the full-overlap U+U collisions. With additional constraints on the asymmetry of the ZDC signals one can further increases the probability of selecting tip-tip events in U+U collisions.

1 Introduction

High energy collisions between heavy ions are used to probe emergent phenomena in Quantum Chromodynamics (QCD), the theory of strong interaction. One feature of QCD is the transition from hadronic matter to a color-deconfined quark-gluon plasma (QGP) [1–3] as the temperature is increased. This transition can occur in heavy-ion collisions of sufficient energy for the system to melt into a hot dense fireball of asymptotically free quarks and gluons.

Relativistic hydrodynamic models have been successful in describing the dynamical evolution of QGP [4]. Motivated as a testing ground for these models, a U+U collisions program was recommended in order to study the unique collision geometry resulting from the prolate deformation of the uranium nucleus [5–11]. Such a program was carried out in 2012 at the Relativistic Heavy Ion Collider (RHIC) at Brookhaven National Lab [12].

To understand the attraction of uranium, consider that the initial temperature distribution of each QGP droplet is controlled by two main factors: deterministic collision geometry (i.e. the shape of the overlap region between two nuclei), and quantum mechanical fluctuations in the nucleon positions. For spherical nuclei, the collision geometry is entirely a function of the impact parameter. However, in prolate deformed uranium, the geometry of the initial temperature distribution also depends on the relative spatial orientation of the two nuclei which can be described by the Euler angles between their long major axis.

We focus in this paper on two limiting cases for fully overlapping uranium collisions. In one extreme we have "tip-tip" events, defined when the major axes of both nuclei are parallel to the beam direction. The opposite limit are "body-body" events, where the major axes of both nuclei are perpendicular to the beam direction and parallel to each other. We are interested in answering the question how, and with what precision, we can distinguish experimentally between these configurations. Their conceptual importance is explained in [7].

2 The model

To model the initial energy density distribution of U+U collisions we employ the two-component (wounded nucleon/binary collision) Monte-Carlo Glauber model. We use the deformed Woods-Saxon distribution

$$\rho(r,\theta,\varphi) = \frac{\rho_0}{1+e^{(r-r(\theta,\varphi))/d}} \tag{1}$$

to sample the positions of nucleons inside a uranium nucleus. In Eq. (1), the surface diffusiveness parameter is $d = 0.44$ fm and the saturation density parameter is $\rho_0 = 0.1660$ fm^{-3} [14, 15]. The spatial configuration of a uranium nucleus is deformed; we model its radius as [16]

$$r(\theta,\varphi) = r_0(1+\sum_{l=1}^{\infty}\sum_{m=-l}^{l}\beta_{lm}Y_l^m(\theta,\phi)), \tag{2}$$

where the average radius $r_0 = 6.86$ fm is adjusted in such a way that, after folding Eq. (1) with the finite charge radius of an individual nucleon, the resulting nuclear charge density distribution agrees with experimental constraints [15]. We assume

the uranium nucleus is azimuthally symmetric and choose [17] the non-vanishing deformation parameters $\beta_{20} = 0.28$ and $\beta_{40} = 0.093$ for the quadrupole and hexadecupole deformations along its main axis, respectively. The choices of these parameters agree well with a recent reanalysis in [18], except for β_{20} for which Ref. [18] gives the value 0.265.

We use the Woods-Saxon density (1) to Monte-Carlo sample the nucleon centers and represent each nucleon in the transverse plane by a gaussian areal density distribution about its center:

$$\rho_n(\vec{\mathbf{r}}_\perp) = \frac{1}{(2\pi B)^{3/2}} e^{-r^2/(2B)}. \tag{3}$$

The width parameter $B = \sigma_{NN}^{in}(\sqrt{s_{NN}})/14.30$ depends on collision energy as described in [19]. The sum of these gaussian nucleon density distributions represents the nuclear density distribution for the sampled nucleus at the time of impact and is used to compute the initial energy density distribution generated in the collision. For this calculation, the two-component Monte-Carlo Glauber model weighs a relative contribution from binary collisions N_b and wounded nucleon participants N_p [20].

The binary collision term counts the entropy deposited by pairs of colliding nucleons and is modeled by a gaussian distribution with the same size as a nucleon (see Eq .(3)) [21]; the total binary collision density per unit transverse area is

$$n_{\mathrm{BC}}(\vec{\mathbf{r}}_\perp) = \sum_{i,j} \gamma_{i,j} \frac{1}{2\pi B} e^{-\left|\vec{\mathbf{r}}_\perp - \vec{\mathbf{R}}_{i,j}\right|^2/(2B)} \tag{4}$$

where the sum is over all pairs of colliding nucleons and the normalization $\gamma_{i,j}$ is a Γ-distributed random variable with unit mean that accounts for multiplicity fluctuations in individual nucleon-nucleon collisions.

Each struck nucleon is said to be wounded by (or participating in) the collision and contributes a portion of the initial entropy density distributed symmetrically about its center; the resulting total wounded nucleon density per unit area is given by

$$n_{\mathrm{WN}}(\vec{\mathbf{r}}_\perp) = \sum_{i} \gamma_i \frac{1}{2\pi B} e^{-|\vec{\mathbf{r}}_\perp - \vec{\mathbf{r}}_{i,\perp}|^2/(2B)} \tag{5}$$

where the sum is over all wounded nucleons in both nuclei and γ_i is again a fluctuating normalization factor with unit mean.

We model multiplicity fluctuations in a single nucleon-nucleon collision by taking the normalizations $\gamma_{i,j}$ and γ_i to be Γ-distributed random variables with unit mean and variances controlled by parameters θ_{BC} and θ_{WN}, respectively. The generic Γ distribution with unit mean and scale parameter θ is given by

$$\Gamma(\gamma;\theta) = \frac{\gamma^{1/\theta - 1} e^{-\gamma/\theta}}{\Gamma(1/\theta)\,\theta^{1/\theta}}, \quad \gamma \in [0,\infty) \tag{6}$$

The multiplicity fluctuations from wounded nucleons and binary collisions are related by requiring [21]:

$$\theta_{pp} = \frac{1-\alpha}{2}\theta_{\mathrm{WN}} = \alpha\theta_{\mathrm{BC}}. \tag{7}$$

where the parameter $\theta_{pp} = 0.9175$ has been fit to the measured multiplicity distributions in p+p collisions [21].

The distribution in the transverse plane of the deposited entropy per unit volume is determined by mixing the binary collision and wounded nucleon sources using

$$s_0(\vec{\mathbf{r}}_\perp) = \frac{\kappa_s}{\tau_0}\left(\frac{1-\alpha}{2} n_{\mathrm{WN}}(\vec{\mathbf{r}}_\perp) + \alpha n_{\mathrm{BC}}(\vec{\mathbf{r}}_\perp)\right) \tag{8}$$

where τ_0 is the starting time for the (hydro)dynamical evolution of the collision fireball. We choose $\kappa_s = 17.16$ and the mixing ratio $\alpha = 0.12$ to reproduce the measured charged multiplicities and their dependence on collision centrality in Au+Au collisions at 200 A GeV. The shape of the resulting energy density distribution in the transverse plane is calculated from the entropy density using the equation of state (EoS) `s95p-v0-PCE` from Lattice QCD [22]. The initial energy profile is evolved using the viscous relativistic fluid dynamic code package `iEBE-VISHNU` [21] with specific shear viscosity $\eta/s = 0.08$. Simulations begin at time $\tau_0 = 0.6\,\mathrm{fm}/c$ and decouple at a temperature $T_{\mathrm{dec}} = 120\,\mathrm{MeV}$. The single particle momentum distribution is then computed using the Cooper-Fyre Formula. A full calculation of charged hadron observables that includes all hadronic resonance decay processes on an event-by-event basis is numerically costly; for this reason we computed only the directly emitted positively charged "thermal pions", π^+, and take this quantity as a measure for total charged multiplicity. At a fixed freeze-out temperature of 120 MeV, the two quantities are related by a constant factor 4.6, $dN_{\mathrm{ch}}/d\eta \simeq 4.6\ dN_{\pi^+}/dy$.

The initial energy density profiles fluctuate from event to event. Each profile can be characterized by the r^n-weighted eccentricity coefficients ε_n and their associated "participant plane angles" Φ_n:

$$\mathcal{E}_n := \varepsilon_n e^{in\Phi_n} = -\frac{\int d\vec{\mathbf{r}}_\perp r^n e^{in\varphi} e(\vec{\mathbf{r}}_\perp)}{\int d\vec{\mathbf{r}}_\perp r^n e(\vec{\mathbf{r}}_\perp)}, \tag{9}$$

where (r, φ) are the standard polar coordinates in the transverse plane and $e(\vec{\mathbf{r}}_\perp)$ is the initial energy density [23,24]. Through the hydrodynamic evolution, these spatial eccentricities $\{\epsilon_n, \Phi_n\}$ translate themselves into the anisotropic flow coefficients $\{v_n, \Psi_n\}$ [24–27]:

$$\mathcal{V}_n := v_n e^{in\Psi_n} = \frac{\int d\varphi_p dp_T e^{in\varphi_p} dN/(p_T dp_T d\varphi_p)}{\int d\varphi_p dp_T dN/(p_T dp_T d\varphi_p)}. \tag{10}$$

Apart from the Monte-Carlo Glauber model, there exist various other initialization models. These include the IP-Glasma model [28], the MC-KLN model [29,30], and the TRENTO model [31]. As we will see, U+U collisions can provide experimental measurements to distinguish between these various initializations.

3 Constraining collision geometry with multiplicity, flow, and ZDC cuts

3.1 Eccentricity and flow coefficients as a function of multiplicity

In Fig. 1, we present the centrality dependence of the initial eccentricities and the final anisotropic flow coefficients of thermal pions for harmonic order $n = 2 - 5$ in U+U collisions at 193 A GeV. In Figs. 1a,c minimum bias results are shown as

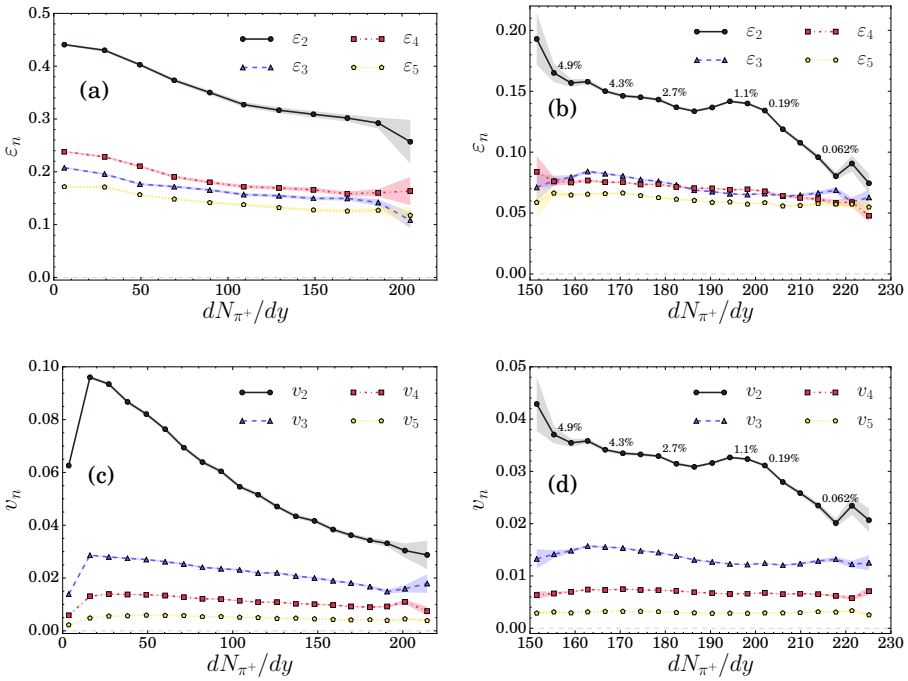

Figure 1: Panels (a,b) show the event-averaged eccentricities ε_n, before hydrodynamic evolution, panels (c,d) the event-averaged flows v_n after hydrodynamic evolution. The left panels (a,c) represent 35,000 minimum bias events that include multiplicity fluctuations whereas the right panels (b,d) were obtained from a different set of 35,000 multiplicity-selected events covering the 0-5% centrality range without multiplicity fluctuations.

functions of the thermal pion yields, dN_{π^+}/dy. We notice that the variance of $\varepsilon_{2,4}$ and $v_{2,4}$ in "most central" (i.e. highest multiplicity) collisions are larger than in the rest of the centrality range. This is because there the two uranium nuclei are colliding almost centrally (i.e. with impact parameter $b \approx 0$) but, as a result of the large spatial deformation, not always with full overlap. A mixture of tip-tip and body-body collisions in these high-multiplicity events increases the variance of the initial $\varepsilon_{2,4}$ which then drives a larger variance in $v_{2,4}$.

In Figs. 1b and 1d, we increase the statistics and focus on the 0-5% most central U+U collisions. We find a "knee" structure in the high multiplicity regime ($< 0.5\%$ centrality) for both ε_2 and v_2. This can be understood as follows: First, while the ellipticity in the transverse plane for a tip-tip collision is small (as the overlap area is approximately circular), body-body collisions produce an ellipsoidally deformed overlap region with larger ellipticity ε_2. Second, although fully overlapping tip-tip and body-body collisions share the same number of participants, more binary collisions between nucleons can happen in the optically thicker tip-tip event, implying (in our two-component Glauber model) a larger initial dS/dy deposited in the tip-tip configuration. In the presence of fluctuations which lead to a range of ε_2 values for a given dS/dy and vice-versa, the larger average multiplicity in tip-tip collisions implies an increasing bias toward small ε_2 when selecting events with larger and larger values of dS/dy. This preferential selection of tip-tip orientations at high multiplicities accounts for the appearance of a knee structure in the initial ellipticity [11] (Fig. 1). We see in Fig. 1c that the knee is preserved after an event-by-event hydrodynamic simulation when plotting the elliptic flow of the final particle distribution as a function of multiplicity.

We emphasize that experimental results from STAR do not show this knee structure [12]. Considering the preservation of the structure after hydrodynamic evolution as seen in Fig. 1, we conclude that, in contrast to Au+Au collisions where it has been extensively tested, the two-component MC-Glauber model fails to correctly identify entropy production in ultra central U+U collisions where the knee is predicted by the model but not found experimentally. Hence the nonlinear dependence of multiplicity on the number of wounded nucleons observed in spherical Au+Au and Pb+Pb collisions as a function of collision centrality cannot be attributed to a binary collision component as implemented in the two-component MC-Glauber model.

Some corrections to the entropy production in these ultra central events arise from the inclusion of p+p multiplicity fluctuations. We see in Fig. 2 that adding said multiplicity fluctuations weakens but does not erase the knee structure in ε_2 vs. dS/dy. Hence, this effect alone does not appear sufficient to reach agreement of the MC-Glauber model with data for ultra central U+U collisions. We acknowledge that more drastic fluctuation models [32] have been suggested in order to more successfully adjust the theoretical predictions of MC-Glauber to experimental results.

Also of note is the success of the gluon saturation physics as implemented in the IP-Glasma model. Interestingly, this model is able to simultaneously accomodate a strong nonlinearity of dN/dy as a function of $N_{\rm part}$ in Au+Au and Pb+Pb and a weak dependence of dN/dy on collision orientation in central U+U at fixed number of participants, while the MC-Glauber model cannot [33]. Alternatively, it has been suggested in [34] that a model that produces entropy according to the number of wounded valence gluons (rather than wounded nucleons) can also reproduce the observed $nonlinearity$ of dN/dy as a function of particpant nucleons in Au+Au and Pb+Pb at RHIC and LHC, without a binary collision component. It would be

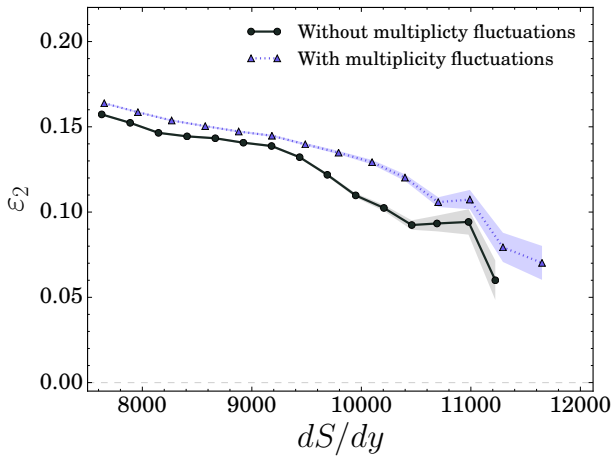

Figure 2: The ellipticity ε_2 as a function of dS/dy from the MC-Glauber model, for collisions roughly in the 0-5% centrality range, with (blue dashed line) and without (black solid line) including multiplicity fluctuations from single p+p collisions.

interesting to study the preduction of such a model for central U+U collisions of varying orientations.

3.2 Selecting high overlap events with combined ZDC and multiplicity cuts

In an experimental analysis of relativistic heavy ion collisions, the charged hadron multiplicity, $dN_{\rm ch}/dy$ and its elliptic flow coefficient v_2 can be used to classify events. Hydrodynamic studies have shown that the initial ε_2 maps linearly to the v_2 of hadrons [26] and the the initial dS/dy is monotonically related the final total particle multiplicity, dN/dy [21]. We can therefore use dS/dy and ε_2 from the initial conditions as a satisfactory proxy for charged hadron $dN_{\rm ch}/dy$ and v_2 to test whether we can select the fully overlapping tip-tip and body-body U+U collisions.

For our analysis, we make theoretical approximations for the use of experimental forward and backward zero degree calorimeters (ZDCs). Placed at zero degrees far from the colliding pair, ZDCs catch information about the spectator neutrons that pass through a collision without participating. We classify our collisions by using the number of spectators $N_s = 476 - N_{\rm part}$ to mimic the experimental ZDC signal [8]. For our study we look at 65,000 events in the 1% most participating ZDC range ($N_s < 19$). Selecting on the most participating ZDC collisions allows for a restriction of the set of collisions to more fully overlapping events. In such a regime, any initial geometric effects should come more exclusively from the deformed shape of the uranium nucleus.

We define the tip-tip and body-body event classes using the pair of angles $(\theta_{1,2}, \phi_{1,2})$ from the two incoming nuclei, where θ denote the polar angle between the long major axis of the uranium nucleus and the beam direction and ϕ is the azimuthal angle in the transverse plane. An event is defined as tip-tip if $\sqrt{\cos^2\theta_1 + \cos^2\theta_2} > 0.86$. We classify an event as a body-body event if both

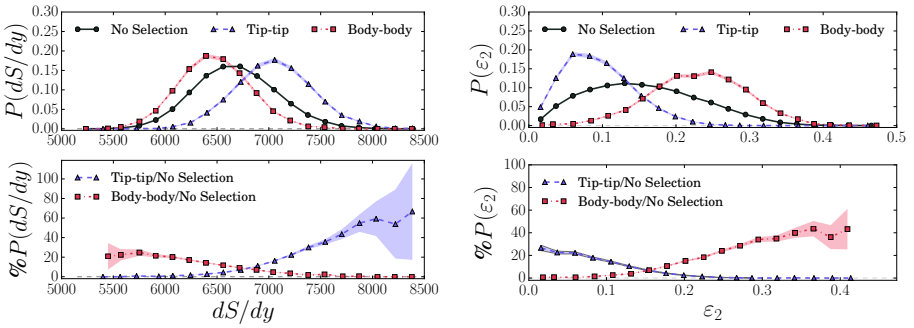

Figure 3: Probability distribution for dS/dy (left) and ε_2 (right) for different event classes within a sample of 1% ZDC events. The top panels show the distributions of tip-tip and body-body collisions scaled according to their contribution to the total population within the 1% ZDC sample. The bottom panels show relative probabilities for tip-tip and body-body events among all events of a given dS/dy (left) or ε_2 (right).

$\sqrt{\cos^2\theta_1 + \cos^2\theta_2} < .31$ and $|\phi_1 - \phi_2| < \pi/10$. The polar angle constraints imply that for equal $\theta_1 = \theta_2$, this common angle θ is less than $\pi/10$ for tip-tip and greater than $4\pi/10$ for body-body. For body-body events, the additional azimuthal constraint forces alignment of the long major axes.

In Fig. 3 we plot the probability distributions for ε_2 and dS/dy. Using our collision definitions we can directly read off from the figure the likelihood of selecting a certain orientation based on a given eccentricity or multiplicity cut. We see in the left bottom panel that by cutting (within our 1% ZDC sample) on events with large dS/dy we can enrich the fraction of tip-tip events to about 50%, whereas cutting on low dS/dy enriches the fraction of body-body events, but never to more than about 20%. The 20% limit arises from admixtures from imperfectly aligned collisions that are not really "full overlap". The enrichment of tip-tip or body-body by varying dS/dy relies on the assumed two-component nature of entropy production which also produced the knee structure discussed before. Indeed, selection efficiency of specific collision geometries by cutting on dS/dy is model dependent.

We therefore consider "event engineering", i.e. selecting events by the magnitude of their v_2 flow vectors (for us, of the linearly related ε_2), shown in the right panels of Fig. 3. Since tip-tip events have on average smaller ellipticities (see upper right panel), selecting events with small ellipticity (or, in experiment, small v_2) enriches the tip-tip fraction. However, in this way we will never reach more than about 25% purity of the tip-tip sample. On the other hand, cutting the 1% ZDC events on large ε_2 (or v_2) will enrich the sample in body-body events, with a purity that can reach about 40% for the largest ε_2 values. While we have not yet been able to verify this with an actual cut on v_2, we expect this feature to survive the hydrodynamic evolution due to the almost perfect linearity between ε_2 and v_2.

The current ZDC cut strategy can be refined further to increase the probability of selecting tip-tip events. Rather than looking at the ZDC signal in one of the two ZDC detectors or the sum of the ZDC signals in both detectors, we can look at the correlation of these two signals. Events with equal forward and backward ZDC signals (i.e. equal numbers of spectators from both nuclei) provide a better

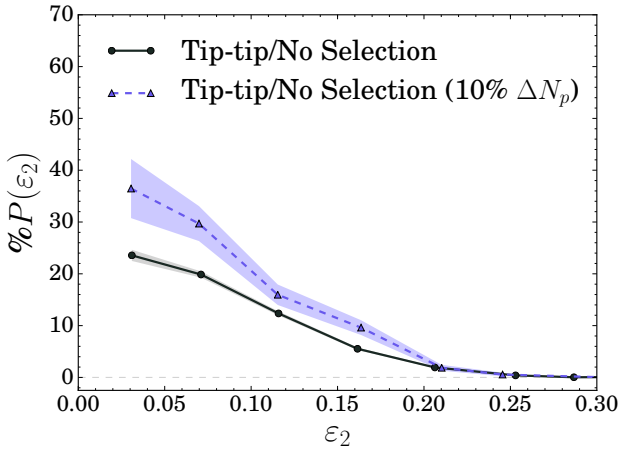

Figure 4: The black curve is the distribution of tip-tip events scaled according to their contribution to the total probability distribution for ε_2 as seen in the bottom right pannel in Fig. 3. The blue dashed curve shows the increased contribution of tip-tip collisions within the 10% of events having the smallest difference in participants $\Delta N_{\rm part}$ (a proxy for ZDC correlation).

definition of the categories full overlap, tip-tip, and body-body than events with asymmetric ZDC signals where all spectators come from only one of the colliding nuclei. The difference in participants $\Delta N_{\rm part} = |N_{\rm part,1} - N_{\rm part,2}|$ quantifies the ZDC correlation in our model. Low values of ΔN_p correspond to the most correlated forward and backward ZDC signals. To demonstrate one application, we reconsider the events from the bottom right panel in Fig. 3 and now select from the sample only events in the lowest 10% of $\Delta N_{\rm part}$. The selection on small values of $\Delta N_{\rm part}$ eliminates from the sample asymmetric configurations that we loosely describe as "tip-body". Collisions of this type produce low values of ε_2 without the angular criteria necessary to be considered tip-tip and therefore dilute the contribution of the true tip-tip configurations at the lower range of ε_2. We show in Fig. 4 that selecting the lowest 10% of $\Delta N_{\rm part}$ increases the selection efficiency of ε_2 for tip-tip configurations by a factor of 1.4. As a final comment, we point out that it might also be interesting to use ZDC correlations in the opposite way and to select and study events with asymmetric tip-body configurations.

4 Conclusion

Within the two-component MC-Glauber model for initial energy production, the prolate deformation of the uranium nucleus was shown to generate a knee in the centrality dependence of the ellipticity of the initial temperature distribution. The knee was seen to be preserved by hydrodynamic evolution, after which it manifests itself in the centrality dependence of v_2. Such a knee structure is not seen in the STAR data. This rules out the two-component MC-Glauber model for initial energy and entropy production. An enrichment of tip-tip configurations by triggering only on high-multiplicity in the U+U collisions thus does not work.

To increase the selection capability between different collision geometries, we impose combined cuts on initial conditions using the spectators (ZDC), dS/dy, and ε_2. For 1% ZDC events, we found that we could enrich tip-tip collision geometries to about 50% by cutting on high multiplicity within that sample, and body-body configurations to about 20% purity by selecting low-multiplicity events. These numbers rely on the binary collision admixture in the two-component MC-Glauber model and are thus model-dependent. They do include effects from multiplicity fluctuations.

We also studied the efficiency of selecting different collision geometries by "event engineering", i.e. by cutting on ε_2 (by cutting on v_2 in the experiment). In this case events selected for high ε_2 can enrich body-body collisions to about 40% purity while cutting on low ε_2 gives a tip-tip sample with about 25% purity. The latter can be boosted to about 35% purity by eliminating events with asymmetric ZDC signals. These results should not be sensitive to the binary collision admixture in the two-component MC-Glauber model and thus should be less model dependent.

Acknowledgments
This work was supported in part by the U.S. Department of Energy, Office of Science, Office of Nuclear Physics under Award No. DE-SC0004286.

References

[1] U. Heinz, Nucl. Phys. A **721**, 30 (2003).

[2] M. Gyulassy, nucl-th/0403032.

[3] E. V. Shuryak, Nucl. Phys. A **750**, 64 (2005).

[4] P. F. Kolb and U. Heinz, In *Hwa, R.C. (ed.) et al.: Quark gluon plasma* 634-714 [nucl-th/0305084].

[5] E. V. Shuryak, Phys. Rev. C **61**, 034905 (2000).

[6] P. F. Kolb, J. Sollfrank and U. Heinz, Phys. Rev. C **62**, 054909 (2000).

[7] U. Heinz and A. Kuhlman, Phys. Rev. Lett. **94**, 132301 (2005).

[8] A. J. Kuhlman and U. Heinz, Phys. Rev. C **72**, 037901 (2005).

[9] C. Nepali, G. Fai and D. Keane, Phys. Rev. C **73**, 034911 (2006).

[10] C. Nepali, G. I. Fai and D. Keane, Phys. Rev. C **76**, 051902 (2007) [Erratum-ibid. C **76**, 069903 (2007)].

[11] S. A. Voloshin, Phys. Rev. Lett. **105**, 172301 (2010).

[12] H. Wang, P. Sorensen *et al.* [STAR Collaboration], Nucl. Phys. **A 932**, 169 (2014).

[13] R. D. Woods and D. S. Saxon, Phys. Rev. **95**, 577 (1954).

[14] L. C. Chamon *et al.* Phys. Rev. C **66**, 014610 (2002).

[15] T. Hirano, P. Huovinen and Y. Nara, Phys. Rev. C **83**, 021902 (2011).

[16] P. Moller, J. R. Nix, W. D. Myers and W. J. Swiatecki, Atom. Data Nucl. Data Tabl. **59**, 185 (1995).

[17] P. Filip, R. Lednicky, H. Masui and N. Xu, Phys. Rev. C **80**, 054903 (2009).

[18] Q. Y. Shou, Y. G. Ma, P. Sorensen, A. H. Tang and H. Wang, arXiv:1409.8375 [nucl-th].

[19] U. Heinz and J. S. Moreland, Phys. Rev. C **84**, 054905 (2011).

[20] A. Bialas, M. Bleszynski and W. Czyz, Nucl. Phys. B **111**, 461 (1976).

[21] C. Shen, Z. Qiu, H. Song, J. Bernhard, S. Bass and U. Heinz, arXiv:1409.8164 [nucl-th].

[22] P. Huovinen and P. Petreczky, Nucl. Phys. A **837**, 26 (2010).

[23] B. Alver and G. Roland, Phys. Rev. C **81**, 054905 (2010) [Erratum-ibid. C **82**, 039903 (2010)].

[24] F. G. Gardim, F. Grassi, M. Luzum and J. Y. Ollitrault, Phys. Rev. C **85**, 024908 (2012).

[25] S. Voloshin and Y. Zhang, Z. Phys. C **70**, 665 (1996).

[26] Z. Qiu and U. Heinz, Phys. Rev. C **84**, 024911 (2011).

[27] Z. Qiu, arXiv:1308.2182 [nucl-th].

[28] B. Schenke, P. Tribedy and R. Venugopalan, Phys. Rev. Lett. **108**, 252301 (2012).

[29] D. Kharzeev and M. Nardi, Phys. Lett. B **507**, 121 (2001); D. Kharzeev, E. Levin and M. Nardi, Nucl. Phys. A **730**, 448 (2004) [Erratum-ibid. A **743**, 329 (2004)].

[30] H.-J. Drescher and Y. Nara, Phys. Rev. C **75**, 034905 (2007); and Phys. Rev. C **76**, 041903 (2007).

[31] J. S. Moreland, J. E. Bernhard and S. A. Bass, arXiv:1412.4708 [nucl-th].

[32] M. Rybczynski, W. Broniowski and G. Stefanek, Phys. Rev. C **87**, 044908 (2013).

[33] B. Schenke, P. Tribedy and R. Venugopalan, arXiv:1403.2232 [nucl-th].

[34] S. S. Adler *et al.* [PHENIX Collaboration], Phys. Rev. C **89**, 044905 (2014).

Chaoticity and Coherence in Bose-Einstein Condensation and Correlations*

Cheuk-Yin Wong[1] † ,Wei-Ning Zhang[2], Jie Liu[2], Peng Ru[2],

[1]Physics Division,Oak Ridge National Laboratory,Oak Ridge,TN,USA
[2]School of Physics and Optoelectric Technology,
Dalian University of Technology, Dalian, Liaoning, China

Abstract

We review the properties of chaoticity and coherence in Bose-Einstein condensation and correlations, for a dense boson system in its mean-field represented approximately by a harmonic oscillator potential. The order parameter and the nature of the phase transition from the chaotic to the condensate states are studied for different fixed numbers of bosons. The two-particle correlation function in momentum space is calculated to investigate how the Bose-Einstein correlation depends on the degree of condensation and other momentum variables. We generalize the Bose-Einstein correlation analysis to three-particle correlations to show its dependence on the degree of condensation.

1 Introduction

As is well known, a fundamental assumption for the occurrence of Bose-Einstein correlation (BEC) is the presence of a chaotic source of identical bosons [1, 2]. The

*Invited talk presented at the Xth Workshop on Particle Correlations and Femtoscopy (WPCF14) at Gyöngyös, Hungary on August 25 to 29, 2014
† Speaker

Bose-Einstein correlation occurs in a chaotic source but not in a coherent source [3, 4, 5, 6, 7, 8].

The properties of chaoticity and coherence are complementary attributes. Both chaoticity and coherence should be examined on equal footings in a single theoretical framework with the description of both the BE condensation and BE correlations. In such a unified framework, it is then possible to investigate not only the states of chaoticity and coherence, but also the transition from a chaotic state to a coherent state. How can the degrees of chaoticity or coherence be quantified? Is the transition from a chaotic state to a coherent state a first-order with a sudden onset, or is it a gradual transition that is closer to a second-order? What is the relevant order parameter that best describes the transition? How does Bose-Einstein condensation quantitatively affects the two-particle and three-particle Bose-Einstein correlations?

Questions of Bose-Einstein correlations and condensation arise not only in atomic physics [9, 10, 11] but also in high-energy heavy-ion collisions [5, 6, 8] where pions are the most copiously produced particles. The use of two-pion Bose-Einstein correlations to probe the source coherence was proposed at the end of 1970s [12, 3]. The introduction of the "chaoticity" parameter λ of BEC in pions is only a tool to represent experimental data. However, the experimental measurement of λ is beset by the presence of many other effects such as particle misidentification, long-live resonance decay, final state Coulomb interaction, non-Gaussian source distribution, etc. [5, 7]. The explanation of the experimental λ results remains an open question. In 1993, S. Pratt proposed a pion laser model in high energy collisions and studied the influence of pion laser on two-pion Bose-Einstein correlation function and the chaoticity parameter [13]. In 1998, T. Csörgő and J. Zimányi investigated the effect of Bose-Einstein condensation on two-pion Bose-Einstein correlations [14]. They utilized Gaussian formulas describing the space and momentum distributions of a static non-relativistic boson system, and investigated the influence of the condensation on pion multiplicity distribution. In 2007, C. Y. Wong and W. N. Zhang studied how λ in Bose-Einstein correlations depends on the degree of Bose-Einstein condensation or chaoticity, for static non-relativistic and relativistic boson gases within a spherical mean-field harmonic oscillator potential [15]. The model can be analytically solved in the non-relativistic case and be used in atomic physics [9, 10, 11]. The limiting conditions and circumstances under which the parameter λ can be approximately related to the degrees of chaoticity were clarified [15]. A similar study for cylindrical static boson gas sources was completed [16] and the chaoticity parameter λ in two-pion Bose-Einstein correlations in an expanding boson gas model was recently examined [17]. The investigation of chaoticity and coherence was also carried out using a model of q-deformed oscillator algebraic commutative relations [18] and the model of partial indistinguishability and coherence of closely located emitters [19]. In another related topic, initial conditions such as the color-glass condensate (CGC) with the coherent production of partons [20] in heavy-ion collisions may also lead to condensate formation [21].

Recently, experimental investigation of the source coherence in Pb-Pb collisions at $\sqrt{s_{NN}} = 2.76$ TeV at the Large Hadron Collider (LHC) was carried out by the ALICE collaboration [22]. A substantial degree of source coherence was measured [22] using a new three-pion Bose-Einstein correlations technique with an improvement over past efforts [23, 24, 25, 26]. Earlier work on three-particle correlations were carried out in [6, 13, 27, 28, 29, 30, 31, 32, 33, 34].

A proper theoretical framework to study the above topics is the theory of the Bose-Einstein condensation and correlations in their own mean field potential [15].

We would like to review the essential elements here and examine further the related question of three-body correlations.

2 Bose-Einstein Condensation for attractively Interacting Bosons

We seek a description of chaoticity in Bose-Einstein correlations through the consideration of Bose-Einstein condensation. Why is Bose-Einstein condensation relevant to Bose-Einstein correlations (BEC)? Glauber in many private communications and in his talk in QM2005 suggested that the consistent experimental observations of $\lambda < 1$ may be due partly to the coherence of the pions in Bose Einstein correlations [35]. Furthermore, there have been major advances in Bose-Einstein condensation in atomic physics [9, 10, 11]. In particular, the works of Politzer [9], and Naraschewski & Glauber [10] reveals that BE condensation and the BE correlations are intimately related.

We envisage the possibility of the occurrence of a Bose-Einstein condensation in dense boson media of identical bosons with the following reasoning [15, 16, 17]

1. Identical bosons with mutual attractive interaction generate a mean field potential, which depends on the boson density $\rho(r)$ as [36]

$$V(r) = -4\pi f(0)\rho(r) \sim \frac{1}{2}\hbar\omega \left(\frac{r}{a}\right)^2, \tag{1}$$

   where $f(0)$ is the forward scattering amplitude, and a is the length scale that defines the spatial region of boson occupation.

2. Therefore, for a given length scale a, the $\hbar\omega$ of the underlying mean-field potential increases with increasing density ρ of the produced bosons.

3. The order parameter that determines the degree of BE coherence or chaoticity is $T/\hbar\omega$. Thus the order parameter $T/\hbar\omega$ decreases with increasing boson density.

4. For a given temperature T at freeze out, a high density of produced bosons will lead to a lower value of the order parameter $T/\hbar\omega$, which in turn will lead to a greater condensate fraction $f_0{=}N_0/N$, where N is the total number of bosons and N_0 is the number of bosons in the lowest state. A greater condensate fraction f_0 brings about a greater coherence in Bose-Einstein correlations and a reduction in the degree of chaoticity.

In high energy heavy-ion collisions when bosons (gluons or pions) are copiously produced within a small region in a short time interval, the density of the bosons increases as the collision energy increases. Following the above reasoning, generalized to systems with differential transverse and longitudinal spatial distributions, we expect the occurrence of boson condensation in high energy heavy-ion collisions at some high collision energies. It is useful to examine the Bose-Einstein condensation for bosons in an exactly solvable model.

3 Bose-Einstein Condensation for Bosons in a Spherical Harmonic Oscillator Potential

We consider a system of N bosons in a spherical harmonic oscillator potential, which arises either externally or from the bosons' own mean-fields. We study how the occupation numbers of different states change as a function of the temperature T, in relation to the oscillator frequency $\hbar\omega$. Bose-Einstein condensation occurs when the occupation number N_0 for the lowest state (the condensate state) is a substantial fraction of the total particle number N. The degree of coherence or chaoticity is quantified by the condensate fraction $f_0 = N_0/N$, which varies as a function of the order parameter $T/\hbar\omega$.

In such a study, it is important to use the proper statistical ensemble [9]. In a grand canonical ensemble, we fix the chemical potential μ and the temperature T, and we allow the number of particles N_n in the n-th single-particle state to vary. We obtain the average occupation number for the single-particle state n to be $N_n = \langle a_n^+ a_n \rangle$. The square fluctuation of N_n is then given by

$$\langle (a_n^+ a_n - \langle a_n^+ a_n \rangle)^2 \rangle \approx N_n(N_n + 1). \tag{2}$$

As the fluctuation of N_n in a grand canonical ensemble is of the same order as the occupation number itself, we cannot treat the lowest $n = 0$ state in the grand canonical ensemble. The lowest $n = 0$ state needs to be treated in the canonical ensemble with a fixed total number of bosons.

It was shown however that while the lowest $n = 0$ state needs to be treated in the canonical ensemble, the $n > 0$ state can be treated in the grand canonical ensemble without incurring large errors [9]. We shall follow such a description for the ensemble of N identical bosons in a spherical harmonic oscillator potential. In such a canonical ensemble for the lowest n=0 state but a grand canonical ensemble for the n>0 states, the total number of bosons is fixed and yields the condensate number condition

$$N = N_0 + \sum_{n=1,2,3,\ldots} N_n = \frac{z}{1-z} + \sum_{n=1,2,3,\ldots} \frac{g_n z e^{-(\epsilon_n - \epsilon_0)/T}}{1 - z e^{-(\epsilon_n - \epsilon_0)/T}}, \tag{3}$$

where $z = e^{\mu/T}$ is the fugacity of the system, g_n is the degeneracy number g_n=(n+1)(n+2)/2 for the n-th single-particle level, and ϵ_n is the single-particle energy in the spherical harmonic oscillator potential

$$\epsilon_n = (n + 3/2)\hbar\omega. \tag{4}$$

For a given N, equation (3) contains only a single unknown, z, which can be solved as a function of the order parameter $T/\hbar\omega$. The solutions of z for N=25, 500, 1000 and 2000 are given in Fig. 1, and the corresponding condensate fractions $f_0 = N_0/N$ are shown in Fig. 2.

We observe in Fig. 1 that the fugacity parameter z is close to unity in the strongly coherent region at low temperatures. In fact, the fugacity parameter z at T=0 assumes the value $z(T{=}0) = N/(N + 1)$. For a given boson number N, the fugacity z decreases very slowly in the form of a plateau, as the temperature increases from $T = 0$. The plateau region persists until the condensate temperature T_c is reached, and z then decreases rapidly thereafter. The greater the number of

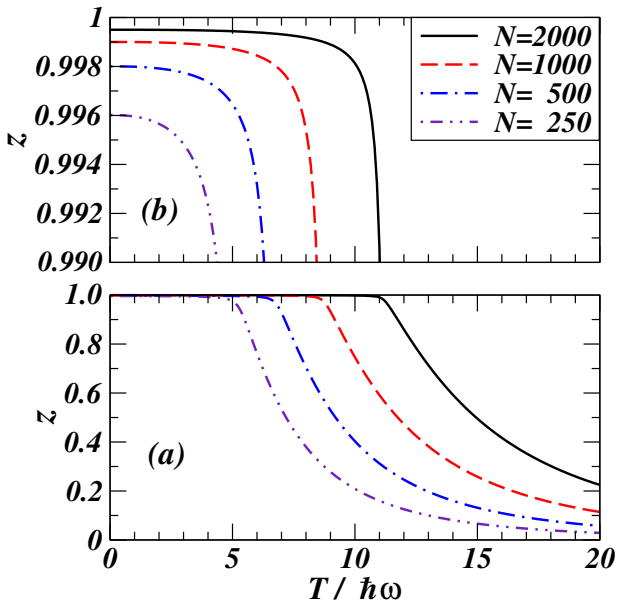

Figure 1: (Color online) (a) The fugacity parameter z satisfying the condensate number condition Eq. (3) for different boson numbers N in a spherical harmonic oscillator potential, as a function of the order parameter $T/\hbar\omega$ and (b) an expanded view in the $z \sim 1$ region.

bosons N, the greater is the plateau region, as shown in Fig. 1(b). For example, for $N = 2000$ the value of z is close to unity for $0 < T/\hbar\omega < 11$ in the plateau,.

We note in Fig. 2 that for a given value of the total number of bosons N in the spherical harmonic oscillator potential, the condensate fraction f_0 is close to unity when the order parameter $T/\hbar\omega$ is below a limit, and this limit depends on N. We can plot the condensate fraction f_0 as a function of the order parameter $T/\hbar\omega$. The functional form of $f_0(T)$ can be approximated by

$$f_0(T) = \begin{cases} 1 - [(T/\hbar\omega)/(T_c/\hbar\omega)]^3 & \text{for } (T/\hbar\omega) \leq (T_c/\hbar\omega), \\ O(1/N) \to 0 & \text{for } (T/\hbar\omega) \geq (T_c/\hbar\omega). \end{cases} \quad (5)$$

The results from the above one-parameter fit to $f_0(T)$ are shown as the dashed curves in Fig. 2, to be compared with the $f_0(T)$ calculated with the condensate configuration condition Eq. (3) shown as the solid curves. The values of $T_c/\hbar\omega$ that give the best fit to $f_0(T)$ for different N values are listed in Table I.

The above results provide a comprehensive description for the transition from a chaotic state to a coherent state. Fig. 2 indicates that the transition from the completely chaotic state with f_0=0 to the state of coherence with $f_0 \to 1$ is a second-order-type transition under a gradual decrease of the order parameter $T/\hbar\omega$. It is not a first-order phase transition.

Table I. Critical order parameter $T_c/\hbar\omega$ obtained from (i) fitting f_0 as a function of $T/\hbar\omega$ with Eq. (5), and from (ii) the analytical formula of Eq. (6).

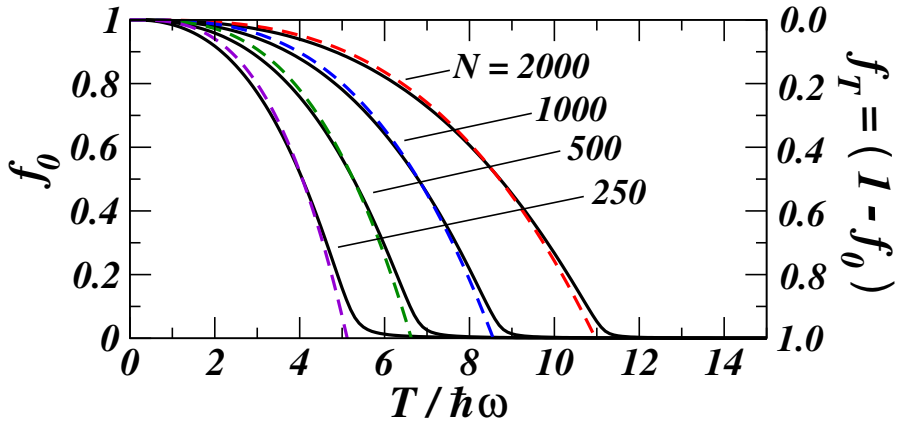

Figure 2: (Color online) Solid curves represent the condensate fractions $f_0(T)$, calculated with the condensate number condition Eq. (3), as a function of $T/\hbar\omega$ for different boson numbers N in a spherical harmonic oscillator potential. The abscissa labels for the corresponding chaotic fraction $f_T(T)$=$[1 - f_0(T)]$ are indicated on the right. The dashed curves are the fits to the solid curve results of $f_0(T)$ with the function $1-[(T/\hbar\omega)/(T_c/\hbar\omega)]^3$ of Eq. (5) where the values of $T_c/\hbar\omega$ for different N values are listed in Table I.

Number of Bosons N	$T_c/\hbar\omega$ obtained from fitting f_0 with Eq. (5)	$T_c/\hbar\omega$ obtained with Eq.(6)
2000	10.97	11.00
1000	8.56	8.53
500	6.63	6.62
250	5.12	5.13

It is remarkable that the critical order parameter $T_c/\hbar\omega$ and the boson number N obeys the following simple relationship

$$T_c/\hbar\omega \quad = \quad 0.6777N^{0.36666}, \tag{6}$$

as shown by the third column in Table I. Thus, the knowledge of N suffices to determine the critical order parameter $T_c/\hbar\omega$ by the above simple equation and the knowledge of $T_c/\hbar\omega$ subsequently yields the approximate condensate fraction at all other temperatures by Eq. (5).

4 Single-particle and Two-Particle Density Matrices in Momentum Space

The determination of the fugacity z from the condensate number condition (3) allows the calculation of various physical quantities. Specifically, the one-body density matrix in momentum space is given by

$$G^{(1)}(\boldsymbol{p}_1, \boldsymbol{p}_1') = \sum_{n=0}^{\infty} u_n^*(\boldsymbol{p}_1') u_n(\boldsymbol{p}_1) \langle \hat{a}_n^\dagger \hat{a}_n \rangle, \tag{7}$$

where $u_n(\boldsymbol{p})$ is the single-particle wave function and the occupation number $N_n{=}\langle\hat{a}_n^\dagger\hat{a}_n\rangle$ can be inferred from the terms in the summation in Eq. (3). The two-particle density matrix in momentum space

$$G^{(2)}(\boldsymbol{p}_1,\boldsymbol{p}_2;\boldsymbol{p}_1',\boldsymbol{p}_2') = \sum_{\rm klmn} u_{\rm k}^*(\boldsymbol{p}_1')u_{\rm l}^*(\boldsymbol{p}_2')u_{\rm m}(\boldsymbol{p}_2)u_n(\boldsymbol{p}_1)\langle\hat{a}_{\rm k}^\dagger\hat{a}_{\rm l}^\dagger\hat{a}_{\rm m}\hat{a}_{\rm n}\rangle \tag{8}$$

can be written in terms of one-body density matrices as [10, 15]

$$\begin{aligned} G^{(2)}(\boldsymbol{p}_1,\boldsymbol{p}_2;\boldsymbol{p}_1',\boldsymbol{p}_2') &= G^{(1)}(\boldsymbol{p}_1,\boldsymbol{p}_1')G^{(1)}(\boldsymbol{p}_2,\boldsymbol{p}_2') + G^{(1)}(\boldsymbol{p}_1,\boldsymbol{p}_2')G^{(1)}(\boldsymbol{p}_2,\boldsymbol{p}_1') \\ &+ \sum_{n=0}^{\infty} u_n^*(\boldsymbol{p}_1')u_n^*(\boldsymbol{p}_2')u_n(\boldsymbol{p}_2)u_n(\boldsymbol{p}_1)\Big\{\langle\hat{a}_n^\dagger\hat{a}_n\hat{a}_n\rangle - 2\langle\hat{a}_n^\dagger\hat{a}_n\rangle\langle\hat{a}_n^\dagger\hat{a}_n\rangle\Big\}. \end{aligned} \tag{9}$$

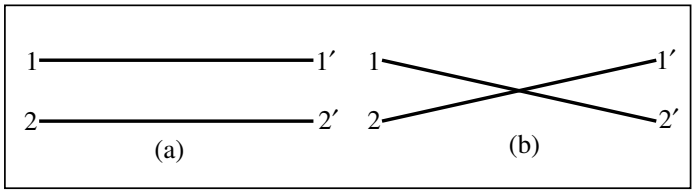

Figure 3: Two-particle distribution function expanded in terms of products of one-particle distribution functions in uncorrelated mean-field approximation.

The uncorrelated part in the first two terms of the above two-particle density matrix, $G^{(1)}(\boldsymbol{p}_1,\boldsymbol{p}_1')G^{(1)}(\boldsymbol{p}_2,\boldsymbol{p}_2') + G^{(1)}(\boldsymbol{p}_1,\boldsymbol{p}_2')G^{(1)}(\boldsymbol{p}_2,\boldsymbol{p}_1')$, is represented schematically by the diagram in Fig. 3. Our task is to obtain the correlated part arising from Bose-Einstein condensation represented by the last term in Eq. (9).

In the limit of a large number of bosons N in a grand canonical ensemble for the non-condensed states, the contributions from the set of $\{n > 0\}$ states in the summation in Eq. (9) can be neglected. We are left with only the $n = 0$ condensate state contribution for this summation.

To describe the contribution from the $n = 0$ condensate state, we shall follow Ref. [9, 10] and use the canonical ensemble which gives the canonical fluctuation

$$\langle(\hat{a}_0^\dagger\hat{a}_0 - \langle\hat{a}_0^\dagger\hat{a}_0\rangle)^2\rangle = \langle\hat{a}_0^\dagger\hat{a}_0^\dagger\hat{a}_0\hat{a}_0\rangle - \langle\hat{a}_0^\dagger\hat{a}_0\rangle\langle\hat{a}_0^\dagger\hat{a}_0\rangle = O(N_0). \tag{10}$$

Thus, we have

$$\langle\hat{a}_0^\dagger\hat{a}_0^\dagger\hat{a}_0\hat{a}_0\rangle - 2\langle\hat{a}_0^\dagger\hat{a}_0\rangle\langle\hat{a}_0^\dagger\hat{a}_0\rangle = -\langle\hat{a}_0^\dagger\hat{a}_0\rangle\langle\hat{a}_0^\dagger\hat{a}_0\rangle + O(N_0). \tag{11}$$

In the limit of a large number of particles, we can neglect the last term $O(N_0)$ in the above equation which is small in comparison with the first term of order N_0^2. The two-particle distribution of Eq. (9) is therefore

$$\begin{aligned} G^{(2)}(\boldsymbol{p}_1,\boldsymbol{p}_2;\boldsymbol{p}_1,\boldsymbol{p}_2) = G^{(1)}(\boldsymbol{p}_1,\boldsymbol{p}_1)G^{(1)}(\boldsymbol{p}_2,\boldsymbol{p}_2) + |G^{(1)}(\boldsymbol{p}_1,\boldsymbol{p}_2)|^2 \\ -N_0^2|u_0(\boldsymbol{p}_1)|^2|u_0(\boldsymbol{p}_2)|^2, \end{aligned} \tag{12}$$

which gives the conditional probability for the occurrence of a pion of momentum $\boldsymbol{p}_1$ in coincidence with another identical pion of momentum $\boldsymbol{p}_2$.

5 Two-Particle Momentum Correlation Function

In BE correlation measurements, we normalize the probability relative to the probability of detecting particle $\boldsymbol{p}_1$ and $\boldsymbol{p}_2$, and define the momentum correlation function $C(\boldsymbol{p}_1, \boldsymbol{p}_2)$ as

$$C(\boldsymbol{p}_1, \boldsymbol{p}_2) = \frac{G^{(2)}(\boldsymbol{p}_1, \boldsymbol{p}_2; \boldsymbol{p}_1, \boldsymbol{p}_2)}{G^{(1)}(\boldsymbol{p}_1, \boldsymbol{p}_1) G^{(1)}(\boldsymbol{p}_2, \boldsymbol{p}_2)}. \tag{13}$$

It is convenient to introduce the average and the relative momenta of the pair

$$\boldsymbol{p} = (\boldsymbol{p}_1 + \boldsymbol{p}_2)/2, \qquad \boldsymbol{q} = \boldsymbol{p}_1 - \boldsymbol{p}_2. \tag{14}$$

The momentum correlation function can be expressed as a function of the kinematic variables $\boldsymbol{p}_1$ and $\boldsymbol{p}_2$ or alternatively of $\boldsymbol{p}$ and $\boldsymbol{q}$. From Eq. (12), we have the general expression for the correlation function

$$C(\boldsymbol{p}, \boldsymbol{q}) = C(\boldsymbol{p}_1, \boldsymbol{p}_2) = 1 + \frac{|G^{(1)}(\boldsymbol{p}_1, \boldsymbol{p}_2)|^2 - N_0^2 |u_0(\boldsymbol{p}_1)|^2 |u_0(\boldsymbol{p}_2)|^2}{G^{(1)}(\boldsymbol{p}_1, \boldsymbol{p}_1) G^{(1)}(\boldsymbol{p}_2, \boldsymbol{p}_2)}. \tag{15}$$

This is the general Bose-Einstein correlation function for all situations: coherent, chaotic, and the transition between coherent and chaotic systems.

The evaluation of the correlation function $C(\boldsymbol{p}, \boldsymbol{q})$ in Eq. (15) requires the knowledge of $G^{(1)}(\boldsymbol{p}_1, \boldsymbol{p}_2)$ and the ground state wave function $u_0(\boldsymbol{p}_1)$. For a system of bosons in a spherical harmonic oscillator, the wave functions are all known, and the correlation function can be written out analytically. Specifically, we have

$$G^{(1)}(\boldsymbol{p}_1, \boldsymbol{p}_2) = \sum_{k=1}^{\infty} z^k \tilde{G}_0(\boldsymbol{p}_1, \boldsymbol{p}_2; k\beta\hbar\omega), \tag{16}$$

$$\tilde{G}_0(\boldsymbol{p}_1, \boldsymbol{p}_2; \tau) = \left(\frac{a^2}{\pi\hbar^2(1 - e^{-2\tau})}\right)^{3/2} \exp\left(-\frac{a^2}{\hbar^2} \frac{(\boldsymbol{p}_1^2 + \boldsymbol{p}_2^2)(\cosh\tau - 1) + (\boldsymbol{p}_1 - \boldsymbol{p}_2)^2}{2\sinh\tau}\right), \tag{17}$$

and the ground state wave function is

$$u_0(\boldsymbol{p}) = \left(\frac{a^2}{\pi\hbar^2}\right)^{3/4} \exp\left\{-\frac{a^2}{\hbar^2} \frac{\boldsymbol{p}^2}{2}\right\}. \tag{18}$$

The knowledge of the single-particle $G^{(1)}(\boldsymbol{p}_1, \boldsymbol{p}_2)$ and $u_0(\boldsymbol{p})$ will then allow the determination of the two-particle correlation function $C(\boldsymbol{p}, \boldsymbol{q})$.

The correlation function $C(\boldsymbol{p}, \boldsymbol{q})$ in Eq. (15) possesses the proper coherent and chaotic limits. For a nearly completely coherent source with almost all particles populating the ground condensate state, $N_0 \to N$, the two terms in the numerator cancel each other and we have $C(\boldsymbol{p}, \boldsymbol{q}) = 1$, with the absence of the BE correlation. For the other extreme of a completely chaotic source with $N_0 \ll N$, the second term in the numerator proportional to N_0^2 in Eq. (15) gives negligible contribution and can be neglected. The correlation function $C(\boldsymbol{p}, \boldsymbol{q})$ then becomes the usual BE correlation for a completely chaotic source.

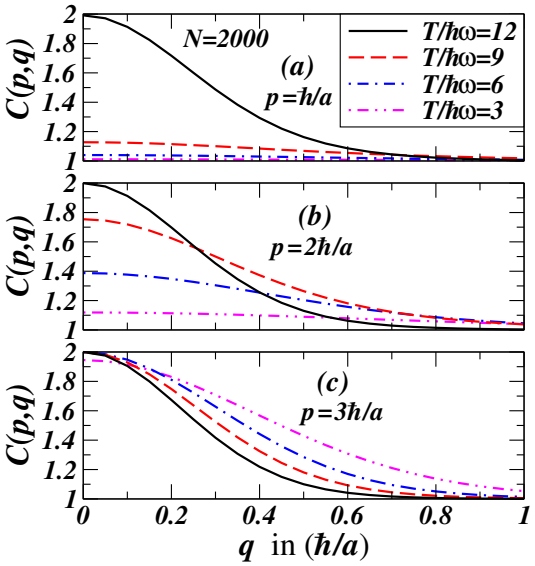

Figure 4: (Color online) The correlation function $C(\boldsymbol{p},\boldsymbol{q})$ at different values of the pair average momentum $pa/\hbar$ and temperatures. Figures (a), (b), and (c) are for p=1, 2, and $3\hbar/a$, respectively.

6 Evaluation of the Two-Particle Momentum Correlation Function

For a given number of bosons N in a spherical harmonic oscillator, the solution of fugacity z obtained as a function of the order parameter $T/\hbar\omega$ allows us to evaluate the momentum correlation function $C(p,q)$ with Eqs. (15)-(18). In Fig. 4, we show $C(p,q)$ for example for the case of N=2000 for which the critical order parameter is $T_c/\hbar\omega$=10.97, as tabulated in Table I. We observe that the correlation function is a complicated function of the average pair momentum p and the order parameter $T/\hbar\omega$. For $p=\hbar/a$ in Fig. 4(a), the correlation function $C(p,q)$ at q=0 is close to unity for temperatures below and up to $T/\hbar\omega$=9 (below $T_c/\hbar\omega$), but increases to 2 rather abruptly at $T/\hbar\omega$=12, (above $T_c/\hbar\omega$). For $p=2\hbar/a$ in Fig. 3(b), the correlation function $C(p,q)$ at $q=0$ is substantially above unity and increases gradually as temperature increases. For $p=3\hbar/a$ in Fig. 4(c), the correlation function $C(p,q)$ at q=0 is about 2 for all cases of temperatures examined. If one follows the standard phenomenological analysis and introduces the "chaoticity" parameter λ to represent the intercept of the correlation function at zero relative momentum, then this parameter λ is a function of the average pair momentum p and temperature T

$$\lambda(p,T) = [C(p,q=0;T) - 1]. \tag{19}$$

We display explicitly the dependence $\lambda(p,T)$ as a function of p in Fig. 5(a) for different order parameters $T/\hbar\omega$, for the case of $N = 2000$. At $T/\hbar\omega$=12, which is above the critical condensate order parameter of $T_c/\hbar\omega$=10.97, the λ parameter is 1 for all p values. At $T/\hbar\omega$=9, as p increases the λ parameter rises gradually from $\sim$0.1 at $p = \hbar/a$ and reaches the constant value of 1 at p=2.4$\hbar/a$. At $T/\hbar\omega$=6 and

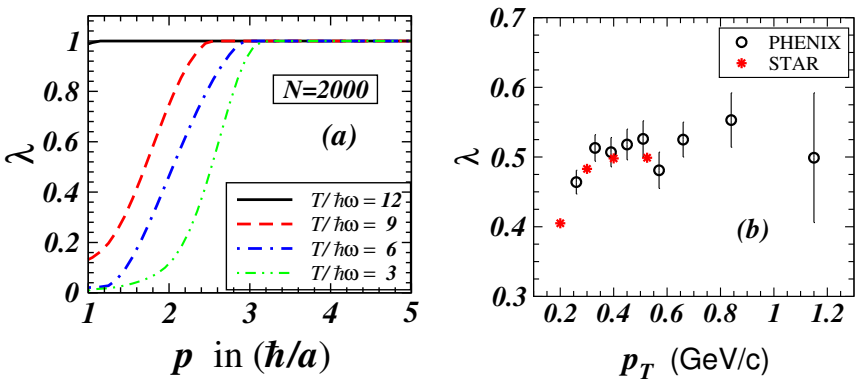

Figure 5: (Color Online) (a) The parameter λ as a function of p for different temperatures for N=2000. (b) Experimental measured values of λ as a function of p_T for AuAu Collisions at RHIC at $\sqrt{s_{\rm NN}}$=200 GeV from the PHENIX Collaboration [37] and the STAR Collaboration [38].

3, for which the systems are significantly coherent with large condensate fractions, the λ parameter starts close to zero at p=$\hbar/a$, but as p increases the λ parameter increases gradually to unity at p=2.9 and 3.1$\hbar/a$ for $T/\hbar\omega$=6 and 3 respectively. The location where the λ parameter attains unity changes with temperature. The lower the temperature, the greater is the value of p at which the λ parameter attains unity.

We conclude from our results that the parameter $\lambda(p,T)$ is a sensitive function of both p and T, and $\lambda(p,T)=1$ is not a consistent measure of the absence of the condensate fraction, as it attains the value of unity in some kinematic regions for significantly coherent systems with large condensate fractions at temperatures much below T_c. Only for the region of small p will the parameter $\lambda(p,T)$ be correlated with the chaotic fraction $f_T(T)$ of the system.

It is interesting to note that experimentally measured values of λ from different collaborations and different method of analysis [37, 38] exhibit an increase of λ as p_T of the average momentum of the pair increase as shown in Fig. 5(b). There is a similar trend of increasing λ as a function of p_T. This may be an indication of the dependence of the correlation function on the average momentum of the pair arising for a partially coherent pion source. The increase of λ as a function of the average pair momentum has also been obtained in the q-deformed harmonic oscillator model of Bose-Einstein correlations [18].

7 Bose-Einstein Condensation of Pions in their Men Fields

With regard to heavy-ion collisions at RHIC & LHC, it is instructive to raise the following question. If we have a pion system that has a root-mean squared radius $r_{\rm rms}$=10 fm, the number of identical pions N from a few hundred to a few thousand, at a freezeout temperature T=80 to 160 MeV, typical of those revealed by Bose-Einstein correlation measurements [37, 38], then, what will be the condensate fraction f_0? To answer this question, it is useful to calculate the root-mean-squared

radius $r_{\rm rms}$ of the pion system as a function of the order parameter $T/\hbar\omega$ for a pion system with N=250 to 2000 as shown in Fig. 6. We can schematically represent the functional relation between $r_{\rm rms}/a$ and $T/\hbar\omega$ in Fig. 6 as

$$r_{\rm rms}/a = f_N(T/\hbar\omega). \tag{20}$$

For a given value of N and $r_{\rm rms}$, as a is equal to $\hbar/\sqrt{m_\pi\hbar\omega}$, the above equation

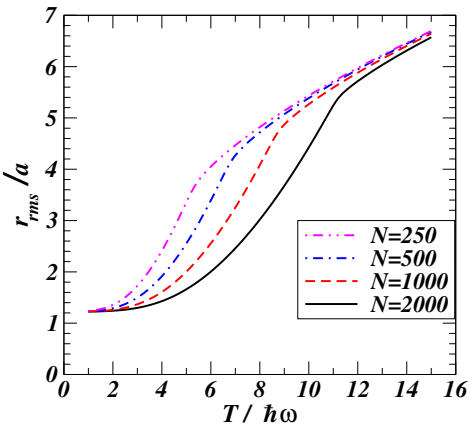

Figure 6: (Color online) The root-mean-squared radius in unit of a and the root-mean-squared momentum in units of $\hbar/a$, as a function of $T/\hbar\omega$ for different numbers of identical bosons in the system.

contains only a single variable $\hbar\omega$ that can be determined as a function of T. Subsequently, the order parameter $T/\hbar\omega$ and the condensate fraction f_0 can also be determined as a function of T as shown in Fig. 7.

One finds that for the pion system with a given root-mean-squared radius of 10 fm, the value of $\hbar\omega$ ranges from about 12 to 20 MeV for N=2000 and about 20 to 30 MeV for N=250. The ratio of $T/\hbar\omega$ about 7 for N=2000, and is about 4.5 for N=250, as shown in Fig. 7(b). From these ratios of $T/\hbar\omega$, one can use Fig. 2 to find out the condensate fraction. The condensate fractions $f_0(T)$ for a pion gas at various temperatures with N=2000 and N=250 are shown in Fig. 7(c). One finds that $f_0(T)$ is about $0.67-0.8$ for N=2000 and is about 0.9 for N=250.

We reach the conclusion from the above study that if a non relativistic pion system maintains a static equilibrium within its mean field, and if it contains a root-mean-squared radius, a pion number, and a temperature typical of those in high-energy heavy-ion collisions, then it will contain a large fraction of the Bose-Einstein pion condensate. For a relativistic pion system, while the absolute scale of the order parameter $T/\hbar\omega$ may change, the condensate fraction f_0 remains substantial [15]. Pion condensation will affect the parameter λ in momentum correlation measurements.

8 Three-particle Correlations and Coherence

Bose-Einstein condensation has important influence on the three-particle correlation function. We can determine the dependence of the three-particle correlation function on the degree of Bose-Einstein coherence in a way similar to what has been carried out for two-particle correlations.

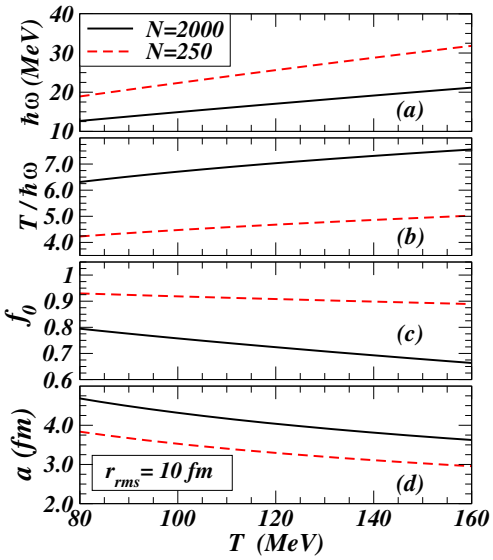

Figure 7: (Color online) (a) the potential strength $\hbar\omega$, (b) the ratio $T/\hbar\omega$, (c) the condensate fraction f_0, and (d) the oscillator length parameter a for non-relativistic boson systems with $N = 2000$ and $N = 250$ in a static equilibrium with a $r_{\rm rms} = 10$ fm, plotted as a function of the temperature T.

The extraction of the coherence properties from experimental three-particle correlation data has the advantage that the problems of the resonances can be minimized. It has however the disadvantage that the statistics in the number of three-particle events may be lowered because of the restriction on the occurrence of three-particle coincidences.

Recently there has much interest in three-particle correlation measurements [22]. Bose-Einstein condensation of pions in a heavy-ion collision may suppress Bose-Einstein correlations. Furthermore, initial conditions such as the color-glass condensate (CGC) with the coherent production of partons [20] may also lead to condensate formation [21]. Experimental results indicate the presence of a substantial condensate fraction [22]. It is of interest to formulate an analytical model to investigate how the three-particle correlation function will depend on the coherence of the underlying boson system. In a completely chaotic source when multi-particle

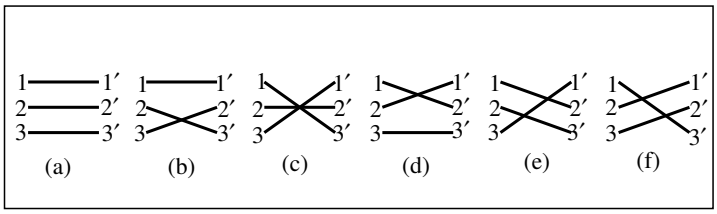

Figure 8: Three-particle distribution function expanded in terms of one-particle distribution function in uncorrelated mean-field approximation.

Bose-Einstein-type correlations are neglected, the three-particle correlation function

can be written in terms of products of one-body distribution functions:

$$\begin{aligned}
&G^{(3)}(p_1,p_2.p_3;p_1',p_2',p_3')\\
&=G^{(1)}(1,1')G^{(1)}(2,2')G^{(1)}(3,3')+G^{(1)}(1,2')G^{(1)}(2,1')G^{(1)}(3,3')\\
&+G^{(1)}(1,3')G^{(1)}(2,2')G^{(1)}(3,1')+G^{(1)}(1,1')G^{(1)}(2,3')G^{(1)}(3,2')\\
&+G^{(1)}(1,3')G^{(1)}(2,1')G^{(1)}(3,2')+G^{(1)}(1,2')G^{(1)}(2,3')G^{(1)}(3,1'), \quad (21)
\end{aligned}$$

as represented by the diagrams in Fig. 8. With Bose-Einstein correlations, we can generalize our two-particle correlation case to the three-particle correlation functions and write down the three-particle correlation function as

$$\begin{aligned}
C(p_1,p_2,p_3) \;&\equiv \left.\frac{G^{(3)}(1,2,3;1',2',3')}{G^{(1)}(1,1')G^{(1)}(2,2')G^{(1)}(3,3')}\right|_{1'\to1,2'\to2,3'\to3}\\
&=1+\frac{G^{(1)}(1,2)G^{(1)}(2,1)-N_0u_0^2(p_1)u_0^2(p_2)}{G^{(1)}(1,1)G^{(1)}(2,2)}\\
&\quad+\frac{G^{(1)}(1,3)G^{(1)}(3,1)-N_0^2u_0^2(p_1)u_0^2(p_3)}{G^{(1)}(1,1)G^{(1)}(3,3)}\\
&\quad+\frac{G^{(1)}(2,3)G^{(1)}(3,2)-N_0^2u_0^2(p_2)u_0^2(p_3)}{G^{(1)}(2,2)G^{(1)}(3,3)}\\
&+\frac{G^{(1)}(1,3)G^{(1)}(2,1)G^{(1)}(3,2)-N_0^3u_0^2(p_1)u_0^2(p_2)u_0^2(p_3)}{G^{(1)}(1,1)G^{(1)}(2,2)G^{(1)}(3,3)}\\
&+\frac{G^{(1)}(1,2)G^{(1)}(2,3)G^{(1)}(3,1)-N_0^3u_0^2(p_1)u_0^2(p_2)u_0^2(p_3)}{G^{(1)}(1,1)G^{(1)}(2,2)G^{(1)}(3,3)}. \quad (22)
\end{aligned}$$

The above correlation function $C(\boldsymbol{p}_1,\boldsymbol{p}_2,\boldsymbol{p}_3)$ possesses the proper coherent and chaotic limits. For a nearly completely coherent source with almost all particles populating the ground condensate state, $N_0\to N$, the terms in the numerator cancel each other and we have $C(\boldsymbol{p}_1,\boldsymbol{p}_2,\boldsymbol{p}_3)$=1, and the BE correlation is absent. For the other extreme of a completely chaotic source with $N_0\ll N$, the second terms in the numerators proportional to N_0^2 give negligible contribution and can be neglected. The correlation function $C(\boldsymbol{p}_1,\boldsymbol{p}_2,\boldsymbol{p}_3)$ becomes the usual BE correlation for a completely chaotic source. These results will allow the evaluation of the three-particle correlation function using the functions of $G^{(1)}(\boldsymbol{p}_1,\boldsymbol{p}_2)$ and $u_0^2(\boldsymbol{p})$ in Eqs. (15)-(18). Different ways of re-combining some of the terms in Eq. (22) in terms of two-particle correlation functions may allow one to extract quantities that minimize the systematic errors in two-particle correlation function measurements.

9 Conclusions and Summary

A proper framework to study Bose-Einstein correlations is the theory of Bose-Einstein condensation. We examine the condition for the occurrence of the Bose-Einstein condensation in an exactly solvable model. We place identical bosons in a spherical harmonic oscillator potential that arises either externally or approximately from its own mean fields. The order parameter is $T/\hbar\omega$, the ratio of the temperature to the energy gap between the lowest and the first excited single-particle state. The degree of chaoticity or condensation is quantified by the condensate fraction $f_0=N_0/N$ which specifies the transition from a chaotic state to a coherent condensate state. The condensate fraction f_0 is a cubic function of the order

parameter $T/\hbar\omega$. The critical order parameter $T_c/\hbar\omega$ varies with the boson number N as $T_c/\hbar\omega$=$0.6777N^{0.3666}$. The transition from the completely chaotic state with f_0=0 to the completely coherent state with $f_0\rightarrow$1 is a second-order-type transition under a gradual decrease of the order parameter $T/\hbar\omega$. It is not a first-order phase transition. A pion gas with $r_{\rm rms}, T$, and N, typical of those in RHIC and LHC, is expected to contain a large condensate fraction and a high degree of suppression of Bose-Einstein correlation.

The evaluation of the two-particle correlation function indicates that the usual "chaoticity parameter" λ can only be interpreted as an experimental tool to label the intercept of the correlation function $C(\boldsymbol{p},\boldsymbol{q})$ at $\boldsymbol{q}$=0. The parameter λ is correlated with the degree of chaoticity only for small values of p but is at variance from such an interpretation of chaoticity at high values of p, as shown in Figs. 4 and 5(a).

We have written out the functional form of the three-particle distribution function as a function of the momenta of the three particles that contains the proper chaotic and coherent limits. It permits the description for the transition from the chaotic states to coherent states. These results will allow the evaluation of the three-particle correlation function in an exactly solvable problem that will assist the comparison with three-particle correlation measurements.

Acknowledgement

This work was supported in part by the Division of Nuclear Physics, U.S. Department of Energy, Contract No. DE-AC05-00OR22725, and the National Natural Science Foundation of China, Contract Nos. 11075027 and 11275037.

References

[1] R. Hanbury Brown and R. Q. Twiss, Nature **178**, 1046 (1956).

[2] R. J. Glauber, Phys . Rev. Lett. **10**, 84 (1963);
R. J. Glauber, Phys. Rev. **130**, 2529 (1963);
R. J. Glauber, Phys. Rev. **130**, 2766 (1963).

[3] M. Gyulassy, K. K. Kauffman, L. W. Wilson, Phys. Rev. **C20**, 2267 (1979).

[4] D.N. Voskresensky, J. Exp. Theor. Phys. **78**, 793 (1994); E.E. Kolomeitsev, D.N. Voskresensky, Phys. Atom. Nucl. **58**, 2082 (1995); E.E. Kolomeitsev, Burkhard Kampfer, D.N. Voskresensky, Acta Phys. Polon. **B27**, 3263 (1996); D.N. Voskresensky, Phys.Atom.Nucl. **59**, 2015 (1996).

[5] U. Wiedemann and U. Heinz, Phys. Rep. **319**, 145 (1999).

[6] R. M. Weiner, Phys. Rept. **327** 249 (2000).

[7] M. A. Lisa, S. Pratt, R. Soltz, and U. Wiedemann, Ann. Rev. Nucl. Part. Sci. **55**, 357 (2005).

[8] For a pedagogical discussion, see Chapter XVII of C. Y. Wong, *Introduction to High-Energy Heavy-Ion Collisions*, World Scientific Publisher, 1994.

[9] H. D. Politzer, Phys. Rev. **A54**, 5048 (1996).

[10] M. Naraschewski and R. Glauber, Phys. Rev. **A59**, 4595 (1999).

[11] J. Viana Gomes, A. Perrin, M. Schellekens, D. Boiron, C. I. Westbrook, and Michael Belsley, Rev. A **74**, 053607 (2006); M. Yasuda and F. Shimizu, Phys. Rev. Lett. **77**, 3090 (1996); D. Hellweg, L. Cacciapuoti, M. Kottke, T. Schulte, K. Sengstock, W. Ertmer, and J. J. Arlt, Phys. Rev. Lett. 91, 010406 (2003); M. Greiner, C. A. Regal, J. T. Stewart, and D. S. Jin, Phys. Rev. Lett. **94**, 110401 (2005); S. Fölling, F. Gerbier, A. Widera, O. Mandel, T. Gericke, and I. Bloch, Nature **434**, 481 (2005); A. Ottl, S. Ritter, M. Kohl, and T. Esslinger, Phys. Rev. Lett. **95**, 090404 (2005); M. Schellekens, R. Hoppeler, A. Perrin, J. Viana Gomes, D. Boiron, A. Aspect, and C. I. Westbrook, Science **310**, 648 (2005); J. Esteve, J.-B. Trebbia, T. Schumm, A. Aspect, C. I. Westbrook, and I. Bouchoule, Phys. Rev. Lett. **96**, 130403 (2006).

[12] C. N. Fowler and R. M. Weiner, Phys. Lett. **B70**, 201 (1977);
C. N. Fowler and R. M. Weiner, Phys. Rev. **D17**, 3118 (1978);
C. N. Fowler, N. Stelte, and R. M. Weiner, Nucl. Phys. **A319**, 349 (1979).

[13] S. Pratt, Phys. Lett. **B301**, 159 (1993).

[14] T. Csörgő and J. Zimányi, Phys. Rev. Lett. **80** 916 (1998);
J. Zimányi and T. Csörgő, Heavy Ion Phys. **9** 241 (1999).

[15] C. Y. Wong and W. N. Zhang, Phys. Rev **C76**, 034905 (2007).

[16] J. Liu, P. Ru, and W. N. Zhang, Int. J. Mod. Phys. **E22**, 1350083 (2013).

[17] J. Liu, P. Ru, and W. N. Zhang, C. Y. Wong, Jour. Phys. **G41**, 125101 (2014).

[18] A. M. Gavrilik, Symmetry, Integrability and Geometry, **2**, 1 (2006);
A. M. Gavrilik, SIGMA, **2**, 74 (2006) [hep-ph/0512357];
A. M. Gavrilik, A. Rebesh, Mod. Phys. Lett. **B25**, 1150030 (2012);
A. M. Gavrilik, I. Kachurik, A. Rebesh, [arXiv:1309.1363];
A. M. Gavrilik, I. Kachurik, Y. Mishchenko, J. Phys. **A56**, 948 (2011);
A. M. Gavrilik, Y. Mishchenko, Phys. Lett. **A376**, 1596 (2012);
A. M. Gavrilik, Y. Mishchenko, Ukr. J. Phys. **58**, 1171 (2013).

[19] Yu. M. Sinyukov and V. M. Shapoval, Phys. Rev. **D87**, 094024 (2013).

[20] L.McLerran and R.Venugopalan, Phys. Rev. **D49**, 2233 (1994);
L.McLerran and R.Venugopalan, Phys. Rev. **D49**, 3352 (1994).

[21] J. P. Blaizot et al., Nucl. Phys. **A873**, 68 (2012).

[22] B. Abelev et al. (ALICE Collaboration), Phys. Rev. **C89**, 024911 (2014).

[23] H. Boggild et al. (NA44 Collaboration), Phys. Lett. **B455** 77 (1999);
I. G. Bearden et al. (NA44 Collaboration), Phys. Lett. **B517** 25 (2001).

[24] M. M. Aggarwal et al. (WA98 Collaboration), Phys. Rev. Lett. **85** 2895 (2000).

[25] J. Adams et al. (STAR Collaboration), Phys. Rev. Lett. **91** 262301 (2001).

[26] K. Morita, S. Muroya, and H. Nakamura, Prog. Theo. Phys. **114**, 583 (2005).

[27] W. A. Zajc, Phys. Rev. **D35**, 3396 (1987).

[28] M. Biyajima, A. Bartl, T. Mizoguchi, N. Suzuki and O. Terazawa, Prog. Theor. Phys. **84** 931 (1990).

[29] I. V. Andreev, M. Plümer, R. M. Weiner, Phys . Rev. Lett. **67**, 3475 (1991); I. V. Andreev, M. Plümer, R. M. Weiner, Int. J. Mod. Phys.**A8**, 4577 (1993).

[30] W. Z. Zhang, Y. M. Liu, S. Wang *et al.*, PHys. Rev. **C47**, 795 (1993); W. N. Zhang, Y. M. Liu, L. Huo *et al.*, Phys. Rev. **C51**, 922 (1995) ; W. N. Zhang, L. Huo, X. J. Chen *et al.*, Phys. Rev. **C58**, 2311 (1998); W. N. Zhang, G. X. Tang, X. J. Chen *et al.*, Phys. Rev. **C62**, 044903 (2000).

[31] W. Q. Chao, C. S. Gao, and Q. H. Zhang, J. Phys. **G21**, 847 (1995); Q. H. Zhang, W. Q. Chao, and C. S. Gao, Phys. Rev. **C52**, 2064 (1995).

[32] U. Heinz and Q. H. Zhang, Phys. Rev. **C56**, 426 (1997); U. Heinz and A. Sugarbaker, Phys. Rev. **C70**, 054908 (2004).

[33] H. Nakamura and R. Seki, Phys. Rev. **C60** , 064904(1999); H. Nakamura and R. Seki, Phys. Rev. **C61**, 054905 (2000).

[34] T. Csörgö, Heavy Ion Phys. **15**, 1 (2002).

[35] R. Glauber, Nucl. Phys. **A774**, 3 (2006).

[36] R. J. Glauber, in Lectures in Theoretical Physics, edited by W. E. Brittin and L. G. Dunham (Interscience, New York, 1959), Vol 1, p. 315.

[37] S. S. Adler *et al.*, (PHENIX Collaboration), Phys. Rev. Lett. **93**, 152302 (2004).

[38] J. Adams *et al.*, (STAR Collaboration), Phys. Rev. **C71**, 044906 (2005).

Excitation function of elastic *pp* scattering from a unitarily extended Bialas-Bzdak model

F. Nemes[1,2]

[1] CERN, CH-1211 Geneva 23, Switzerland

T. Csörgő[2,3]

[2] Wigner Research Centre for Physics, Hungarian Academy of Sciences
H-1525 Budapest 114, P.O.Box 49, Hungary

[3]KRF, H-3200 Gyöngyös, Mátrai út 36, Hungary

M. Csanád[4]

[4] Eötvös University, Department of Atomic Physics
H-1117 Budapest, Pázmány Péter s., 1/A Hungary

Abstract

The Bialas-Bzdak model of elastic proton-proton scattering assumes a purely imaginary forward scattering amplitude, which consequently vanishes at the diffractive minima. We extended the model to arbitrarily large real parts in a way that constraints from unitarity are satisfied. The resulting model is able to describe elastic *pp* scattering not only at the lower ISR energies but also at $\sqrt{s}$ =7 TeV in a statistically acceptable manner, both in the diffractive cone and in the region of the first diffractive minimum. The total cross-section as well as the differential cross-section of elastic proton-proton scattering is predicted for the future LHC energies of $\sqrt{s}$ =8, 13, 14, 15 TeV and also to 28 TeV. A non-trivial, significantly non-exponential feature of the differential cross-section of elastic proton-proton scattering is analyzed and the excitation function of the non-exponential behavior is predicted. The excitation function of the shadow profiles is discussed and related to saturation at small impact parameters.

1 Introduction

In a pair of recent papers the Bialas-Bzdak model [1] (BB) of small angle elastic proton-proton (pp) scattering at high energies was studied at 7 TeV LHC energy [2,3]. In those papers a terse overview is reported about the field of elastic scattering at high energies. Here we would like to highlight only some recent works which influenced us.

In this manuscript the BB model is extrapolated to future LHC energies. Our method to include the energy evolution of the parameters is somewhat similar to the so-called "geometric scaling" discussed in Ref. [4] and also in Ref. [5].

Using 2012 data the TOTEM experiment recently made an important experimental observation at $\sqrt{s} = 8$ TeV: the pp elastic differential cross-section shows a deviation from the most simple non-exponential behavior at low-$|t|$, [6] where t is the squared four-momentum transfer of the pp scattering process. This feature of the $\sqrt{s} = 8$ TeV (preliminary) TOTEM dataset, was related to t-channel unitarity of the forward scattering amplitude (FSA) in Ref. [7], a concept that we also focus on, using and generalizing in a unitary manner the quark-diquark model of Bialas and Bzdak for the determination of the shape of the FSA of elastic pp scattering.

In its original form, the BB model [1] assumes that the real part of the FSA is negligible, correspondingly, the FSA vanishes at the diffractive minima. At the ISR energies of $\sqrt{s}$ =23.5−62.5 GeV, that were first analyzed in the inspiring paper of Bialas and Bzdak [1], this assumption is indeed reasonable, as confirmed in Ref. [2]. At these ISR energies, only very few data points were available in the dip region around the first diffractive minimum of elastic pp scattering, which were then left out from the BB model fits of Ref. [2] to achieve a quality description of the remaining data points. However, in recent years, TOTEM data [8] explored the dip region at the LHC energy of 7 TeV in great details, at several different values of the squared four-momentum transfer t. Ref. [2] demonstrated, that the original BB model cannot describe this dip region, not without at least a small real part that has to be added to its FSA in a reasonable way.

Subsequently, the BB model has been generalized in Ref. [3] by allowing for a perturbatively small real part of the FSA, which improved the agreement of the model with TOTEM data on elastic pp scattering at the LHC energy of $\sqrt{s} = 7$ TeV. It was expected that the main reason for the appearance of this real part is that certain rare elastic scattering of the constituents of the protons may be non-collinear thus may lead to inelastic events even if the elementary interactions are elastic. The corresponding phenomenological generalization of the Bialas-Bzdak model [3] was indeed based on the assumption that the real part of the FSA is small, and can be handled perturbatively. The resulting α-generalized Bialas-Bzdak (αBB) model was compared to ISR data in Ref. [3], and it was demonstrated that a small, of the order of 1 % real part of the FSA indeed results in excellent fit qualities and a statistically acceptable description of the data in the region of the diffractive minimum or dip. However, at the LHC energy of 7 TeV, the same αBB model does not result in a satisfactory, statistically acceptable fit quality, although the visual quality of the fitted curves improve significantly as compared to that of the original BB model [3].

These results indicate that at the LHC energies the real part of the FSA

may reach significant values where unitarity constraints may already play an important role. The unitarity of the S-matrix provides also the basis for the optical theorem, which in turn provides a method to determine the total cross-section from an extrapolation of the elastic scattering measurements to the $t = 0$ point.

In the αBB model of Ref. [3], unitarity constraints were not explicitly considered: as the original BB model with zero real parts obeyed unitarity, adding a small real part may possibly resulted only in small violations of unitarity and the optical theorem. However, when the model was fitted to the 7 TeV TOTEM data in the dip region in Ref. [3], the extrapolation to the point of $t = 0$ and the related value of the total cross-section underestimated the measured total cross-section by about 40%, suggesting, that perhaps the real part of the FSA may be large, and unitarity relations should be explicitly considered.

These indications motivate the present manuscript, where the Bialas-Bzdak model is further generalized to arbitrarily large real parts of the FSA, fully taking into account unitarity constraints. The resulting model is referred to as the real extended Bialas-Bzdak (ReBB) model.

The structure of the manuscript is as follows: in Section 2, the general form of the forward scattering amplitude is re-derived for the case of a non-vanishing real part starting from S-matrix unitarity. Then this result is applied to the extension of the BB model to a non-vanishing and possibly large real part of the FSA.

In Section 3, the resulting ReBB model is fitted to TOTEM data on elastic pp scattering at $\sqrt{s} = 7$ TeV, both in the diffractive cone [9, 10] and in the dip region [8], separately.

Based on these fits and comparisons of the ReBB model to $\sqrt{s} = 7$ TeV data, in Section 4.1 the shadow profile function A(b) is evaluated. This function characterizes the probability of inelastic pp scattering at a given impact parameter b, and is compared to the shadow profile functions of elastic pp collisions at lower, ISR energies. Section 4.2 is devoted to study the structure of the differential cross-section $d\sigma/dt$ at low-$|t|$ values and also to compare it with a purely exponential behavior.

In Section 5, the excitation function of the fit parameters is investigated and their evolution with $\sqrt{s}$ is obtained based on a geometrical picture. The model parameters are extrapolated to the expected future LHC energies of 8, 13, 14 and 15 TeV, as well as for 28 TeV, that is not foreseen to be available at man-made accelerators in the near future, but may be relevant for the investigation of cosmic ray events. The excitation functions of the shadow profile functions $A(b)$ are also discussed. Finally we summarize and conclude.

2 The real extended Bialas-Bzdak model

Although the original form of the Bialas-Bzdak model neglects the real part of the FSA in high energy elastic pp scattering, the model is based on Glauber scattering theory and obeys unitarity constraints.

The phenomenological generalization of the Bialas-Bzdak model [3] is based on the assumption, that the real part of the FSA is small, and can be handled perturbatively, so unitarity constraints are not violated strongly. However, it turned out that the addition of a small real part does not lead to a statistically

acceptable description of TOTEM data on elastic pp collisions at $\sqrt{s} = 7$ TeV. In this manuscript, we consider the case, when the real part of the FSA is not perturbatively small. We restart from S-matrix unitarity, and consider how the BB model can be extended to significant, real values of the FSA while satisfying the constraints of unitarity.

2.1 S-matrix unitarity in the context of elastic proton-proton scattering

In this subsection some of the basic equations of quantum scattering theory are recapitulated. The scattering or S matrix describes how a physical system changes in a scattering process. The unitarity of the S matrix ensures that the sum of the probabilities of all possible outcomes of the scattering process is one.

The unitarity of the scattering matrix S is expressed by the equation

$$SS^{\dagger} = I\,, \tag{1}$$

where I is the identity matrix. The decomposition $S = I + iT$, where T is the transition matrix, leads the unitarity relation Eq. (1) to

$$T - T^{\dagger} = iTT^{\dagger}\,, \tag{2}$$

which can be rewritten in the impact parameter b representation as

$$2\,\mathrm{Im}\,t_{el}(s,b) = |t_{el}(s,b)|^2 + \tilde{\sigma}_{inel}(s,b)\,, \tag{3}$$

where s is the squared total center-of-mass energy.

The functions $\tilde{\sigma}_{inel}(s,b) = d^2\sigma_{inel}/d^2b$ and $|t_{el}(s,b)|^2 = d^2\sigma_{el}/d^2b$ are the inelastic and elastic scattering probabilities per unit area, respectively. The elastic amplitude $t_{el}(s,b)$ is defined in the impact parameter space and corresponds to the ℓth partial wave amplitude $T_\ell(s)$ through the relation $\ell + 1/2 \leftrightarrow b\sqrt{s}/2$, which is valid in the high energy limit, $\sqrt{s} \to \infty$.

The unitarity relation (3) is a second order polynomial equation in terms of the (complex) elastic amplitude $t_{el}(s,b)$. If one introduces the opacity or eikonal function [11–16]

$$t_{el}(s,b) = i\left[1 - e^{-\Omega(s,b)}\right]\,, \tag{4}$$

$\tilde{\sigma}_{inel}$ can be expressed as

$$\tilde{\sigma}_{inel}(s,b) = 1 - e^{-2\,\mathrm{Re}\,\Omega(s,b)}\,.$$

The formula for t_{el} is the so called eikonal form. From Eq. (4) the real part of the opacity function $\Omega(s,b)$ can be expressed as

$$\mathrm{Re}\,\Omega(s,b) = -\frac{1}{2}\ln\left[1 - \tilde{\sigma}_{inel}(s,b)\right]\,. \tag{5}$$

In the original BB model it is assumed that the real part of t_{el} vanishes. In this case Eqs. (4) and (5) implies that

$$t_{el}(s,b) = i\left[1 - \sqrt{1 - \tilde{\sigma}_{inel}(s,b)}\right]\,. \tag{6}$$

If the imaginary part Im Ω is taken into account in Eq. (4) the result is

$$t_{el}(s,b) = i\left[1 - e^{-i\,\mathrm{Im}\,\Omega(s,b)}\sqrt{1-\tilde{\sigma}_{inel}(s,b)}\right] , \tag{7}$$

where the concrete parametrization of $\mathrm{Im}\,\Omega(s,b)$ is discussed later.

To compare the model with data the amplitude Eq. (7) has to be transformed into momentum space

$$T(s,\Delta) = \int_{-\infty}^{+\infty}\int_{-\infty}^{+\infty} e^{i\vec{\Delta}\cdot\vec{b}} t_{el}(s,b)\mathrm{d}^2 b \tag{8}$$

$$= 2\pi i \int_0^{\infty} J_0\left(\Delta\cdot b\right)\left[1 - e^{-\Omega(s,b)}\right] b\,\mathrm{d}b\,, \tag{9}$$

where $b = |\vec{b}|$, $\Delta = |\vec{\Delta}|$ is the transverse momentum and J_0 is the zero order Bessel-function of the first kind. In the high energy limit, $\sqrt{s} \to \infty$, $\Delta(t) \simeq \sqrt{-t}$ where t is the squared four-momentum transfer. Consequently the elastic differential cross-section can be evaluated as

$$\frac{\mathrm{d}\sigma}{\mathrm{d}t} = \frac{1}{4\pi}\left|T\left(s,\Delta\right)\right|^2 . \tag{10}$$

According to the optical theorem the total elastic cross-section is

$$\sigma_{tot} = 2\,T(s,\Delta)|_{t=0} , \tag{11}$$

while the ratio of the real to the imaginary FSA is

$$\rho = \frac{\mathrm{Re}\,T(s,0)}{\mathrm{Im}\,T(s,0)}\,. \tag{12}$$

2.2 The Bialas-Bzdak model with a unitarily extended amplitude

The original BB model [1] describes the proton as a bound state of a quark and a diquark, where both constituents have to be understood as "dressed" objects that effectively include all possible virtual gluons and $q\bar{q}$ pairs to valence or dressed quarks. The quark and the diquark are characterized with their positions with respect to the proton's center of mass using their transverse position vectors $\vec{s}_q$ and $\vec{s}_d$ in the plane perpendicular to the proton's incident momentum. Hence, the coordinate space H of the colliding protons is spanned by the vector $h = (\vec{s}_q, \vec{s}_d, \vec{s}\,'_q, \vec{s}\,'_d)$ where the primed coordinates indicate the coordinates of the second proton.

The inelastic proton-proton scattering probability $\tilde{\sigma}_{inel}(b)$ in Eq. (6) is calculated as an average of "elementary" inelastic scattering probabilities $\sigma(h;\vec{b})$ over the coordinate space H [17]

$$\tilde{\sigma}_{inel}(b) = \left\langle \sigma(h;\vec{b})\right\rangle_H = \int_{-\infty}^{+\infty} ... \int_{-\infty}^{+\infty} \mathrm{d}h\, p(h)\cdot\sigma(h;\vec{b})\,, \tag{13}$$

where the weight function $p(h)$ is a product of probability distributions

$$p(h) = D(\vec{s}_q, \vec{s}_d) \cdot D(\vec{s}'_q, \vec{s}'_d)\,. \tag{14}$$

The $D(\vec{s}_q, \vec{s}_d)$ function is a two-dimensional Gaussian, which describes the center of mass distribution of the quark and diquark with respect to the center of mass of the proton

$$D\left(\vec{s}_q, \vec{s}_d\right) = \frac{1+\lambda^2}{R_{qd}^2\,\pi} e^{-(s_q^2+s_d^2)/R_{qd}^2} \delta^2(\vec{s}_d + \lambda \vec{s}_q),\ \lambda = \frac{m_q}{m_d}\,. \tag{15}$$

The parameter R_{qd}, the standard deviation of the quark and diquark distance, is fitted to the data. Note that the two-dimensional Dirac δ function preserves the proton's center of mass and reduces the dimension of the integral in Eq. (13) from eight to four.

Note that the original BB model is realized in two different ways: in one of the cases, the diquark structure is not resolved. This is referred to as the $p = (q, d)$ BB model. A more detailed variant is when the diquark is assumed to be a composition of two quarks, referred as the $p = (q, (q, q))$. Our earlier studies using the αBB model indicated [3], that the $p = (q, d)$ case gives somewhat improved confidence levels as compared to the $p = (q, (q, q))$ case. So for the present manuscript we discuss results using the $p = (q, d)$ scenario only, however, it is trivial to extend the investigations to the $p = (q, (q, q))$ case and they result in fits which are not acceptable at $\sqrt{s} = 7$ TeV. For the case of brevity we do not present the results of the analysis with the $p = (q, (q, q))$ variant of the ReBB model, only the fit quality is reported.

It is assumed that the "elementary" inelastic scattering probability $\sigma(h; \vec{b})$ can be factorized in terms of binary collisions among the constituents with a Glauber expansion

$$\sigma(h; \vec{b}) = 1 - \prod_a \prod_b \left[1 - \sigma_{ab}(\vec{b} + \vec{s}'_a - \vec{s}_b)\right]\,, \quad a, b \in \{q, d\}\,, \tag{16}$$

where the indices a and b can be either quark q or diquark d.

The $\sigma_{ab}\left(\vec{s}\right)$ functions describe the probability of binary inelastic collision between quarks and diquarks and are assumed to be Gaussian

$$\sigma_{ab}\left(\vec{s}\right) = A_{ab} e^{-s^2/S_{ab}^2},\ S_{ab}^2 = R_a^2 + R_b^2, \quad a, b \in \{q, d\}\,, \tag{17}$$

where the R_q, R_d and A_{ab} parameters are fitted to the data.

The inelastic cross-sections of quark, diquark scatterings can be calculated by integrating the probability distributions Eq. (17) as

$$\sigma_{ab,\mathrm{inel}} = \int_{-\infty}^{+\infty} \int_{-\infty}^{+\infty} \sigma_{ab}\left(\vec{s}\right) \mathrm{d}^2 s = \pi A_{ab} S_{ab}^2\,. \tag{18}$$

In order to reduce the number of free parameters, it is assumed that the ratios of the inelastic cross-sections $\sigma_{ab,\mathrm{inel}}$ satisfy

$$\sigma_{qq,\mathrm{inel}} : \sigma_{qd,\mathrm{inel}} : \sigma_{dd,\mathrm{inel}} = 1 : 2 : 4\,, \tag{19}$$

which means that in the BB model the diquark contains twice as many partons than the quark and also that these quarks and diquarks do not "shadow" each other during the scattering process. This assumption is not trivial. The $p = (q,(q,q))$ version of the BB model allows for different $\sigma_{qq,\mathrm{inel}} : \sigma_{qd,\mathrm{inel}} : \sigma_{dd,\mathrm{inel}}$ ratios. However, as it was mentioned before, the $p = (q,(q,q))$ is less favored by the data as compared to the $p = (q,d)$ case presented below.

Using the inelastic cross-sections Eq. (18) together with the assumption Eq. (19) the A_{qd} and A_{dd} parameters can be expressed with A_{qq}

$$A_{qd} = A_{qq}\frac{4R_q^2}{R_q^2+R_d^2}\,,\ A_{dd} = A_{qq}\frac{4R_q^2}{R_d^2}\,. \tag{20}$$

In this way only five parameters have to be fitted to the data R_{qd}, R_q, R_d, λ, and A_{qq}. In practice we fix $A_{qq} = 1$ assuming that head on quark-quark (qq) collisions are completely inelastic according to Eq. (17).

The last step in the calculation is to perform the Gaussian integrals in the average Eq. (13) to obtain a formula for $\tilde{\sigma}_{inel}(b)$. The Dirac δ function in Eq. (15) expresses the protons' diquark position vectors as a function of the quarks position

$$\vec{s}_d = -\lambda\,\vec{s}_q,\ \ \vec{s}\,'_d = -\lambda\,\vec{s}\,'_q\,. \tag{21}$$

After expanding the products in the Glauber expansion Eq. (16) the following sum of contributions is obtained

$$\begin{aligned}\sigma(h;\vec{b}) =&\sigma_{qq} + 2\cdot\sigma_{qd} + \sigma_{dd} - (2\sigma_{qq}\sigma_{qd} + \sigma_{qd}^2 + \sigma_{qq}\sigma_{dd} + 2\sigma_{qd}\sigma_{dd})\\ &+ (\sigma_{qq}\sigma_{qd}^2 + 2\sigma_{qq}\sigma_{qd}\sigma_{dd} + \sigma_{dd}\sigma_{qd}^2) - \sigma_{qq}\sigma_{qd}^2\sigma_{dd}\,,\end{aligned} \tag{22}$$

where the arguments of the $\sigma_{ab}(\vec{s})$ functions are suppressed to abbreviate the notation.

The average over H in Eq. (13) has to be calculated for each term in the above expansion Eq. (22). Take the last, most general, term and calculate the average; the remaining terms are simple consequences of it. The result is

$$I = \left\langle -\sigma_{qq}\sigma_{qd}^2\sigma_{dd}\right\rangle_H = \int\limits_{-\infty}^{+\infty}\ldots\int\limits_{-\infty}^{+\infty}\mathrm{d}h\,p(h)\cdot(-\sigma_{qq}\sigma_{qd}^2\sigma_{dd}\,)\,, \tag{23}$$

where the $p(h)$ weight function Eq. (14) is a product of the quark-diquark distributions, given by Eq. (15). Substitute into this result Eq. (23) the definitions of the quark-diquark distributions Eq. (15)

$$I = -\frac{4v^2}{\pi^2}\int\limits_{-\infty}^{+\infty}\int\limits_{-\infty}^{+\infty}\mathrm{d}^2s_q\mathrm{d}^2s'_q\,e^{-2v\left(s_q^2+s_q'^2\right)}\prod_k\prod_l\sigma_{kl}(\vec{b}-\vec{s}_k+\vec{s}\,'_l),\quad k,l\in\{q,d\}\,, \tag{24}$$

where $v = (1+\lambda^2)/(2\cdot R_{qd}^2)$ and the integral over the coordinate space H is explicitly written out; it is only four dimensional due to the two Dirac δ functions in $p(h)$. Using the definitions of the $\sigma_{ab}\,(\vec{s})$ functions Eq. (17) and the expression $A = A_{qq}A_{qd}A_{dq}A_{dd}$ the integral Eq. (24) can be rewritten, to make

all the Gaussian integrals explicit

$$I = -\frac{4v^2 A}{\pi^2} \int\limits_{-\infty}^{+\infty} \int\limits_{-\infty}^{+\infty} \mathrm{d}^2 s_q \mathrm{d}^2 s'_q \, e^{-2v\left(s_q^2 + s_q'^2\right)} \prod_k \prod_l e^{-c_{kl}\left(\vec{b} - \vec{s}_k + \vec{s}'_l\right)^2} , \tag{25}$$

where the abbreviations $c_{kl} = S_{kl}^{-2}$ refer to the coefficients in Eq. (17). Finally, the four Gaussian integrals have to be evaluated in our last expression Eq. (25), which leads to

$$I = -\frac{4v^2 A}{B} e^{-b^2 \frac{\Gamma}{B}} , \tag{26}$$

where

$$\begin{aligned} B &= C_{qd,dq} \left(v + c_{qq} + \lambda^2 c_{dd}\right) + (1-\lambda)^2 D_{qd,dq} , \\ \Gamma &= C_{qd,dq} D_{qq,dd} + C_{qq,dd} D_{qd,dq} , \end{aligned} \tag{27}$$

and

$$\begin{aligned} C_{kl,mn} &= 4v + (1+\lambda)^2 \left(c_{kl} + c_{mn}\right) , \\ D_{kl,mn} &= v \left(c_{kl} + c_{mn}\right) + (1+\lambda)^2 c_{kl} c_{mn} . \end{aligned} \tag{28}$$

Each term in Eq. (13) can be obtained from the master formula Eq. (26), by setting one or more coefficients to zero, $c_{kl} = 0$ and the corresponding amplitude to one, $A_{kl} = 1$.

Up to now, according to Eq. (5) and Eq. (6), $t_{el}(s,b)$ is purely imaginary and $\Omega(s,b)$ is real. Now we have to specify the imaginary part of the opacity function, that determines the real part of the FSA. Here several model assumptions are possible, but from the analysis of the ISR data and the first studies of the 7 TeV TOTEM data at LHC we learned, that the real part of the FSA is perturbatively small at ISR energies, it becomes non-perturbative at LHC but the scattering is still dominated by the imaginary part of the scattering amplitude.

We have studied several possible choices. One possibility is to introduce the imaginary part of the opacity function so that it is proportional to the probability of inelastic scatterings, which is known to be a decreasing function of the impact parameter b. A possible interpretation of this assumption may be that the inelastic collisions arising from non-collinear elastic collisions of quarks and diquarks follow the same spatial distributions as the inelastic collisions of the same constituents

$$\mathrm{Im}\, \Omega(s,b) = -\alpha \cdot \tilde{\sigma}_{inel}(s,b) , \tag{29}$$

where α is a real number.

For the $\alpha = 0$ case, one recovers the $p = (q,d)$ version of the BB model of Ref. [1], while in the $|\alpha| \ll 1$ perturbative limit the αBB model of Ref. [3] is obtained (but note the that the values of the parameter α in the two models need to be correspondingly re-scaled).

The above proportionality between $\mathrm{Im}\, \Omega(s,b)$ and $\tilde{\sigma}_{inel}(b)$ in formula (29) provided the best fits from among the relations that we have tried. For example, we have also investigated the assumption that the real and the imaginary parts of the opacity function are proportional to one another

$$\mathrm{Im}\, \Omega(s,b) = -\alpha \cdot \mathrm{Re}\, \Omega(s,b) . \tag{30}$$

However, as the results using Eq. (30) were less favorable as the results obtained with Eq. (29), we do the data analysis part, described in the next section, using Eq. (29). We mention this possibility to highlight that here some phenomenological assumptions are necessary as the ReBB model does allow for a broad range of possibilities for the choice of the imaginary part of the opacity function.

In this way, the ReBB model is fully defined, and at a given colliding energy only six parameters determine the differential (10) and total cross-sections (11) and also the ρ parameter, defined with Eq. (12). The parameters that have to be fitted to the data include the three scale parameters, R_q, R_d, R_{qd}, that fix the geometry of the proton-proton collisions, as well as the three additional parameters α, λ and A_{qq}. Two of the latter three can be fixed: $\lambda = 0.5$ if the diquark is very weakly bound, so that its mass is twice as large as that of the valence quark, while $A_{qq} = 1$ suggests that head-on qq collisions are inelastic with a probability of 1. Thus in the actual data analysis only four parameters are fitted to the data at each $\sqrt{s}$: the three scale parameters R_q, R_d and R_{qd}, as well as the parameter α. As we shall see, the parameter α will play a key role when describing the shape of the dip of the differential cross-sections of elastic pp scatterings at LHC energies.

3 Fit method and results

The proton-proton elastic differential cross-section data measured by the LHC TOTEM experiment at 7 TeV is a compilation of two subsequent measurements [8, 9]. The squared four-momentum transfer value $t_{sep} = -0.375$ GeV^2 separates the two data sets.[1] Note, that the two datasets were taken with two different settings of the machine optics of the LHC accelerator.

The ReBB model, defined with Eq. (10), was fitted to the data at ISR energies and at LHC energy of $\sqrt{s} = 7$ TeV. The relation between the imaginary part of $\Omega(s, b)$ and α is defined with Eq. (29). In agreement with our previous investigations the $A_{qq} = 1$ and $\lambda = \frac{1}{2}$ parameters can be kept constant, which reduces the number of free parameters to four R_{qd}, R_q, R_d and α.

First we have attempted to fit the ReBB model in the $0 < |t| < 2.5$ GeV^2 range, fitting simultaneously both the low-$|t|$ and the dip region. In the course of the minimization of the ReBB model at $\sqrt{s} = 7$ TeV in this t-range, covering the two different TOTEM data sets, we found that the χ^2/NDF value decreases significantly, if a relative normalization constant γ is introduced between the fit of the two data sets. Therefore, the calculated differential cross-section is fitted with

$$\frac{\mathrm{d}\sigma}{\mathrm{d}t} \to \gamma \cdot \frac{\mathrm{d}\sigma}{\mathrm{d}t}\,, \tag{31}$$

if $|t| < |t_{sep}|$, where γ is an additional parameter to be minimized. The fit at $\sqrt{s} = 7$ TeV is shown in Fig. 1.

Although the fit looks reasonable and reproducing the data qualitatively rather well, the fit quality it is not yet statistically acceptable, when the fit is extended to the whole t-region of the combined data set. Note that we determined the fit quality using statistical errors only, and as claimed in the

[1] The squared four-momentum transfer value t_{sep} separates the bin centers at the common boundary, the two bins actually overlap [8, 9].

original TOTEM publications [8, 9], the systematic errors in the two data set might be slightly different, that is rather difficult to handle correctly in the present analysis. So instead of determining the systematic errors of the model parameters from the systematic errors of the data we decided to analyze the two TOTEM data sets separately and check for the consistency of the results. As detailed below, this strategy lead to a reasonable fit qualities (CL = 2.6 %, statistically acceptable fit in the cone region and CL = 0.04 %, statistically marginal fit in the dip region) with a remarkable stability of fit parameters as detailed below.

$\sqrt{s}$ [GeV]	23.5	30.7	52.8	62.5	7000	
$\|t\|$ [GeV^2]	$(0, 2.5)$				$(0, \|t_{sep}\|)$	$(\|t_{sep}\|, 2.5)$
χ^2/NDF	124.7/102	95.9/47	100.1/48	76.6/47	109.9/83	120.42/73
CL [%]	6.3	3×10^{-3}	2×10^{-3}	0.41	2.6	4×10^{-2}
R_q $[fm]$	0.27±0.01	0.28±0.01	0.27±0.01	0.28±0.01	0.45±0.01	0.43±0.01
R_d $[fm]$	0.72±0.01	0.74±0.01	0.74±0.01	0.75±0.01	0.94±0.01	0.91±0.01
R_{qd} $[fm]$	0.30±0.01	0.29±0.01	0.33±0.01	0.32±0.01	0.33±0.01	0.37±0.02
α	0.03±0.01	0.02±0.01	0.04±0.01	0.04±0.01	0.12	0.12±0.01

Table 1: The values of the fitted ReBB model parameters. The proton-proton elastic $d\sigma/dt$ data measured by the TOTEM experiment at 7 TeV is a composition of two subsequent measurements, which can be separated at t_{sep}. The overall fit involving the whole $0 < |t| < 2.5$ GeV^2 range provides $\chi^2/NDF = 336.4/159$ which is not statistically acceptable, while the fits below and above $|t_{sep}|$ provide either a statistically acceptable (CL $> 0.1\%$) or marginally good (CL = 0.04%) fit quality.

If a *separated* fit to $\sqrt{s} = 7$ TeV elastic differential cross-section $d\sigma/dt$ data is evaluated, below and above the separation $|t_{sep}|$, a quality result can be obtained, which is shown in Figs. 2 and 3 and reported in Table 1, together with our results at ISR energies [8, 9, 18, 19]. Note that the normalization factor γ, introduced in Eq. (31), is not applied at $\sqrt{s} = 7$ TeV, as the two data set were fitted separately.

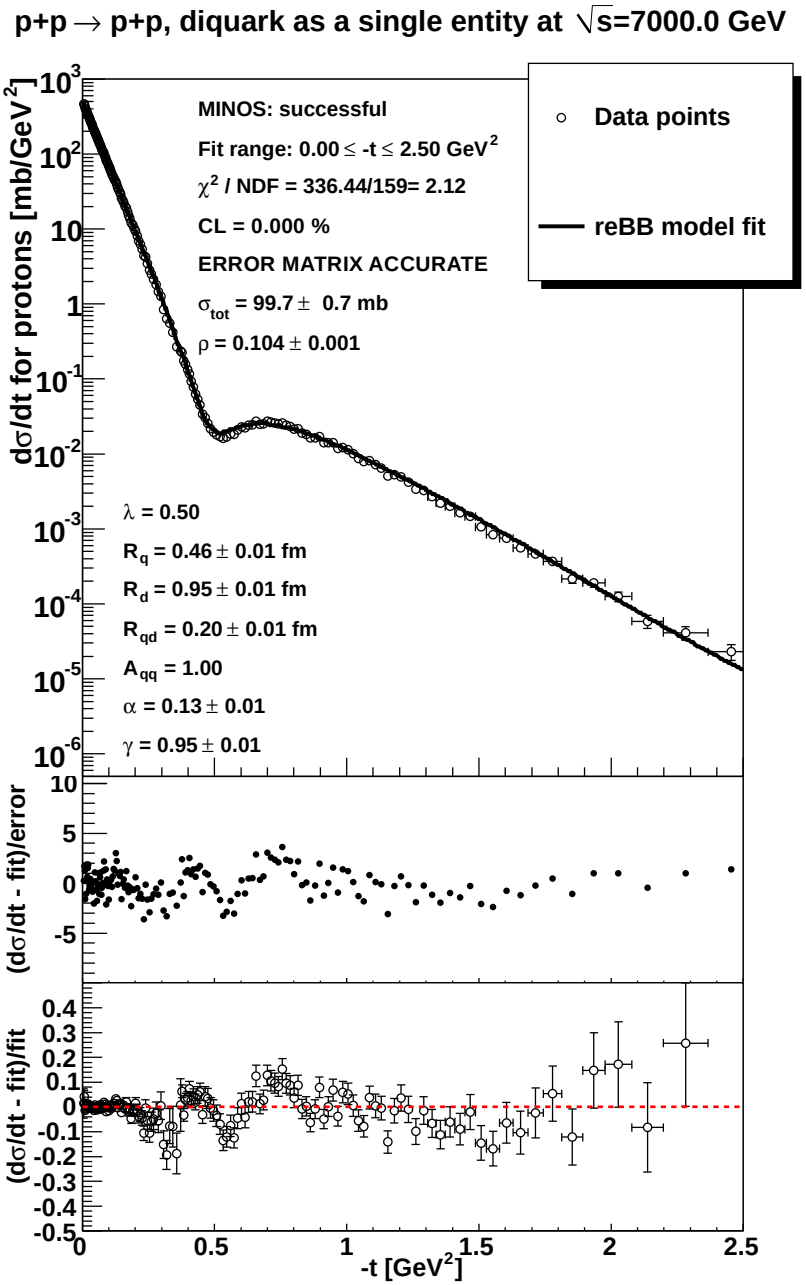

Figure 1: The fit of the ReBB model at $\sqrt{s} = 7$ TeV in the $0 < |t| < 2.5$ GeV^2 squared four momentum $|t|$ range. The real part of the amplitude t_{el} is defined with expression Eq. (29). According to Eq. (31) we use a relative normalization constant γ between the two TOTEM datasets at $\sqrt{s} = 7$ TeV. The fitted parameters are shown in the left bottom corner, parameters without errors were fixed in the minimization. The total cross-section σ_{tot} and the parameter ρ are derived quantities according to Eqs. (11) and (12), respectively.

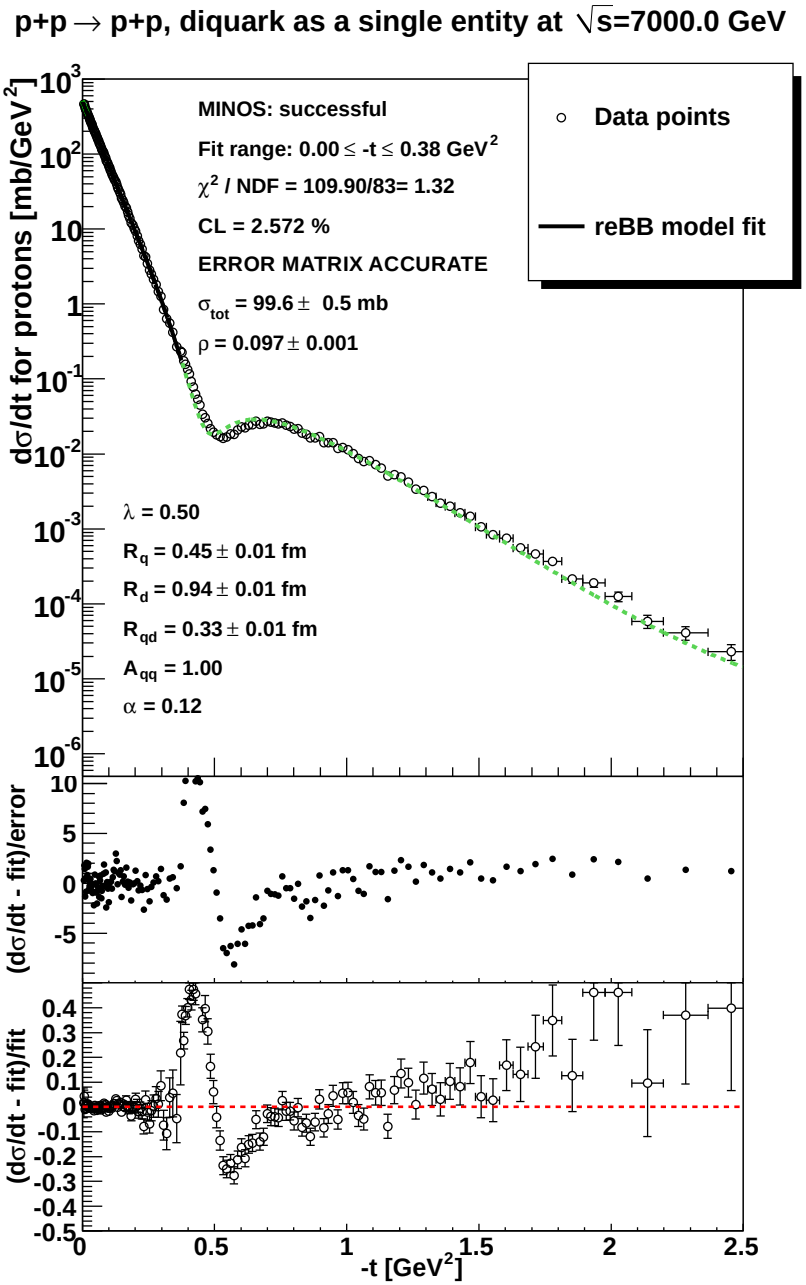

Figure 2: The same as Fig. 1, but the fit is evaluated in the $0 < |t| < |t_{sep}|$ range. The fitted curve is shown with solid line, its extrapolation above $|t_{sep}|$ is indicated with a dashed line. Note that the extrapolated curve remains close to the data points, following the measured differential cross-sections well even far away from the region where the model was fitted to the data.

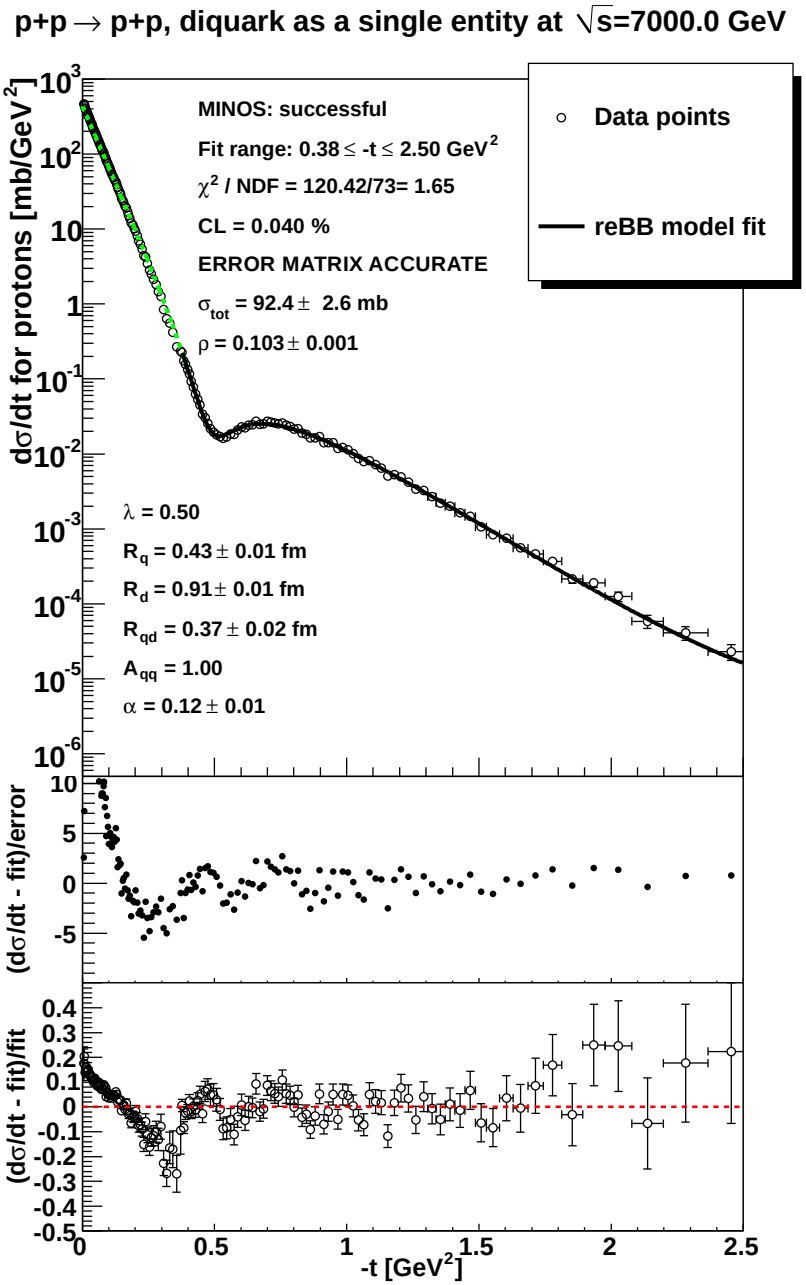

Figure 3: The same as Fig. 1, but the fit is performed in the $|t_{sep}| < |t| < 2.5$ GeV^2 range. The fitted curve is shown with solid line, its extrapolation is indicated with a dashed line. Note that when the curve is extrapolated to the low-$|t|$ region, the extrapolated curve again follows the measured differential cross-section remarkably well even far away the fit region: the ReBB model fit is remarkably stable over the whole $|t|$-range.

The resulting parameters coming from the two separate fits at 7 TeV $d\sigma/dt$,

over and below the $|t_{sep}|$ value, are *consistent* with each other within 2σ error. Note that at $\sqrt{s} = 7$ TeV the dip is not part of the fit range $(0, |t_{sep}|)$, thus the minimization procedure cannot determine the value of parameter α. In this case we have fixed α to the value of the fit from the other $|t|$ range above $|t_{sep}|$. The MINUIT status of the fit is successful in both cases.

Due to the stability of the fit parameters the extrapolation of the fit curves to the not fitted $|t|$ range remains close to the data points. The stability and consistency of the model description is visible in Fig. 2 and 3.

The calculated total cross-section of the low-$|t|$ fit $\sigma_{tot} = 99.6 \pm 0.5$ mb, where the uncertainty is the propagated uncertainty of the fit parameters, agrees well with the value $\sigma_{tot} = 98.0 \pm 2.5$ mb measured by the TOTEM experiment at $\sqrt{s} = 7$ TeV [10].

The parameter ρ can be better estimated from the fit over $|t_{sep}|$ which includes the dip. As the measured value of the ρ parameter $\rho = 0.145 \pm 0.091$ has large uncertainty the $\rho = 0.103 \pm 0.001$ calculated from the ReBB model is consistent with the measurement, see Fig. 2.

Also note that if $\mathrm{Im}\,\Omega(s, b)$ is defined to be proportional to $\mathrm{Re}\,\Omega(s, b)$, according to Eq. (30), the MINUIT fit result of $\chi^2/NDF = 405.6/159 = 2.55$ is obtained at $\sqrt{s} = 7$ TeV, which is disfavored as compared to fits with Eq. (29).

In our introduction we shortly mentioned the $p = (q, (q, q))$ version of the ReBB model, when the diquark is assumed to be a composition of two quarks [3]. This scenario provides a fit results with $\chi^2/NDF = 15509/159 \approx 97.5$, which means that the $p = (q, (q, q))$ ReBB version can be clearly rejected. The failure of this version is basically due the wrong shape of the differential cross-section: the second diffractive minimum appears too close to the first one.

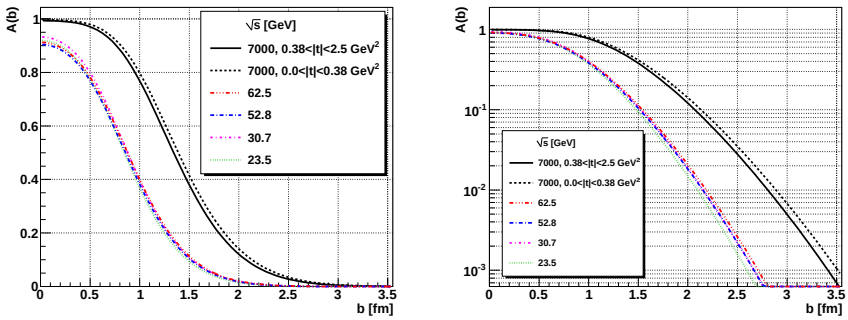

Figure 4: The shadow profile functions $A(b)$ indicate a saturation effect at LHC, while at ISR energies a Gaussian shape can be observed. Note that the dashed black curve is based on the statistically acceptable fit result in the $0 < |t| < 0.38$ GeV^2 range. The distributions' edge shows approximately the same width at each energy, corresponding to a constant "skin-width" of the proton.

4 Discussion

4.1 Shadow profile functions and saturation

The fits, from which the model parameters were determined, also permit us to evaluate the shadow profile function

$$A(s,b) = 1 - \left|\exp\left[-\Omega(s,b)\right]\right|^2 . \tag{32}$$

The obtained curves to $A(b)$ are shown in Fig. 4. The shadow profile functions at ISR energies exhibit a Gaussian like shape, which smoothly change with the center of mass energy $\sqrt{s}$. At LHC something new appears: the innermost part of the distribution shows a saturation, which means that around $b = 0$ the function becomes almost flat and stay close to $A(b) \approx 1$. Consequently, the shape of the shadow profile function $A(b)$ becomes non-Gaussian and somewhat "distorted" with respect to the shapes found at ISR.

At the same time the width of the edge of the shadow profile function A(b), which can be visualized as the proton's "skin-width", remains approximately independent of the center of mass energy $\sqrt{s}$.

4.2 Non-exponential behavior of $d\sigma_{el}/dt$

To compare the obtained ReBB fit with a *purely* exponential distribution the following exponential parametrization is used

$$\frac{\mathrm{d}\sigma_{\mathrm{el}}}{\mathrm{dt}} = \left.\frac{\mathrm{d}\sigma_{\mathrm{el}}}{\mathrm{dt}}\right|_{t=0} \cdot e^{-B\cdot|t|} , \tag{33}$$

where $\mathrm{d}\sigma_{\mathrm{el}}/\mathrm{dt}|_{t=0} = 506.4$ mb/GeV^2 and slope parameter $B = 19.89$ GeV^{-2} is applied, according to the TOTEM paper Ref. [9].

The result, shown in Fig. 5, indicates a clear non-exponential behavior of the elastic differential cross-section in the $0.0 \leq |t| \leq 0.2$ GeV^2 range at $\sqrt{s}$ =7 TeV. Note that a similar non-exponential behavior was recently discussed by the TOTEM experiment [6] and also by the theoretical work of Ref. [7].

5 Extrapolation to future LHC energies and beyond

The ReBB model can be extrapolated to energies which have not been measured yet at LHC. The fit results of Table 1 and the parametrization

$$P(s) = p_0 + p_1 \cdot \ln\left(s/s_0\right) \tag{34}$$

is applied for each parameter $P \in \{R_q, R_d, R_{qd}, \alpha\}$, where $s_0 = 1$ GeV^2. The parametrization Eq. (34) implies that the four free parameters of the original ReBB model are replaced with eight parameters p_i. The fit of the ReBB parameters are shown in Fig. 6 and the fit parameters are collected in Table 2.

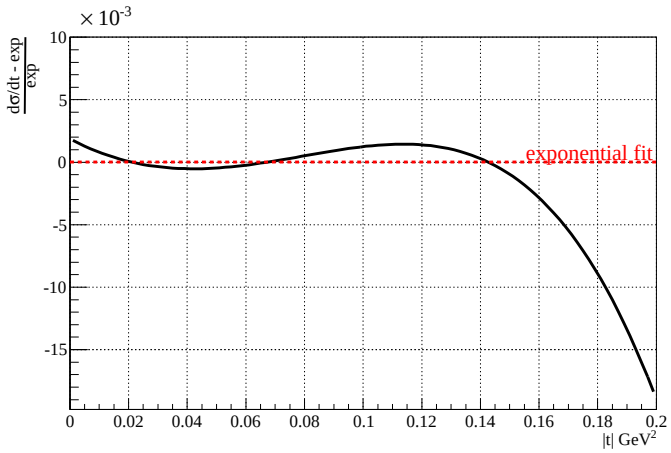

Figure 5: The ReBB model, fitted in the $0.0 \leq |t| \leq 0.36$ GeV^2 range, with respect to the exponential fit of Eq. (33). In the plot only the $0.0 \leq |t| \leq 0.2$ GeV^2 range is shown. The curve indicates a significant deviation from the simple exponential at low $|t|$ values.

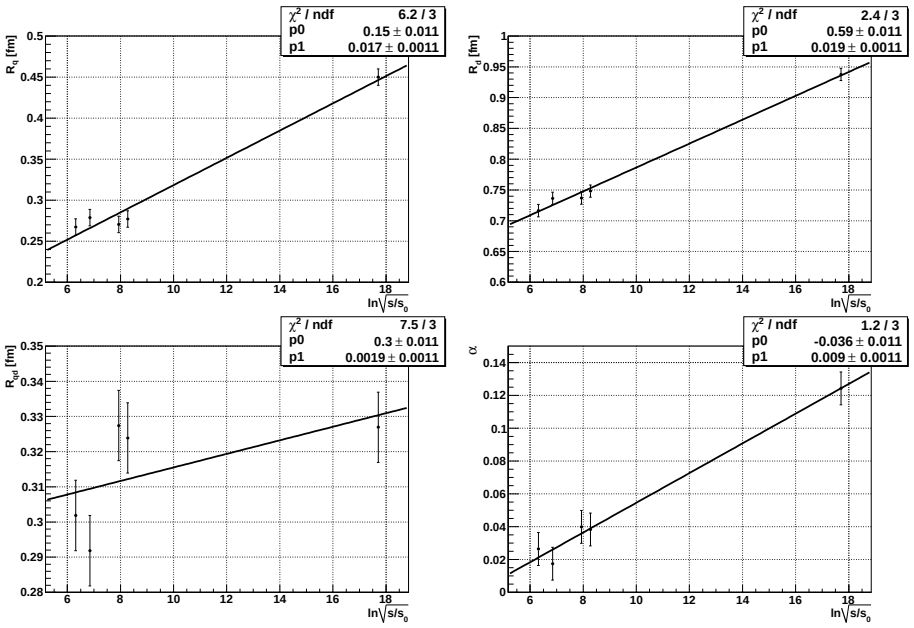

Figure 6: The results, collected in Table 1, are fitted with Eq. (34) for each parameter R_q, R_d, R_{qd} and α. The plots about the resulting fits are collected here, the parameters are collected in Table 2. The statistically acceptable quality of these fits allow the ReBB model to be extrapolated to center of mass energies which have not been measured yet at LHC.

The logarithmic dependence of the geometric parameters on the center of mass energy $\sqrt{s}$ in the parametrization Eq. (34) is motivated by the so-called

"geometric picture" based on a series of studies [20–25].

Table 2 shows that the rate of increase with $\sqrt{s}$, parameter p_1, is an order of magnitude larger for R_q and R_d than for R_{qd}. The saturation effect, described in Section 4.1, is consistent with this observation as the increasing components of the proton, the quark and the diquark, are confined into a volume which is increasing more slowly.

Parameter	R_q $[fm]$	R_d $[fm]$	R_{qd} $[fm]$	α
χ^2/NDF	6.2/3	2.4/3	7.5/3	1.2/3
CL [%]	10.2	49.4	5.8	75.3
p_0	0.15 ± 0.01	0.59 ± 0.01	0.3 ± 0.01	-0.036 ± 0.01
p_1	0.017 ± 0.001	0.019 ± 0.001	0.0019 ± 0.001	0.009 ± 0.001

Table 2: Table 1 allows the extrapolation of the model parameters over the center of mass energy $\sqrt{s}$. The parametrization Eq. (34) is applied to extrapolate the ReBB model and the fits are shown in Fig. 6. The fit quality information is provided in the first and second row of the table. Note that the fit quality is acceptable for each parameter.

Using the extrapolation formula Eq. (34) and the value of the parameters from Table 2 it is straightforward to calculate the values of the parameters at expected future LHC energies of $\sqrt{s}$ =8, 13, 14, 15 TeV and also at 28 TeV, which is beyond the LHC capabilities. Using the extrapolated values of the parameters we plot our predicted pp elastic differential cross-section curves at each mentioned energy in Fig. 7. The shadow profile functions $A(b)$ can be also extrapolated, see Fig. 8. The shadow profile functions even allow us to visualize the increasing effective interaction radius of the proton in the impact parameter space in Fig. 9.

It is also important to see how the most important features change with center of mass energy $\sqrt{s}$: the extrapolated values of the total cross-section σ_{tot}, the position of the first diffractive minimum $|t_{dip}|$ and the parameter ρ is given in Table 3.

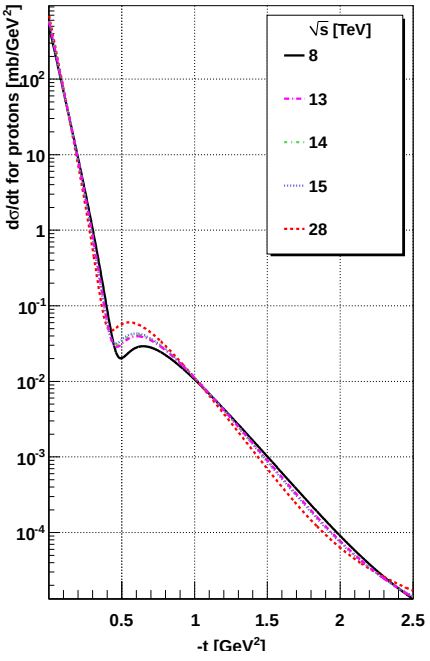

Figure 7: The pp elastic differential cross-section is extrapolated to future LHC energies and beyond.

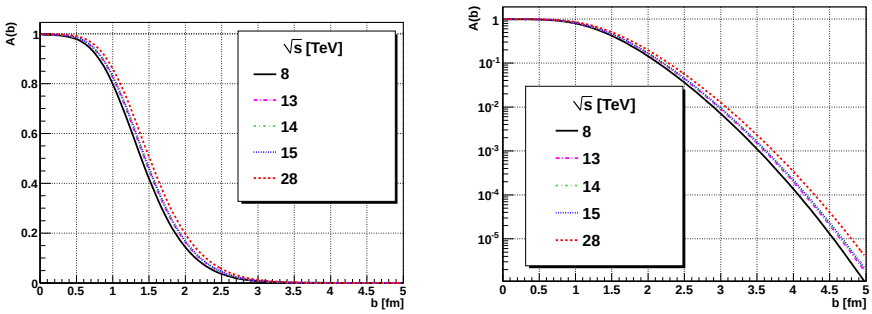

Figure 8: The shadow profile function at the extrapolated energies $\sqrt{s}$. The results show the increase of the proton interaction radius with increasing $\sqrt{s}$ energies. Also note that the "edge" of the distributions remains of approximately constant width and shape.

According to the results, the predicted value of $|t_{dip}|$ and σ_{tot} moves more than 10% when $\sqrt{s}$ increases from 8 TeV to 28 TeV, while the value of $C_{exp} = |t_{dip}| \cdot \sigma_{tot} \approx 49.8$ mb GeV^2 changes only about 2 %, which is an approximately constant value, within the errors of the extrapolation.

$\sqrt{s}$ [TeV]	σ_{tot} [mb]	$\lvert t_{dip}\rvert$[GeV^2]	ρ	$\lvert t_{dip}\rvert \cdot \sigma_{tot}$ [mb GeV^2]
8	100.1	0.494	0.103	49.45
13	107.1	0.465	0.108	49.8
14	108.1	0.461	0.108	49.83
15	109.1	0.457	0.109	49.86
28	118.5	0.426	0.114	50.48

Table 3: The extrapolated values of the total cross-section σ_{tot} at future LHC energies and beyond. The position of the first diffractive minimum $|t_{dip}|$, the parameter ρ and the $|t_{dip}| \cdot \sigma_{tot}$ value is also provided at each energy. Note that the predicted value of $|t_{dip}|$ and σ_{tot} moves more than 10% when $\sqrt{s}$ increases from 8 TeV to 28 TeV, while the value of $|t_{dip}| \cdot \sigma_{tot}$ changes only about 2%.

A similar, and exact, scaling can be derived for the case of photon scattering on a black disk, where the elastic differential cross-section is [26]

$$\frac{d\sigma_{black}}{dt} = \pi R^4 \left[\frac{J_1(q \cdot R)}{q \cdot R}\right]^2 , \tag{35}$$

where $t = -q^2$ and R is the radius of the black disk. The total cross-section is given by

$$\sigma_{tot,black} = 2\pi R^2 . \tag{36}$$

In this simple theoretical model the position of the first diffractive minimum, following from Eq. (35), and the total cross-section Eq. (36) satisfies

$$C_{black} = |t_{dip,black}| \cdot \sigma_{tot,black} = 2\pi j_{1,1}^2 (\hbar c)^2 \approx \ 35.9\,\text{mb GeV}^2 , \tag{37}$$

where $j_{1,1}$ is the first root of the first order Bessel-function of the first kind $J_1(x)$.

The scaling behavior indicated by the stability of the value C_{exp} is somewhat different from the black disk model, described by Eq. (37), as the corresponding value C_{black} is significantly different

$$C_{black} \neq C_{exp}\,. \tag{38}$$

In this sense the value of C_{exp} indicates a more complex scattering phenomena, than the photon black disc scattering.

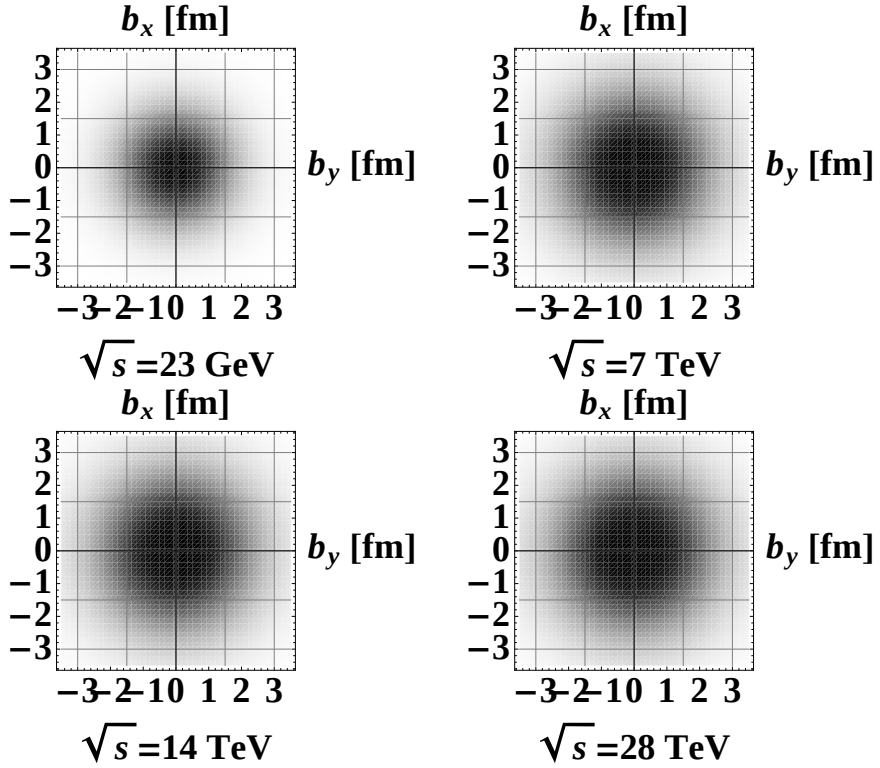

Figure 9: Visualization of the shadow profile functions $A(b)$ in the transverse plane of the impact parameter vector (b_x, b_y). The figures show the increase of the proton effective interaction radius in the impact parameter space with increasing center of mass energy $\sqrt{s}$. It can be also observed that the black innermost core of the distributions is increasing, while the thickness of the proton's "skin", the gray transition part of the distributions, remains approximately independent of the center of mass energy $\sqrt{s}$.

6 Summary and conclusions

The real part of the forward scattering amplitude (FSA) is derived from unitarity constraints in the Bialas-Bzdak model leading to the so-called ReBB model. The added real part of the FSA significantly improves the model ability to describe the data at the first diffractive minimum. In total the ReBB model describes

both the ISR and LHC data in the $0 < |t| < 2.5$ GeV^2 squared momentum transfer range in a statistically acceptable manner; in the latter case the fit range has to be divided to two parts, according to the compilation of the two independent TOTEM measurements. The results are collected in Table 1.

The fit results also permit us to evaluate the shadow profile functions $A(b)$, see Fig. 4. The plots indicate a Gaussian shape at ISR energies, while at LHC a saturation effect can be observed: the innermost part of the shadow profile function $A(b)$ around $b = 0$ is almost flat and close to $A(b) \approx 1$. The elastic differential cross-section can be compared to a purely exponential distribution and the comparison shows a significant deviation from pure exponential in the $0.0 \leq |t| \leq 0.2$ GeV^2 range.

The fit results allow the determination of the excitation functions of the ReBB model at future LHC energies and beyond, with parameters collected in Table 2 and predicted differential cross-section curves shown in Fig. 7. The shadow profile functions can be also extrapolated, see Fig. 8, which predicts that the saturated part of the proton is expected to increase with increasing center of mass energy $\sqrt{s}$. The edge of the distribution, the "skin-width" of the proton, expected to remain approximately constant. It is worth to mention that the extrapolated version of the ReBB model utilizes of only eight parameters, the p_i parameters of Table 2, and in this sense a "minimal" set of parameters is applied.

Acknowledgement

The authors are grateful to G. Gustafson and L. Jenkovszky for inspiring and fruitful discussions. This work was supported by the OTKA grant NK 101438 (Hungary) and the Ch. Simonyi Fund (Hungary).

References

[1] A. Bialas and A. Bzdak, Acta Phys. Polon. B **38** (2007) 159 [hep-ph/0612038].

[2] F. Nemes and T. Csörgő, Int. J. Mod. Phys. A **27** (2012) 1250175

[3] T. Csörgő and F. Nemes, Int. J. Mod. Phys. A **29** (2014) 1450019

[4] E. Ferreira, T. Kodama and A. K. Kohara, arXiv:1411.3518 [hep-ph].

[5] A. K. Kohara, E. Ferreira and T. Kodama, Eur. Phys. J. C **74** (2014) 11, 3175 [arXiv:1408.1599 [hep-ph]].

[6] S. Giani, "Overview of TOTEM results on total cross-section, elastic scattering and diffraction at LHC", talk given at WPCF 2014, Gyöngyös, Hungary, August 2014, `https://indico.cern.ch/event/300974/session/2/contribution/34` .

[7] L. Jenkovszky and A. Lengyel, arXiv:1410.4106 [hep-ph].

[8] G. Antchev *et al.*TOTEM Collaboration, Europhys. Lett. **96** (2011) 21002

[9] G. Antchev *et al.* [TOTEM Collaboration], Europhys. Lett. **101** (2013) 21002.

[10] G. Antchev *et al.* [TOTEM Collaboration], Europhys. Lett. **101** (2013) 21004.

[11] R. J. Glauber, Lectures in Theoretical Physics, Vol. 1. Interscience, New York 1959.

[12] E. Levin, hep-ph/9808486.

[13] V. A. Khoze, A. D. Martin and M. G. Ryskin, arXiv:1402.2778 [hep-ph].

[14] M. G. Ryskin, A. D. Martin and V. A. Khoze, Eur. Phys. J. C **72** (2012) 1937 [arXiv:1201.6298 [hep-ph]].

[15] M. G. Ryskin, A. D. Martin, V. A. Khoze and A. G. Shuvaev, J. Phys. G **36** (2009) 093001 [arXiv:0907.1374 [hep-ph]].

[16] A. D. Martin, H. Hoeth, V. A. Khoze, F. Krauss, M. G. Ryskin and K. Zapp, PoS QNP **2012** (2012) 017

[17] P. Lipari and M. Lusignoli, Eur. Phys. J. C **73**, 2630 (2013) [arXiv:1305.7216 [hep-ph]].

[18] E. Nagy, R. S. Orr, W. Schmidt-Parzefall, K. Winter, A. Brandt, F. W. Busser, G. Flugge and F. Niebergall *et al.*, Nucl. Phys. B **150** (1979) 221.

[19] U. Amaldi and K. R. Schubert, Nucl. Phys. B **166** (1980) 301.

[20] H. Cheng and T. T. Wu, Phys. Rev. Lett. **22** (1969) 666.

[21] H. Cheng and T. T. Wu, Phys. Rev. **182** (1969) 1852.

[22] H. Cheng and T. T. Wu, Phys. Rev. **182** (1969) 1868.

[23] H. Cheng and T.T. Wu, Expanding Protons: Scattering at High Energies , M.I.T. Press, Cambridge, MA (1987)

[24] C. Bourrely, J. Soffer and T. T. Wu, Phys. Rev. D **19** (1979) 3249.

[25] C. Bourrely, J. Soffer and T. T. Wu, arXiv:1405.6698 [hep-ph].

[26] M. M. Block, Phys. Rept. **436** (2006) 71 [hep-ph/0606215].

Two particle correlation effects and Differential HBT for rotation in heavy ion collisions.

L.P. Csernai, S. Velle and D.J. Wang

[1]Department of Physics and Technology, University of Bergen, Allegaten 55, 5007 Bergen, Norway

Abstract

Peripheral heavy ion reactions at ultra relativistic energies have large angular momentum that can be studied via two particle correlations using the Differential Hanbury Brown and Twiss method. We analyze the possibilities and sensitivity of the method in a rotating system. We also study an expanding solution of the fluid dynamical model of heavy ion reactions.

1 Introduction

Collective flow is one of the most dominant observable features in heavy ion reactions up to the highest available energies, and its global symmetries as well as its fluctuations are extensively studied. Especially at the highest energies for peripheral reaction the angular momentum of the initial state is substantial, which leads to observable rotation according to fluid dynamical estimates [1]. Furthermore the low viscosity quark-gluon fluid may lead to to initial turbulent instabilities, like the Kelvin Helmholtz Instability (KHI), according to numerical fluid dynamical estimates [2], which is also confirmed in a simplified analytic model [3]. These turbulent phenomena further increase the rotation of the system, which also leads to a large vorticity and circulation of the participant zone one order of magnitude larger than from random fluctuations in the transverse plane [4, 5, 6].

The Differential Hanbury Brown and Twiss (DHBT) method has been introduced in [9]. The method has been applied to a high resolution Particle in Cell Relativistic

(PICR) fluid dynamical model [10].

2 The two particle correlation

The pion correlation function is defined as the inclusive two-particle distribution divided by the product of the inclusive one-particle distributions, such that [12]:

$$C(p_1, p_2) = \frac{P_2(p_1, p_2)}{P_1(p_1) P_1(p_2)}, \tag{1}$$

where p_1 and p_2 are the 4-momenta of the pions and k and q are the average and relative momentum respectively.

We use a method for moving sources presented in Ref.[14]. In the formulae the $\hbar = 1$ convention is used and k and q are considered as the wavenumber vectors. The correlation function is:

$$C(k, q) = 1 + \frac{R(k, q)}{\left| \int d^4x \, S(x, k) \right|^2} \ , \tag{2}$$

where

$$R(k, q) = \int d^4x_1 \, d^4x_2 \, \cos[q(x_1 - x_2)] S(x_1, k + q/2) \, S(x_2, k - q/2) \ . \tag{3}$$

Here $R(k, q)$ can be calculated [14] via the function and we obtain the $R(k, q)$ function as

$$R(k, q) = \mathrm{Re} \left[J(k, q) \, J(k, -q) \right] \tag{4}$$

The corresponding $J(k, q)$ function will become

$$J(k, q) = \int d^4x \ S(x, k) \, \exp \left[-\frac{q \cdot u(x)}{2T(x)} \right] \, \exp(iqx) \ . \tag{5}$$

For the phase space distribution we frequently use the Jüttner (relativistic Boltzmann) distribution, in terms of the local invariant scalar particle density the Jüttner distribution is [15]

$$f^J(x, p) = \frac{n(x)}{C_n} \exp \left(-\frac{p^\mu u_\mu(x)}{T(x)} \right) \ , \tag{6}$$

where $C_n = 4\pi m^2 T K_2(m/T)$. We assume a spatial distribution:

$$G(x) = \gamma n(x) = \gamma n_s \exp \left(-\frac{x^2 + y^2 + z^2}{2R^2} \right). \tag{7}$$

Here n_s is the average density of the Gaussian source, s, (or fluid cell) of mean radius R.

Asymmetric Sources: we have seen in few source model examples [9] that a highly symmetric source may result in correlation functions that are sensitive to rotation, however, these results were not sensitive to the direction of the rotation, which seems to be unrealistic. We saw that this result is a consequence of the assumption that both of the members of a symmetric pair contribute equally to the correlation function even if one is at the side of the system facing the detector and

the other is on the opposite side. The expansion velocities are also opposite at the opposite sides. The dense and hot nuclear matter or the Quark-gluon Plasma are strongly interacting, and for the most of the observed particle types the detection of a particle from the side of the system, – which is not facing the detector but points to the opposite direction, – is significantly less probable. The reason is partly in the diverging velocities during the expansion and partly to the lower emission probability from earlier (deeper) layers of the source from the external edge of the timelike (or spacelike) FO layer.

For the study of realistic systems where the emission is dominated by the side of the system, which is facing the detector, we cannot use the assumption of the symmetry among pairs or groups of the sources from opposite sides of the system. Even if the FO layer has a time-like normal direction, $\hat{\sigma}^\mu$ the $(k^\mu \hat{\sigma}^\mu)$ factor yields a substantial emission difference between the opposite sides of the system.

The correlation function, $C(k,q)$ is always measured in a given direction of the detector, $\vec{k}$. Obviously only those particles can reach the detector, which satisfy $k^\mu \hat{\sigma}_\mu > 0$. Thus in the calculation of $C(k,q)$ (see Fig. 1) for a given $\hat{\vec{k}}$- direction we can exclude the parts of the freeze out layer where $k^\mu \hat{\sigma}_\mu < 0$ (see Eq. (10) of Ref.[16] or Ref.[18]. For time-like FO a simplest approximation for the emission possibility is $P_{esc}(x) \propto k^\mu u_\mu(x)$ [17].

3 The DHBT method and fluid dynamical results

Based on the few source model results the Differential HBT method [9] was introduced by evaluating the difference of two correlation functions measured at two symmetric angles, forward and backward shifted in the reaction plane in the participant c.m. frame by the same angle, i.e. at $\eta = \pm$const., so that

$$\Delta C(k,q) \equiv C(k_+, q_{out}) - C(k_-, q_{out}). \tag{8}$$

For the exactly $\pm x$ -symmetric spatial configurations (i.e. $k_{+x} = k_{-x}$ and $k_{+z} = -k_{-z}$), e.g. central collisions or spherical expansion, $\Delta C(k,q)$ would vanish! It would become finite if the rotation introduces an asymmetry.

The sensitivity of the standard correlation function on the fluid cell velocities decreases with decreasing distances among the cells. So, with a large number of densely placed fluid cells where all fluid cells contribute equally to the correlation function, the sensitivity on the flow velocity becomes negligibly weak.

Thus, the emission probability from different ST regions of the system is essential in the evaluation. This emission asymmetry due to the local flow velocity occurs also when the FO surface or layer is isochronous or if it happens at constant proper time.

We studied the fluid dynamical patterns of the calculations published in Ref. [2], where the appearance of the KHI is discussed under different conditions. We chose the configuration, where both the rotation [1], and **the KHI occurred**, at $b = 0.7 b_{max}$ with high cell resolution and low numerical viscosity at LHC energies, where the angular momentum is large, $L \approx 10^6 \hbar$ [13]. Fig. 2 shows the DHBT for the FD model.

The standard correlation function is both influenced by the ST shape of the emitting source as well as its velocity distribution. The correlation function becomes

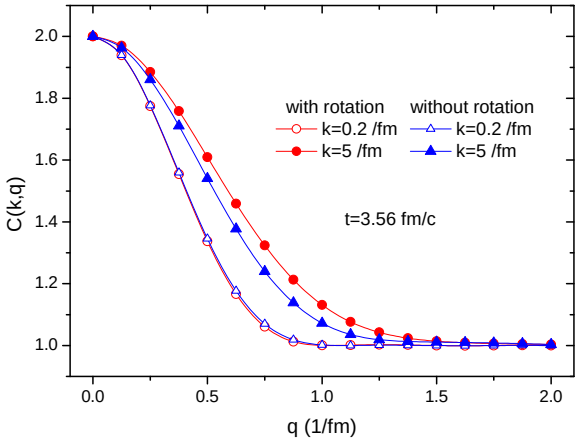

Figure 1: (color online) The dependence of the standard correlation function in the $\vec{k}_+$ direction from the collective flow, at the final time. From ref. [10].

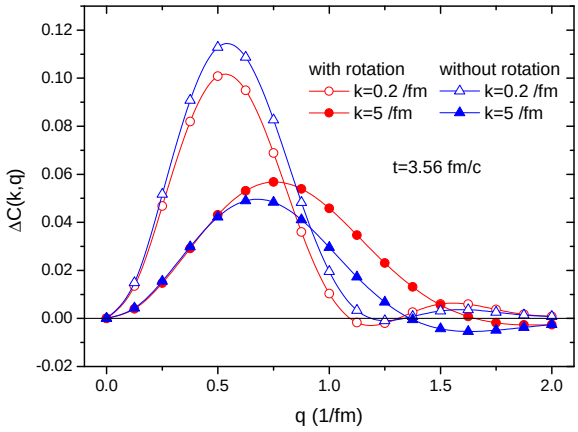

Figure 2: (color online) The differential correlation function $\Delta C(k,q)$ at the final time with and without rotation. From ref. [10].

narrower in q with increasing time primarily due to the rapid expansion of the system. At the initial configuration the increase of $|\vec{k}|$ leads to a small increase of the width of the correlation function.

Nevertheless, in theoretical models we can switch off the rotation component of the flow, and analyse how the rotation influences the correlation function and especially the DCF, $\Delta C(k,q)$.

Fig. 1 compares the standard correlation functions with and without the rotation component of the flow at the final time moment. Here we see that the rotation leads to a small increase of the width in q for the distribution at high values of $|\vec{k}|$, while at low momentum there is no visible difference.

In Fig. 2 $\Delta C(k,q)$ is shown for the configuration with and without rotation. For $k = 5$/fm the rotation increases both the amplitude and the width of ΔC. The dependence on $|\vec{k}|$ is especially large at the final time.

Fig. 3 shows the result where the rotation component of the velocity field is

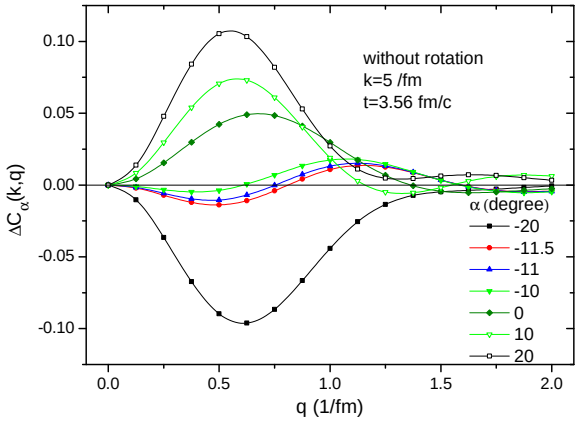

Figure 3: (color online) The Differential Correlation Function (DCF) at average pion wavenumber, $k = 5/\text{fm}$ and fluid dynamical evolution time, $t = 3.56\text{fm/c}$, as a function of the functions of momentum difference in the "out" direction q (in units of $1/\text{fm}$). The DCF is evaluated in a frame rotated in the reaction plane, in the c.m. system by angle α. From ref. [10].

removed. The DCF shows a minimum in its integrated value over q, for $\alpha = -11$ degrees. The shape of the DCF changes characteristically with the angle α. Unfortunately this is not possible experimentally, so the direction of the symmetry axes should be found with other methods, like global flow analysis and/or azimuthal HBT analysis.

Finally we separated the effect of the rotation by finding the symmetry angle where the rotation-less configuration yields vanishing or minimal DCF for a given transverse momentum k. This could be done in the theoretical model. We did this for two different energies, Pb+Pb / Au+Au at $\sqrt{s_{NN}} = 2.36/0.2$ TeV respectively, while all other parameters of the collision were the same. The deflection angle of the symmetry axis was $\alpha = -11/-8$ degrees[1] respectively. In these deflected frames we evaluated the DCF for the original, rotating configurations, which are shown in Fig. 4. This provides an excellent measure of the rotation.

4 Summary

We show that two particle correlation measurements can be sensitive to the rotation of the emitting system. The analysed model calculations show that the Differential HBT analysis can give a good quantitative measure of the rotation in the reaction plane of a heavy ion collision.

References

[1] L.P. Csernai, V.K. Magas, H. Stöcker, and D.D. Strottman, Phys. Rev. C **84**, 024914 (2011).

[1]The negative angles are arising from the fact that our model calculations predict rotation, with a peak rotated forward [1].

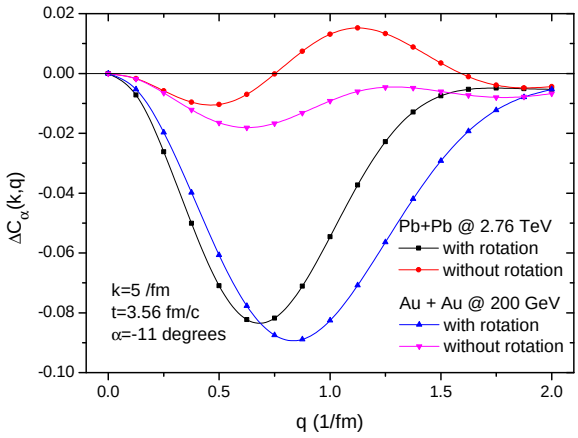

Figure 4: (color online) The differential correlation function (DCF) with and without rotation in the reference frames, deflected by the angle α, where the rotation-less DCF is vanishing or minimal. In this frame the DCF of the original, rotating configuration indicates the effect of the rotation only. The amplitude of the DCF of the original rotating configuration doubles for the higher energy (higher angular momentum) collision. From ref. [10].

[2] L.P. Csernai, D.D. Strottman and Cs. Anderlik, Phys. Rev. C **85**, 054901 (2012).

[3] D.J. Wang, Z. Néda, and L.P. Csernai Phys. Rev. C **87**, 024908 (2013).

[4] L.P. Csernai, V.K. Magas, and D.J. Wang, Phys. Rev. C 87, 034906 (2013).

[5] S. Floerchinger and U. A. Wiedemann, Journal of High Energy Physics, JHEP **11**, 100 (2011);

[6] S. Floerchinger and U. A. Wiedemann, J. Phys. G: Nucl. Part. Phys. **38**, 124171 (2011).

[7] R. Hanbury Brown and R.Q. Twiss, Phil. Mag. **45**, 663 (1954);

[8] R. Hanbury Brown and R.Q. Twiss, Nature, **178**, 1046 (1956).

[9] L.P. Csernai, S. Velle Int. J. Mod. Phys. E **23**, 1450043 (2014).

[10] L. P. Csernai, S. Velle, and D. J. Wang , Phys. Rev. C **89**, 034916 (2014);

[11] T. Csörgő and M.I. Nagy, Phys. Rev. C **89**, 044901 (2014).

[12] W. Florkowski: *Phenomenology of Ultra-relativistic heavy-Ion Collisions*, World Scientific Publishing Co., Singapore (2010).

[13] V. Vovchenko, D. Anchishkin, and L.P. Csernai, Phys. Rev. C **88**, 014901 (2013).

[14] A.N. Makhlin, Yu.M. Sinyukov, Z. Phys. C **39**, 69-73 (1988).

[15] F. Jüttner, Ann. Phys. und Chemie, **34** (1911) 856.

[16] Yu.M. Sinyukov, Nucl. Phys. A498, 151c (1989).

[17] T. Csörgő, Heavy Ion Phys. **15**, 1-80, (2002); arXiv: hep-ph/0001233v3.

[18] K.A. Bugaev, Nucl. Phys. A **606**, 559 (1996).

Femtoscopic pΛ Correlations in Pb-Pb Collisions at $\sqrt{s_{\rm NN}} = 2.76$ TeV with ALICE

Hans Beck*

Institut für Kernphysik, Goethe-Universität, Frankfurt, Germany

for the ALICE Collaboration

Abstract

Two-particle correlations at small relative momenta give insight into the size of the emitting source. Of particular interest is the test of hydrodynamic models which predict a universal, apparent decrease of the extent of the system with increasing transverse mass $m_{\rm T}$ as a consequence of the strong radial flow in heavy-ion collisions at LHC energies. This contribution presents a study of correlations for protons and Λ particles in Pb-Pb collisions at $\sqrt{s_{\rm NN}} = 2.76$ TeV measured with ALICE. The investigated particle species expand the experimental reach in $m_{\rm T}$ due to their high rest mass. Residual impurities in the samples from misidentification and contributions from feed-down are corrected using data-driven techniques. Correlation functions are obtained in several centrality classes and $m_{\rm T}$ intervals at large $m_{\rm T}$ and show the expected decrease in volume of the strongly interacting fireball for more peripheral collisions. We observe the decrease of the source size with $m_{\rm T}$, predicted by hydrodynamical calculations, out to $\langle m_{\rm T} \rangle = 2.18$ GeV/c^2.

1 Introduction

Femtoscopy aims at measuring the size of the particle emitting source. Experimentally, this is achieved by studying two-particle correlations at small relative

*email: Hans.Beck@cern.ch

momenta. If the size of the system is large, the emissions of the two particles will likely be substantially separated in space. Therefore, no interaction or symmetrization will take place and the momenta will be uncorrelated. If – on the other hand – the extent of the source is small, the vicinity of the emanation points will trigger the species-specific interplay with a characteristic dependence of the correlation on the momentum difference. Given that the two-particle interaction is known, a source size can be inferred from the correlation function.

No Coulomb or quantum-statistical effects take place in the pΛ system and the strong interaction parameters are sufficiently well known from, e. g., bubble chamber experiments. A typical reaction for studying the pΛ final-state interaction is the production of Λ baryons by shooting a beam of negatively charged kaons on a hydrogen target as done with the Saclay bubble chamber [1]. The Λ hyperon – created via $K^- + p \rightarrow \Lambda + \pi^0$ – can subsequently scatter elastically off another proton. Measuring the cross-section of the elastic process differentially vs. the excess energy directly quantifies the attractive final-state strong interaction, which turns out to be comparable to the nucleon-nucleon one.

Based on the model by Lednický and Lyuboshits [2], the sensitivity of the pΛ correlation function to the volume of the hot and dense medium created in heavy-ion collisions was first explored in [3]. The correlation was found to be affected in height and shape by the size of the source. Furthermore, the interdependence of the two momenta was shown to keep its susceptibility to a change in source size for radii larger than 4 fm – an advantage over the Coulomb-depleted proton-proton correlations.

A particularly interesting subject is the investigation of the reaction dynamics of the strongly interacting matter generated in Pb-Pb collisions. The large pressure gradients give rise to an expansion of the medium. The resulting collective velocity competes with the thermal velocity $\sqrt{T/m_{\mathrm{T}}}$; consequently the m_{T} dependence of the radii probes the dynamics of the source. At low m_{T}, no strong collective motion is present and the particles will be correlated over the full extent of the source. At high m_{T} in contrast, the radial flow introduces a positive correlation between the emission point and the particle's momentum. Looking only at pairs of particles with a small momentum difference, the couple's constituents will originate from the same region, which is smaller than the geometrical size of the fireball, leading to the apparent shrinking of the particle source with m_{T}. To probe the high m_{T} regime, it is experimentally beneficial to investigate particles with a high rest mass. So far, the pΛ system is the heaviest studied system [4–6].

2 Particle Selection

The analyzed Pb-Pb data was taken with ALICE [7]. The T0 and V0 scintillator arrays provided an event-trigger signal and an estimate for the collision centrality. The main detectors for particle tracking in ALICE are the Inner Tracking System, Time Projection Chamber (TPC), and Transition Radiation Detector. Particle identification for this analysis was performed by the TPC and the Time Of Flight (TOF) detector. The vanishing μ_B at the LHC entails that matter and anti-matter are produced in equal abundance. While the correlation functions for pairs of pΛ and $\overline{\mathrm{p}}\overline{\Lambda}$ were obtained separately, the selections for particles discussed in the following hold true for their charge conjugates as

well.

The proton selection depended on the reconstructed momentum and used the TPC and/or TOF. The resolution of the truncated specific energy loss measurement ($\mathrm{d}E/\mathrm{d}x$) can be parametrized with a Gaussian of width σ. The TPC provided a separation of the most probable $\mathrm{d}E/\mathrm{d}x$ measurement for protons to the one of any other species of more than four σ up to $p = 0.75$ GeV/c. Above this kinematic restriction, the expected $\mathrm{d}E/\mathrm{d}x$ for protons and the ultra-relativistic electrons becomes too similar, which impeded an unambiguous particle identification by the TPC alone. For higher momenta up to $p = 5.0$ GeV/c, TOF allowed for an unambiguous proton identification [8]. With the chosen criteria a proton purity – defined as the number of protons over the number of all selected particles including misidentified tracks – above 99% was achieved over the full dynamic span.

The Λ selection was based upon a V^0 topology finder, which reconstructs the charged decay $\Lambda \to \mathrm{p} + \pi^-$; the hyperon is identified via the invariant mass. Fig. 1 (left) shows a fit to the invariant mass distribution of all Λ candidates employing a Monte-Carlo template for the signal shape in an exemplary phase-space bin with a high yield, namely $0.5 < |y| < 0.6$ and $1.0 \leq p_{\mathrm{T}}$ (GeV/c) < 1.5, for the 10% most central events. The parametrization allows to determine the purity of the sample – defined as the ratio of picked Λ particles to all taken V^0 vertices – which amounts in this case to $\mathrm{pur}_{\Lambda} = 91\%$ within the window in invariant mass of ± 4 MeV around the PDG value. Determining the purity enables one to correct the correlation function for the uncorrelated background in a following step. Fig. 1 (right) shows the evolution of the Λ purity as a function of rapidity and transverse momentum for the 10% most central events. Protons knocked-out from an interaction with the detector material resemble displaced tracks from weak particle decay vertices. A contribution of protons from material manifests itself in a degradation of the purity for $p_{\mathrm{T}} < 0.5$ GeV/c; the effect is absent for the case of $\overline{\Lambda}$. For higher transverse momenta, the purity is 81% for $|y| > 1.0$, within $|\eta| < 0.9$ it is better than 90%.

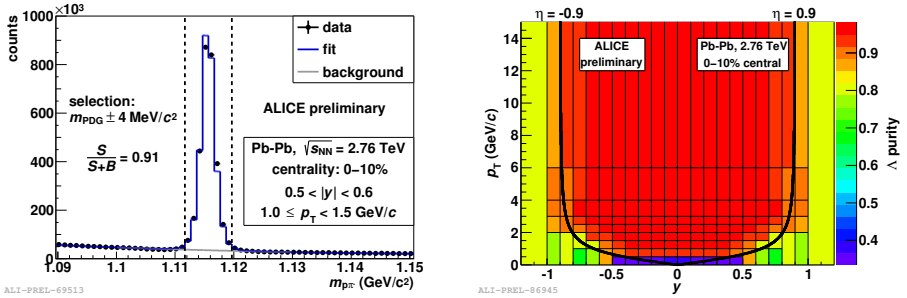

Figure 1: Left: Invariant mass spectrum of Λ candidates in an exemplary phase-space bin with a fit using a Monte-Carlo template for the signal shape. Right: Λ purity as a function of rapidity and transverse momentum for the 10% most central events.

3 Feed-Down Determination

The pΛ strong interaction is limited in its range to a few fm. Hence, any product from electro-magnetic or weak decays will not contribute to the excess seen at small relative momenta. The contamination in the proton sample mostly stems from the decay $\Lambda \rightarrow \mathrm{p_{dec}}\pi^-$. Since no significant ΛΛ correlation was seen by the STAR Collaboration [9], the decay proton will also not carry any residual correlation [10–12] from the mother particle.[1] The determination of the amount of this uncorrelated feed-down allows for a correction of the pΛ correlation function with the feed-down fraction $f_\mathrm{p} = \frac{\text{non-primary}}{\text{all}}$. The outstanding performance of ALICE allows to determine this feed-down fraction in the proton sample directly from the data via the distance of closest approach (DCA) of the track extrapolation to the primary vertex. The two-dimensional (transverse and longitudinal) DCA distribution was obtained differentially in rapidity, transverse momentum, and centrality for the data, as well as for templates from Monte-Carlo simulations for primary protons[2], protons from weak decays, and protons from an interaction with the detector material. The distinct shapes of the templates – almost flat in DCA for the material contribution, wide for the weak decays, and peaked for the primaries – allow to disentangle the different origins of the charged nucleons by fitting the templates to the data, as pictured in Fig. 2 (left). Selecting only tracks with a DCA smaller than 1 mm in the transverse and smaller than 1.5 mm in the longitudinal direction enhances the primaries in the sample. In the exemplary phase-space bin $0.0 \leq y < 0.25$ and $1.0 \leq p_\mathrm{T}$ (GeV/c) < 1.5, the feed-down fraction f_p totals to 15%. This arises from the amount of particles which are from weak decays and from material of 15% and less than 1%, respectively.

Also the Λ sample is contaminated by feed-down. The contributing, dominating weak decays are $\Xi^0 \rightarrow \Lambda\pi^0$ (BR 99.5%), $\Xi^- \rightarrow \Lambda\pi^-$ (BR 99.9%), $\Omega^- \rightarrow \Lambda\mathrm{K}^-$ (BR 67.8%), and $\Omega^- \rightarrow \Xi(\rightarrow \Lambda\pi)\pi$ (BR 32.2%). The reconstruction efficiencies with the chosen Λ selection criteria in this analysis for all $\mathrm{Y} = \Xi^0, \overline{\Xi}^0, \Xi^-, \overline{\Xi}^+, \Omega^-$, and $\overline{\Omega}^+$ were obtained three-dimensionally in $p_\mathrm{T}^\mathrm{Y} \rightarrow (p_\mathrm{T}^\Lambda, y^\Lambda)$ for each centrality class of [15] from a Monte-Carlo simulation. Using the p_T-differential spectra of $\Xi^-, \overline{\Xi}^+, \Omega^-$, and $\overline{\Omega}^+$ measured by ALICE [15] for several centrality classes and assuming isospin symmetry for the unmeasured Ξ^0 and $\overline{\Xi}^0$, enabled us to determine the fraction of Λ hyperons from weak decays.

The $c\tau$ = 22 pm of the electro-magnetic decay $\Sigma^0 \rightarrow \Lambda\gamma$ (BR 100%) is much larger than the range of the strong interaction, but also too small to be resolved experimentally. In [16] it was found that the final-state interaction in the $\mathrm{p}\Sigma^0$ channel is much smaller than in the pΛ system. Thus, a significant fraction of Λ come from Σ^0 and are uncorrelated with primary protons. We use the fraction of Λ from Σ^0 – properly taking into account all strongly decaying resonances – from the thermal model of [17], while systematically considering the study in [18] with an additional variation in the freeze-out temperature, and the results of [19] with the value at the kinetic and chemical freeze-out. All models give that about 30% of the Λ originate from a electromagnetic decay.

[1] Recent data from ALICE [13] and STAR [14] suggest a slight ΛΛ anti-correlation. The momentum released in the Λ decay will wash this correlation out; the small fraction of $\mathrm{p_{dec}}\Lambda$ pairs in the pΛ sample will make it a tiny, likely negligible, correction.

[2] According to the common ALICE definition, primary protons include decay products, except products from weak decays of strange hadrons.

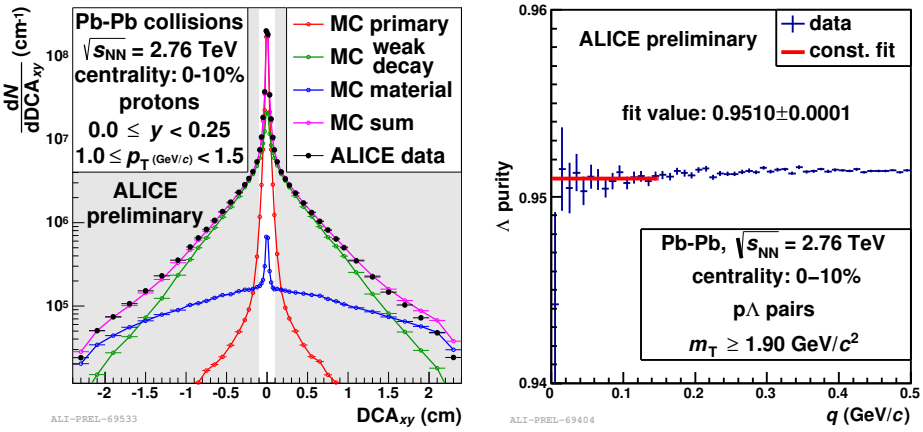

Figure 2: Left: Distribution of the transverse distance of closest of approach of protons to the primary vertex in data with a fit utilizing Monte-Carlo templates in an exemplary phase-space bin. Right: Λ pair purity for pairs with $m_{\mathrm{T}} \geq 1.9$ GeV/c for the 10% most central events with a constant fit in the region $0.0 \leq q$ (GeV/c) < 0.15.

We unite the fraction from weak and electromagnetic hyperon decays in the feed-down fraction f_{Λ}.

4 Corrections and Results

The raw pΛ correlation as a function of the momentum difference is obtained as the ratio of pairs from real events over those reconstructed from mixed events for three centrality divisions and up to four m_{T} classes for each centrality class. Dealing with non-identical particles, we use the generalized momentum difference introduced in [20] by R. Lednický $\tilde{q} = |q - P(qP)/P^2|, q = p_1 - p_2, P = p_1 + p_2$, where p_1 and p_2 are the momenta of the particles. In the following, we omit the tilde. The overall pair purity factorizes: $\mathrm{pur}(q, m_{\mathrm{T}}) = \mathrm{pur}_{\Lambda}(q, m_{\mathrm{T}}) \cdot (1 - f_{\mathrm{p}}(q, m_{\mathrm{T}})) \cdot (1 - f_{\Lambda}(q, m_{\mathrm{T}}))$. The Λ pair purity $\mathrm{pur}_{\Lambda}(q, m_{\mathrm{T}})$ is shown exemplary in Fig. 2 (right) for the 10% most central events and the highest m_{T} class, $m_{\mathrm{T}} \geq 1.9$ GeV/c^2. Its value of 95.1% is constant over the region of interest $q < 0.15$ (GeV/c) and beyond. It is obtained by looking up the single-particle Λ purity in the (y, p_{T})-differential histograms for the given centrality; the same holds for f_{p} and f_{Λ} accordingly. All impurities constitute – as discussed – an uncorrelated background. Hence, the corrected correlation function can be attained by scaling the raw correlation function with the inverse pair purity:

$$C_2^{\mathrm{corr.}}(q, m_{\mathrm{T}}) = \left(\frac{1}{\mathrm{pur}(q, m_{\mathrm{T}})} \cdot (C_2^{\mathrm{raw}}(q, m_{\mathrm{T}}) - 1) \right) + 1. \quad (1)$$

The effect of the finite momentum resolution was studied with a Monte-Carlo simulation. For small relative momenta, i. e. $(q_{\mathrm{rec}} + q_{\mathrm{gen}})/2 \leq 0.1$ GeV/c, where q_{rec} is the reconstructed and q_{gen} is the generated relative momentum, the

deviation, quantified as $(q_{\mathrm{rec}} - q_{\mathrm{gen}})/\sqrt{2}$, can be parametrized with a Gaussian with a mean of -0.32 ± 0.02 and -0.38 ± 0.08 MeV/c and a width of 7.26 ± 0.02 and 7.13 ± 0.07 MeV/c for the 0–10 and 30–50% most central events. In an m_{T}-differential study, the width turned out to slightly increase by less than 2 MeV/c for higher m_{T}.

Fig. 3 shows a set of exemplary correlation functions corrected via Eq. 1, i. e. remedied for the uncorrelated background coming from weak and electromagnetic decays. The correlation functions for pairs of particles and pairs of anti-particles were merged following the recipe of the Particle Data Group [21]. The systematic errors include a variation of the correction for the electromagnetic feed-down, a change in the hyperon input spectra for the correction of the Λ from weak decays, an altered momentum resolution, normalization, invariant mass selection of the Λ, changed DCA cuts on the proton, a varied two-track resolution cut, and dominantly the uncertainty on the pΛ interaction when fitting the data. The top panel shows the centrality dependence, i. e. the 0–10% most central events in red and the 30–50% most central events in blue; both samples have a mean transverse mass of 1.5 GeV/c^2. One clearly sees the expected effect of an increased width and height of the excess at small relative momenta, which translates into a smaller source size, for the more peripheral collisions. The bottom panel shows the dependence on m_{T} with the green points representing $1.0 \leq m_{\mathrm{T}}$ (GeV/c^2) < 1.4 resulting in $\langle m_{\mathrm{T}} \rangle = 1.27$ GeV/c^2 and the orange symbols depicting $m_{\mathrm{T}} \geq 1.9$ GeV/c^2 yielding $\langle m_{\mathrm{T}} \rangle = 2.18$ GeV/c^2 for the 0–10% most central events. Also here, a clear ordering is apparent with the higher m_{T} giving evidence for a smaller source than at lower m_{T}, matching the expectation within the hydrodynamic picture outlined in the introduction. Note that the correlation function with $\langle m_{\mathrm{T}} \rangle = 2.18$ GeV/c^2 exceeds the $\langle m_{\mathrm{T}} \rangle$ of any previous measurement from [6] at the SPS, [5] at RHIC or [22, 23] at the LHC.

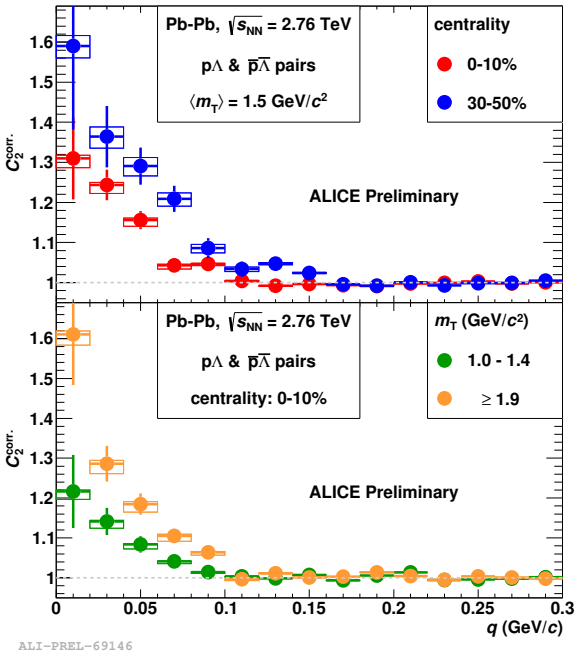

Figure 3: Exemplary pΛ and $\overline{\mathrm{p}}\overline{\Lambda}$ correlation function corrected for weak and electromagnetic decays. Centrality dependence at the top, m_{T} dependence at the bottom.

5 Summary

The supreme performance of ALICE makes it possible to collect very pure samples of protons and Λ with rich statistics. We obtained pΛ correlation functions multi-differentially in centrality and transverse mass. They were corrected for misidentification and contamination from weak and electromagnetic decays, employing data-driven methods to quantify the impurities. The correlation functions presented here represent the largest m_{T} reach of any femtoscopic measurement, with result being shown for $m_{\mathrm{T}} \geq 1.9$ GeV/c^2. The conveyed centrality dependence of the pΛ correlations exhibits the expected behavior of a smaller source for more peripheral collisions. The communicated m_{T}-differential correlations, spanning a range in $\langle m_{\mathrm{T}} \rangle$ of more than 0.9 GeV/c^2, display the decrease in source size with m_{T}, qualitatively agreeing with hydrodynamic predictions, out to highest $\langle m_{\mathrm{T}} \rangle = 2.18$ GeV/c^2.

References

[1] B. Sechi-Zorn, B. Kehoe, J. Twitty, and R.A. Burnstein, Phys. Rev. **175**, 1735 (1968)

[2] R. Lednický and V.L. Lyuboshits, Sov. J. Nucl. Phys. **35**, 770 (1982)

[3] F. Wang and S. Pratt, Phys. Rev. Lett. **83**, 3138 (1999)

[4] J. Adams *et al.* (STAR Collaboration), Phys. Rev. C **74**, 064906 (2006)

[5] H.P. Gos for the STAR Collaboration, Eur. Phys. J. C **49**, 75 (2007)

[6] T. Anticic *et al.* (NA49 Collaboration), Phys. Rev. C **83**, 054906 (2011)

[7] The ALICE Collaboration, JINST **3**, S08002 (2008)

[8] The ALICE Collaboration, Int. J. Mod. Phys. A **29**, 1430044 (2014)

[9] N. Shah for the STAR Collaboration, Nucl. Phys. A **914**, 410 (2013)

[10] F. Wang, Phys. Rev. C **60**, 067901 (1999)

[11] V.M. Shapoval, B. Erazmus, R. Lednický, and Yu.M. Sinyukov, arXiv:1405.3594 [nucl-th]

[12] A. Kisiel, H. Zbroszczyk, and M. Szymański, Phys. Rev. C **89**, 054916 (2014)

[13] J. Salzwedel for the ALICE Collaboration, Talk given at WPCF 2014

[14] The STAR Collaboration, arXiv:1408.4360 [nucl-ex]

[15] The ALICE Collaboration, Phys. Lett. B **27**, 216 (2014)

[16] P. Kowina *et al.*, Eur. Phys. J. A **22**, 293 (2004)

[17] M. Chojnacki, A. Kisiel, W. Florkowski, and W. Broniowski, arXiv:1102.0273 [nucl-th]

[18] A. Andronic, P. Braun-Munzinger, and J. Stachel, Nucl. Phys. A **772**, 167 (2006)

[19] F. Becattini, M. Bleicher, J. Steinheimer, and R. Stock, PoS **CPOD 2013**, 010 (2013)

[20] R. Lednický, arXiv:nucl-th/0112011

[21] K.A. Olive *et al.* (Particle Data Group), Chin. Phys. C **38**, 090001 (2014)

[22] M.P. Szymański for the ALICE Collaboration, Nucl. Phys. A **904-905**, 447c (2013)

[23] H. Beck for the ALICE Collaboration, J. Phys.: Conf. Ser. **446**, 012013 (2013)

A Monte Carlo Study of Multiplicity Fluctuations in Pb-Pb Collisions at LHC Energies

Ramni Gupta*

Department of Physics & Electronics, University of Jammu, Jammu, India

Abstract

With large volumes of data available from LHC, it has become possible to study the multiplicity distributions for the various possible behaviours of the multiparticle production in collisions of relativistic heavy ion collisions, where a system of dense and hot partons has been created. In this context it is important and interesting as well to check how well the Monte Carlo generators can describe the properties or the behaviour of multiparticle production processes. One such possible behaviour is the self-similarity in the particle production, which can be studied with the intermittency studies and further with chaoticity/erraticity, in the heavy ion collisions. We analyse the behaviour of erraticity index in central Pb-Pb collisions at centre of mass energy of 2.76 TeV per nucleon using the AMPT monte carlo event generator, following the recent proposal by R.C. Hwa and C.B. Yang, concerning the local multiplicity fluctuation study as a signature of critical hadronization in heavy-ion collisions. We report the values of erraticity index for the two versions of the model with default settings and their dependence on the size of the phase space region. Results presented here may serve as a reference sample for the experimental data from heavy ion collisions at these energies.

*email:ragupta@cern.ch

1 Introduction

Dynamics of the initial processes, that is the distributions and the nature of interactions of quarks and gluons, in the heavy ion collisions affect the final distribution of the particles produced [1]. Of the various distributions, multiplicity distributions play fundamental role in extracting first hand information on the underlying particle production mechanism. If QGP is formed at these energies the QGP-hadron phase transition is expected to be accompanied by large local fluctuations in the number of produced particles in the regions of phase space [2]. Thus the study of fluctuations in the multiplicity is an important tool to understand the dynamics of initial processes and consequently the processes of strong interactions, phase transition and also to understand correlations of QGP formation [3].

A comprehensive theoretical model which can explain and give answers to all the complexities of the physics involved at high energy and densities, as is created in the heavy ion collisions, is still not available. A successful model focussed on one aspect of the problem may not say much about the other aspects, but at least should not contradict what is observed. The measures which are studied in the present work rely on the large bin multiplicities. At LHC energies multiplicities are high and it is possible to have detailed study of the local properties in (η, ϕ) space for narrow p_T bins and thus to explore the dynamical properties of the system created in the heavy ion collisions. Thus as an initial attempt to understand the nature of global properties, as manifested in local fluctuations, here we develop and test the methodology and effectiveness of the analysis, analysing simulated events for Pb-Pb collisions at $\sqrt{s_{NN}}$= 2.76 TeV using A Multi-Phase Transport (AMPT) model.

Study of charged particle multiplicity fluctuations is one of the sensitive probes to learn about the properties of the system produced in the heavy ion collisions. Factorial moments are one of the convenient tools for studying fluctuations in the particle production. The concept of factorial moments was first used by A. Bialas and R. Peschanski [4] to explain unexpectedly large local fluctuations in high multiplicity events recorded by the JACEE Collaboratin. Advantage of studying fluctuations using factorial moments is that these filter out statistical fluctuations. The normalised factorial moment F_q is defined as

$$F_q(\delta^d) = \frac{\langle n!/(n-q)!\rangle}{\langle n\rangle^q} \tag{1}$$

where n is the number of particles in a bin of size δ^d in a d-dimensional space of observables and $\langle \ldots \rangle$ is either vertical or horizontal averaging. q is the order of the moment and is a positive integer ≥ 2. Then a power-law behaviour

$$F_q(\delta) \propto \delta^{-\varphi_q} \tag{2}$$

over a range of small δ is referred to as *intermittency*. In terms of the number of bins $M \propto 1/\delta$, Eq. 2 may be written as

$$F_q(M) \propto M^{\varphi_q} \tag{3}$$

where φ_q is the intermittency index, a positive number.

Even if the scaling behaviour in Eq. 2 is not satisfied, to a high degree of accuracy, F_q satisfies the power law behaviour

$$F_q \propto F_2^{\beta_q} \tag{4}$$

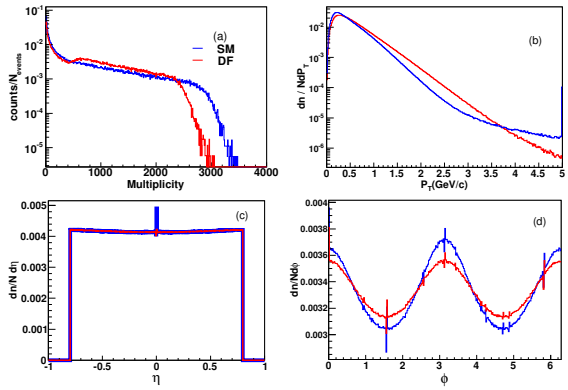

Figure 1: (a) Multiplicity distribution (b) p_T (c) η and (d) ϕ distributions of charged particles generated in Pb-Pb collisions at $\sqrt{s_{NN}}$ =2.76 TeV using the DF and SM AMPT.

This is referred to as F-scaling. In attempts to quantify systems undergoing second order phase transition, in Ginzburg-Landau (GL) theory [5], it is observed that

$$\beta_q = (q-1)^{\nu}, \qquad \nu = 1.304, \tag{5}$$

the scaling exponent, ν, is essentially idependent of the details of the GL parameters.

Factorial moments (F_q's) do not fully account for the fluctuations that the system exhibits. Vertically averaged horizontal moments, can gauge the spatial fluctuations, neglecting the event space fluctuations. On the other hand, horizontally averaged vertical moments lose information about spatial fluctuations and only measure the fluctuations from event-to-event. *Erraticity analysis* introduced in [6], where one finds moments of factorial moment distribution, takes into account the spatial as well as the event space fluctuations. It measures fluctuations of the spatial patterns and quantifies this in terms of an index named as *erraticity index* (μ_q). In a recent work [7], μ_q is observed to be a measure sensitive to the dynamics of the particle production mechanism and hence to the different classes of quark-hadron phase transition.

In erraticity analysis, event factorial moments are studied, defined for an e^{th} event as

$$F_q^e(M) = \frac{f_q^e(M)}{[f_1^e(M)]^q} \tag{6}$$

wherein,

$$f_q^e(M) = \langle n_m(n_m-1).....(n_m-q+1)\rangle_h \tag{7}$$

where $n_m \geq q$ is the bin multiplicity of the m^{th} bin, and $\langle \ldots \rangle_h$ is the average over all bins such that for M^2 cells

$$f_q^e(M) = \frac{1}{M^2}\sum_{m=1}^{M^2} n_m(n_m-1)\ldots(n_m-q+1) \tag{8}$$

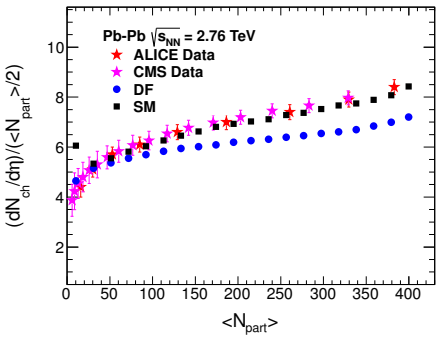

Figure 2: $dN_{ch}/d\eta$ versus N_{part} plot for DF and the SM AMPT, compared with the ALICE and CMS data

Now if $F_q^e(M)$ fluctuates from event-to-event, then the deviation of $F_q^e(M)$ from $\langle F_q^e(M)\rangle_v$ ($\langle\ldots\rangle_v$ is for averaging over all events) for each event can be quantified using p^{th} order moments of the normalised q^{th} order factorial (horizontal) moments that can be defined as

$$C_{p,q}(M) = \langle \phi_q^p(M)\rangle_v \tag{9}$$

where p is a positive real number and

$$\phi_q^p(M) = \frac{[F_q^e(M)]^p}{\langle F_q(M)\rangle_v^p} \tag{10}$$

To search for M-independent property of $C_{p,q}(M)$ one looks for a power-law behaviour of $C_{p,q}(M)$ in M,

$$C_{p,q}(M) \propto M^{\psi_q(p)} \tag{11}$$

this is referred to as *erraticity* [6]. If $\psi_q(p)$ is found to have a linear dependence on p, then *erraticity index* μ_q can be defined as

$$\mu_q = \frac{d\psi_q(p)}{dp} \tag{12}$$

in the linear region so that it is independent of both M and p. μ_q is a number that characterizes the fluctuations of spatial patterns from evevt-to-event. μ_4 is observed [7] to be an effective measure to distinguish different criticality classes, viz., critical, quasicritical, pseudocritical and non-critical, having low value for critical hadronization compared to those having random hadronization. To a good approximation, it is observed [7] that for the model with contraction owing to confinement, μ_4(critical and quasicritical case) $= 1.87 \pm 0.84$ and for models without contraction μ_4(pseudocritical and noncritical) $= 4.65 \pm 0.06$. These model values are suggestive of the significance of erraticity index to characterize dynamical processes.

2 Data Analysed

Charged particles in $|\eta| \leq 0.8$ and full azimuth, generated using two versions of A MultiPhase Transport (AMPT) model [8, 9], in Pb-Pb collisions at $\sqrt{s_{NN}} = 2.76$ TeV are analysed. AMPT model is a hybrid model that includes both initial

p_T **window**	**Default** $< N >$	**String Melting** $< N >$
$0.2 \leq p_T \leq 0.3$	285.2	434.8
$0.3 \leq p_T \leq 0.4$	279.2	355.5
$0.4 \leq p_T \leq 0.5$	243.7	271.6
$0.6 \leq p_T \leq 0.7$	163.3	155.5
$0.9 \leq p_T \leq 1.0$	80.5	66.1

Table 1: Average Multiplicity of the Simulated Data sets analyzed in different p_T windows

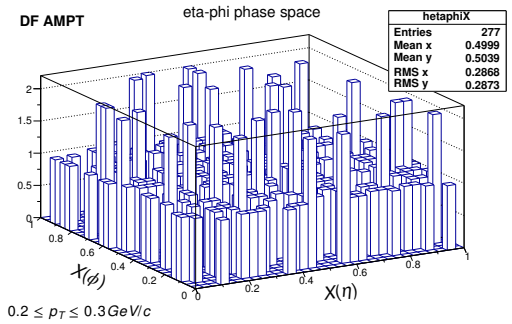

Figure 3: $(X(\eta), X(\phi))$ phase space of an event with $M = 32$ in DF and SM case

partonic and the final hadronic state interactions and transition between these two phases. This model addresses the non-equilibrium many body dynamics. Depending on the way the partons hadronize there are two versions, default (DF) and the string melting (SM). In the DF version partons are recombined with their parent strings when they stop interacting and the resulting strings are converted to hadrons using Lund String Fragmentation model. Whereas in the SM version, a quark coalescence model is used to obtain hadrons from the partons.

We have generated 23424 DF and 19669 SM events with impact parameter, $b \leq 5$, using the model parameters, a = 2.2, b = 0.5, $\mu = 1.8$ and $\alpha = 0.47$. Multiplicity, p_T, pseudorapidity and ϕ distributions of the simulated events is shown in the Figure 1. Charged particles generated in the $|\eta| \leq 0.8$ and full azimuth having $p_T \leq 1.0$ GeV/c in the small p_T bins of width 0.1 GeV/c are studied for the local multiplicity fluctuations in the spatial patterns. Five p_T bins are considered in the present analysis, as tabulated in the Table 1, along with the average multiplicity of the generated charged particles in the respective p_T bins.

Though AMPT does not contain the dynamics of collective interactions that are responsible for critical behaviour, but it is a good model to test the effectiveness of the methodology of analysis for finding observable signal of quark-hadron phase transition (intermittency analysis) and the quantitative measure of critical behaviour of the system (erraticity analysis) at LHC energies.

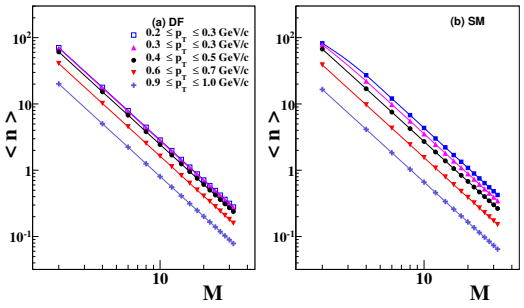

Figure 4: Average bin multiplicity dependence on M for the five p_T bins, in case of DF and the SM AMPT model

3 Analysis and Observations

For an 'e^{th}' event, the q^{th} order event factorial moment ($F_q^e(M)$) as defined in Eq. (6) are determined so as to obtain a simple characterization of the spatial patterns in two dimensional (η, ϕ) space in narrow p_T windows. However we first obtain flat single particle density distribution using cumulative variable $X(\eta)$ and $X(\phi)$ [10], which are defined as

$$X(y) = \frac{\int_{y_{min}}^{y} \rho(y)dy}{\int_{y_{min}}^{y_{max}} \rho(y)dy} \tag{13}$$

here y is η or ϕ, y_{min} and y_{max} denote respectively the minimum and maximum values of y interval considered. η and ϕ is mapped to X(η) and X(ϕ) between 0 and 1 such that $\rho(y)$ is the single particle η or ϕ density. $(X(\eta), X(\phi))$ unit square of an event in a selected p_T window, is binned into a square matrix with M^2 bins where the maximum value that M can take depends on the multiplicity in the Δp_T interval and the order parameter, so that the important part of the M dependence is captured.

To give a visualization of the binning in the (η, ϕ) space in narrow p_T bin, alego plot for an arbitrary event from DF AMPT data, in $0.2 \leq p_T \leq 0.3$ window, with M = 32, is shown in Fig. 3.

As value of M and p_T increases, the (η, ϕ) space becomes empty, as is observed from Figure 4 which shows the dependence of the average bin multiplicity ($\langle n \rangle$) on M. Because of the denominator in Eq. (6), a cluster of particles with multiplicity $n \geq q$ in an event would produce a large value for $F_q^e(M)$ for that event. On the other hand, if the particles are evenly distributed, $F_q^e(M)$ would be smaller. Thus the spatial pattern of the event structure should be revealed in the distribution of $F_q^e(M)$ after collecting all events.

Study of the event factorial moment distributions, $(P(F_q))$ reveal that the distributions become wider as M increases and develop long tailsat higher q, especially at higher M values. Further the peaks of the distributions shift towards left with increase in M leading to decrease in $\langle F_q^e \rangle$ (referred to as F_q hereafter) with M whereas the upper tails move towards right, at higher q values as M increases. It means that in small bins the average bin multiplicity $\langle n \rangle$ is so small that when there is a spike of particles in one such bin with $n \geq q$, the non-vanishing numerator in

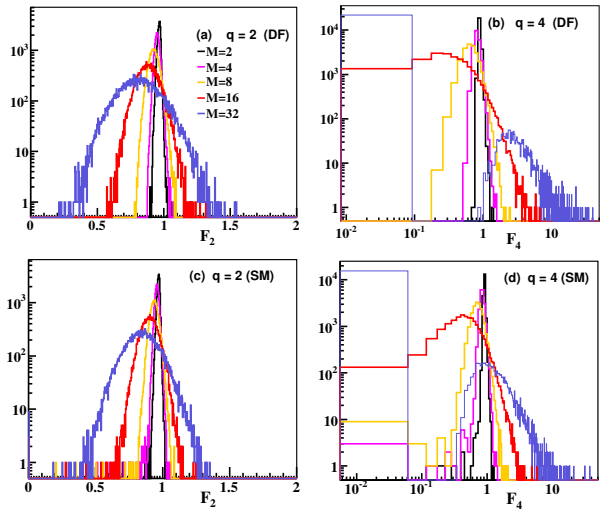

Figure 5: $P(F_q^e)$ distributions for order moment $q = 2$ and $q = 4$ for DF and SM ($0.3 \leq p_T \leq 0.4$). M values in multiples of 2 are shown only.

Eq. (6) results in a large value for $F_q^e(M)$ for that e^{th} event.

Dependence of F_q on M can be studied in log-log plots as shown in Fig. 6 for various p_T cuts. From the plots, it is observed that F_q's decrease as the bin size decreases or in other words, as M value increases. We observe for both the DF and SM in AMPT that relationship between $F_q(M)$ and M is inverse of that in the Eq. (3); that is

$$F_q^{\text{AMPT}}(M) \propto M^{\varphi_q^-}, \qquad \varphi_q^- < 0 \tag{14}$$

Hence, with negative φ_q^- it is found that *the charged particles generated by the default and the string melting version of the AMPT model exhibit negative intermittency*.

Eq. (14) suggests that $F_q^{\text{AMPT}}(M) \to 0$ at large M and q, implying that in AMPT there are too few rare high-multiplicity spikes anywhere in phase space. Eq. (14) is a quantification of the phenomenon exemplified by Fig. 3 for one event, and is a mathematical characterization after averaging over many events. This same behaviour was observed in [7] for the events belonging to the non-critical class.

We plot F_q versus F_2 in Fig. 7 to check F-scaling. For each set of p_T bins linear fit has been performed to determine the value, β_q, the slope, as exemplified by the straight lines in Fig. 7 (a). The dependence of β_q on $(q-1)$ is shown in Fig. 8, which exhibits good linearity in the log-log plots. Thus we obtain a scaling exponent, denoted here as ν_-. In Table 2 are given the value of the negative scaling exponent for different p_T windows and for both versions of the AMPT model studied here. Since the scaling that is there in Eq. 3 is different to that we observe here for AMPT data, thus the scaling exponent obtained here cannot be compared with the $\nu = 1.304$ for the second order phase transition, as obtained from the GL theory.

Since large fluctuations result in the high F_q tails of $P(F_q)$, as exemplified in Fig. 5 (b) and (d), it is advantageous to put more weight on the high F_q side in averaging over $P(F_q)$. That is just what the double moment $C_{p,q}(M)$ does. We have determined $C_{p,q}(\text{M})$ for q = 2, 3, 4, 5 and p = 1.0, 1.25, 1.5, 1.75 and 2.0.

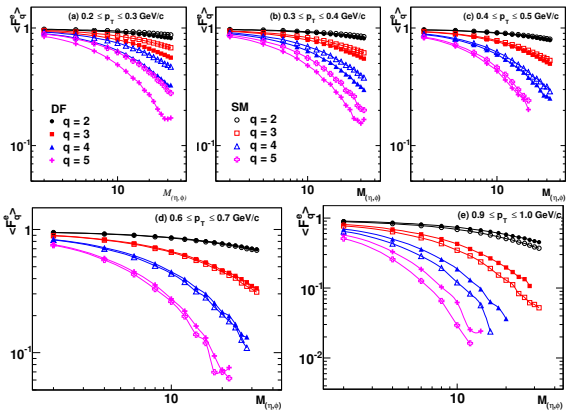

Figure 6: M Dependence of F_q, for DF as well as SM.

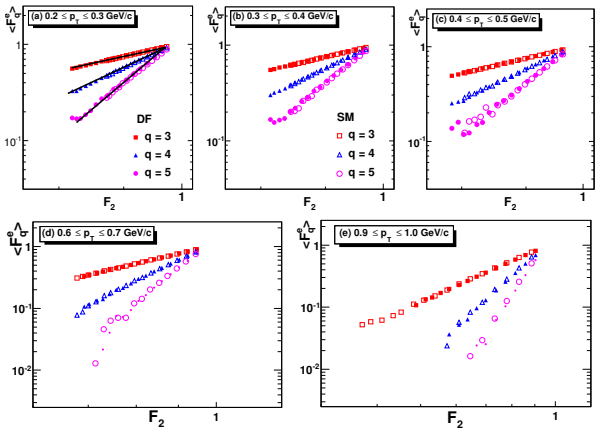

Figure 7: F-Scaling for DF as well as SM mode of AMPT

The number of bins, M, takes on values from 2 to the maximum value possible while having reasonable $\langle n_m \rangle$ such that $F_q \neq 0$. To check whether $C_{p,q}(\mathrm{M})$ follows the scaling behaviour with M, $C_{p,q}$ is plotted against M. Fig. 9 (a) to (d) shows respectively, for $q = 2$, 3, 4 and 5, the $C_{p,q}$ versus M plot in the log-log scale for the window $0.6 \leq p_T \leq 0.7$ GeV/c, and for various values of p between 1 and 2. As expected for all values of q, for $p = 1.0$, the $C_{p,q} = 1$. For $p > 1.0$, $C_{p,q}$ increases with M and q values. Similar calculations are also done for the other p_T windows. In the high M region linear fits are performed for each q and p value so as to determine $\psi_q(p)$. We see in Fig. 10 that for $0.6 \leq p_T \leq 0.7$ $\psi_q(p)$ depends on p linearly for each q. Thus the erraticity indices defined in Eq. (12) are determined. Similar plots are obtained for the other p_T windows also and the values of μ_q are given in Table 3. It can be seen from the table that as p_T value increases, the erraticity indices increase for both versions of the AMPT model.

Comparing the μ_q values for the DF and SM data within the same window and for the same values of q, it is observed that μ_q has higher values for the DF version in comparison to SM for the p_T windows below 0.6 GeV/c. That phenomenon

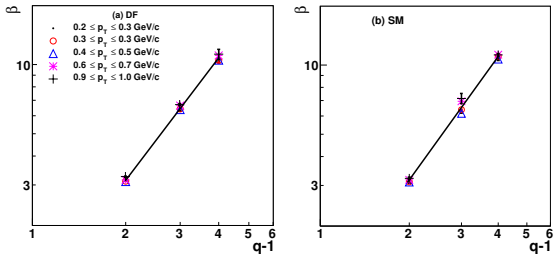

Figure 8: β_q versus $(q-1)$ plot for determination of the scaling exponents.

p_T	ν_- **(Default)**	ν_- **(String Melting)**
$0.2 \leq p_T \leq 0.3$	1.738 ± 0.008	1.753 ± 0.004
$0.3 \leq p_T \leq 0.4$	1.774 ± 0.007	1.793 ± 0.005
$0.4 \leq p_T \leq 0.5$	1.758 ± 0.006	1.755 ± 0.006
$0.6 \leq p_T \leq 0.7$	1.824 ± 0.008	1.869 ± 0.016
$0.9 \leq p_T \leq 1.0$	1.778 ± 0.013	1.781 ± 0.011

Table 2: Scaling exponents for negative intermittency in the Default and String Melting versions of the AMPT Model

is related to the average multiplicities of the two versions reversing their relative magnitudes at higher p_T. However it is to be noted from Fig. 10 that the dependence of $\psi_q(p)$ on p is better distinguishable for the two versions of the AMPT for only q = 4. Coincidentally, as observed in [7], μ_4 seems to be a good measure to compare the erraticity indices of the different systems and data sets at these energies.

We observe that the values of μ_4^{DF} and μ_4^{SM} for all p_T windows are larger than those obtained for the critical data set in [7], on the same side as the non-critical case. We have found φ^- to be negative because $P(F_q)$ broadens, as M increases, with $\langle F_q e \rangle$ shifting to the lower region of F_q^e, thus resulting in negative intermittency. We did notice that the upper tails move to the right, suggesting the presence of some degree of clustering. To emphasize that part of $P(F_q)$ we have taken higher p-power moments of $\phi_q(M)$, which suppress the lower side of F_q while boosting the upper side. The scaling properties of $C_{p,q}(M)$ therefore deemphasize what leads to negative intermittency. Thus the erraticity indices μ_q reveal a different aspect of the fluctuation patterns than the scaling indices ν^-. Our study here has revealed interesting properties of scale-invariant fluctuations that should be compared to the real data.

4 Summary

Fluctuations in the spatial patterns of charged particles and their event-by-event fluctuations, as are present in the events generated using the default and string melting version of A MultiPhase Transport (AMPT) model are studied. This is a first attempt to study intermittency and erraticity at such high energies. It is observed that as the bin size decreases, the factorial moments decrease. This behaviour is in contrast to usual properties of intermittency observed at lower energies indicating

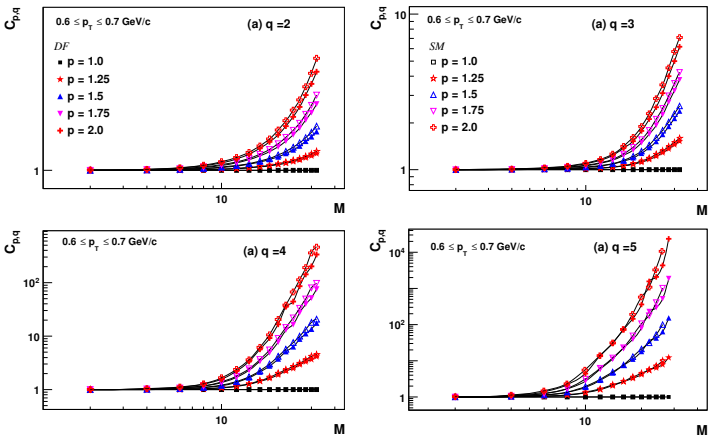

Figure 9: M dependence of $C_{p,q}$ for the p_T window $0.6 \leq p_T \leq 0.7$ GeV/c in case of DF and SM versions of the AMPT model

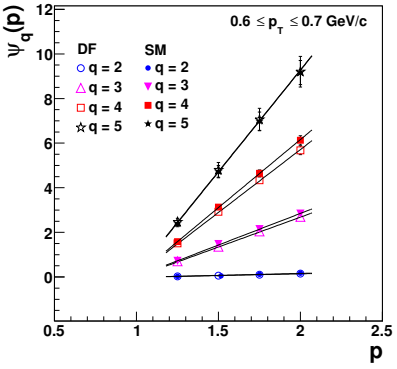

Figure 10: The ψ_q dependence on the p for DF and SM AMPT in the $0.6 \leq p_T \leq 0.7$ GeV/c window.

that events with localization of even moderate multiplicities in the small bins, at low p_T are not present in the AMPT. Further the erraticity analysis of the model shows that the systems generated in it is not near criticality. The μ_q values determined here give the quantification of the event-by-event fluctiations in the spatial patterns of the charged particles in the midrapidity region, which can be used effectively to compare with other models. More importantly comparison of the values with that from the LHC would help to get a better understanding of the particle production mechanism at high energies.

References

[1] S. Gavin and George Moschelli, Phys. Rev. C **85**, 014905 (2012).

[2] M.I. Adamovich *et al.*, Phys. Lett. B, **201**, 3, 397 (1988).

	AMPT (Default)	AMPT (String Melting)
p_T	μ_2	μ_2
$0.2 \leq p_T \leq 0.3$	0.043 ± 0.002	0.016 ± 0.001
$0.3 \leq p_T \leq 0.4$	0.045 ± 0.002	0.027 ± 0.001
$0.4 \leq p_T \leq 0.5$	0.062 ± 0.003	0.048 ± 0.002
$0.6 \leq p_T \leq 0.7$	0.154 ± 0.008	0.174 ± 0.011
$0.9 \leq p_T \leq 1.0$	0.739 ± 0.043	1.014 ± 0.064
	μ_3	μ_3
$0.2 \leq p_T \leq 0.3$	0.901 ± 0.081	0.328 ± 0.025
$0.3 \leq p_T \leq 0.4$	0.904 ± 0.081	0.531 ± 0.043
$0.4 \leq p_T \leq 0.5$	1.304 ± 0.118	1.019 ± 0.077
$0.6 \leq p_T \leq 0.7$	2.678 ± 0.155	2.832 ± 0.137
$0.9 \leq p_T \leq 1.0$	4.502 ± 0.147	4.960 ± 0.305
	μ_4	μ_4
$0.2 \leq p_T \leq 0.3$	4.325 ± 0.243	2.481 ± 0.183
$0.3 \leq p_T \leq 0.4$	4.532 ± 0.234	3.385 ± 0.235
$0.4 \leq p_T \leq 0.5$	5.478 ± 0.258	3.935 ± 0.021
$0.6 \leq p_T \leq 0.7$	5.640 ± 0.203	6.101 ± 0.214
$0.9 \leq p_T \leq 1.0$	7.484 ± 0.361	7.359 ± 0.305
	μ_5	μ_5
$0.2 \leq p_T \leq 0.3$	6.202 ± 0.302	5.143 ± 0.022
$0.3 \leq p_T \leq 0.4$	6.150 ± 0.175	5.745 ± 0.312
$0.4 \leq p_T \leq 0.5$	7.396 ± 0.437	6.159 ± 0.280
$0.6 \leq p_T \leq 0.7$	9.107 ± 0.693	8.360 ± 0.533
$0.9 \leq p_T \leq 1.0$	8.643 ± 0.537	7.655 ± 0.358

[3] L. VanHove, Z. Phys. C **27** (1985), M. Guylassy *et al.*, Nucl. Phys. B **237**, 477-501 (1984).

[4] A. Bialas and R. Peschanski, Nucl. Phys B **273** 703 (1986); B **308**, 867 (1988).

[5] R.C. Hwa and M.T. Nazirov, Phys. Rev. Lett. **69**, 741 (1992).

[6] Z. Cao, R. Hwa, Phys. Rev. Lett. **75**, 1268 (1995), Phys. Rev. D **53**, 6608 (1996); Phys. Rev. D **54**, 6674 (1996).

[7] R.C. Hwa and C.B. Yang, Phys. Rev. C **85**, 044914 (2012).

[8] B. Zhang, C.M. Ko, B.A. Li and Z.W. Lin, Phys. Rev. C **61**, 067901 (2000).

[9] Z.W. Lin, C.M. Ko, B.A. Li, B. Zhang and S. Pal, Phys. Rev. C **72**, 064901 (2005).

[10] W. Ochs, Z Phys. C **50**, 339 (1991).

Multidimensional analysis of Bose-Einstein correlations in pp collisions at 2.76 and 7 TeV in CMS

Sandra S. Padula[1] (for the CMS Collaboration)

[1] Instituto de Física Teórica–UNESP, São Paulo, SP, Brazil

Abstract

Multidimensional two-particle Bose-Einstein correlation functions of charged hadrons are reported for pp collisions at 2.76 and 7 TeV in terms of different components of the pair relative momentum, extending the previous one-dimensional (1-D) analyses of CMS. This allows for investigating the extension of the source accessible to the femtoscopic correlation technique in different directions, revealing a more detailed picture of the emitting source in these collisions at increasing energies. The measurements are performed for different intervals of the pair average transverse momentum, k_T, and for increasing charged particle multiplicitiy, N_{ch}. Results in 1-D, 2-D and 3-D show a decrease of the fit radius parameters with k_T, whereas a clear rise with N_{ch} is observed in all cases. In addition, the fit radius parameters at both energies show close similarity in size and behavior within the same intervals of (N_{ch}, k_T).

1 Introduction

Femtoscopic Bose-Einstein correlations, also known as HBT/GGLP effect, were investigated in Ref. [3, 4] by CMS for pp collisions at $\sqrt{s}$ =0.9 TeV [3, 4], 2.36 TeV [3] and 7 TeV [4]. Such phenomenon was discovered by Goldhaber, S. Goldhaber, W. Lee and A. Pais (GGLP effect) [1], being the analogous in high-energy collisions to a similar method proposed by R. Hanbury-Brown and R. Q. Twiss (HBT effect)

[2] for estimating angular dimensions of stars. A broad investigation was carried out in these studies in terms of the invariant relative momenum $Q_{\rm inv}$. In Ref. [4], similarly to what was previously observed in e^+e^- collisions [5], an anticorrelation was reported. This result required a study of different fitting functions, as had been suggested in the case of small systems, such as the τ model [6], which considers strong correlations between the space-time coordinates and the momentum components of the emitted particles, and was found to describe better the overall behavior of the correlation functions.

A natural extension of those analyses is to investigate the GGLP/HBT correlations with respect to different components of the pair relative momentum, which allows for exploring the source sizes in different directions. Such analyses have also been studies by other experiments at RHIC and LHC [7, 8, 9, 10, 11, 12, 13]. Therefore, the HBT/GGLP correlation is measured in two-dimensions (2-D) as a function of the relative momenta along and transverse to the beam direction, q_L and q_T, respectively. In three-dimensions (3-D) the Bose-Einstein correlations are studied in terms of q_L, q_O and q_S, these last two obtained, respectively, by projecting the transverse component $\vec{q_T}$ in orthogonal directions, i.e., parallel to the average transverse momentum of the pair (k_T), and orthogonal to both q_L and q_O.

Using the same framework as in Ref. [3, 4], the HBT/GGLP effect is further scrutinised here for charged hadrons produced in minimum bias events in pp collisions at $\sqrt{s} = 2.76$ and 7 TeV with the data collected by CMS at the CERN LHC. New 1-D results at both these energies are discussed and then the analysis is extended to 2-D and 3-D cases.

2 Bose-Einstein Correlation measurements

2.1 Event and Track Selections

The data sets used in this analysis correspond to minimum bias samples obtained in pp collisions at 2.76 and 7 TeV recorded with the CMS detector at the LHC [15]. A detailed description of the CMS detector can be found in Ref. [14]. The minimum bias sample at $\sqrt{s} = 2.76$ TeV was triggered on-line by requiring at least one track with $p_T > 0.4$ GeV to be found in the pixel tracker with $|\eta| < 2.4$ for a pp bunch crossing. Besides, in the offline analysis hadronic collisions were selected by requiring a coincidence of at least one Forward Hadronic (HF) calorimeter tower with more than 3 GeV of total energy in each of the HF detectors. In the case of pp collisions at 7 TeV events were selected by a trigger signal in each side of the Beam Scintillation Counter (BSC), coincident with a signal from either of the two detectors indicating the presence of at least one proton bunch crossing the interaction point (IP). Collision events were then selected offline by requiring a Beam Pickup for Timing for the eXperiments (BPTX) signal from both beams passing the IP.

The set of pp collision events at $\sqrt{s} = 2.76$ TeV used in this analysis comprises the data collected by CMS in 2013 at the CERN LHC (3.4 million events). At $\sqrt{s} = 7$ TeV, a combined sample from pp collisions was considered, which uses data from three periods of the CMS data taking, i.e., commissioning run (23 million events), as well as from the runs 2010A (16 million events) and run 2010B (4 million events), where the first is almost pileup free, while the later has a non-negligible fraction of events with multiple interactions. A filter was used for reducing the contamination in case of multiple vertices (the reconstructed vertex with the

largest number of associated tracks is selected at 7 TeV, while in pp collisions at 2.76 TeV, an additional primary vertex might be identified as originating from a second pp collision by looking at its properties). To assess the related systematic uncertainty, an alternative event selection for reducing pileup contamination was also investigated by considering only single reconstructed vertex events.

In the case of pp collisions at 2.76 TeV, three Monte Carlo samples were used. For obtaining the BEC results, minimum bias events simulated with Pythia 6 Z2 Tune [16, 17] were employed, whereas Pythia D6T and Pythia Z2star [16, 17] were used for estimating the systematic uncertainties related to the choice of Monte Carlo tune. Each of them contained 2 million events. For the analysis at 7 TeV about 33 million Monte Carlo events were simulated using Pythia 6 Z2 Tune.

The track selection employed in both cases above follows the same criteria as in Ref. [3, 4], and are discussed in details in these references, as well as in [15].

2.2 The Bose-Einstein Correlation

The procedure adopted is the same as described in Refs. [3, 4]. Although no particle identification is considered in this analysis, the contamination from non-pions is not expected to be sizeable, as discussed in [3, 4], since pions are the dominant type of hadrons in the sample. For each event, the signal containing the Bose-Einstein correlations is identified by pairing same charge tracks from the same event and distributing them in bins of the relative momentum of the pair, for instance, $q^{\mu} = k_1^{\mu} - k_2^{\mu}$, being k_i^{μ} the four-momenta of the individual particles in the pair. The background distribution or reference sample is formed similarly, by pairing charged particles from different events and within the same η range (where the full pseudorapidity interval is divided in three subranges $\Delta\eta$, corresponding to $-2.4 \leq \eta \leq -0.8$, $-0.8 \leq \eta \leq 0.8$, and $0.8 \leq \eta \leq 2.4$), as in Ref. [4]. This mixed event technique is referred to as "same track density in $\Delta\eta$". A single ratio is then formed, having the signal pair distribution as numerator and the reference sample as denominator, with the appropriate normalization, i.e., $R = (\frac{\mathcal{N}_{\rm ref}}{\mathcal{N}_{\rm sig}}) \frac{(\mathrm{d}N_{\rm sig}/\mathrm{d}Q_{\rm inv})}{(\mathrm{d}N_{\rm ref}/\mathrm{d}Q_{\rm inv})}$. The invariant relative momentum of the pair is defined as $Q_{\rm inv} = \sqrt{-q^{\mu}q_{\mu}} = \sqrt{-(k_1 - k_2)^2}$; $\mathcal{N}_{\rm sig}$ is the integral of the signal pair distribution of all the events, whereas $\mathcal{N}_{\rm ref}$ is the equivalent in the reference sample. A double ratio technique is then taken with the data and the Monte Carlo single ratios corresponding to the $Q_{\rm inv}$ distributions, in terms of which the Bose-Einstein Correlation (BEC) effect is investigated [3, 4], $\mathcal{R}(Q_{\rm inv}) = \frac{R}{R_{\rm MC}} = \left(\frac{\mathrm{d}N_{\rm sig}/\mathrm{d}Q_{\rm inv}}{\mathrm{d}N_{\rm ref}/\mathrm{d}Q_{\rm inv}}\right) \Big/ \left(\frac{\mathrm{d}N_{\rm MC}/\mathrm{d}Q_{\rm inv}}{\mathrm{d}N_{\rm MC,\,ref}/\mathrm{d}Q_{\rm inv}}\right)$, where $R_{\rm MC}$ is the single ratio computed with the simulated events generated without BEC. In each case, the reference samples for data and simulation are obtained in the same way. This double-ratio procedure has the advantage of considerably reducing the sources of bias due to track inefficiency and other detector-related effects, as well as other Bose-Einstein correlations.

The GGLP/HBT method reflects not only the quantum statistics of the pair of identical particles, but is also sensitive to the underlying dynamics. In particular, in the case of charged hadrons, the correlation function may be distorted by strong, as well as by Coulomb interactions. For pions, the strong interactions can usually be neglected in femtoscopic measurements. As in Ref. [3, 4], the depletion (enhancement) in the correlation function caused by the Coulomb repulsion (attrac-

tion) of equal (opposite) charge pairs in the case of pions is corrected by weighting pair-wise with the inverse Gamow factor [18]. This factor, in case of same charge and opposite charge, is given by $G_w^{SS}(\eta_w) = \frac{2\pi\eta_w}{e^{2\pi\eta_w}-1}$, $G_w^{OS}(\eta_w) = \frac{2\pi\eta_w}{1-e^{-2\pi\eta_w}}$, with $\eta_w = \alpha_{em} m_\pi / Q_{\rm inv}$, where m_π the pion mass and $Q_{\rm inv}$ the invariant relative momentum of the pair.

For performing the multidimensional analysis, the double ratios are investigated in terms of the projections of the relative momentum $\mathbf{q} = \mathbf{k_1} - \mathbf{k_2}$ in two or three directions. In the 2-D case, the decomposition is made in q_L (*longitudinal* component, along the beam direction), and q_T (*transverse* component). In the 3-D case, additional projections are considered in the transverse plane, resulting in q_O (*outwards*), and q_S (*sidewards*), respectively along the average transverse momentum of the pair, $k_T = (k_{T_1} + k_{T_2})/2$, and orthogonal to it; q_O, q_S, and q_L are mutually orthogonal. This decomposition of the relative momentum of the pair is also known as Bertsch-Pratt variables [19, 20, 21]. The investigations are carried out in center-of-mass (CM), i.e., the LHC laboratory frame, as well as in the Local Co-Moving System (LCMS), characterized by the frame in which the longitudinal component of the pair average momentum ($k_L = (k_{L_1} + k_{L_2})/2 = (k_{z_1} + k_{z_2})/2$) is zero. Details about the 2-D and 3-D relative momentum projections, as well as the boost to the LCMS can be found in Ref. [22].

The parameterizations used to fit the correlation functions in one- (1-D), two- (2-D) and three-dimensions (3-D), respectively in terms of $Q_{\rm inv}$, (q_L, q_T) and (q_S, q_L, q_O), are listed below. Throughout this analysis $\hbar = c = 1$ is adopted.

$$\mathcal{R}(Q_{\rm inv}) = C[1 + \lambda e^{-(Q_{\rm inv}R_{\rm inv})^\alpha}]\,(1 + \delta\, Q_{\rm inv}), \tag{1}$$

$$\mathcal{R}(q_L q_T) = C\Big\{1+\lambda \exp\Big[-\Big|q_T^2R_T^2 + q_L^2R_L^2 + 2q_Tq_LR_{LT}^2\Big|^{a/2}\Big]\Big\}\times(1+\alpha q_T+\beta q_L), \tag{2}$$

$$\begin{aligned}\mathcal{R}(q_S, q_L, q_O) &= C\Big\{1 + \lambda \exp\Big[-\Big|q_S^2R_S^2 + q_L^2R_L^2 + q_O^2R_O^2 + 2q_Oq_LR_{LO}^2\Big|^{a/2}\Big]\Big\}\times \\ &\quad (1 + \alpha q_S + \beta q_L + \gamma q_O).\end{aligned} \tag{3}$$

In the above expressions, λ is the intercept parameter (intensity of the correlation in the smallest bin of the pair relative momentum), C, $\delta, \alpha, \beta, \gamma$ are constants. The exponent a is the Lévy index of stability satisfying the inequality $0 < a \leq 2$. In all the above cases, if treated as a free parameter when fitting the double ratios, this exponent usually results into a number between the value characterizing the exponential ($a = 1$) and the Gaussian ($a = 2$) functions. More details can be found in Ref. [23]. For the sake of clarity, we denote the longitudinal component of the relative momentum in the CM frame as q_L, and in the LCMS, as q_L^*. In particular, in the case $a = 1$ the exponential term coincides with the Fourier transform of the source function $\rho(t, \vec{x})$, characterised by a Lorentzian distribution; the radius parameters $R_{\rm inv}$, (R_T, R_L), (R_S, R_L, R_O), correspond to the lengths of homogeneity fitted to the correlation function in 1-D, 2-D and 3-D, respectively. The additional polinomial terms are introduced for accommodating possible deviations of the baseline from unity at large values of these variables (long-range correlations), as well as for allowing a better quality fit. In the 2-D and 3-D cases, $a = 1$ leads to the so-called *stretched exponential* function. In Eq. (2), $R_T = \bar{R}_T + \tau\beta_T \cos\phi$ and $R_L = \bar{R}_L + \tau\beta_L$ where $\beta_{\mathbf{T}} = \frac{\mathbf{k_T}}{k^0}$ and $\beta_L = \frac{k_L}{k^0}$, originated in the mass-shell constraint ($q^\mu k_\mu = 0 \rightarrow q^0 = \frac{\mathbf{q}.\mathbf{k}}{k^0}$); ϕ is the angle between the directions of $\mathbf{q_T}$

and $\mathbf{k_T}$ and τ is the source life-time. In Eq. (3) $R_S^2 = \bar{R}_S^2$, $R_L^2 = \bar{R}_L^2 + \tau^2\beta_L^2$, $R_O^2 = \bar{R}_O^2 + \tau^2\beta_T^2$ and $R_{LO}^2 = \tau^2\beta_L^2\beta_T^2$. Both in Eq. (2) and (3) a frame dependent cross-term, respectively proportional to $q_T q_L$ and $q_O q_L$ is present. However, when the analysis is performed in the LCMS, this cross-term does not contribute for sources symmetric along the longitudinal direction.

2.3 Systematic uncertainties

Various sources of systematical uncertainties were considered in this analysis, as listed in Table 1, the first four being similar to what was discussed in Ref. [3, 4]. Two additional studies were also performed: the effect of separating positive from negative charges in the single ratios (since $(++)$, as well as $(--)$ charges are added in the signal; in the reference sample, besides these two combinations, the $(+-)$ case is also added to the sample). The second study added is the effect of pileup events, investigated by comparing the results to the case where only single-vertex events are considered. The exponential function in Eq.(1) (Lévy type with $a = 1$) was adopted for this investigation. The total values of the systematic uncertainties are calculated by adding the individual contributions in quadrature. The systematic uncertainties estimated in 1-D and summarized in Table 1 are extended to both the 2-D and the 3-D cases.

Table 1: Spread with respect to the mean values at $\sqrt{s} = 2.76$ TeV and 7 TeV

Systematical Uncertainties				
$\sqrt{s}$	2.76 TeV		7 TeV	
Origin of Systematics	λ	$R_{\rm inv}$ (fm)	λ	$R_{\rm inv}$ (fm)
Monte Carlo tune	0.032	0.160	0.032	0.160
Reference Sample	0.009	0.047	0.051	0.188
Coulomb Corrections	0.016	0.009	0.018	0.020
Track Cuts	0.014	0.119	0.014	0.119
Charge Dependence	0.006	0.012	0.007	0.006
Pileup filter	5.0 e-4	0.011	0.001	0.0025
Total	0.040	0.206	0.065	0.275

3 Analysis Results

3.1 One-dimensional results

The current analysis extends the previous one for pp at $\sqrt{s} = 7$ TeV reported in Ref. [4] to full data sample, as well as at $\sqrt{s} = 2.76$ TeV with full available statistics. The corresponding results for single and double ratios are shown in Fig. 1. The fits to the double ratios were produced with the exponential function in Eq. (1), with $a = 1$.

Figure 2 shows results for the intercept parameter λ and the invariant radius $R_{\rm inv}$ from pp collisions at 2.76 and 7 TeV (full statistics), in terms of N_{ch} and k_T. It can be seen that the results corresponding to the two energies are very similar for the different (N_{ch}, k_T) combinations. The intercept λ decreases with increasing k_T and N_{ch}, whereas $R_{\rm inv}$ steadily increases with multiplicity and seem to decrease with k_T, at least for the two largest N_{ch} bins, showing that the lengths of homogeneity accessible to interferometric measurements decrease with the average

pair momentum, as has been previously observed in several different collision systems and energy ranges [3, 4, 9, 10, 11, 12, 13].This behavior is expected in the case of emitting sources originated from expanding systems.

In Fig. 3 (left), $R_{\rm inv}$ is investigated as a function of the charged particle multiplicity, $< N_{ch} >$ (efficiency and acceptance corrected), where the curves are fits proportional to $N_{ch}^{1/3}$. The results for pp collisions at 2.76 TeV and at 7 TeV are consistent with former studies reported in Ref. [4] at 0.9 and 7 TeV, showing a similar increase with $N_{ch}^{1/3}$. Such results also suggest an approximate scaling property of the lengths of homogeneity with increasing collision center-of-mass energy.

As discussed in [4], an anticorrelation (value below unity) was observed in the double ratios for values of $Q_{\rm inv}$ away from the Bose-Einstein peak, whose depth was shown to decrease with increasing N_{ch}, for integrated values in k_T. This dip structure is also observed in the present analysis and its depth is further investigated. More details and discussion on the results are presented in Ref. [15]. An additional function, $\mathcal{R}(q) = C\left\{1 + \lambda[\cos\left[(qr_0)^2 + \tan(\alpha\pi/4)(qr_\alpha)^\alpha\right] e^{-(qr_\alpha)^\alpha}]\right\} \cdot (1 + \delta q)$, was used to fit the data points, which better describes such anticorrelation, as discussed in [4, 15]. It is based on the so-called τ Model [6], which parameterizes the time evolution of the source by means of a one-sided asymmetric Lévy distribution. The dip's depth [4] is estimated by the difference of the base-line function, $C(1+\delta q)$, and the remaining fit function based on the τ model at its minimum, leading to the results shown in Fig. 3 (right), where the results for pp collisions at both 0.9 and 7 TeV from Ref. [4] and the new ones for 2.76 TeV and the full sample at 7 TeV are shown together (see [15] for details).

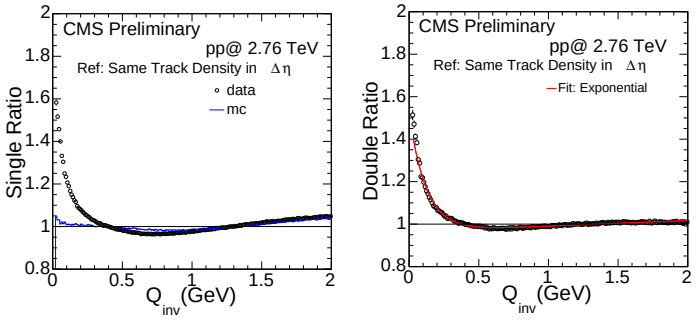

Figure 1: 1-D single ratios as a function of $Q_{\rm inv}$ for data and Monte Carlo (Pythia 6-Z2 tune) from to pp collisions at 2.76 TeV are shown (left), as well as the corresponding double ratio superimposed by the exponential fit (right).

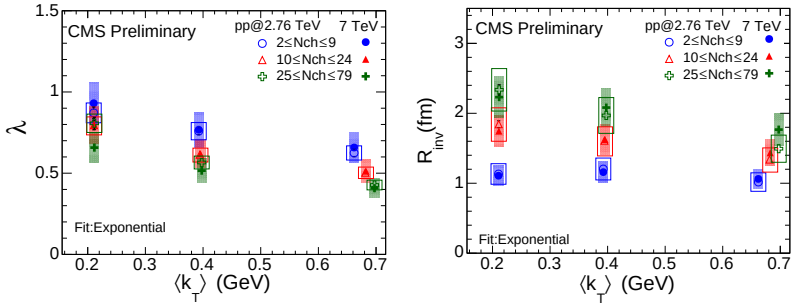

Figure 2: The fit parameters λ (left) and $R_{\rm inv}$ (right) from exponential fits to the double ratios are shown in different N_{ch} and k_T bins, from pp collisions at 2.76 and 7 TeV (full sample). The statistical uncertainties are indicated by error bars (in some cases, smaller than the marker's size), the systematic ones by empty (2.76 TeV data) or shaded boxes (7 TeV data).

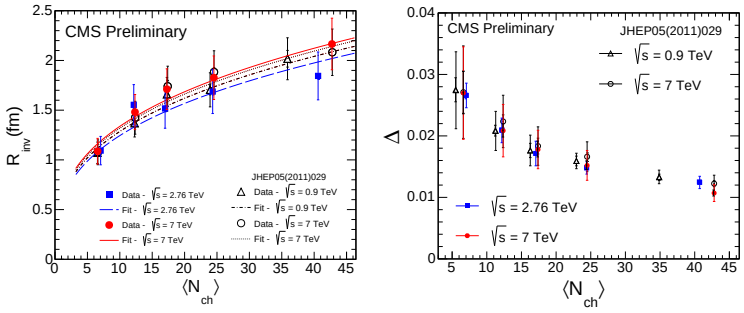

Figure 3: Comparative plots with results in Ref. [4]. Left: $R_{\rm inv}$ versus $< N_{ch} >$ (acceptance and efficiency corrected), for pp collisions at 2.76 and 7 TeV (fit curves are proportional to $N_{ch}^{1/3}$). The inner error bars represent statistical uncertainties and the outer ones, statistical and systematic uncertainties added in quadrature. Right: The anticorrelation's depth, Δ, versus $< N_{ch} >$.

3.2 Two-Dimensional Results

The BEC analysis is extended to the 2-D case in terms of the components q_L, q_T of the pair relative momentum, with the data samples from pp collisions at $\sqrt{s} = 2.76$ TeV and 7 TeV. It is performed both in the CM frame and in the LCMS, in which the cross-term depending on $q_T q_L$ in 2-D, or $q_L q_O$, in 3-D, does not contribute, in case of longitudinally symmetric systems.

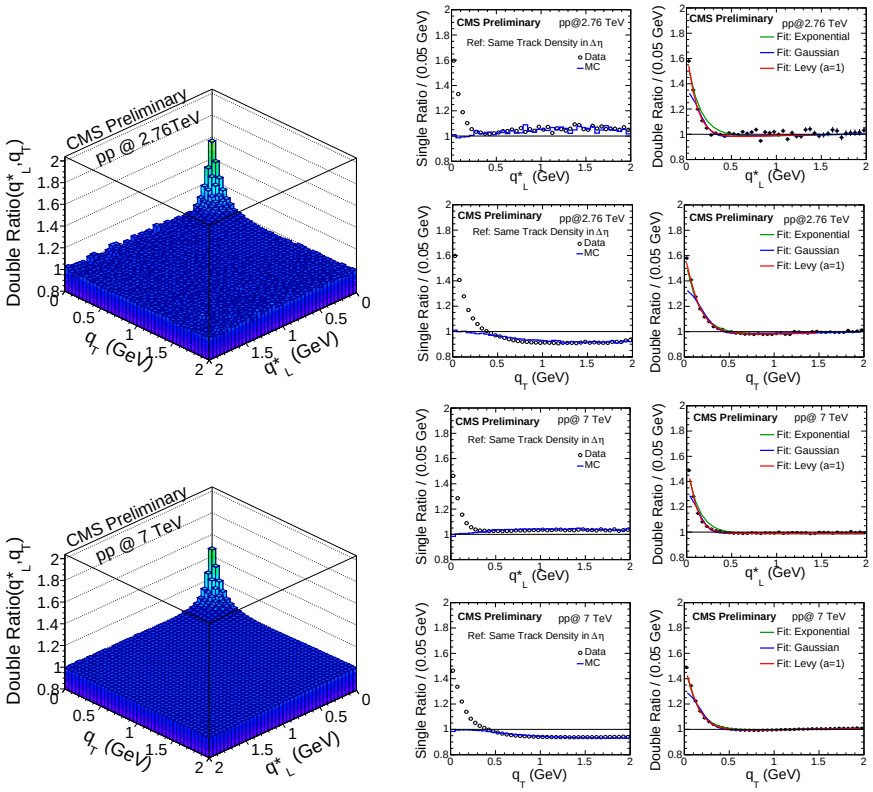

Figure 4: The left panel shows double ratios as a function of (q_L^*, q_T), with data from pp collisions at 2.76 TeV (top) and 7 TeV (bottom) in the LCMS corresponding to results integrated in all N_{ch} and k_T bins. The right panel shows the corresponding 1-D projections of the single and double ratios in terms of q_L^* (for $|q_T| < 0.05$ GeV) and q_T (for $|q_L^*| < 0.05$ GeV). Gaussian, exponential and Lévy (with $a = 1$) fit functions are shown superimposed to the data points.

As an illustration, the double ratios in the LCMS are shown in Fig. 4, as a 2-D plot (left panel) in terms of (q_L^*, q_T), and the corresponding 1-D projections (right panel) for pp collisions at 2.76 TeV (top), and for 7 TeV (bottom). The 1-D projections, when plotted in terms of q_L^*, considers only the first bin in q_T (i.e., $q_T < 0.05$ GeV), and vice-versa, with the data superimposed by the Gaussian, exponential and Lévy (with $a = 1$) fit functions.

Analogously to the studies performed in 1-D the double ratios in 2-D were also investigated in terms of (q_L, q_T), in three intervals of the pair average momentum, k_T, and in different N_{ch} bins. The results from the *stretched exponential* fit

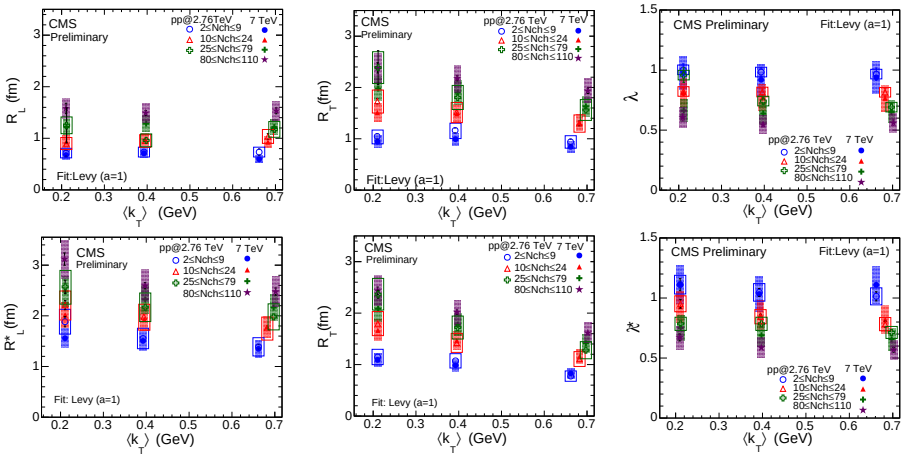

Figure 5: The fit parameters obtained with the *stretched exponential* (Lévy-type with $a = 1$) function are shown for pp collisions at 2.76 and 7 TeV in the CM frame (top) and in the LCMS (bottom), as a function of $\langle k_T \rangle$ and for different N_{ch} bins. The statistical uncertainties are indicated by error bars (in some cases, smaller than the marker's size), whereas the systematic ones are indicated by empty (at 2.76 TeV) or shaded boxes (at 7 TeV).

(Lévy-type with $a = 1$) [23] to the double ratios, performed both in the CM frame (top) and in the LCMS (bottom), are compiled in Fig. 5. The behaviour of the directional lengths of homogeneity is very similar in both frames, with R_L (R_L^*) and R_T increasing with charged multiplicity, N_{ch}, and decreasing with the average transverse momentum, k_T, at least in the larger multiplicity bins, a behaviour similar to that observed in the 1-D case and expected for expanding sources. Another interesting feature of the data than can be observed in Fig. 5 is that R_L^* (LCMS) $> R_L$ (CM) for the same bins of N_{ch} and k_T, suggesting an effect of Lorentz boost contraction in the longitudinal length of homogeneity in the CM frame. Regarding λ, as shown in Fig. 5, no significant sensitivity of the intercept is seen as a function of k_T. However, within each k_T range, λ slowly decreases with increasing track multiplicity in an similar way in both frames.

Table 2: 2-D fit parameters for in the LCMS

$\sqrt{s}$	2.76 TeV	7 TeV
λ	0.830 ± 0.010 (stat.) $\pm$ 0.040 (syst.)	0.700 ± 0.002 (stat.) $\pm$ 0.065 (syst.)
R_T (fm)	1.498 ± 0.013 (stat.) $\pm$ 0.206 (syst.)	1.640 ± 0.003 (stat.) $\pm$ 0.206 (syst.)
R_L^* (fm)	1.993 ± 0.022 (stat.) $\pm$ 0.206 (syst.)	2.173 ± 0.005 (stat.) $\pm$ 0.275 (syst.)

Table 2 collects the values of the radius, R_L^*, R_T, and of the intercept, λ, fit parameters, integrated both in N_{ch} and k_T, and obtained with the *stretched* exponential fit (i.e., Lévy-type with $a = 1$). From Table 2 it can be seen that, in the LCMS, the rest frame of the pair along the longitudinal direction, $R_L^* \approx 4R_T/3$, suggesting that the source is longitudinally elongated, at both energies.

In Fig. 6 the 2-D results for the double ratios versus (q_L^*, q_T) in the LCMS are

zoomed along the correlation function axis, which cuts the BEC peak above 1.2. Figure 6 also shows the 1-D projections in terms of each of these variables, having the complementary one within the first bin, i.e, $|q_i| < 0.05$ GeV. The results are shown in four bins of charged particle multiplicity, N_{ch}, which increases from the top left panel to the bottom right one.

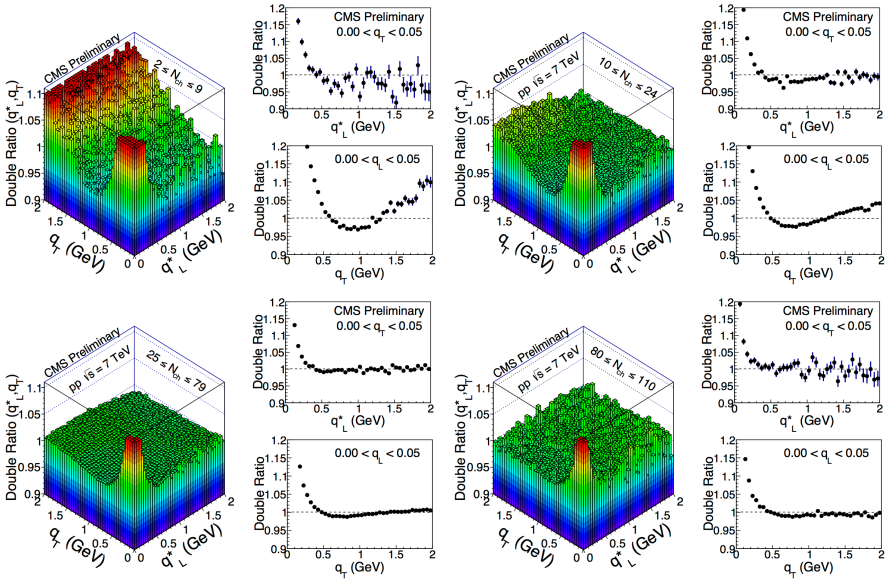

Figure 6: Results obtained in the LCMS for the 2-D double ratios with zoomed axes, with the BEC peak cut above 1.2, as a function of (q_L^*, q_T) for four charged multiplicity bins, N_{ch}, increasing from top left to bottom right. The 1-D projections in q_L^* (for $|q_T| < 0.05$ GeV) and q_T (for $|q_L^*| < 0.05$ GeV) are shown side-by-side to the corresponding 2-D double ratios.

3.3 Three-Dimensional Results

The 3-D correlation function in terms of the variables (q_S, q_L^*, q_O) can be visualised through 2-D projections in terms of the combinations (q_S, q_L^*), (q_L^*, q_O), and (q_O, q_S), with the complementary components within $|q_O| < 0.05$ GeV, $|q_S| < 0.05$ GeV, $|q_L^*| < 0.05$ GeV, respectively, corresponding to the width of the first bins. The 1-D projections in the LCMS of the single and double ratios are shown in Fig. 7 for pp collisions at 7 TeV. The points represent the data and the curves the exponential, *stretched exponential* (Lévy-type with $a = 1$) and Gaussian fit functions. The fits are performed to the 3-D double ratios and then projected in the directions of q_S, q_L^*, q_O, similarly to the projections of the data points.

The values of the lengths of homogeneity in the Bertsch-Pratt parameterization for pp collisions at 7 TeV, obtained with the *stretched* exponential fit in the LCMS, integrating over all N_{ch} and k_T ranges, are summarized in Table 3, together with the corresponding intercept fit parameter. Comparing the lengths of homogeneity in the 3-D case in the LCMS, from Table 3 it is found that $R_L^* \approx 1.5\ R_O$ fm and $R_L^* \approx 1.2\ R_S$ at 7 TeV. Therefore, the source seems to be more elongated along the

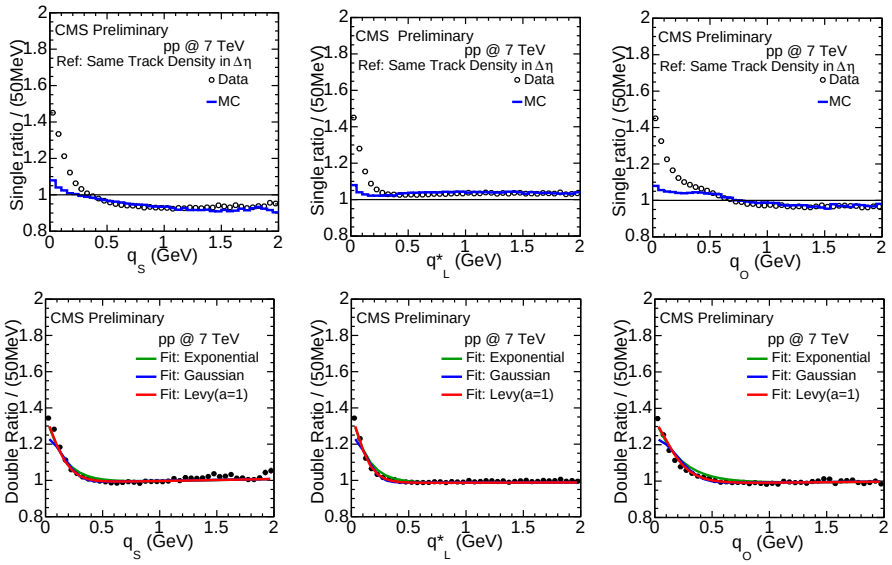

Figure 7: The top panel shows the 1-D projections of the 3-D single ratios of data and Monte Carlo, in terms of the relative momentum components (q_S, q_L^*, q_O) analyzed in the LCMS, for pp collisions at 7 TeV; the bottom panel shows the corresponding double ratios. The Gaussian, the exponential and the Lévy (with $a = 1$) fit functions are shown superimposed to the data points.

longitudinal direction in the LCMS also in the 3-D case, with the relation among the lengths of homogeneity such as $R_L^* > R_S > R_O$.

Table 3: 3-D fit parameters for pp collisions at $\sqrt{s} = 7$ TeV in the LCMS

$\sqrt{s}$	7 TeV
λ	0.568 ± 0.002 (stat.) $\pm$ 0.065 (syst.).
R_O (fm)	1.370 ± 0.004 (stat.) $\pm$ 0.275 (syst.)
R_S (fm)	1.784 ± 0.004 (stat.) $\pm$ 0.275 (syst.)
R_L^* (fm)	2.105 ± 0.005 (stat.) $\pm$ 0.275 (syst.)

The fits to the 3-D double ratios were also investigated in three k_T bins (integrating over all N_{ch}). The fit parameters were obtained with Gaussian, exponential and Lévy (with $a = 1$) fit functions (when treated as a fit parameter a returned values close to unity also in the 3-D case, both in the CM and in the LCMS). The results are compiled in Fig. 8 for the data from pp collisions at 7 TeV, showing to depend noticeably on the type of fit used, the radius parameters being considerably larger in the case of the Lévy-type function. The dependence on k_T, however, seems to be similar for the three fit functions. The R_S fit values are among the largest (except for the Gaussian fit) and seem insensitive to k_T, in both frames. Also R_L seems to be insensitive to k_T, and is the smallest radius parameter in the CM frame. However, it shows opposite behavior in the LCMS, where its decrease with increasing k_T is more pronounced, also attaining the largest values of the three

radius parameters, suggesting an effect related to the Lorentz boost in the longitudinal direction, as in the 2-D case. The R_O fit values are slightly smaller in the LCMS as compared to the CM frame, and decrease moderately with increasing k_T. Its dependence on k_T is similar in both frames, although it has a slightly steeper decrease with increasing k_T in the LCMS.

The fits to the double ratios were also studied in four N_{ch} bins (integrating over all k_T). The corresponding results are shown as a function of $\langle N_{ch} \rangle$ (efficiency and acceptance corrected) in Fig. 9, obtained both in the CM frame (top) and in the LCMS (bottom). A clear behavior can be seen, common to all fit functions and in all directions of the relative momentum components: the fit radius parameters R_S, R_L and R_O increase with increasing average multiplicity, indicating an increase in the lengths of homogeneity with N_{ch}, similar to what was seen in the 1-D and 2-D cases.

The intercept parameter λ was also studied as a function of k_T and N_{ch}, both in the CM frame and in the LCMS. The corresponding results are shown in Fig. 10. The values of $\langle N_{ch} \rangle$ shown in the plots were corrected for efficiency and acceptance. A moderate decrease with increasing k_T is observed. As a function of increasing N_{ch}, λ first decreases and then seems to saturate.

In the 2-D and 3-D cases, the values of the longitudinal radius fit parameters coincide within the experimental uncertainties [15], as expected, since both correspond to the length of homogeneity in the beam direction. From Figures 8 and 9 it can seen that there is an approximate scaling of R_L (R_L^*) and R_T with N_{ch}, when comparing the results at 2.76 TeV and at 7 TeV.

In Fig. 11 the 3-D results for the double ratios in the LCMS (integrated in N_{ch} and k_T) are shown as 2-D projections in terms of pairs of q_S, q_L, q_O (the complementary one within $|q_i| < 0.05$ GeV). The plots are zoomed along the correlation function axis, cutting values above 1.2. The corresponding 1-D projections along variable q_S, q_L, and q_O (other two variables within $|q_{i,j}| < 0.05$ GeV) are also shown.

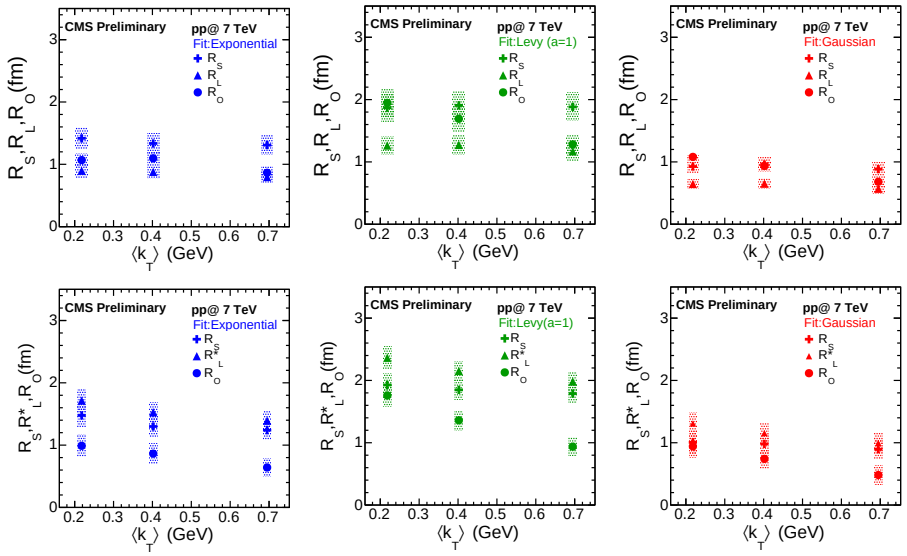

Figure 8: The radius parameters in the CM frame (top) and in the LCMS (bottom), for pp collisions at 7 TeV, obtained from fits to the double ratios with three different functions, are shown versus $\langle k_T \rangle$, integrated in N_{ch}. The statistical uncertainties are indicated by error bars (in some cases, smaller than the marker's size), whereas the systematic ones are indicated by shaded boxes.

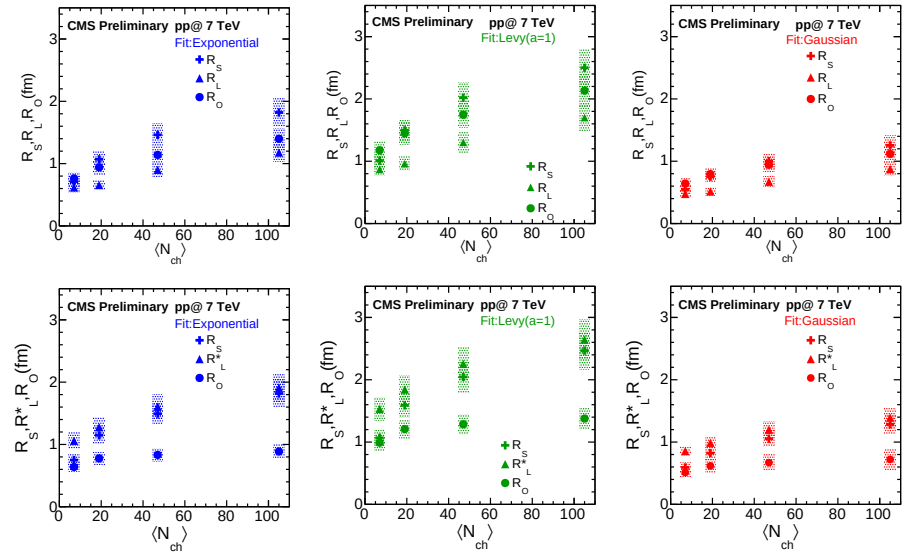

Figure 9: Results of fits to the double ratios with three different fit functions in the CM frame (top) and in the LCMS (bottom) for pp collisions at 7 TeV are shown as a function of $\langle N_{ch} \rangle$ (efficiency and acceptance corrected), integrated in k_T. The statistical uncertainties are indicated by error bars (in some cases smaller than the marker's size), whereas the systematic ones are indicated by the shaded boxes.

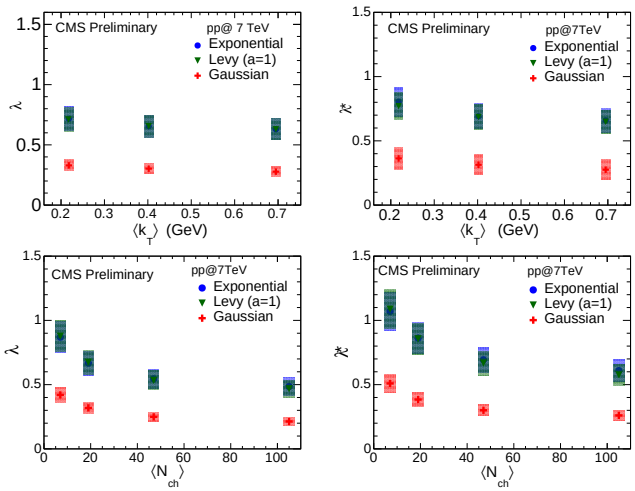

Figure 10: Results corresponding to the intercept parameter λ in the CM frame (left panel) and in the LCMS (right panel) are shown on top as a function of $\langle k_T \rangle$ (integrated in N_{ch}), and on the bottom as a function of $\langle < N_{ch} > \rangle$ (integrated in k_T). The values of N_{ch} were corrected for efficiency and acceptance. Statistical uncertainties are indicated by error bars (in some cases smaller than the marker's size), whereas systematic ones are indicated by shaded boxes.

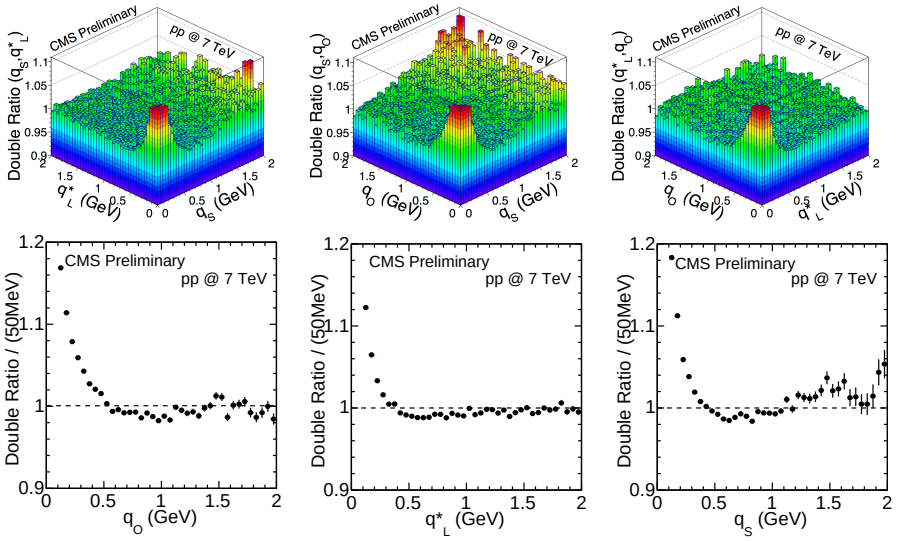

Figure 11: The results for the 3-D double ratios obtained in the LCMS are shown, the upper panel corresponding to the 2-D projections in (q_L^*, q_S), (q_O, q_S), and (q_O, q_L^*), integrated in N_{ch} and k_T, with $|q_O| < 0.05$ GeV, $|q_L^*| < 0.05$ GeV and $|q_S| < 0.05$ GeV, respectively. The bottom panel shows 1-D projections of the same data, with the complementary two variables constrained to be within the first bin (i.e., $|q_{i,j}| < 0.05$ GeV).

4 Summary and conclusions

The analysis discussed here extends the 1-D results reported in the two BEC publications in [3, 4] by measuring the correlation functions in terms of different components of the pair relative momentum, as is usually studied by other experiments. This allows to investigate the extension of the source accessible to the correlation technique in different directions. Two main projections are considered: in two-dimensions (2-D), the femtoscopic correlation is investigated as a function of the variables q_L and q_T, and in three-dimensions (3-D), as function of q_L, q_S, q_O, being q_L the same as in the 2-D case. For achieving this purpose, minimum bias events produced in proton-proton collisions at 2.76 and 7 TeV (full data sample) are scrutinised in detail, as if by means of a magnifying lens. At 7 TeV, the full data sample is used and the corresponding results are compared with the ones at the same energy recorded during the commissioning run at the LHC in 2010. This analysis also extends the measurements of the BEC correlations to the full minimum bias sample from pp collisions at 2.76 TeV collected in 2013, which is a very important baseline for the measurements of this second order interferometry in PbPb collisions at the same energy per nucleon. In 1-D are the results from both energies are compared with the ones in Ref. [3, 4] at lower energies, as well as at $\sqrt{s} = 7$ TeV, recorded during the commissioning run at the LHC in 2010. In particular, comparisons showed that $R_{\rm inv}$ steadly increases with the charged multiplicity proportionally to $N_{ch}^{1/3}$.

The measurements were performed both in the collision center-of-mass (CM) frame and in the Local Co-Moving System (LCMS), where the average longitudinal momentum of the pair is zero. In the 2-D case, for integrated values of N_{ch} and k_T, the lengths of homogeneity in the LCMS suggest that the source is elongated along the beam direction, i.e., $R_L^* > R_T$. In the 3-D case, it was found that $R_L^* > R_S > R_O$. In addition, it can be observed that the fit values for the longitudinal radius parameter, R_L are consistent in 2-D and in 3-D cases, as should be expected, since they correspond to the length of homogeneity in the longitudinal direction in both cases. This conclusion is attained with respect to the R_L fit parameter in the CM frame, as well as R_L^* in the LCMS [15].

The anticorrelation observed in 1-D and reported in Ref. [4], was also observed in minimum bias pp collisions at 2.76 TeV and further investigated here with the full statistics at 7 TeV. These new 1-D results are also compared with those in Ref. [4], verifying a consistent behavior both for the invariant radius parameter and for the dip's depth measurements at 2.76 and 7 TeV. Such comparisons showed that the dip's depth decreases with increasing N_{ch}.

References

[1] G. Goldhaber *et al.*, Phys. Rev. **120**, 300 (1960).

[2] R. Hanbury Brown and R. Q. Twiss, Phil. Magazine **45**, 663 (1954); Nature **27**, 177 (1956); Nature **178**, 1046 (1956).

[3] V. Khachatryan et al. (CMS Collaboration), Phys. Rev. Lett. **105**, 032001 (2010).

[4] V. Khachatryan et al. (CMS Collaboration) JHEP**05**, 029 (2011).

[5] P. Achard et al. (L3 Collaboration), Eur. Phys. J. **C71**, 1648 (2011).

[6] T. Csörgő and J. Zimányi, Nucl. Phys. **A517**, 588 (1990).

[7] T. Åkesson et al. (AFS Collaboration), Phys. Lett. **B129**, 269 (1983).

[8] T. Åkesson et al. (AFS Collaboration), Phys. Lett. **B155**, 128 (1985).

[9] T. Alexopoulos et al. (E735 Collaboration), Phys. Rev. **D48**, 1931 (1993).

[10] J. Adams et al. (STAR Collaboration), Phys. Rev. **C71**, 044906 (2005).

[11] B. B. Back et al. (PHOBOS Collaboration), Phys. Rev. **C73**, 031901(R) (2006).

[12] S. Afanasiev et al. (PHENIX Collaboration), Phys. Rev. Lett. **100**, 232301 (2008).

[13] K. Aamodt et al. (ALICE Collaboration), Phys. Rev. **D82**, 052001 (2010).

[14] S. Chatrchyan et al. (CMS Collaboration), JINST **3**, S08004 (2008).

[15] CMS Collaboration, "Multidimensional analysis of Bose-Einstein correlations in pp collisions at 2.76 and 7 TeV", CMS PAS FSQ-13-002 (2014) (https://twiki.cern.ch/twiki/bin/view/CMSPublic/PhysicsResultsFSQ13002).

[16] T. Sjöstrand, S. Mrenna and P.Z. Skands, JHEP 05 (2006) 026.

[17] R. Field, "Early LHC Underlying Event Data - Findings and Surprises", arXiv:1010.3558.

[18] M. Gyulassy, S. K. Kaufmann, and L. W. Wilson, Phys. Rev. **C20**, 2267 (1979).

[19] S. Pratt, Phys. Rev. Lett. **53**, 1219 (1984).

[20] Y. Hama and Sandra S. Padula, Phys. Rev. **D37**, 3237 (1988).

[21] G. F. Bertsch, Nucl. Phys. **A498**, c173 (1989).

[22] M. A. Lisa et al., Annu. Rev. Nucl. Part. Sci. **55**, 357 (2005).

[23] T. Csörgő, S. Hegyi, W. A. Zajc, Eur. Phys. J. **C36**, 67 (2004).

v_2 of charged hadrons in a 'soft + hard' model for PbPb collisions at $\sqrt{s} = 2.76$ ATeV

K. Urmossy [1], T. S. Biró [1], G. G. Barnaföldi [1] and Z. Xu [2],

[1] Wigner Research Center for Physics of the HAS,
29–33 Konkoly–Thege Miklós Str.
H-1121 Budapest, Hungary
[2] Physics Department, Brookhaven National Laboratory,
Upton, NY 11973, USA

Abstract

We describe transverse spectra *as well as* azimuthal anisotropy (v_2) of charged hadrons stemming from various centrality PbPb collisions at $\sqrt{s} =$ 2.76 ATeV *analytically* in a 'soft + hard' model. In this model, we propose that hadron yields produced in heavy-ion collisions are simply the sum of yields stemming from jets (hard yields) and yields stemming from the Quark-Gluon Plasma (soft yields). The hadron spectra in both types of yields are approximated by the Tsallis distribution. It is found that the anisotropy decreases for more central collisions.

1 Introduction

Because of its short lifetime, the only way to examine the Quark-Gluon Plasma (QGP) formed in ultra-relativistic heavy-ion collisions (HIC), is looking at the particles stemming from it. Spectra, angular correlations and their dependence on the circumstances of the collision can then be studied. These distributions are effected by hadron yields stemming not only from the QGP (we refer to as 'soft' yields), but also from jets (we call 'hard' yields).

As a first approximation, we make out hadron spectra in HICs as

$$p^0 \frac{dN}{d^3\mathbf{p}} = p^0 \frac{dN}{d^3\mathbf{p}}^{\text{hard}} + p^0 \frac{dN}{d^3\mathbf{p}}^{\text{soft}} , \tag{1}$$

where we describe both types of yields by a Tsallis distribution with different parameters for the following reasons.

Hard yields: On the experimental side, the Tsallis distribution describes measured transverse spectra of charged and identified hadrons in proton-proton collisions [1]–[14]. On the theoretical side, the Tsallis distribution provides a reasonably good approximation for the transverse spectra of charged pions stemming from pp collisions [13, 14], and central as well as peripheral PbPb collisions obtained via perturbative quantum chromodynamics (pQCD) improved parton model calculations for transverse momenta $p_T \gtrsim$ 4–6 GeV/c [18].

Soft yields: The Tsallis distribution has been widely used for the description of hadron yields stemming from the QGP [19]–[32]. However, in those models, the hard part of the spectrum has not been subtracted. For the emergence of the Tsallis distribution in the soft part of the spectrum, there is a chance to bring statistical arguments based on non-extensive thermodynamics [30, 33], or on super-statistics [7, 20, 21, 22, 29, 32, 39, 40].
We note that transverse spectra and v_2 of various identified hadrons measured at RHIC energy have been described by a similar model [23, 24, 25]. In that model, spectra measured in pp collisions have been used as hard yields, and it has been conjectured that hard yields are suppressed at low p_T.

In Sec. 2, analytic formulas are decuced for the hadron spectrum and v_2. Sec. 3 contains fits to charged hadron spectra and v_2 measured in various centrality PbPb collisions at $\sqrt{s} = 2.76$ ATeV by the CMS [41, 42] and the ALICE [43] collaborations. Summary is given in Sec. 4.

2 Transverse Spectrum and v_n

In statistical models, we obtain the transverse spectrum as a sum of hadrons with momentum p^μ, coming from sources flying with velocities u^μ as

$$p^0 \frac{dN}{d^3p}\bigg|_{y=0} = \int_{-\infty}^{+\infty} d\zeta \int_0^{2\pi} d\alpha \, f\left[u_\mu p^\mu\right] . \tag{2}$$

Here, α is the azimuth angle and $\zeta = \frac{1}{2}\ln[(t+z)/(t-z)]$. We parametrize hadron momenta as

$$p^\mu = (m_T \cosh y, m_T \sinh y, p_T \cos\varphi, p_T \sin\varphi) , \tag{3}$$

with $y = \frac{1}{2}\ln[(p^0+p^z)/(p^0-p^z)]$ and φ being the azimuth angle of the hadron momentum. We parametrize the flow as

$$u^\mu = (\gamma\cosh\zeta, \gamma\sinh\zeta, \gamma v\cos\alpha, \gamma v\sin\alpha) , \tag{4}$$

with $\gamma = 1/\sqrt{1-v^2}$, and assume that v depends only on α. Though, it is assumed that in each source, the momentum distribution of hadrons f is a function of the co-moving energy

$$u_\mu p^\mu|_{y=0} = \gamma\big[m_T \cosh\zeta - v p_T \cos(\varphi - \alpha)\big] \ , \tag{5}$$

the sources may be fireballs [34]–[36], clusters [8, 9, 12, 37, 38] or even jets [39, 40].

We write the transverse flow as a series,

$$v(\alpha) = v_0 + \sum_{m=1}^{\infty} \delta v_m \cos(m\alpha) \equiv v_0 + \delta v(\alpha) \ , \tag{6}$$

and suppose that $\delta v(\alpha) << 1$. We use the Taylor expansion

$$f\big[u_\mu p^\mu\big]\big|_{y=0} = \sum_{m=0}^{\infty} \frac{[\delta v(\alpha)]^m}{m!} \frac{\partial^m}{\partial v_0^m} \ f\big[u_\mu p^\mu\big]\big|_{\,y\,=\,0}^{\,v(\alpha)\,=\,v_0} \ , \tag{7}$$

and keep only the leading non-vanishing terms in $\delta v(\alpha)$.

Provided that f is a rapidly decreasing function, we approximate integrals with respect to ζ and φ by the maximal value of the integrands times the integration interval. Thus, the φ integrated transverse spectrum becomes

$$\begin{aligned} \frac{dN}{2\pi p_T dp_T dy}\bigg|_{\,y\,=\,0} \ &= \ \int_0^{2\pi} \frac{d\varphi}{2\pi} \ p^0 \ \frac{dN}{d^3p}\bigg|_{\,y\,=\,0} \ = \ \sum_{m=0}^{\infty} \frac{a_m}{m!} \frac{\partial^m}{\partial v_0^m} f\big[E(v_0)\big] \ \approx \\ &\approx \ f\big[E(v_0)\big] \ + \ \mathcal{O}\left(\delta v^2\right) \ , \end{aligned} \tag{8}$$

with $E(v_0) = \gamma_0(m_T - v_0 p_T)$ and $a_m = \int\limits_0^{2\pi} d\alpha \ [\delta v(\alpha)]^m$. Similarly, the azimuthal anisotropy becomes

$$v_n = \frac{\int\limits_0^{2\pi} d\varphi \cos(n\varphi) \ p^0 \ \dfrac{dN}{d^3p}\bigg|_{y=0}}{\int\limits_0^{2\pi} d\varphi \ p^0 \ \dfrac{dN}{d^3p}\bigg|_{y=0}} \approx \frac{\delta v_n \gamma_0^3}{2} \frac{(v_0\, m_T - p_T) f'\big[E(v_0)\big]}{f\big[E(v_0)\big]} + \mathcal{O}\left(\delta v^2\right) \tag{9}$$

with δv_n defined in Eq. (6).

For example, in the case of the Boltzmann-distribution $f \sim \exp\big[-\beta E(v_0)\big]$, the anisotropy is

$$v_n^{\rm BG} \approx \frac{\delta v_n \, \beta \, \gamma_0^3}{2} (p_T - v_0 \, m_T) \ + \ \mathcal{O}\left(\delta v^2\right) \ . \tag{10}$$

Thus, $v_n^{\rm BG} \propto p_T$ if $p_T >> m$.

In the case of the Tsallis distribution, $f \sim [1 + (q-1)\,\beta\, E(v_0)]^{-1/(q-1)}$, the anisotropy

$$v_n^{\rm TS} \approx \frac{\delta v_n \, \beta \, \gamma_0^3}{2} \frac{p_T - v_0 \, m_T}{1 + (q-1)\,\beta\,\gamma_0 (m_T - v_0\, p_T)} \ + \ \mathcal{O}\left(\delta v^2\right) \ . \tag{11}$$

Thus, $v_n^{\rm TS}$ saturates when $(q-1)\,\beta\,\gamma_0(1-v_0)p_T >> 1$.

3 Fits to the spectrum and v_2 of charged hadrons in PbPb collisions at $\sqrt{s_{NN}} = 2.76$ ATeV

As conjectured in Sec. 1, we make out the transverse spectrum of charged hadrons by the sum of hard and soft yields

$$\left.\frac{dN}{2\pi p_T dp_T dy}\right|_{y=0} = \sum_i A_i \left[1 + \frac{(q_i-1)}{T_i}[\gamma_i(m_T - v_i p_T) - m]\right]^{-1/(q_i-1)} , \quad (12)$$

(i = soft or hard) where both contributions are assumed to be Tsallis-distributions. These yields have maxima at $p_{T,\,i}^{max} = \gamma_i\, m\, v_i$. As long as these maxima are below the measurement range, which is the case in this analysis, the isotropic part of the transverse flow, v_i (denoted by v_0 in Eq. (6) in Sec. 2) cannot be determined accurately. As the dominant part of charged hadrons consists of pions, the argument in Eqs. (12) may be approximated by $[\gamma_i(m_T - v_i p_T) - m]/T_i \approx p_T/T_i^{Dopp}$ with the Doppler-shifted parameters

$$T_i^{Dopp} = T_i \sqrt{\frac{1+v_i}{1-v_i}} . \quad (13)$$

As can be seen in the top panels of Fig. 1, Eq. (12) describes CMS [41] and ALICE [43] data on transverse spectra of charged hadrons stemming from PbPb collisions of various centralities. Fitted parameters are enlisted in [18] and shown in the bottom panels of Fig. 1. The dependence of the q and T^{Dopp} parameters of the soft and hard yields on the event centrality (number of participating nucleons N_{part}) can be fitted by

$$\begin{aligned} q_i &= q_{2,\,i} + \mu_i \ln(N_{part}/2) , \\ T_i^{Dopp} &= T_{1,\,i} + \tau_i \ln(N_{part}) . \end{aligned} \quad (14)$$

Though the actual value of the transverse flow velocity cannot be determined in this model from the spectra of charged hadrons, it may be guessed using the value of the QGP-hadronic matter transition temperature obtained from lattice-QCD calculations. As the values of fitted T_{soft}^{Dopp} scatter around 340 MeV, in case of a flow velocity of $v_{soft} \approx 0.6$, the real T_{soft} values would scatter around 170 MeV, which is close to the lattice result obtained e.g. in [44].

While the tendencies of how fit parameters depend on N_{part} are similar, they are not the same within errors in the case of CMS [41] and ALICE [43] measurements. It is to be noted that in [43], centrality is determined using the distribution of hits in the VZERO detector, which has a rapidity coverage of $2.8 \leq \eta \leq 5.1$ and $-3.7 \leq \eta \leq -1.7$. In the meanwhile, in [41, 42], the collision event centrality is determined from the event-by-event total energy deposition in both Hadron Forward calorimeters having rapidity coverage of $2.9 \leq |\eta| \leq 5.2$.

As seen from Sec. 2, up to $\mathcal{O}\left(\delta v^2\right)$, the transverse spectrum in Eq. (12) results in an azimuthal anisotropy of

$$v_2 = \frac{w_{hard}\, f_{hard} + w_{soft}\, f_{soft}}{f_{hard} + f_{soft}} , \quad (15)$$

where the coefficient functions are

$$w_i = \frac{\delta v_i\, \gamma_i^3}{2T_i} \frac{p_T - v_i\, m_T}{1 + \dfrac{q_i - 1}{T_i}\left[\gamma_i(m_T - v_i\, p_T) - m\right]} . \quad (16)$$

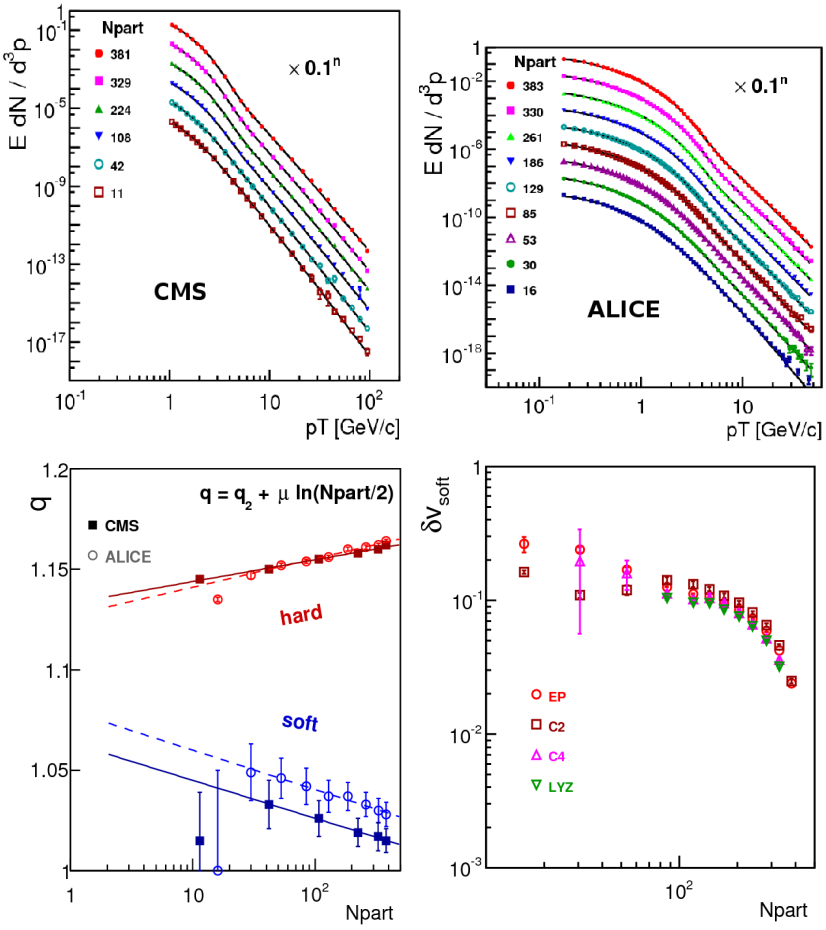

Figure 1: **Top,** transverse spectra of charged hadrons stemming from various centrality PbPb collisions at $\sqrt{s} = 2.76$ ATeV measured by the CMS [41] (**left**) and ALICE [43] (**right**) Collaborations. Curves are fits of Eq. (12). **Bottom,** centrality dependence of the fitted q (**left**) and δv_{soft} (**right**) parameters. Straight lines are in Eq. (14) with parameters enlisted in [18].

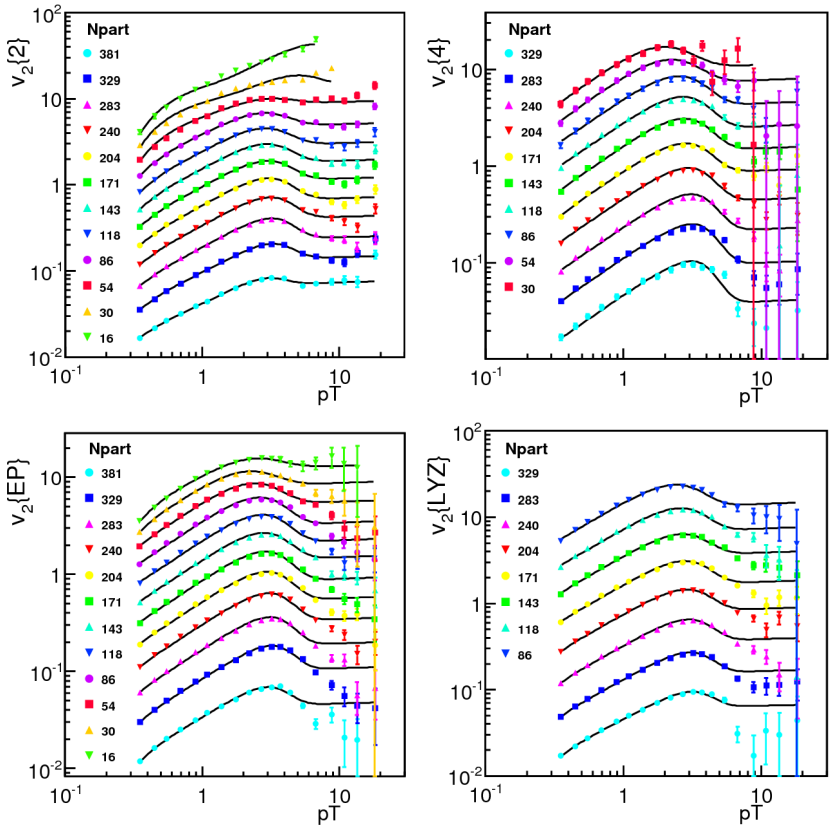

Figure 2: Fits of Eqs. (15) – (16) to CMS data on v_2 [42] in the case of four types of methods (event plane $v_2\{EP\}$, 2^{nd} and 4^{th} order cumulant $v_2\{2\}$ and $v_2\{4\}$ and Lee-Yang zeros $v_2\{LYZ\}$ methods). Fit parameters are plotted and enlisted in [18].

Again, $i =$ soft or hard, v_i are the isotropic part of the transverse flow (denoted by v_0 in Eq. (6) in Sec. 2). And δv_i are the coefficients of $\cos(2\alpha)$ (denoted by δv_2 in Eq. (6) in Sec. 2).

Fits of Eqs. (15) – (16) to CMS data [42] on v_2 are found in Fig. 2. The four different methods used in [42] for the extraction of v_2 are the 2^{nd} and 4^{th} order cumulant methods denoted by $v_2\{2\}$ and $v_2\{4\}$, the event-plane $v_2\{EP\}$ and Lee–Yang zeros $v_2\{LYZ\}$ methods. Fitted parameters are listed in [18].

Finally, all four methods for the extraction of v_2 in [42] suggest that δv_{soft} (the 2^{nd} Fourier components of the transverse flow of the soft yields) decreases for more central collisions (see bottom-right panel of Fig. 1). This observation is in accordance with smaller anisotropy in more central collisions.

4 Summary

In this paper, we have *simultanously* reproduced the transverse spectra *and* the azimuthal anisotropy (v_2) of charged hadrons stemming from various centrality PbPb collisions at $\sqrt{s} = 2.76$ ATeV. In the proposed model, the hadron spectrum is assumed to be simply the sum of yields originated from 'soft' and 'hard' processes, Eq. (1). It is conjectured that hadrons are distributed according to the Tsallis distribution in both types of yields. As for the hard yields, this assumption is supported by the observation that the Tsallis distribution provides a reasonably good approximation for pion spectra obtained via pQCD-improved parton model calculations for central or peripheral PbPb collisions at LHC energy [18]. Furthermore, the Tsallis distribution describes hadron spectra in pp collisions as well. The soft yields (which we identified by what remains of the hadron spectra after the subtraction of the hard yields) can also be described by a Tsallis distribution with different parameters.

Analytic formulas have been obtained for the spectra and for v_2 in the limit of small transverse flow velocity fluctuations as a function of the azimuth angle. The parameters of the soft and hard Tsallis distributions have been determined from fits to transverse spectra and v_2 data measured by the CMS [41, 42] and ALICE [43] collaborations. The dependence of the fitted parameters on the event centrality (N_{part}) have been found similar in the case of the CMS and ALICE data. Fits to CMS data on v_2 suggest that in this model, the anisotropy decreases for more central collisions. Fit parameters are enlisted in [18].

Acknowledgement

This work was supported by Hungarian OTKA grants K104260, NK106119, and NIH TET 12 CN-1-2012-0016. Author GGB also thanks the János Bolyai Research Scholarship of the Hungarian Academy of Sciences.

References

[1] The PHENIX Collab., Phys. Rev. D, 83, 052004 (2011)

[2] Cheuk-Yin Wong, G. Wilk, *Acta Physica Polonica B*, **42**, 2047, (2012)

[3] J. Cleymans, Proc. of: 1^{st} *International Conference on New Frontiers in Physics ICFP*, (2012)

[4] J. Cleymans, D. Worku, *J. Phys. G: Nucl. Part. Phys.*, **39**, 025006, (2012)

[5] J. Cleymans, D. Worku, *Eur. Phys. J. A*, **48**, 11, 160, (2012)

[6] G. G. Barnaföldi et al., *J. Phys. Conf. Ser.*, **270**, 012008, (2011)

[7] K. Urmossy, arXiv:1212.0260

[8] T. Wibig, I. Kurp, *JHEP*, **0312**, 039, (2003);

[9] T. Wibig, *J. Phys. G: Nucl. Part. Phys.*, **37**, 115009, (2010)

[10] Khandai, *Int. J. Mod. Phys. A*, **28** (2013) 1350066,

[11] M. Praszalowicz, *Physics Letters B*, **727**, (2013) 461

[12] T. Wibig, *Eur. Phys. J. C*, **74**, (2014), 2966

[13] Cheuk-Yin Wong, Grzegorz Wilk, Conference: C13-05-30, (2013)

[14] Cheuk-Yin Wong, Grzegorz Wilk, *Phys. Rev. D*, **87**, 114007 (2013)

[15] G. G. Barnaföldi, G. Kalmár, K. Urmossy et.al, *Gribov 80 - Memorial Volume*, (ISBN: 978-981-4350-18-1), p. 357., World Scientific, Singapore, (2011)

[16] Y. Zhang et.al., *Phys. Rev. C*, **65**, 034903 (2002).

[17] G. G. Barnafoldi, J. Barrette, M. Gyulassy et.al., *Phys. Rev. C*, **85**, 024903 (2012)

[18] K. Urmossy, G. G. Barnaföldi, T. S. Biró, Z. Xu, arXiv:1405.3963, (2014)

[19] M. Rybczynski, Z. Wlodarczyk, G. Wilk, *J. Phys. G: Nucl. Part. Phys.*, **39**, 095004, (2012)

[20] G. Wilk, Z. Wlodarczyk, *Eur. Phys. J. A*, **48**, (2012) 161

[21] G. Wilk, Z. Wlodarczyk, *Cent. Eur. J. Phys.*, **10**, Issue 3, pp.568-575, (2011)

[22] G. Wilk, Z. Wlodarczyk, *J. Phys. G*, **38**, 065101, (2011)

[23] Z. Tang, L. Yi, L. Ruan, et al., arXiv:1101.1912, (2011)

[24] Z. Tang, Y. Xu, L. Ruan et.al., *Phys. Rev. C:* **79**, 051901 (R), (2009)

[25] M. Shao, L. Yi, Z. Tang, et al., *J. Phys. G:* **37**, 085104, (2010)

[26] D. D. Chinellato, J. Takahashi, I. Bediaga, *J. Phys. G:* **37**, 094042, (2010)

[27] K. Urmossy, T. S. Biro, *Phys. Lett. B:* **689**, 14-17, (2010)

[28] B. De, G. Sau, S. K. Biswas et.al., *J. Mod. Phys. A:* **25**, 1239-1251, (2010)

[29] G. Wilk, Z. Wlodarczyk, *Eur. Phys. J. A*, **40**, 299-312, (2009)

[30] T. S. Biro (ed.) *et al.*, *Eur. Phys. J. A*: **40** 255-344, (2009)

[31] J. Cleymans, G. Hamar, P. Levai et.al., *J. Phys. G:* **36**, 064 018, (2009)

[32] M. Biyajima, T. Mizoguchi, N. Nakajima et.al., *Eur. Phys. J. C:* **48**, 597-603, (2006)

[33] T. S. Biro, A. Jakovac, *Phys. Rev. Lett.*, **94** (2005) 132302

[34] R. Hagedorn, *Suppl. Nuovo Cim.*, **3**, 147, (1965);

[35] M. Szczekowski, G. Wilk, *Phys. Lett. B*, **374**, 225, (1996)

[36] K. Redlich, A. Andronic, F. Beutler et.al., *J. Phys. G*, **36**, 064021, (2009)

[37] F. Becattini, G. Passaleva, *Eur. Phys. J. C*, **23**, 551-583, (2002)

[38] F. M. Liu, K. Werner, J. Aichelin et.al., *J. Phys. G*, **30**, 589-594, (2004)

[39] K. Urmossy, G. G. Barnaföldi, T. S. Biró, *Phys. Lett. B*, **718**, 125-129, (2012),

[40] K. Urmossy, G. G. Barnaföldi, T. S. Biró, *Phys. Lett. B*, **701**, 111-116, (2011),

[41] CMS Collaboration, *Eur. Phys. J. C*, **72** 1945 (2012)

[42] CMS Collaboration, *Phys. Rev. C*, **87** 014902 (2013)

[43] The ALICE Collab., Phys. Lett. B, 720 (2013) 52-62

[44] S. Borsanyi, Z. Fodor, C. Hoelbling et.al., *Phys. Lett. B*, **370**, (2014) 99-104

Study of in-medium mass modification at J-PARC

K. Aoki[1] for the J-PARC E16 Collaboration

[1]KEK, High Energy Accelerator Research Organization,
Tsukuba, Ibaraki 305-0801, Japan

Abstract

Study of in-medium mass modification has attracted interest in terms of the restoration of the spontaneously broken chiral symmetry, which is responsible for the generation of hadron mass. Many experiments were performed to measure in-medium property of hadrons but there is no consensus yet. J-PARC E16 has been proposed to study in-medium property of vector mesons via dilepton decay channel. The status of spectrometer R & D is explained. Other related experiments planned at J-PARC are also introduced.

1 Introduction

Spontaneous breaking of the chiral symmetry is considered to be the origin of hadron mass. The chiral symmetry is expected to be (partially) restored in finite density and the hadron mass is predicted to decrease, even at the normal nuclear density. Our purpose is to investigate the origin of hadoron mass through mass modification of hadrons.

The dilepton decay channel of vector mesons produced in nuclear reactions is a good probe of in-medium mass modification since it is free from the final state interactions. We take $p + A \rightarrow \phi + X$ reaction as an example to explain the expected invariant mass distribution of the vector meson. A ϕ meson produced inside a target nucleus travels and then decays inside or outside the target nucleus. When the ϕ meson decays outside the target nucleus, the mass spectrum is well-known invariant mass in vacuum as in Fig. 1(a). When the ϕ meson decays inside the target nucleus, the observed mass is the one in medium. So if in-medium mass

modification exists, the mass distribution is modified to some extent as in Fig. 1(b). What we experimentally measure is the sum of these cases as in Fig. 1(c).

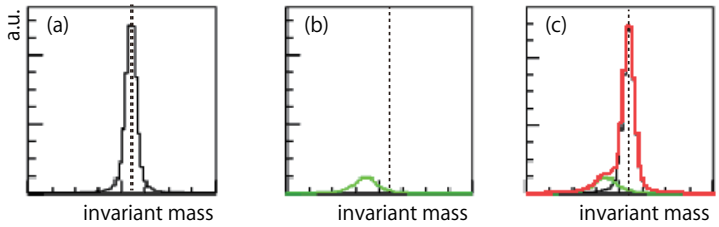

Figure 1: Invariant mass spectra of ϕ meson (a) in vacuum , and (b) in medium. (c) is the sum of (a)+(b). The dashed line indicates the ϕ meson mass in vacuum.

The KEK E325 experiment was performed at KEK Proton Synchrotron to search for in-medium mass modification using the method explained above. They measured the invariant mass spectra of e^+e^- pairs produced in 12 GeV proton beam induced nuclear reactions. As the nuclear targets, C and Cu were used. The mass resolution was about 11 MeV/c^2. Figure 2 shows the invariant mass spectrum of ϕ meson produced in Cu target with $\beta\gamma(= P/M) < 1.25$ [1]. The blue line represents an expected line shape assuming mass in vacuum including experimental effects. There is an excess on the lower side of the ϕ mass peak over the expected line shape. Figure 3 shows the amount of excess versus $\beta\gamma$ of ϕ mesons. This figure support the picture that slower ϕ meson in larger nuclear target have higher probability to decay inside the nuclear target so that it experience medium modification. To quantitatively extract information on the medium effect, they assume linear dependence of the mass on density as,

$$\frac{m(\rho)}{m(0)} = 1 - k\frac{\rho}{\rho_0}, \tag{1}$$

where $m(\rho)$ is the mass at density ρ, ρ_0 is the normal nuclear density, and k is the parameter to be determined. Similarly for the width, they assume

$$\frac{\Gamma(\rho)}{\Gamma(0)} = 1 + k_2\frac{\rho}{\rho_0}, \tag{2}$$

where $\Gamma(\rho)$ is the width at density ρ, and k_2 is the parameter to be determined. They obtained $k = 0.034^{+0.006}_{-0.007}$ and $k_2 = 2.6^{+1.8}_{-1.2}$, which means that the mass of ϕ decreases by 3.4% and the width gets wider by 3.6 times at the normal nuclear density. They also observed modification of ρ and ω mass and concluded that $k = 0.092 \pm 0.002$, assuming that the parameter is common for ρ and ω [2]. Width broadening was not necessary to reproduce the observed invariant mass. The mass shift parameters k for ρ/ω, and ϕ are at the same level as the calculations based on QCD sum rule [3]

The CLAS g7 experiment at Jefferson Laboratory used $\gamma + A$ reactions and the light vector mesons were reconstructed using e^+e^- decay channel [4]. The results obtained with ^{2}H, C, Fe, Ti targets were presented. For ω and ϕ meson, no mass shift was assumed in the analysis due to their long life. The ω and ϕ contributions were subtracted to extract the invariant mass spectra of ρ meson. The mass of ρ

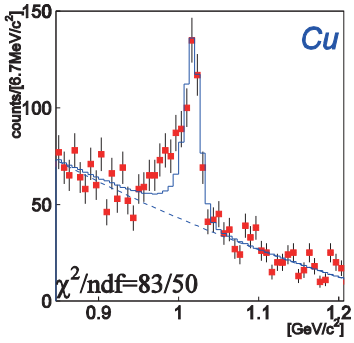

Figure 2: Invariant mass spectrum of ϕ meson obtained with p+Cu reactions by KEK E325 experiment. $\beta\gamma$ of ϕ is < 1.25.

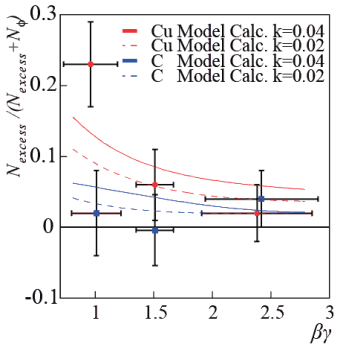

Figure 3: Amount of excess versus $\beta\gamma$ of ϕ measured by KEK E325 experiment.

meson in nuclear medium does not show any mass shift. The width are broadened and it is consistent with an expectation from collisional broadening.

Dilepton invariant mass spectra were also measured in heavy ion collisions. CERES /NA45 reported e^+e^- invariant mass measured in 158 AGeV Pb+Au collisions [5]. An in-medium broadening of the ρ mass scenario is favored over a ρ mass dropping scenario. PHENIX also reported invariant mass spectra of e^+e^- in Au+Au collisions at $\sqrt{s} = 200$A GeV [6]. An enhancement is observed in the low mass region (below ϕ peak). The enhancement at quite low mass ($m_{ee} < 0.3$ GeV/c^2) and high p_T ($1 < p_T < 5$ GeV/c) is interpreted as the production of virtual direct photons, which leads to their temperature measurement. No theoretical models could explain quantitatively the enhancement at the low mass and low p_T region.

2 J-PARC E16 Experiment

There exists some modification in e^+e^- mass spectrum but the origin is not yet clear. There are even contradiction in the interpretation. We propose to pursue this problem using the same reaction as KEK-E325 but with 100 times more statistics (10^3 $\phi \rightarrow 10^5$ ϕ) and with two times better mass resolution (11 MeV/c^2 $\rightarrow$ 5 MeV/c^2). The proposal was approved as stage-1 and the experiment was named E16 [7]. We use 30 GeV $p + A \rightarrow \rho/\omega/\phi\ X$ reactions and measure dilepton invariant mass spectra. As the nuclear target, CH_2, C, Cu, Pb are used. The J-PARC E16 experiment has the following advantages and disadvantages compared to other experiments. It observes e^+e^- decay channel so it can eliminate final state interactions in contrast to the case of experiments using hadronic decay channels. However, e^+e^- decay channel has very tiny branching ratio ($\sim 3 \times 10^{-4}$ for ϕ meson). The E16 experiment uses proton induced reactions, therefore, the system is cold and static so is simpler compared to that of heavy ion collisions. The E16 experiment is expected to measure ϕ meson invariant mass modification. Compared to ρ and ω mesons, ϕ meson has a non-overlapping separated peak and a narrower width. However, the production cross section of ϕ meson is much smaller than that

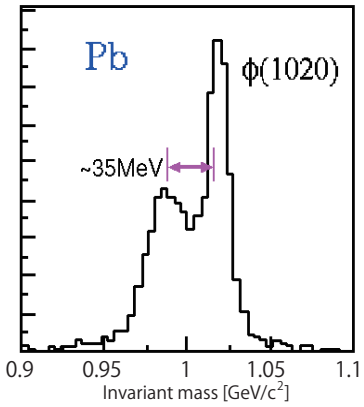

Figure 4: Invariant mass distribution of ϕ meson with $\beta\gamma < 0.5$ expected to be observed by J-PARC E16 experiment using Pb target.

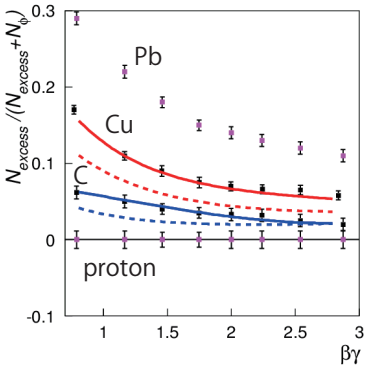

Figure 5: Amount of excess versus $\beta\gamma$ of ϕ expected to be obtained by J-PARC E16 experiment.

of ρ and ω, thus it is difficult to collect high statistics and CLAS-g7 and CERES cannot discuss the mass spectra of ϕ. The disadvantages, mainly come from the fact that $\phi \to e^+e^-$ is a rare probe, are overcome by collecting high statistics data.

When the statistics is achieved, the invariant mass distribution of slowly moving ϕ meson whose $\beta\gamma$ is less than 0.5 which is obtained with Pb target is expected to have double peak as in Fig. 4. Note that the modification parameters obtained by KEK-E325 are assumed. The $\beta\gamma$ and the target size dependence of the modification expected to be obtained is in Fig. 5. So more systematic study is possible. We are able to obtain dispersion relation as the blue points in Fig. 6, which is qualitatively new information. These new information can give further insight on the in-medium modification.

2.1 J-PARC and the high momentum beam line

To achieve 100 times more statistics, We utilize 10 times more intense beam (10^9 protons per pulse (ppp) $\to 10^{10}$ ppp), a spectrometer with 5 times larger acceptance, and 2 times larger production rate due to the increased beam energy (12 GeV $\to$ 30 GeV).

The J-PARC E16 experiment plans to use the high momentum beam line which will be constructed at J-PARC Hadron Experimental Facility. J-PARC, Japan Proton Accelerator Research Complex, is a high intensity proton accelerator and is located at Tokai village in Japan. The Main Ring (MR) of J-PARC can accelerate protons up to 30 GeV. Figure 7 shows the plan view of the switchyard and the Hadron Experimental Facility. The protons in the MR are slowly extracted to LINE-A. The proton beam follows LINE-A through the switchyard and is delivered to the Hadron Experimental Facility. The protons collide the T1 target to provide secondary beams to the existing beam lines such as K1.8, K1.8BR, and KL. The beam power was 24 kW as of 2013, which corresponds to 3×10^{13} ppp. To make primary proton beam available to E16 experiment, the high momentum beam line which is called

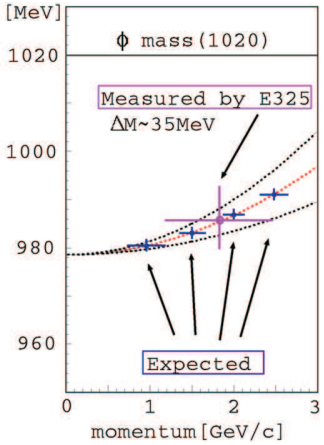

Figure 6: Dispersion relation. The red dotted curve shows a theory calculation by S.H. Lee [8]. Note that the calculation is limited for momentum of less than 1 GeV/c and is extrapolated to 3 GeV/c. Black dotted curve shows the uncertainty of the calculation. Blue points shows the statistical uncertainties expected to be obtained by the J-PARC E16 experiment. The center values are taken from the theoretical calculation mentioned above. Purple point is the results obtained by KEK E325 experiment.

LINE-B is being constructed. LINE-B borrows a small piece of the beam ($\sim 10^{-4}$) in LINE-A with a Lambertson-type magnet at the switchyard. The beam is extracted to the south side of the Hadron Experimental Facility where E16 spectrometer is to be built.

2.2 E16 spectrometer

A 3D view of the J-PARC E16 spectrometer is shown on the left side of Fig. 8. The E16 detectors are all installed inside a giant dipole magnet with a field strength of 1.7 T at the center. A horizontal cut view at the center is presented on the right side of Fig. 8. The proton beam runs from bottom to the top of the figure, and hit the target at the center of the spectrometer. The spectrometer consists of GEM Trackers (GTR) [9], Hadron Blind Detectors (HBD) [11], and lead glass (LG) calorimeters.

A module is defined as a set of GTR, HBD and LG which covers 30 degrees both horizontally and vertically. The full design of the spectrometer consists of 26 modules. GTR is made of three layers of position-sensitive GEM tracking chambers with the sizes of 100 $\times$ 100 mm^2, 200 $\times$ 200 mm^2 and 300 $\times$ 300 mm^2, respectively. HBD is a cherenkov counter and is used for electron identification together with LG. Particle tracks in the magnetic field are reconstructed with GTR so that the momenta are measured. Electron candidates are selected with HBD and LG. Position resolution of 100 μm with incident angles of up to 30 degrees is required for GTR. Rejection factors of 100 and 25 are required for HBD and LG, respectively.

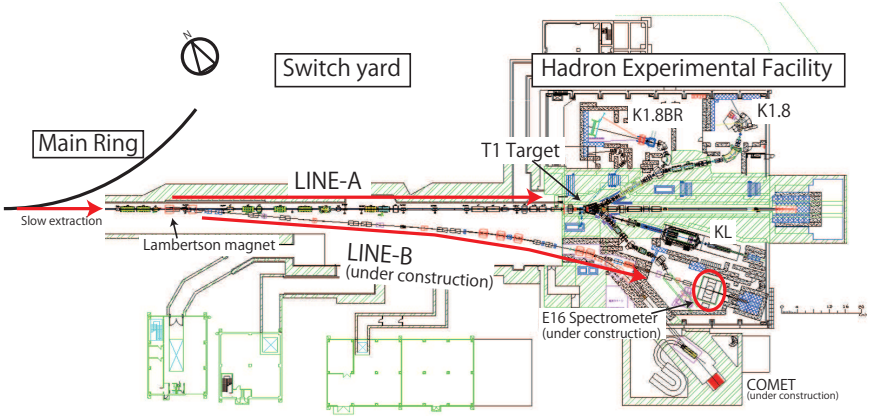

Figure 7: Plan view of the switchyard and the Hadron Experimental Facility.

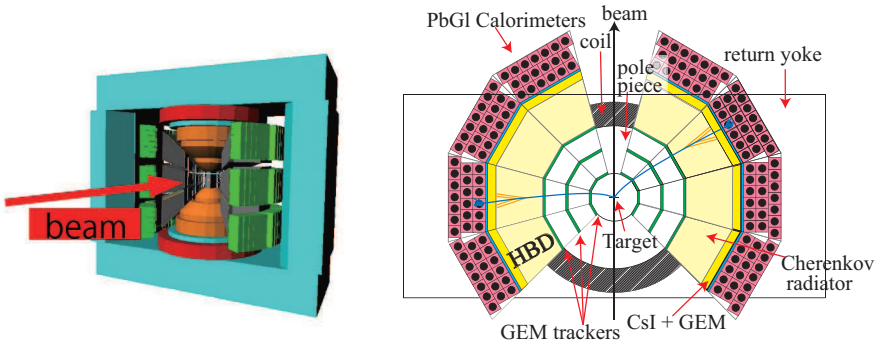

Figure 8: 3D view (Left) and plan view (Right) of the E16 spectrometer.

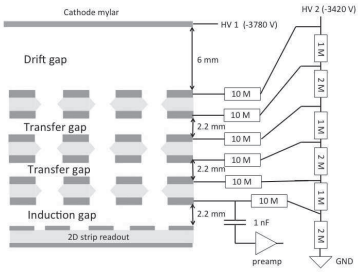

Figure 9: Schematic of a GEM tracking chamber.

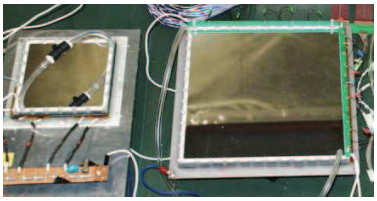

Figure 10: Picture of the production type of the GEM tracking chambers. The sizes are 100 × 100 mm^2 and 200 × 200 mm^2, respectively.

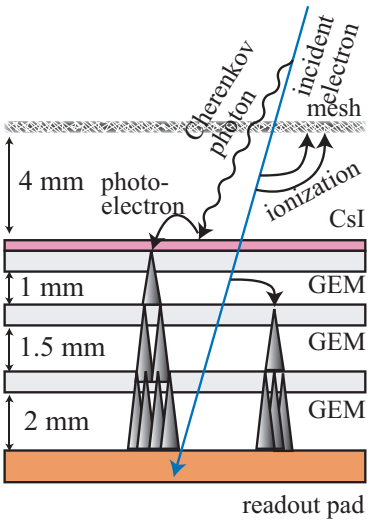

Figure 11: Schematic of the photocathode of HBD.

Figure 12: Picture of a prototype of HBD in real size.

2.3 R & D status of the spectrometer

A schematic of a GEM tracking chamber is shown in Fig. 9. Ar + CO2 (70:30) is used as the amplification gas. Three GEM foils are placed and they amplify the ionization electrons produced by a traversing charged particle in the gap above the top GEM. The amplified signal is readout with two dimensional strip readout board. A custom preamp board using APV25 chip [10] has been developed. The mass production type of GEM tracking chambers with three different sizes and preamp boards have been built. The performance of them was evaluated with charged particle beams at J-PARC and ELPH. The required resolution of 100 μm was achieved for incident angles of up to 30 degrees. A picture of the GEM chambers with two sizes are shown in Fig. 10. First level trigger is readout from the bottom of the GEM foil. A prototype of ASD (Amplifier-Shaper-Discriminator) ASIC for the trigger readout has also been developed.

HBD is a type of cherenkov detector using CsI evaporated GEM as a photocathode. Our HBD has been developed based on the PHENIX HBD experience [12]. CF_4 serves as radiator and amplification gas. With the radiator length of 50 cm, 11 photoelectrons are expected. A schematic of the photocathode is shown in Fig. 11. The incident electron emit cherenkov photons. The photons are converted into photoelectrons by the CsI layer which is evaporated on top of the top GEM. The photoelectrons are then amplified by the GEMs. A weak reverse bias field is applied in the gap between the mesh and the top GEM, so that the ionization electrons in the gap are swept into the mesh. Even with the reverse bias field, photoelectrons produced near the top GEM surface are still attracted by the GEM's field and are amplified to be detected. Therefore, HBD is blind to ionization while is sensitive to cherenkov photons. The size of the photocathode of a HBD module is 600 $\times$ 600 mm^2 and four photocathodes with a size of 300 $\times$ 300 mm^2 are used to fill the module. Extensive R & D effort has been performed to establish HBD compo-

nents such as efficient and robust CsI GEMs, airtight chambers and readout boards. Prototypes of GEMs with and without CsI, chambers and readout boards in small sizes and real sizes were produced. A picture of a prototype of the HBD chamber in real size is shown in Fig. 12. It corresponds to a module of the spectrometer. A beam test was performed with negatively charged particle beam of 1.0 GeV/c at the J-PARC K1.1BR to evaluate the performance of a prototype HBD in small size. A pion rejection factor of 100 with an electron efficiency of 80% was achieved using cluster size analysis. The prototype of HBD in real size also operates well. The performance meet the required rejection and efficiency for the experiment.

2.4 Schedule

The experiment was approved as stage-1 in 2007. Detector R&D started in 2008. The construction budget of the high-p beam line was approved in 2013. Technical design report was submitted and the mass production of detectors started in 2014. Due to the budgetary limitation, we start with one third of the full design. The one third of the full design will be ready for the first physics run which is anticipated in JFY2016.

3 Other related experiments at J-PARC

J-PARC E26 experiment has been proposed to investigate ω meson in nuclear medium[13, 14]. It plan to use π^- beam at J-PARC K1.8 beam line with a momentum of 1.8 GeV/c and with an intensity of 1×10^7 / pulse. The reaction $\pi^- A \to \omega n X$ is used. Invariant mass of ω meson is measured with $\omega \to \pi^0\gamma \to 3\gamma$ decay mode. When neutron is detected at zero degree, recoilless ω production is realized. The condition is suitable for the study of in-medium effect. Nuclear ω bound state can be searched via forward neutron measurement.

J-PARC E29 experiment has been proposed to investigate in-medium mass modification of ϕ meson via ϕ meson bound state in target nucleus[15, 16]. It plan to use $\bar{p}$ beam with a momentum of 1.1 GeV/c and with an intensity of 1×10^6/pulse. When four strangeness are identified in the final state, the double ϕ production, $\bar{p} + p \to \phi\phi$, dominates. The forward-going ϕ meson is detected via K^+K^- decay. The ϕ meson in nucleus is detected via ΛK^+ decay, which occur only when ϕ is in nucleus ($\phi + p \to \Lambda K^+$). Missing mass spectrum is calculated with the beam momentum and the forward-going ϕ momentum. The backward ϕ is at the same order of Fermi momentum which is detected via ΛK^+ decay in nucleus.

When high intensity high resolution secondary beam line (HIHR) which was proposed by RCNP is realized, experimental study of ϕ meson in nuclear medium using a similar method as J-PARC E26 can be done. A 10^9/pulse π^- beam with a momentum of ~ 2 GeV is used to induce the $\pi^- + p \to \phi n$ reaction. If the neutron is identified at the forward angle, ultra slow ϕ is selected. Forward neutron measurement may lead to observation of nuclear ϕ bound state. About 10 times more ϕ compared to E16 is expected to be collected with $\beta\gamma < 0.5$.

4 Summary

The origin of hadron mass is studied through mass modification of vector mesons. There are many measurements of dilepton invariant mass in hot and cold system. There exists some modification but the origin is not yet clear. J-PARC E16 experiment pursue it by collecting 100 times more statics compare to the KEK E325 experiment. We expect to obtain double peak structure in ϕ meson invariant mass spectra, wide range of system size dependence of the in-medium modification, and the dispersion relation of ϕ meson in nuclear medium. We start with one-third of the design configuration and physics run is anticipated in JFY2016. More experiments regarding vector meson mass modification are planned and whole together provide further insights on the origin of mass, and the chiral symmetry.

5 Acknowledgments

We would like to give our thanks to the staff of KEK Fuji test beam line, ELPH at Tohoku University, LEPS at SPring-8, J-PARC Hadron Experimental Facility and RIKEN RI Beam Factory for their support for the beam test of detectors. We also would like to thank to KEK electronics system group (e-sys) for their help in the development and test of the readout circuits. This study was partly supported by Grant-in-Aid for JSPS Fellows 12J01196, RIKEN SPDR program, and MEXT/JSPS KAKENHI Grant Numbers 19654036, 19340075, 21105004 and 26247048.

References

[1] R. Muto *et al.*, Phys. Rev. Lett. **98**, 042501 (2007)

[2] K. Ozawa *et al.*, Phys. Rev. Lett. **86**, 5019 (2001).
M. Naruki *et al.*, Phys. Rev. Lett. **96**, 092301 (2006).

[3] T. Hatsuda and S. H. Lee, Phys. Rev. C **46**, R34 (1992).

[4] M. H. Wood *et al.*, Phys. Rev. C **78**, 015201 (2008).

[5] D. Adamova *et al.*, Phys. Lett. B **666**, 425 (2008).

[6] A. Adare, *et al.*, Phys. Rev. C **81**, 034911 (2010).

[7] `http://rarfaxp.riken.go.jp/~yokkaich/paper/jparc-proposal-0604.pdf`

[8] S. H. Lee, Phys. Rev. C **57**, 927 (1998).
S. H. Lee, Phys. Rev. C **58**, 3771 (1998).

[9] Y. Komatsu *et al.*, Nucl. Instrum. and Meth. A **732**, 241 (2013).

[10] M. Raymond *et al.*, IEEE NSS Conference Record **2**, 9/113 (2000).

[11] K. Aoki *et al,*, Nucl. Instrum. and Meth. A **628**, 300 (2011).

[12] A. Kozlov *et al.*, Nucl. Instrum. and Meth. A **523**, 345 (2004).

[13] `http://j-parc.jp/researcher/Hadron/en/pac_0903/pdf/Ozawa.pdf`

[14] http://j-parc.jp/researcher/Hadron/en/pac_1007/pdf/KEK_J-PARC-PAC2010-08.pdf

[15] http://j-parc.jp/researcher/Hadron/en/pac_0907/pdf/Ohnishi.pdf

[16] http://j-parc.jp/researcher/Hadron/en/pac_1007/pdf/KEK_J-PARC-PAC2010-02.pdf

Pion Transverse Momentum Spectrum, Elliptic Flow and Interferometry in the Granular Source Model in Ultra-Relativistic Heavy Ion Collisions

Jing Yang[1], Yan-Yu Ren[2] and Wei-Ning Zhang[1,2]

[1]School of Physics and Optoelectronic Technology,
Dalian University of Technology, Dalian, China
[2]Department of Physics, Harbin Institute of Technology, Harbin, China

Abstract

We systematically investigate the pion transverse momentum spectrum, elliptic flow, and Hanbury-Brown-Twiss (HBT) interferometry in the granular source model of quark-gluon plasma droplets in ultra-relativistic heavy ion collisions. The granular source model can well reproduce the experimental results of the Au-Au collisions at $\sqrt{s_{NN}} = 200$ GeV and the Pb-Pb collisions at $\sqrt{s_{NN}} = 2.76$ TeV with different centralities. We examine the parameters of the granular source models with an uniform and Woods-Saxon initial energy distributions in a droplet. The parameters exhibit certain regularities for collision centrality and energy.

1 Introduction

Single particle transverse momentum spectrum, elliptic flow, and Hanbury-Brown-Twiss (HBT) interferometry are three important final particle observables in high energy heavy ion collisions. They reflect the characters of the particle-emitting sources in different aspects and at different stages. Therefore, a combined investigation of these observables can provide very strong constrains for source models.

So far, much progress has been made in understanding the experimental data of the heavy ion collisions at the top energies of the Relativistic Heavy Ion Collider (RHIC) [1, 2, 3, 4, 5, 6, 7, 8, 9]. However, more detailed investigations of the physics beneath the data through multiobservable analyses are still needed. On the other hand, the experimental data of the Pb-Pb collisions at $\sqrt{s_{NN}} = 2.76$ TeV at the Large Hadron Collider (LHC) have been recently published [10, 11, 12, 13]. It is an ambitious goal for models to explain the experimental data of particle spectra, elliptic flow, and HBT interferometry in different centrality region consistently for the heavy ion collisions at the RHIC and LHC.

In Refs. [14, 15, 16], W. N. Zhang *et al.* proposed and developed a granular source model of quark-gluon plasma (QGP) droplets to explain the HBT data of the RHIC experiments [17, 18, 19, 20]. In Ref. [21, 22], the granular source model was used to explain the pion transverse momentum spectrum and HBT data of the most central heavy ion collisions at the RHIC and LHC. Motivated by these successes, we systematically investigate the pion transverse momentum spectrum, elliptic flow, and HBT interferometry for the granular sources in the heavy ion collisions at the RHIC and LHC energies with different centralities. The granular source parameters for an uniform and Woods-Saxon initial energy distributions in a droplet are examined and compared.

2 Granular Source Model

The granular source model of QGP droplets regards the whole source evolution as the superposition of the evolutions of many QGP droplets. Each droplet has a position-dependent initial velocity and evolves hydrodynamically. The model construction is based on the following suggestions. In the heavy ion collisions at top RHIC energies and LHC energies, the created strong coupled QGP (sQGP) systems at central rapidity region may reach local equilibrium at a very short time, and then expand rapidly along the beam direction (z-axis). Because the local equilibrium system is not uniform in the transverse plane (x-y plane) [23]. The system may form many tubes along the beam direction during the subsequent fast longitudinal expansion and finally fragment into many QGP droplets with the effects of "sausage" instability, surface tension, and bulk viscosity [15, 24, 25, 26].

As in Ref. [15], we suppose the QGP droplets of the granular source initially distribute within a cylinder along z-axis by

$$\frac{dN_d}{dx_0 dy_0 dz_0} \propto \left[1 - e^{-(x_0^2+y_0^2)/\Delta\mathcal{R}_T^2}\right]\theta(\mathcal{R}_T - \rho_0) \times\theta(\mathcal{R}_z - |z_0|). \quad (1)$$

Here $\rho_0 = \sqrt{x_0^2 + y_0^2}$ and z_0 are the initial transverse and longitudinal coordinates of the droplet centers. The parameters $\mathcal{R}_T$ and $\mathcal{R}_z$ describe the initial transverse and longitudinal sizes of the source, and $\Delta\mathcal{R}_T$ is a transverse shell parameter [15].

In Ref. [22], the Bjorken hypothesis [27] of longitudinal boost-invariant is used to describe the longitudinal velocity of droplet for the most central collisions, and the transverse velocity of droplet has a form of exponential power. Considering the longitudinal velocity of droplet varying with collision centrality, we introduce here also a longitudinal power parameter, which will be determined by experimental data, to describe the longitudinal velocity phenomenologically. The initial velocities

of the droplets in granular source frame are assumed as [15]

$$v_{\mathrm{d}i} = \mathrm{sign}(r_{0i}) \cdot a_i \left(\frac{|r_{0i}|}{\mathcal{R}_i} \right)^{b_i}, \qquad i = 1,\, 2,\, 3, \tag{2}$$

where r_{0i} is x_0, y_0, or z_0 for $i = 1$, 2, or 3, and sign(r_{0i}) denotes the signal of r_{0i}, which ensures an outward droplet velocity. In Eq. (2), $\mathcal{R}_i = (\mathcal{R}_T, \mathcal{R}_T, \mathcal{R}_z)$, $a_i = (a_x, a_y, a_z)$ and $b_i = (b_x, b_y, b_z)$ are the magnitude and exponent parameters in x, y, and z directions, which are associated with the early thermalization and pressure gradients of the system at the breakup time. It is also convenient to use the equivalent parameters $\overline{a}_T = (a_x + a_y)/2$ and $\Delta a_T = a_x - a_y$ instead of a_x and a_y. The parameters $\overline{a}_T$ and Δa_T describe the transverse expansion and asymmetric dynamical behavior of the system at the breakup time, respectively. For simplicity, we take $b_x = b_y = b_T$ in calculations. The parameters b_T and b_z describe the coordinate dependence of exponential power in transverse and longitudinal directions.

In the calculations of the hydrodynamical evolution of the droplet, we use the equation of state (EOS) of the S95p-PCE165-v0 [28], which combines the lattice QCD data at high temperature with the hadron resonance gas at low temperature. We assume systems fragment when reaching a certain local energy density ϵ_0, and take the initial energy density of the droplets to be 2.2 GeV/fm^3 for all considered collisions for simplicity [22]. The initial droplet radius r_0 is supposed satisfying a Gaussian distribution with the standard deviation $\sigma_d = 2.5$ fm in the droplet local frame [22]. We consider an uniform initial energy distribution in droplet and a Woods-Saxon distribution,

$$\epsilon(r) = \epsilon_0 \frac{1}{e^{\frac{r-r_0}{a}} + 1}, \tag{3}$$

where $a = 0.1 r_0$.

With the evolution of the hot droplets, the final pions freeze out at temperature T_f with the momenta obeying Bose-Einstein distribution. To include the resonance decayed pions emitted later as well as the directly produced pions at chemical freeze out earlier, a wide region of T_f is considered with the probability [22]

$$\begin{aligned} \frac{dP}{dT_f} \quad \propto \quad & f_{\mathsf{dir}}\, e^{-\frac{T_{\mathsf{chem}} - T_f}{\Delta T_{\mathsf{dir}}}} + (1 - f_{\mathsf{dir}}) \\ & \times e^{-\frac{T_{\mathsf{chem}} - T_f}{\Delta T_{\mathsf{dec}}}}, \quad (T_{\mathsf{chem}} > T_f > 80 \text{ MeV}), \end{aligned} \tag{4}$$

where f_{dir} is the fraction of the direct emission around the chemical freeze out temperature T_{chem}, ΔT_{dir} and ΔT_{dec} are the temperature widths for the direct and decay emissions, respectively. In the calculations, we take $f_{\mathsf{dir}} = 0.75$, $\Delta T_{\mathsf{dir}} = 10$ MeV, and $\Delta T_{\mathsf{dec}} = 90$ MeV as in Ref. [22]. The value of T_{chem} is taken to be 165 MeV as it be taken in the S95p-PCE165-v0 EOS [28].

After fixing the parameters used in the calculations of hydrodynamical evolution and freeze-out temperature, the free model parameters are the three source geometry parameters (R_T, ΔR_T, R_z) and the five droplet velocity parameters ($\overline{a}_T$, Δa_T, a_z, b_T, b_z). They are associated with the initial sizes, expansion, and directional asymmetry of system, and have significant influence on the observables of pion momentum sprectra, elliptic flow, and HBT radii in the granular source model. In next section, we will determine these parameters by the experimental data of these observable, and examine their variations with collision energy and centrality for the heavy ion collisions at the RHIC and LHC.

3 Results of Pion Momentum Spectrum, Elliptic Flow and Interferometry

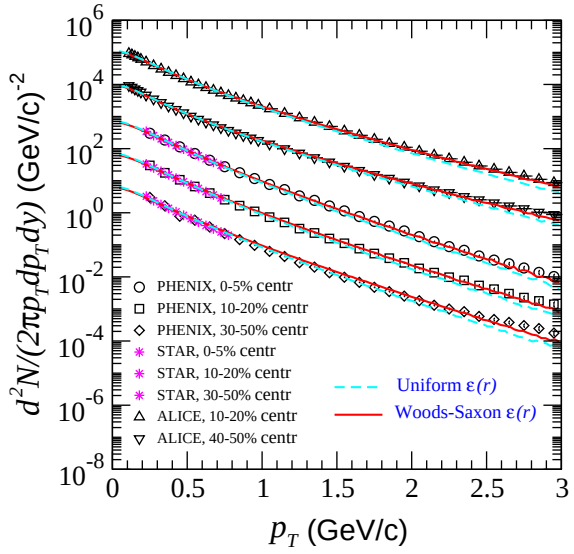

Figure 1: (Color online) The pion transverse momentum spectra of the granular sources for the RHIC Au-Au collisions at $\sqrt{s_{NN}} = 200$ GeV and the LHC Pb-Pb collisions at $\sqrt{s_{NN}} = 2.76$ TeV, for the uniform and Woods-Saxon initial energy distributions in a droplet. The experimental data of PHENIX [31], STAR [32], and ALICE [10] are also plotted.

In high energy heavy ion collisions, the invariant momentum distribution of final particles can be written in the form of a Fourier series [29, 30],

$$E\frac{d^3N}{d^3p} = \frac{1}{2\pi}\frac{d^2N}{p_T dp_T dy}\left[1 + \sum_n 2v_n \cos(n\phi)\right], \tag{5}$$

where E is the energy of the particle, p_T is the transverse momentum, y is the rapidity, and ϕ is the azimuthal angle with respect to the reaction plane. In Eq. (5), the first term on right is the transverse momentum spectrum in the rapidity region dy, and the second harmonic coefficient v_2 in the summation is called elliptic flow.

In Fig. 1, we plot the pion transverse momentum spectra of the granular sources with the uniform and Woods-Saxon initial energy distributions in a droplet. The experimental data of the Au-Au collisions at $\sqrt{s_{NN}} = 200$ GeV at the RHIC [31, 32] and the Pb-Pb collisions at $\sqrt{s_{NN}} = 2.76$ TeV at the LHC [10] are also plotted. In Fig. 2, we plot the pion elliptic flow results of the granular sources with the uniform and Woods-Saxon initial energy distributions, and the experimental data of the Au-Au collisions [33] and the Pb-Pb collisions [11].

The transverse momentum spectrum and elliptic flow of the granular sources are well in agreement with the experimental data, except for the elliptic flow results at

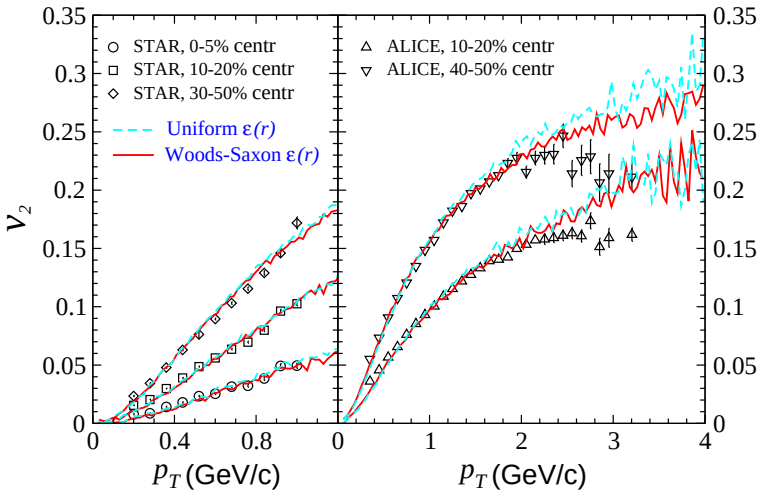

Figure 2: (Color online) The pion elliptic flow of the granular sources for the RHIC Au-Au collisions at $\sqrt{s_{NN}} = 200$ GeV and the LHC Pb-Pb collisions at $\sqrt{s_{NN}} = 2.76$ TeV, for the uniform and Woods-Saxon initial energy distributions in a droplet. The experimental data of STAR [33], and ALICE [11] are also plotted.

$p_T > 2$ GeV/c. The differences between the results of the granular sources with the uniform and Woods-Saxon initial energy distributions are small. The experimental data of the momentum spectrum and elliptic flow at the same centralities can simultaneously give the strong constraints to the velocity parameters of the granular sources. After then, the geometry parameters of the granular sources for the collisions with the different centralities can be further determined by the experimental data of HBT interferometry at the same centralities.

Two-particle HBT correlation function is defined as the ratio of the two-particle momentum spectrum $P(\mathbf{p}_1, \mathbf{p}_2)$ to the product of two single-particle momentum spectra $P(\mathbf{p}_1)P(\mathbf{p}_2)$. It has been widely used to extract the space-time geometry, dynamic and coherence information of the particle-emitting source in high energy heavy ion collisions [34, 35, 36, 37, 38]. In the usual HBT analysis in high energy heavy ion collisions, the two-pion correlation functions are fitted by the Gaussian parameterized formula

$$C(q_{\rm out}, q_{\rm side}, q_{\rm long}) = 1 + \lambda\, e^{-R^2_{\rm out}q^2_{\rm out} - R^2_{\rm side}q^2_{\rm side} - R^2_{\rm long}q^2_{\rm long}}, \qquad (6)$$

where $q_{\rm out}$, $q_{\rm side}$, and $q_{\rm long}$ are the Bertsch-Pratt variables [39, 40], which denote the components of the relative momentum $\mathbf{q} = \mathbf{p}_1 - \mathbf{p}_2$ in transverse out and side directions and in longitudinal direction, respectively. In Eq. (6) λ is chaoticity parameter of source, $R_{\rm out}$, $R_{\rm side}$, and $R_{\rm long}$ are the HBT radii in out, side, and long directions.

We plot in Fig. 3 the two-pion HBT results for the granular sources and the experimental data of the RHIC Au-Au collisions [20] and the LHC Pb-Pb collisions [13] with the same centralities as the experimental data of the spectrum and elliptic

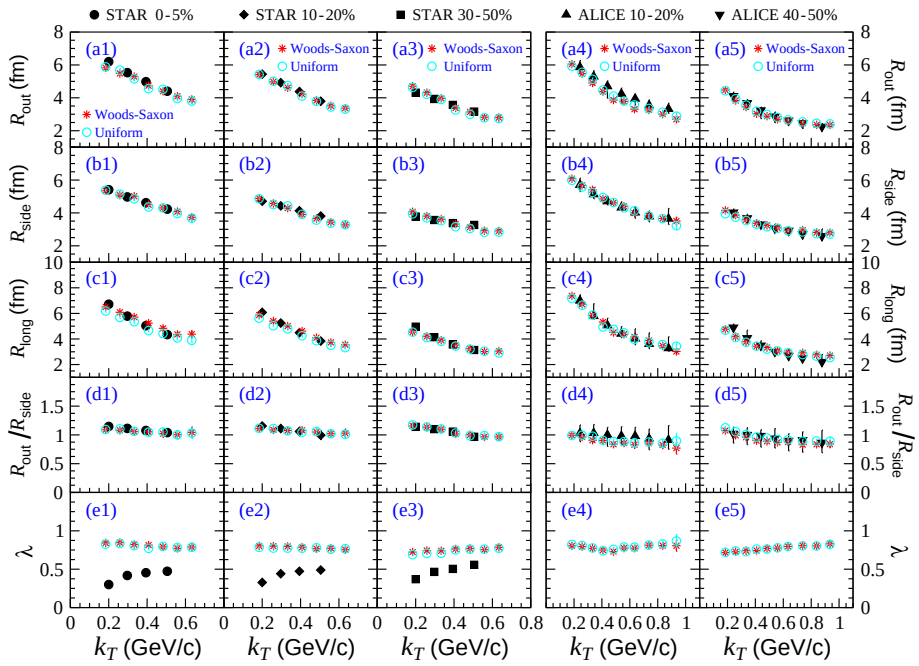

Figure 3: (Color online) The HBT results of the granular sources for the uniform and Woods-Saxon initial energy distribution, and the experimental data for the Au-Au collisions at the RHIC [20] and the Pb-Pb collisions at the LHC [13] with different centralities.

flow. Here, k_T is the transverse momentum of pion pair. One can see that the granular source models can well reproduce the experimental HBT radii and their variations with k_T. The results of the chaotic parameters λ of the granular sources are larger than the experimental data, because there are many effects in experiments can decrease λ [34, 35, 36, 37, 38], which exceed our considerations.

In Table 1, we present the parameters of the granular sources with uniform initial energy distribution in a droplet, determined by the experimental data of the momentum spectra, elliptic flow, and HBT radii. The values of the source geometry parameters indicate that the sources are a short cylinder with small shell effect (small ΔR_T). For certain collision energy, the source geometry parameters R_T, ΔR_T and R_z increase with the collision centralities. However, for the 10-20% centrality, these geometry parameters for the LHC collisions are larger than those for the RHIC collisions. The large difference between the droplet velocity parameters b_T and b_z indicates the different dynamical behaviors of the sources in the transverse and long directions. The parameter Δa_T increases with decreasing centrality. And, the values of $\overline{a}_T$ and a_z are almost independent of collision centrality. A detail analysis on the relationships between the source parameters and the granular source space-time evolution can be seen in Ref. [41].

Table 1: The geometry parameters (in fm unit) and velocity parameters of the granular sources with uniform initial energy distribution in a droplet.

Centrality	$\mathcal{R}_T$	$\Delta\mathcal{R}_T$	$\mathcal{R}_z$	$\overline{a}_T$	Δa_T	a_z	b_T	b_z
RHIC, 0–5 %	5.8	0.7	3.9	0.469	0.066	0.593	0.76	0.13
RHIC, 10–20%	4.5	0.5	2.9	0.454	0.115	0.593	0.56	0.11
RHIC, 30–50%	2.5	0.3	0.5	0.437	0.156	0.593	0.37	0.06
LHC, 10–20%	6.0	0.9	5.5	0.431	0.092	0.592	0.35	0.13
LHC, 40–50%	2.5	0.4	1.8	0.407	0.131	0.590	0.23	0.03

Table 2: The geometry parameters (in fm unit) and velocity parameters of the granular sources with Woods-Saxon initial energy distribution in a droplet.

Centrality	$\mathcal{R}_T$	$\Delta\mathcal{R}_T$	$\mathcal{R}_z$	$\overline{a}_T$	Δa_T	a_z	b_T	b_z
RHIC, 0–5 %	5.8	0.7	5.1	0.469	0.066	0.52	0.76	0.13
RHIC, 10–20%	4.5	0.5	4.0	0.457	0.122	0.52	0.56	0.11
RHIC, 30–50%	2.8	0.3	1.8	0.453	0.156	0.52	0.37	0.06
LHC, 10–20%	6.0	0.9	5.5	0.496	0.092	0.59	0.43	0.13
LHC, 40–50%	2.5	0.4	1.8	0.434	0.127	0.59	0.23	0.03

In Table 2, we present the parameters of the granular sources with Woods-Saxon distribution of initial energy in a droplet, determined by the experimental data of the momentum spectra, elliptic flow, and HBT radii. By Comparing the two set parameters in Table 1 and Table 2, one can see that there are some differences between the R_z and a_z values for the RHIC collisions. Also, for the LHC collisions, the values of $\bar{a}_T$ for for the granular sources with the Woods-Saxon distribution are larger.

4 Summary and Conclusions

We systemically investigate the pion transverse momentum spectrum, elliptic flow, and HBT interferometry in the granular source model for the heavy ion collisions at the RHIC highest energy and the LHC energy. The centrality dependence of the observables at the two energies are examined. By comparing the granular source results with the experimental data of the Au-Au collisions at $\sqrt{s_{NN}} = 200$ GeV at the RHIC and the Pb-Pb collisions at $\sqrt{s_{NN}} = 2.76$ TeV at the LHC with different collision centralities, we investigate the geometry and velocity parameters in the granular source models with an uniform and Woods-Saxon initial energy distributions in a droplet. The parameters as a function of collision centrality and energy are examined. Our investigations indicate that the granular source model can well reproduce the experimental data of pion transverse momentum spectra, elliptic flow, and HBT radii in the Au-Au collisions at $\sqrt{s_{NN}} = 200$ GeV with 0–5%, 10–20%, and 30–50% centralities [20, 31, 32, 33], and in the Pb-Pb collisions at $\sqrt{s_{NN}} = 2.76$ TeV with 10–20% and 40–50% centralities [10, 11, 13]. The experimental data of pion momentum spectra, elliptic flow, and HBT radii impose very strict constraints on the parameters in the granular source model. They exhibit certain regularities for collision centrality and energy.

Acknowledgement

This work was supported by the National Natural Science Foundation of China, Contract No. 11275037.

References

[1] I. Arsene et al. (BRAHMS Collaboration), Nucl. Phys. A **757**, 1 (2005); B. B. Back et al. (PHOBOS Collaboration), *ibid.*, 28; J. Adams et al. (STAR Collaboration), *ibid.*, 102; K. Adcox et al. (PHENIX Collaboration), *ibid.*, 184.

[2] J. Lajoie (PHENIX Collaboration), J. Phys. G **34**, S191 (2007); L. Ruan (STAR Collaboration), *ibid.*, S199; I. G. Bearden (BRAHMS Collaboration), *ibid.*, S207; D. J. Hofman (PHOBOS Collaboration), *ibid.*, S217; M. C. de la Barca (STAR Collaboration), *ibid.*, S225.

[3] J. P. Blaizot, J. Phys. G **34**, S243 (2007); L. McLerran, *ibid.*, S583.

[4] A. Franz (PHENIX Collaboration), J. Phys. G **35**, 104002 (2008); R. Debbe (BRAHMS Collaboration), *ibid.*, 104004; B. Wosiek (PHOBOS Collaboration), *ibid.*, 104005; B. Mohanty (STAR Collaboration), *ibid.*, 104006; T. C. Awes (PHENIX Collaboration), *ibid.*, 104007.

[5] L. McLerran, J. Phys. G **35**, 104001 (2008); R. Venugopalan, *ibid.*, 104003; R. K. Seto, *ibid.*, 104043; E. Shuryak, *ibid.*, 104044.

[6] W. A. Zajc, Nucl. Phys A **830**, 3c (2009).

[7] S. Bathe (PHENIX Collaboration), J. Phys. G **38**, 124001 (2011). H. Masui (STAR Collaboration), *ibid.*, 124002; S. Esumi (PHENIX Collaboration), *ibid.*, 124010; P. Sorensen (STAR Collaboration), *ibid.*, 124029.

[8] B. Schenke, J. Phys. G **38**, 124009 (2011); F. Antinori, *ibid.*, 124038.

[9] U. A. Wiedemann, Nucl. Phys A **904-905**, 3c (2013); B. Hippolyte, D. H. Rischke, *ibid.*, 318c.

[10] B. Abelev *et al.* (ALICE Collaboration), Phys. Rev. C **88**, 044910 (2013).

[11] R. Snellings (ALICE Collaboration), J Phys. G **38**, 124013 (2011).

[12] K. Aamodt *et al.* (ALICE Collaboration), Phys. Lett. B **696**, 328 (2011).

[13] A. Kisiel on behalf of ALICE Collaboration, talk at The Seventh Workshop on Particle Correlations and Femtoscopy, September 20-24, 2011, Tokyo, Japan; PoS (WPCF2011) 003.

[14] W. N. Zhang, M. J. Efaaf, and C. Y. Wong, Phys. Rev. C **70**, 024903 (2004).

[15] W. N. Zhang, Y. Y. Ren, and C. Y. Wong, Phys. Rev. C **74**, 024908 (2006).

[16] W. N. Zhang, Z. T. Yang, and Y. Y. Ren, Phys. Rev. C **80**, 044908 (2009).

[17] C. Adler *et al.* (STAR Collaboration), Phys. Rev. Lett. **87**, 082301 (2001).

[18] K. Adcox *et al.* (PHENIX Collaboration), Phys. Rev. Lett. **88**, 192302 (2002).

[19] S. S. Adler *et al.* (PHENIX Collaboration), Phys. Rev. Lett. **93**, 152302 (2004).

[20] J. Adams *et al.* (STAR Collaboration), Phys. Rev. C **71**, 044906 (2005).

[21] W. N. Zhang, talk at The Seventh Workshop on Particle Correlations and Femtoscopy, September 20-24, 2011, Tokyo, Japan; PoS (WPCF2011) 051.

[22] W. N. Zhang, H. J. Yin, and Y. Y. Ren, Chin. Phys. Lett **28**, 122501 (2011).

[23] A. Adare, M. Luzum, H. Petersen, Phys. Scripta **87**, 048001 (2013); arXiv:1212.5388[nucl-th]

[24] C. Y. Wong, Ann. Phys. **77**, 279 (1973).

[25] G. Torrieri, B. Tomášik, I. Mishustin, Phys. Rev. C **77**, 034903 (2008).

[26] J. Takahashi, B. M. Tavares, W. L. Qian *et al.* Phys. Rev. Lett. 103, 242301 (2009).

[27] D. J. Bjorken, Phys. Rev. D **27**, 140 (1983).

[28] C. Shen, U. Heinz, P. Huovinen, and H. C. Song, Phys. Rev. C **82**, 054904 (2010).

[29] S. Voloshin and Y. Zhang, Z. Phys. C **70**, 665 (1996).

[30] A. M. Poskanzer and S. A. Voloshin, Phys. Rev. C **58**, 1671 (1998).

[31] S. S. Adler *et al.* (PHENIX Collaboration), Phys. Rev. C **69**, 034909 (2004).

[32] J. Adams *et al.* (STAR Collaboration), Phys. Rev. Lett. **92**, 112301 (2004).

[33] J. Adams *et al.* (STAR Collaboration), Phys. Rev. C **72**, 014904 (2005).

[34] M. Gyulassy, S. K. Kauffmann, and L. W. Wilson, Phys. Rev. C **20**, 2267 (1979).

[35] C. Y. Wong, *Introduction to High-Energy Heavy-Ion Collisions* (World Scientific, Singapore, 1994), Chap. 17.

[36] U. A. Wienemann and U. Heinz, Phys. Rep **319**, 145 (1999).

[37] R. M. Weiner, Phys. Rep **327**, 249 (2000).

[38] M. A. Lisa, S. Pratt, R. Soltz, U. Wiedemann, Annu. Rev. Nucl. Part. Sci **55**, 357 (2005).

[39] G. Bertsch, M. Gong, and M. Tohyama, Phys. Rev. C **37**, 1896 (1988); G. Bertsch, Nucl. Phys. A **498**, 173c (1989).

[40] S. Pratt, T. Csörgo, and J. Zimányi, Phys. Rev.C **42**, 2646 (1990).

[41] J. Yang, Y. Y. Ren and W. N. Zhang, Advances in High Energy Physics, 2014, 846154 (2014).

Charge splitting of directed flow and charge-dependent effects in pion spectra in heavy ion collisions

A. Rybicki[1], A. Szczurek[1,2], M. Kłusek-Gawenda[1], M. Kiełbowicz[3]

[1]H.Niewodniczański Institute of Nuclear Physics, Polish Academy of Sciences, Radzikowskiego 152, 31-342 Kraków, Poland
[2]University of Rzeszów, Rejtana 16, 35-959 Rzeszów, Poland
[3]The Tadeusz Kościuszko Cracow University of Technology, Warszawska 24, 31-155 Kraków, Poland

Abstract

The large and rapidly varying electric and magnetic fields induced by the spectator systems moving at ultrarelativistic velocities induce a charge splitting of directed flow, v_1, of positive and negative pions in the final state of the heavy ion collision. The same effect results in a very sizeable distortion of charged pion spectra as well as ratios of charged pions (π^+/π^-) emitted at high values of rapidity. Both phenomena are sensitive to the actual distance between the pion emission site and the spectator system. This distance d_E appears to decrease with increasing rapidity of the pion, and comes below $\sim$1 fm for pions emitted close to beam rapidity. In this paper we discuss how these findings can shed new light on the space-time evolution of pion production as a function of rapidity, and on the longitudinal evolution of the system created in heavy ion collisions.

1 Introduction

The presence of large and rapidly varying electric and magnetic fields in relativistic heavy ion collisions results in charge-dependent effects, visible in a series of observables in the final state of the collision. These effects can be used as a new source of information on the space-time evolution of the non-perturbative process of particle production, and on the space-time properties of the system created in the heavy ion collision. To give one example, in 2007 we demonstrated that the distortion which the electromagnetic repulsion (attraction) of positive (negative) pions induced on charged pion (π^+/π^-) ratios brought new information on the space-time scenario of fast pion production [1]. In recent years, the general problematics of electromagnetically-induced effects in ultrarelativistic heavy ion reactions was subject of an important theoretical and experimental interest [2, 3, 4, 5] as it was connected to very interesting phenomena like the chiral magnetic effect (CME [6, 7]).

In the present paper we review our earlier studies of the electromagnetic distortion of charged pion spectra in the context of our more recent findings on the influence of spectator-induced $\vec{E}$ and $\vec{B}$ fields on the azimuthal anisotropies of charged pions. Special attention is put on tracing the utility of both observables for studying the longitudinal evolution of the expanding matter created in the collision. A phenomenological model analysis is presented, aimed at explaining the space-time features of pion production which we deduced from the observed electromagnetic phenomena.

2 Charged-dependent effects in pion spectra at the SPS

The relatively moderate collision energy range available to the SPS makes corresponding fixed-target experiments suitable for studying the electromagnetic influence of the spectator system on charged particle spectra in a large range of available rapidity. Importantly, this includes the region of very low transverse momenta where the corresponding effects are expected to be largest. A detailed double-differential study of π^+ and π^- densities as a function of longitudinal and transverse pion momentum is presented in Fig. 1. The NA49 experimental data cover, in the longitudinal direction expressed in terms of the c.m.s. Feynman variable $x_F = 2p_L/\sqrt{s_{NN}}$, the whole region from "mid-rapidity" ($x_F = y = 0$) up to $x_F = 0.4$ which is about one unit above beam rapidity at lowest transverse momenta. The smooth exponential-like shape of the transverse momentum distribution gets visibly distorted in the region of low p_T, where a dramatic decrease of invariant π^+ density and an accumulation of π^- density is apparent as indicated by the arrows. This "deformation" is caused by the spectator system, which modifies the trajectories of charged pions by means of its space- and time-dependent $\vec{E}$ and $\vec{B}$ fields.

The ratio of π^+ over π^- density, Fig. 2(a), appears particularly sensitive to the spectator-induced electromagnetic field in the region of higher rapidity ($x_F > 0.1$) and lower transverse momenta. Here, a deep two-dimensional "valley" is apparent with the π^+/π^- ratio approaching zero in the region $y \approx y_{\rm beam}$ ($x_F = 0.15 = m_\pi/m_N$ at low p_T). Note that with the Pb nucleus composed of 39% protons over 61% neutrons, this implies breaking of isospin symmetry which unequivocally confirms the electromagnetic origin of the observed effect. Quantitatively, this is confirmed in Fig. 2(b), where the observed distortion can be fairly well described

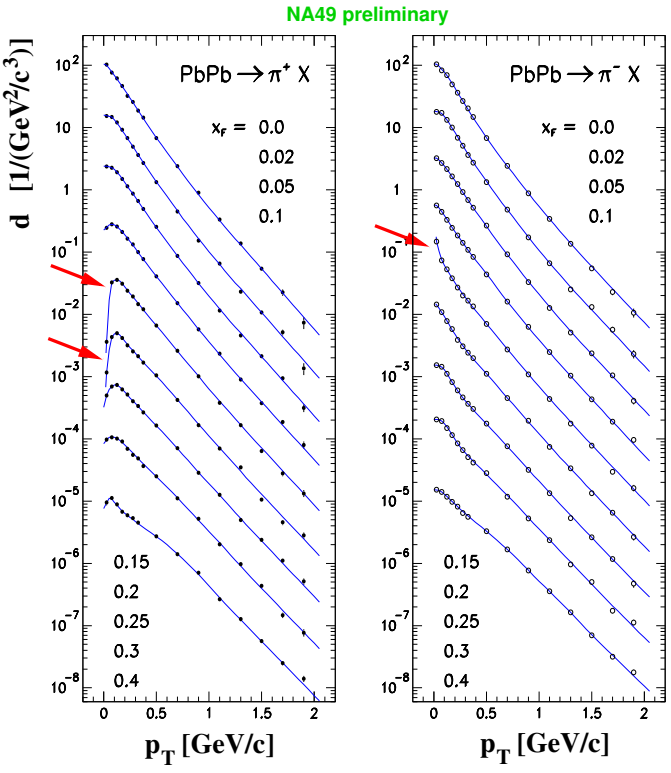

Figure 1: Distibutions of invariant density $d = E\frac{d^3n}{dp^3}$ of positively and negatively charged pions produced in peripheral Pb+Pb collisions at $\sqrt{s_{NN}} = 17.3$ GeV. The pion invariant density is drawn as a function of transverse momentum in fixed bins of x_F as marked from top to bottom. The subsequent distributions are consecutively multiplied by 0.2. The arrows point at the regions where the distortion induced by the spectator EM-field is most visible. From [8].

by means of a simple two-spectator model with the two spectators assumed as Lorentz-contracted homegenously charged spheres, and isospin effects being taken into account [9]. It is important to underline that the unique free parameter in the model is the distance d_E, in the longitudinal direction, between the pion emission point and the center of the spectator system. The reasonable agreement between data and model demonstrated in Figs 2(a),(b) is obtained for values of d_E in the range of 0.5 - 1 fm [9]; different values of d_E lead to different detailed shapes of the distortion of π^+/π^- ratios as described in [1].

3 Directed flow

In full analogy to charged pion ratios, the *directed flow* of charged pions emitted close to beam rapidity is also strongly affected by spectator-induced EM effects. This is shown in Fig. 2(c) where our prediction for a *purely electromagnetic effect* on the directed flow v_1 of positive pions is shown for three different values of the

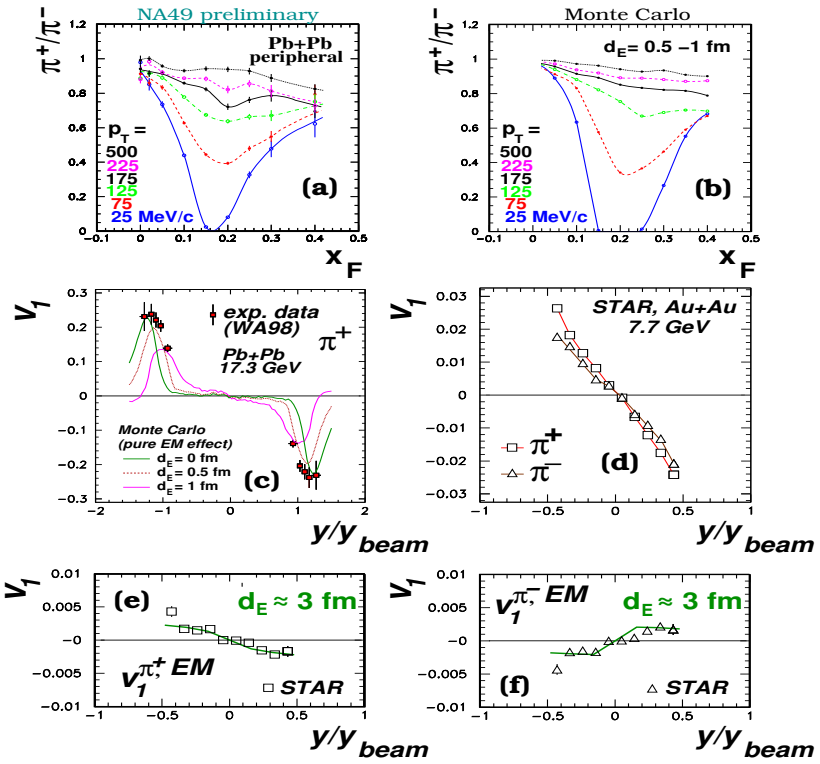

Figure 2: (a) Ratio of charged pions emitted in peripheral Pb+Pb collisions at $\sqrt{s_{NN}}$ = 17.3 GeV, (b) model simulation of this ratio as described in the text, (c) our Monte Carlo prediction for the (pure) electromagnetically-induced directed flow of positive pions, compared to the data from the WA98 experiment [10], (d) directed flow of charged pions in intermediate centrality Au+Au collisions [11], (e), (f) electromagnetic component of π^+ and π^- directed flow, extracted from STAR data [11] and compared to our simulation made assuming $d_E \approx 3$ fm. From: [8] (panels a,b), [12] (panel c), [13] (panels d,e,f).

distance d_E: 0, 0.5 and 1 fm. As it can be seen in the figure, our Monte Carlo calculation shows that very large values of directed flow can be induced by the sole effect of electromagnetic repulsion of positive pions by the spectator system. Our prediction is compared to the measurements provided by the WA98 Collaboration at the same energy, $\sqrt{s_{NN}}$ = 17.3 GeV [10]. This comparison indicates that a very sizeable part of positive pion directed flow in the region close to beam/target rapidity can in fact come from the electromagnetic origin. At the same time, the WA98 experimental data apparently constrain the possible values of the distance d_E, yielding the possible range of d_E from 0 up to 1 fm. Thus consistently from both observables (π^+/π^- ratios, Fig. 2(a) and directed flow, Fig. 2(c)), the longitudinal distance between the actual pion emission site and the center of the spectator system appears quite small, in the range below 1 fm. This small distance is to be viewed with respect to the longitudinal extent of the Lorentz-contrated spectator system which is itself of the order of about 1 fm at this collision energy.

The situation changes significantly when passing to pions produced close to *central* rather than *beam* rapidity. Here experimental data on intermediate centrality Au+Au reactions exist from the STAR experiment at RHIC [11] at different collision energies (from $\sqrt{s_{NN}} = 7.7$ up to 200 GeV). The directed flow of positive and negative pions at the lowest available energy is presented in Fig. 2(d). A *charge splitting* is apparent between π^+ and π^-. As shown in Figs 2(e),(f), the latter splitting can again be understood as a spectator-induced EM effect, provided that a value of d_E far larger than in the preceding case, $d_E \approx 3$ fm, is assumed.

4 Space-time picture of the collision

This apparent sensitivity of the electromagnetic distortion of final state charged pion ratios and directed flow to the distance between the pion formation zone and the spectator system provides, in the opinion of the authors, a completely new and very welcome tool for studying the space-time evolution of charged particle production in the soft sector of ultrarelativistic heavy ion collisions. Specifically, the elongation of the distance d_E with decreasing pion rapidity is the reflection of the longitudinal evolution of the system created in the collision. Summing up the findings from the precedent section, in our studies we obtained:

- $d_E \leq 1$ fm for pions moving at rapidities comparable to $y_{\rm beam}$ (from our study based on NA49 [8] and WA98 [10] data);
- $d_E \approx 3$ fm for pions moving at central rapidities ($-1 < y < 1$, from our study based on STAR data [11]).

While the mere fact that d_E evolves with pion rapidity is simply the confirmation of the expansion of the system in the longitudinal direction, the latter is, especially at high pion rapidities, poorly known to hydrodynamical calculations due to the presence of a sizeable baryochemical potential [14], and difficult to access experimentally e.g. in LHC experiments (in contrast to SPS energies where the NA49 and NA61/SHINE experiments cover the whole region from $y = 0$ to $y = y_{\rm beam}$ and above in the collision c.m.s. [15]).

In the present section we discuss this issue in the context of energy-momentum conservation in the initial state of the collision, in a model proposed by A.S. The spatial nuclear matter distribution in the volume of the two colliding nuclei is considered in a two-dimensional (x, y) projection perpendicular to the collision axis; peripheral Pb+Pb collisions at top SPS energy are presented in Fig. 3(a). The resulting "strips" of highly excited nuclear (or partonic) matter, Fig. 3(b), define the kinematical properties of the longitudinal expansion of the system as a function of collision geometry. These are shown in Figs 3(c) and (d) in the perpendicular (x, y) plane. For the peripheral collision considered here, the overall energy available for particle production (invariant mass of the "strips" as defined assuming local energy-momentum conservation) has a well-defined "hot" peak at mid-distance between the centers of the two nuclei, and gradually decreases when approaching each of the two "cold" spectator systems. On the other hand, the longitudinal velocity β of the "strips" depends strongly on their position in the (x, y) plane. A careful comparison of Figs 3(c)-(d) shows that significantly excited volume elements of the longitudinally expanding system can move at very large longitudinal velocities, comparable to that of the spectator system. Assuming a given proper hadronization

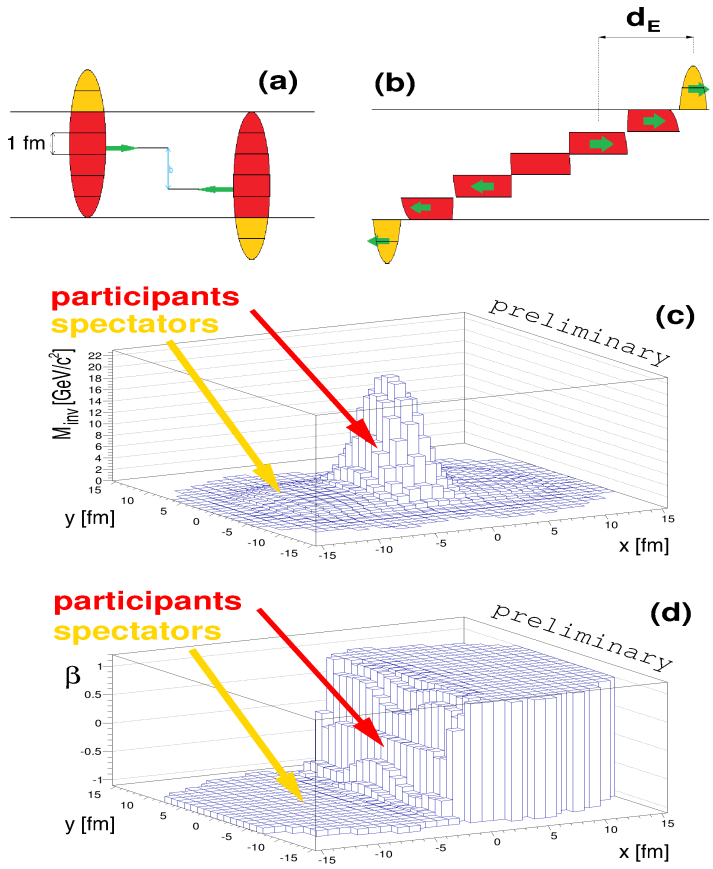

Figure 3: Model study of the kinematical characteristics of matter created in the peripheral Pb+Pb collision at $\sqrt{s_{NN}} = 17.3$ GeV. (a) Subdivision of the nuclear matter distribution into longitudinal "strips". (b) Kinematical characteristics of the "strips" as a function of their position in the perpendicular plane; the distance d_E is indicated in the plot. (c) Invariant mass of the "strips" projected in the perpendicular (x, y) plane, where x is the direction of the impact parameter vector. (d) Longitudinal velocity β of the "strips" as a function of their position. The "hot" participant and "cold" spectator regions are indicated in the plots.

time of the different volume elements, a natural picture emerges. Pions produced at high rapidity (dominantly from "strips" moving at large values of the longitudinal velocity β) will emerge at a small distance from the "cold" spectator systems; these originating from "hot" central "strips", at smaller values of y, will evidently show up at larger values of the distance d_E.

5 Conclusions

Altogether, we conclude that a non-negligible amount of experimental data on charge-dependent effects in particle spectra and anisotropic flow exists, and much

more can be obtained from existing fixed-target as well as collider experiments. These data can be used to trace the influence of the electric and magnetic fields in heavy ion collisions, which should be useful in future studies related to the chiral magnetic effect, the electromagnetic properties of the quark-gluon plasma, and others. Our own studies demonstrate the sensitivity of the EM-induced distortions of charged particle spectra and directed flow to the space-time scenario of particle production in heavy ion collisions, and allow us to trace the longitudinal evolution of the expanding matter created in the course of the collision.

Acknowledgments

The authors, and especially A.R., gratefully thank the organizers of the X Workshop on Particle Correlations and Femtoscopy (WPCF 2014), for their invitation and for the excellent organization of such a fruiful and interesting Workshop.

This work was supported by the Polish National Science Centre (on the basis of decision no. DEC-2011/03/B/ST2/02634).

References

[1] A. Rybicki, A. Szczurek, Phys. Rev. C **75**, 054903 (2007) [nucl-th/0610036].

[2] U. Gürsoy, D. Kharzeev and K. Rajagopal, Phys. Rev. C **89**, 054905 (2014) [arXiv:1401.3805 [hep-ph]].

[3] V. Voronyuk, V. D. Toneev, S. A. Voloshin and W. Cassing, Phys. Rev. C **90**, no. 6, 064903 (2014) [arXiv:1410.1402 [nucl-th]].

[4] Y. Hirono, M. Hongo and T. Hirano, Phys. Rev. C **90**, no. 2, 021903 (2014) [arXiv:1211.1114 [nucl-th]].

[5] L. Adamczyk *et al.* [STAR Collaboration], Phys. Rev. Lett. **113**, 052302 (2014) [arXiv:1404.1433 [nucl-ex]].

[6] D. E. Kharzeev, L. D. McLerran and H. J. Warringa, Nucl. Phys. A **803**, 227 (2008) [arXiv:0711.0950 [hep-ph]].

[7] K. Fukushima, D. E. Kharzeev and H. J. Warringa, Phys. Rev. D **78**, 074033 (2008) [arXiv:0808.3382 [hep-ph]].

[8] A. Rybicki, PoS(EPS-HEP 2009) 031.

[9] M. Klusek-Gawenda, E. Kozik, A. Rybicki, I. Sputowska and A. Szczurek, Acta Phys. Polon. Supp. **6**, 451 (2013) [arXiv:1303.6423 [nucl-ex]], and references therein.

[10] H. Schlagheck (WA98 Collaboration), Nucl. Phys. A **663**, 725 (2000) [nucl-ex/9909005].

[11] L. Adamczyk *et al.* (STAR Collaboration), Phys. Rev. Lett. **112**, 162301 (2014) [arXiv:1401.3043 [nucl-ex]].

[12] A. Rybicki and A. Szczurek, Phys. Rev. C **87**, 054909 (2013) [arXiv:1303.7354 [nucl-th]], and references therein.

[13] A. Rybicki, A. Szczurek and M. Klusek-Gawenda, EPJ Web Conf. **81**, 05024 (2014).

[14] R. Ryblewski, private communication.

[15] N. Abgrall *et al.* (NA61/SHINE Collaboration), Eur. Phys. J. C **74**, no. 3, 2794 (2014) [arXiv:1310.2417 [hep-ex]], and references therein.

Energy dependence of space-time extent of pion source in nuclear collisions *

V.A. Okorokov[1],

[1]National Research Nuclear University "MEPhI"
(Moscow Engineering Physics Institute),
Kashirskoe Shosse 31, 115409 Moscow, Russia

Abstract

Energy dependence of space-time parameters of pion emission region at freeze-out is studied for collisions of various ions and for all experimentally available energies. The using of femtoscopic radii scaled on the averaged radius of colliding ions is suggested. This approach allows the expansion of the set of interaction types, in particular, on collisions of non-symmetrical ion beams which can be studied within the framework of common treatment. There is no sharp changing of femtoscopic parameter values with increasing of initial energy. Analytic functions suggested for smooth approximations of energy dependence of femtoscopic parameters demonstrate reasonable agreement with most of experimental data at $\sqrt{s_{NN}} \geq 5$ GeV. Estimations of some observables are obtained for energies of the LHC and FCC project.

1 Introduction

At present femtoscopic measurements in particular that based on Bose – Einstein correlations are unique experimental method for the determination of sizes and lifetimes of sources in high energy and nuclear physics. The study of nucleus-nucleus (AA) collisions in wide energy domain by correlation femtoscopy seems important for

*Manuscript contributed to the proceedings that could not be presented at WPCF 2014

better understanding both the equation of state (EOS) of strongly interacting matter and general dynamic features of soft processes. The discussion below is focused on specific case of femtoscopy, namely, on correlations in pairs of identical charged pions with small relative momenta – HBT-interferometry – in nucleus-nucleus collisions. The general view for phenomenological parameterization of correlation function (CF) for two identical particles is discussed in the [1, 2]. Below the experimental results obtained for AA collisions within the standard 3d approach are taken into account [2]. The set of main femtoscopic observables $\mathcal{G}_1 \equiv \{\mathcal{G}_1^i\}_{i=1}^4 = \{\lambda, R_{\mathsf{s}}, R_{\mathsf{o}}, R_{\mathsf{l}}\}$ is under consideration as well as the set of some important additional observables which can be calculated with help of HBT radii $\mathcal{G}_2 \equiv \{\mathcal{G}_2^j\}_{j=1}^3 = \{R_{\mathsf{o}}/R_{\mathsf{s}}, \delta, V\}$. Here $\delta = R_{\mathsf{o}}^2 - R_{\mathsf{s}}^2$, $V = (2\pi)^{3/2} R_{\mathsf{s}}^2 R_{\mathsf{l}}$ is the volume of source at freeze-out. The set of parameters $\mathcal{G}_1$ characterizes the correlation strength and source's 4-dimensional geometry at freeze-out stage completely. The most central collisions are usually used for study the space-time characteristics of final-state matter, in particular, for discussion of global energy dependence of femtoscopic observables. Therefore scaled parameters $\mathcal{G}_1^i$, $i = 2-4$, δ and $\mathcal{G}_2^3$ are calculated as follows [1, 2]:

$$R_i^n = R_i/R_{\mathsf{A}},\ i = \mathsf{s,o,l}; \quad \delta^n = \delta/R_{\mathsf{A}}^2; \quad V^n = V/V_{\mathsf{A}}. \tag{1}$$

Here $R_{\mathsf{A}} = R_0 A^{1/3}, V_{\mathsf{A}} = 4\pi R_{\mathsf{A}}^3/3$ is radius and volume of spherically-symmetric nucleus, $R_0 = (1.25 \pm 0.05)$ fm [3, 4]. The change $R_{\mathsf{A}} \to \langle R_{\mathsf{A}} \rangle = 0.5(R_{\mathsf{A}_1} + R_{\mathsf{A}_2})$ is made in the relation (1) in the case of non-symmetric nuclear collisions [1, 2]. In general case the scale factor in (1) should takes into account the centrality of nucleus-nucleus collisions. The normalization procedure suggested in [1] allows the consideration of all available data for nucleus-nucleus collisions [2]. As development of previous analyses [1, 2] the proton-proton (pp) results at high energies [5, 6] are also considered here with replacing $R_{\mathsf{A}} \to R_{\mathsf{p}}$ in (1).

2 Energy dependence of space-time extent of pion source

Table 1: Values of fit parameters for AA data with statistical errors

HBT	Fit parameter			
parameter	a_1	a_2	a_3	χ^2/n.d.f.
λ	1.21 ± 0.09	-0.30 ± 0.04	0.38 ± 0.04	3656/29
	0.717 ± 0.003	-0.051 ± 0.001	1.0 (fixed)	3786/23
R_{s}^n	0.656 ± 0.002	$(6 \pm 3) \times 10^{-5}$	3.11 ± 0.19	195/25
	0.599 ± 0.003	0.019 ± 0.001	1.0 (fixed)	280/26
R_{o}^n	0.10 ± 0.02	6.3 ± 1.7	0.068 ± 0.006	402/25
	0.758 ± 0.004	0.008 ± 0.001	1.0 (fixed)	415/26
R_{l}^n	0.022 ± 0.002	23 ± 3	0.258 ± 0.005	502/25
	0.634 ± 0.004	0.043 ± 0.001	1.0 (fixed)	615/26

Detail study for (quasi)symmetric heavy ion collisions [1, 2] demonstrates that

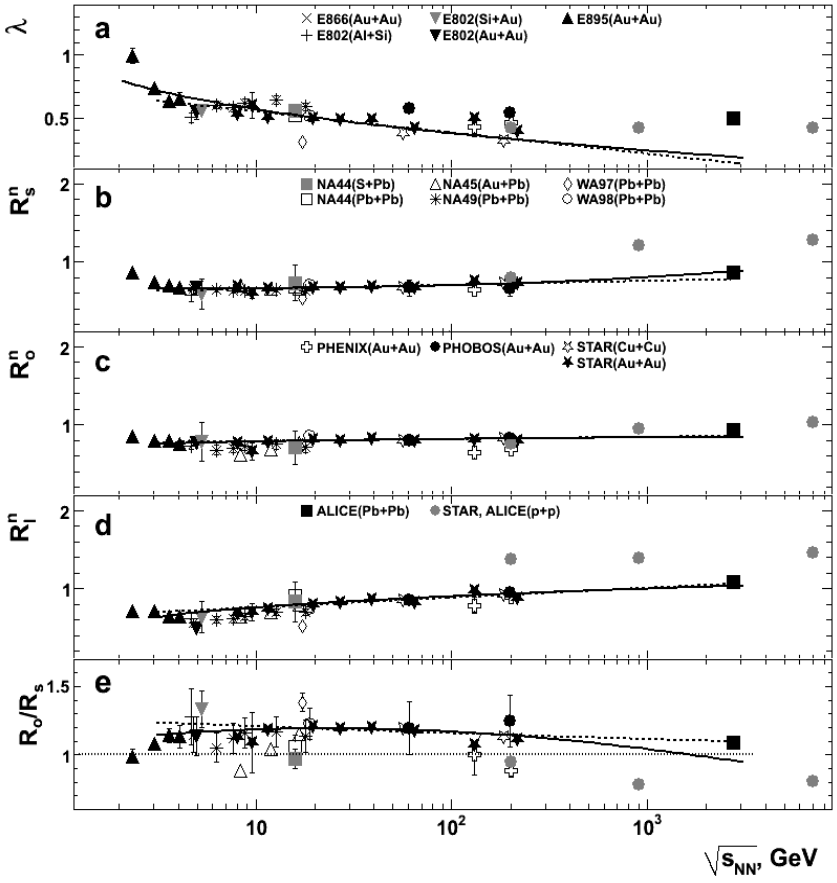

Figure 1: Energy dependence of λ parameter (a), scaled HBT-radii (b – d) and ratio $R_{\rm o}/R_{\rm s}$ (e) in various collisions. Experimental data are from [2, 5, 6]. Statistical errors are shown (for NA44 – total uncertainties). The solid lines (a – d) correspond to the fits by function (2) and dashed lines – to the fits by specific case of (2) at fixed $a_3 = 1.0$. Smooth solid and dashed curves at (e) correspond to the ratio $R_{\rm o}/R_{\rm s}$ calculated from the fit results for $R_{\rm s}^n$ and $R_{\rm o}^n$ in AA, dotted line is the level $R_{\rm o}/R_{\rm s} = 1$.

the fit function ($\varepsilon \equiv s_{NN}/s_0$, $s_0 = 1$ GeV^2)

$$f(\sqrt{s_{NN}}) = a_1\,[1 + a_2(\ln\varepsilon)^{a_3}] \tag{2}$$

agrees reasonably with experimental dependence $\mathcal{G}_1^i(\sqrt{s_{NN}})$, $i = 1 - 4$ at any collision energy for λ and at $\sqrt{s_{NN}} \geq 5$ GeV for HBT radii. Fig. 1 shows the energy dependence of λ (a), scaled HBT-radii (b – d) and $R_{\rm o}/R_{\rm s}$ ratio (e) for both the symmetric and non-symmetric collisions of various nuclei. Fits of experimental dependencies for AA interactions are made by (2) in the same energy domains as well as for (quasi)symmetric heavy ion collisions. The numerical values of fit parameters are presented in Table 1, fit curves are shown in Fig. 1 by solid lines for (2) and by dashed lines for specific case of fit function at $a_3 = 1.0$ with taking into account statistical errors. There is dramatic growth of χ^2/n.d.f. values

for fits of λ data (Fig. 1a) despite of qualitative agreement between smooth approximations and experimental λ values for range $10 \lesssim \sqrt{s_{NN}} \lesssim 200$ GeV. The fit by (2) underestimates the λ value at the LHC energy $\sqrt{s_{NN}} = 2.76$ TeV significantly. The λ values for asymmetric nucleus-nucleus collisions at intermediate energies $\sqrt{s_{NN}} \lesssim 20$ GeV agree well with values of λ in symmetric heavy ion collisions at close energies. On the other hand the λ for Cu+Cu collisions is smaller systematically than λ in Au+Au collisions in energy range $\sqrt{s_{NN}} = 62 - 200$ GeV (Fig. 1a). New experimental data are important for verification of the suggestion of separate dependencies $\lambda(\sqrt{s_{NN}})$ for moderate and heavy ion collisions. Also the development of some approach is required in order to account for type of colliding beams in the case of λ parameter and improve quality of approximation. Smooth curves for normalized HBT radii and ratio $R_{\mathsf{o}}/R_{\mathsf{s}}$ are in reasonable agreement with experimental dependencies in fitted domain of collision energies $\sqrt{s_{NN}} \geq 5$ GeV (Figs. 1b – e). Dramatic improvement of the fit qualities for scaled HBT radii at transition from the data sample with statistical errors to the data sample with total errors is dominated mostly by the uncertainty in r_0 leads to additional errors due to scaling (1). The scaled HBT-radii in pp are larger significantly than those in AA collisions at close energies. Because feature of Regge theory [7] the following relation is suggested to take into account the expanding of proton with energy: $R_{\mathsf{p}} = r_0(1 + k\sqrt{\alpha'_{\mathcal{P}} \ln \varepsilon})$, where $r_0 = (0.877 \pm 0.005)$ fm is the proton's charge radius [8], parameter $\alpha'_{\mathcal{P}} \propto \ln \varepsilon$ because of diffraction cone shrinkage speeds up with collision energy in elastic pp scattering [9]. The k is defined from the boundary condition $R_{\mathsf{p}} \to 1/m_\pi$ at $\varepsilon \to \infty$ with choice of appropriate asymptotic energy $\sqrt{s^a_{NN}}$. The detail study demonstrates that the increasing of $\sqrt{s^a_{NN}}$ from 6 PeV [10] to 10^3 PeV influences weakly on R^n_{i}, $i = \mathsf{s}, \mathsf{o}, \mathsf{l}$ in pp collisions and calculations are made for the first case. The normalized transverse radii agree in both the pp and the AA collisions (Figs. 1b, c) at $\sqrt{s_{NN}} = 200$ GeV with excess of R^n_{s} in pp with respect to the AA in TeV-region. The R^n_{l} in pp is larger than that for AA in domain $\sqrt{s_{NN}} \geq 200$ GeV. It should be stressed that the additional study is important, at least, for choice of $R_{\mathsf{p}}(\varepsilon)$.

The corresponding dependencies for δ^n and V^n are demonstrated in Fig. 2 and Fig. 3, respectively. As well as in [1, 2] results for $\pi^+\pi^+$ pairs are shown in Figs. 1 – 3 also because femtoscopy parameters from the set $\mathcal{G}_1$ depend on sign of electrical charge of secondary pions weakly. The relation $R_{\mathsf{o}} < R_{\mathsf{s}}$ is observed for $\approx 11\%$ of points in Fig. 2. Detail discussion for points with $\delta < 0$ is in the [2]. The dependence $\delta^n(\sqrt{s_{NN}})$ is almost flat within large error bars in all energy domain under consideration. Taking into account the STAR high-statistics results [11] only one can see the indication on change of behavior of $\delta^n(\sqrt{s_{NN}})$ inside the range of collision energy $\sqrt{s_{NN}} = 11.5 - 19.6$ GeV. This observation is in agreement with features of behavior of emission duration $(\Delta\tau)$ dependence on $\sqrt{s_{NN}}$ discussed in [2]. The estimation of energy range agrees well with results of several studies in the framework of the phase-I of the beam energy scan (BES) program at RHIC which indicate on the transition from dominance of quark-gluon degrees of freedom to hadronic matter at $\sqrt{s_{NN}} \lesssim 19.6$ GeV. But future precise measurements are crucially important for extraction of more definite physics conclusions. Smooth solid and dashed curves shown in Fig. 2 are calculated for δ^n from the fit results for R^n_{s} and R^n_{o} (Table 1). The calculation based on the fit function (2) at free a_3 agrees reasonably with experimental points at $\sqrt{s_{NN}} \leq 200$ GeV but underestimates δ^n in TeV-region significantly. The large errors in Fig. 3 for strongly asymmetric AA collisions is dominated by large difference of radii of colliding moderate and heavy

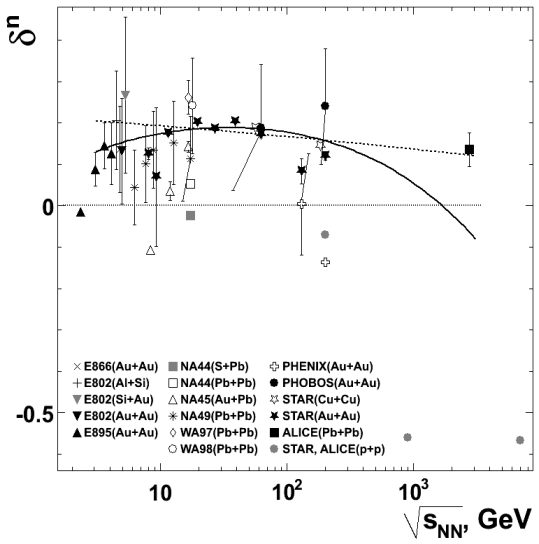

Figure 2: Dependence $\delta^n(\sqrt{s_{NN}})$ in various collisions. Experimental data are from [2, 5, 6]. Error bars are only statistical (for NA44 – total uncertainties). Dotted line is the level $\delta^n = 0$. Smooth curves are derived from (1) and the fit results for $R^n_{\rm s}$, $R^n_{\rm o}$ in AA. The solid line corresponds to the fits of normalized HBT radii by function (2) and dashed line – to the fits by specific case $R^n_i \propto \ln\varepsilon$, $i = {\rm s}, {\rm o}$.

nuclei and corresponding large uncertainty for $\langle R_{\rm A}\rangle$. Smooth solid and dashed curves shown in Fig. 3 are calculated for V^n from it's definition (1) and the fit results for $R^n_{\rm s}$, $R^n_{\rm l}$ (Table 1). The fit results for normalized HBT radii obtained with general function (2) lead to very good agreement between smooth curve and experimental data in TeV-region in contrast with the curve obtained from corresponding fit results for (2) at $a_3 = 1.0$. There is significant difference between pp and AA collisions for δ^n in TeV-region (Fig. 2) and for V^n at $\sqrt{s_{NN}} \geq 200$ GeV (Fig. 3).

Estimations for λ, $R_{\rm o}/R_{\rm s}$, and normalized femtoscopic parameters at the LHC and the FCC energies are shown in Table 2 for fits of various AA collisions with inclusion of statistical errors, the second line for each collision energy corresponds to the using of the specific case of (2) at $a_3 = 1.0$. All the smooth approximations discussed above predict amplification of coherent pion emission with significant decreasing of λ. Uncertainties are large for estimations obtained on the basis of results of fits by function (2) at free a_3. Thus values of femtoscopic observables in Table 2 are equal within errors for general and specific case of (2) at $\sqrt{s_{NN}} = 5.52$ TeV (LHC) and $\sqrt{s_{NN}} = 39.0$ TeV (FCC).

The energy dependencies for sets $\mathcal{G}_m$, $m = 1, 2$ of femtoscopic parameters with taking into account the scaling relation (1) demonstrate the reasonable agreement between values of parameters obtained for interactions of various ions (Figs. 1 – 3). The observation confirms the suggestion [1] that normalized femtoscopic parameters allow us to unite the study both the symmetric and the asymmetric AA collisions within the framework of united approach. This qualitative suggestion is confirmed indirectly by recent study of two-pion correlations in the collisions of the lightest

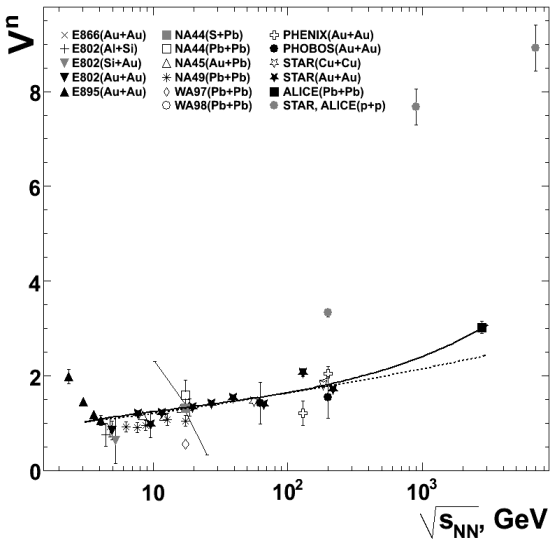

Figure 3: Energy dependence of V^n in various collisions. Experimental data are from [2, 5, 6]. Error bars are only statistical (for NA44 – total uncertainties). Smooth curves are derived from (1) and the fit results for $R^n_{\rm s}$, $R^n_{\rm l}$ in AA. The solid line corresponds to the fits of normalized HBT radii by function (2) and dashed line – to the fits by specific case $R^n_i \propto \ln\varepsilon$, $i = {\rm s}, {\rm l}$.

Table 2: Estimations for observables based on fit results

$\sqrt{s_{NN}}$,	HBT parameter for AA			
TeV	λ	$R^n_{\rm s}$	$R^n_{\rm o}$	$R^n_{\rm l}$
5.52	0.16 ± 0.19	0.9 ± 0.2	0.8 ± 0.3	1.06 ± 0.16
	0.091 ± 0.004	0.792 ± 0.009	0.860 ± 0.010	1.099 ± 0.013
39.0	0.07 ± 0.21	1.2 ± 0.4	0.9 ± 0.3	1.11 ± 0.16
	–	0.836 ± 0.011	0.883 ± 0.012	1.205 ± 0.015
	$R_{\rm o}/R_{\rm s}$	δ^n	V^n	
5.52	0.9 ± 0.4	-0.2 ± 0.6	3.5 ± 1.6	
	1.086 ± 0.018	0.11 ± 0.02	2.59 ± 0.07	
39.0	0.7 ± 0.3	-0.7 ± 1.1	6 ± 4	
	1.06 ± 0.02	0.08 ± 0.03	3.17 ± 0.09	

nucleus (d) with heavy ion (Au) at RHIC. Estimations of space-time extent of the pion emission source in d+Au collisions at top RHIC energy [12] in dependence on kinematic observables show similar patterns with corresponding dependencies in Au+Au collisions and indicate on similarity in expansion dynamics in collisions of various systems (d+Au and Au+Au at RHIC, p+Pb and Pb+Pb at LHC). The scaling results for some radii indicate that hydrodynamic-like collective expansion is driven by final-state rescattering effects [12]. On the other hand the normalized

femtoscopic parameters allow us to get the common kinematic dependencies only without any additional information about possible general dynamic features in different collisions. Thus the hypothesis discussed above is qualitative only. The future quantitative theoretical and phenomenological studies are essential for verification of general features of soft stage dynamics for different collisions at high energies.

3 Summary

The main results of present study are the following.

Energy dependence is investigated for range of all experimentally available initial energies and for estimations of the main femtoscopic parameters from set the $\mathcal{G}_1$ (λ and radii) derived in the framework of Gauss approach as well as for the set of important additional observables $\mathcal{G}_2$ contains ratio of transverse radii, δ and HBT volume. There is no dramatic change of femtoscopic parameter values in AA with increasing of $\sqrt{s_{NN}}$ in domain of collision energies $\sqrt{s_{NN}} \geq 5$ GeV. The energy dependence is almost flat for the δ^n in nucleus-nucleus collisions within large error bars. The indication on possible curve knee at $\sqrt{s_{NN}} \sim 10 - 20$ GeV obtained in the STAR high-statistics data agree with other results in the framework of the phase-I of the BES program at RHIC. But additional precise measurements are crucially important at various $\sqrt{s_{NN}}$ in order to confirm this feature in energy dependence of additional femtoscopic parameters. The normalized some HBT radii and source volume in pp are larger significantly than those in AA collisions especially in TeV-region. The fit curves demonstrate qualitative agreement with experimental AA data for λ at all available collision energies and for normalized HBT radii in energy domain $\sqrt{s_{NN}} \geq 5$ GeV. Smooth curves calculated for energy dependence of parameters from the set $\mathcal{G}_2$ agree reasonably with corresponding experimental AA data in the most cases. Estimations of femtoscopic observables are obtained on the basis of the fit results for energies of the LHC and the FCC project. For multi-TeV energy domain the emission region of pions in nucleus-nucleus collisions will be characterized by decreased correlation strength, linear sizes about $8.5 - 9.5$ fm in longitudinal direction and $7 - 8$ fm in transverse plane, volume of about 10^4 fm^3.

References

[1] V. A. Okorokov, arXiv: 1312.4269 [nucl-ex]. 2013.

[2] V. A. Okorokov, arXiv: 1409.3925 [nucl-ex]. 2014.

[3] L. Valentin, *Subatomic physics: nuclei and particles* V. **I** (Ermann, Paris, 1982).

[4] K. N. Mukhin, *Experimental nuclear physics* V. **I** (Energoatomizdat, Moscow, 1993).

[5] M. M. Aggarwal *et al.*, Phys. Rev. C**83**, 064905 (2011).

[6] K. Aamodt *et al.*, Phys. Rev. D**84**, 112004 (2011).

[7] P. Collins, *An introduction to Regge theory and high energy physics* (Cambridge Univ. Press, Cambridge, 1977).

[8] J. Beringer *et al.*, Phys. Rev. D**86**, 010001 (2012).

[9] V. A. Okorokov, arXiv: 1501.01142 [hep-ph]. 2015.

[10] C. Bourrely *et al.*, arXiv: 1202.3611 [hep-ph]. 2012.

[11] L. Adamczyk *et al.*, arXiv: 1403.4972 [nucl-ex]. 2014.

[12] A. Adare *et al.*, arXiv: 1404.5291 [nucl-ex]. 2014.

Three-component Pomeron model in high energy $pp-$ and $\overline{p}p-$ elastic scattering *

A. Lengyel, Z. Tarics

Institute of Electron Physics, Ukrainian Nat. Ac. of Sci.
Universitetska, 21, Uzhgorod, Ukraine

Abstract

We assume that the Pomeron is a sum of Regge multipoles, each corresponding to a finite gluon ladder. From the fit to the data of $pp-$ and $\overline{p}p-$ scattering at high energy and all available momentum transfer we found that taking into account the spin, three-term multipole Pomeron and Odderon with different form-factors are substantial for good description of differential, total cross section and ratio ρ in the whole high energy experimental domain.

1 Introduction

The Pomeron being an infinite gluon ladder [1]-[4] may appear as a finite sum of gluon ladders corresponding to a finite sum of Regge multipoles with increasing multiplicities [5]-[7]. The first term in $\ln s$ series contributes to the total cross-section with a constant term and can be associated with a simple pole, the second one (double pole) goes as $\ln s$, the third one (triple pole) as $ln^2 s$, etc. All Pomeron poles have unit intercept. Previously the multipole Pomeron and many-Pomerons approaches were investigated on different applications [8]-[11] (see also review [12]). Due to the recent experiments on elastic and inelastic proton-proton scattering by the TOTEM Collaboration at the LHC [13], data in a wide range, from lowest up to TeV energies, both for proton-proton and antiproton-proton scattering in a

*Manuscript contributed to the proceedings that could not be presented at WPCF 2014

wide span of transferred momenta are now available. The experiments at TeV energies give a chance to verify different Pomeron and Odderon models because the secondary Reggeon contributions at these energies are small. Note that none of the existing models of elastic scattering was able to predict the value of the differential cross section beyond the first cone, as clearly seen in Fig.4 of the TOTEM paper [13, 14]. This problem is still remains actual and inspired some people to construct the new and revitalize a well-known old fashioned models. Consequently for this time it is necessary to revise our concept on exchange mechanism in this distant region of energies [15]-[18]. A number of models have been refined and developed [19]-[22]. In fact, several of used Pomeron models, as a rule, have intercept > 1 which requires the unitarisation [23], other ones have complicated structure and the overall number of parameters was fairly high [24, 25].

Here we suggest the three-component Pomeron model inspired by the finite sum of gluon ladders extended to the whole range of available momentum transfer of high-energy $pp-$ and $\overline{p}p-$ elastic scattering and performed a simultaneous fit to the σ_{tot}, ρ and $d\sigma/dt$ data. Our goal is to investigate the capabilities of Pomeron model as a finite sum of gluon rungs ($\ln s$ power) equivalent to single pole + dipole + tripole Pomeron with sufficiently account the spin influence and non-linear trajectory for $pp-$ and $\overline{p}p-$ scattering in first and second diffraction cone. Our strategy is two fold: one to select a core set of experimental data, as well as models of reference, most appropriately describing the details of this basic set. First we take the set [26], and then - the paper [25].

This paper is organized as follows. In the next section, one introduces the main formulas and features of the model. In Sec. 3, we perform the comparison with experiment. In the last section, the conclusions are drawn up.

2 The model

The reduced form of nucleon-nucleon amplitude without double spin-flip accounting is [27]:

$$A(s,t) = A_{00}(s,t) + \frac{\sqrt{-t}}{2m_p}\, A_{01}(s,t), \tag{1}$$

where $A_{00}(s,t)$ is spin-nonflip component and $A_{01}(s,t)$ is spin-flip component of scattering amplitude.

Our ansatz for the spin-nonflip scattering amplitude component $A_{00}(s,t)$ is:

$$A_{00}(s,t) = P_{00}(s,t) + R_f(s,t) \pm \left[R_\omega\left(s,t\right) + O\left(s,t\right)\right] \tag{2}$$

for $\overline{p}p$ (upper symbol) and pp (lower symbol) scattering respectively. For the spin-flip scattering amplitude component $A_{01}(s,t)$

$$A_{01} = P_{01}(s,t) + R_f(s,t) \pm \left[R_\omega\left(s,t\right) + g_{od} O\left(s,t\right)\right]. \tag{3}$$

We suppose that the contribution of the subleading reggeons to the spin-flip amplitude is the same as to the spin-nonflip amplitude and the contribution of Odderon to the spin-flip amplitude differ from one to the spin-nonflip amplitude by the factor g_{od}, where the Pomeron contribution we introduce in form:

$$P_{00}\left(s,t\right) = is\left(-i\frac{s}{s_0}\right)^{\alpha_P(t)-1} \sum_{j=0}^{2} a_{0j} \ln^j\left(-i\frac{s}{s_0}\right) e^{\varphi_{0j}(t)} \tag{4}$$

and

$$P_{01}\left(s,t\right)=is\left(-i\frac{s}{s_0}\right)^{\alpha_P(t)-1}\sum_{j=0}^{2}g_{1j}\ln^j\left(-i\frac{s}{s_0}\right)e^{\varphi_{1j}(t)}. \tag{5}$$

The Pomeron trajectory is:

$$\alpha_P(t)=1+\alpha_P' t+\alpha_P''\left(\sqrt{t_\pi}-\sqrt{t_\pi-t}\right), \tag{6}$$

where the lowest two-pion threshold $t_\pi=4m_\pi^2$. The residue functions are:

$$\varphi_{0j}(t)=\gamma_{0j}\left(\sqrt{t_\pi}-\sqrt{t_\pi-t}\right), \tag{7}$$

$$\varphi_{1j}(t)=\gamma_{1j}\left(\sqrt{t_\pi}-\sqrt{t_\pi-t}\right). \tag{8}$$

In (2),(3) the $R_f(s,t), R_\omega(s,t)$ and $O(s,t)$ contain the subleading reggeons as well as the Odderon contributions to the scattering amplitude:

$$R_f\left(s,t\right)=g_f\left(-i\frac{s}{s_0}\right)^{\alpha_f(t)}e^{b_f t} \tag{9}$$

and

$$R_\omega\left(s,t\right)=ig_\omega\left(-i\frac{s}{s_0}\right)^{\alpha_\omega(t)}e^{b_\omega t}, \tag{10}$$

where

$$\alpha_j\left(t\right)=1+\alpha_j^{'}t,\quad j=f,\omega;\quad s_0=1\ GeV^2. \tag{11}$$

To describe the different behavior of proton-proton and antiproton-proton differential cross-section in region of dip-bump one needs to include the Odderon contribution, which we use in a simple form:

$$O\left(s,t\right)=s\left(-i\frac{s}{s_0}\right)^{\alpha_O(t)-1}\sum_{j=0}^{2}g_j\ln^j\left(-i\frac{s}{s_0}\right)e^{\phi_j(t)}. \tag{12}$$

The Odderon trajectory is

$$\alpha_O(t)=1+\alpha_O' t. \tag{13}$$

The residue functions are:

$$\phi_j(t)=\delta_j\left(\sqrt{t_\pi'}-\sqrt{t_\pi'-t}\right), \tag{14}$$

$t_\pi'=9m_\pi^2$.

3 Comparison with experiment

In order to determine the parameters that control the s-dependence of $A\left(s,0\right)$ we applied a wide energy range $5GeV\leq\sqrt{s}\leq 7000GeV$ and used the available data for total cross sections and ρ ([26]). A total of 107 experimental points were included for $t=0$. For the differential cross sections we selected the data at the energies $\sqrt{s}=19;23;31;44;53;62;7000GeV$ (for $pp-$scattering)(1633 experimental points) and $\sqrt{s}$=31;53;62;546;1800GeV (510 experimental points) for $\overline{p}p-$ scattering [26]. The squared 4-momentum covers entire available range

Table 1: Parameters, quality of the fit obtained in the whole interval in s and t.

Parameter	Value	Error
a_{00}	8.449	0.121
a_{01}	-0.855	0.0188
a_{02}	0.06519	$0.81.10^{-2}$
a_{10}	-0.3690	0.0250
a_{11}	6.134	0.0910
a_{12}	-0.1938	0.00461
α'_P, GeV^{-1}	0.04638	$0.523.10^{-2}$
γ_{00}, GeV^{-1}	2.107	0.037
γ_{01}, GeV^{-1}	0.5742	0.0562
γ_{02}, GeV^{-1}	1.422	0.0633
γ_{10}, GeV^{-1}	2.623	0.0515
γ_{11}, GeV^{-1}	6.540	0.02655
γ_{12}, GeV^{-1}	5.176	0.0354
g_{00}	-0.4855	0.0188
g_{01}	-0.4855	0.0188
g_{02}	0.06519	$0.81.10^{-3}$
α'_O, GeV^{-2}	0.05197	$0.117.10^{-2}$
δ_0, GeV^{-1}	2.623	0.0515
δ_1, GeV^{-1}	6.450	0.026
δ_2, GeV^{-1}	5.176	0.035
g_{od}	553.6	47.7
a_f	-10.75	0.75
α_f	0.5395	0.0185
a_ω	10.17	0.44
α_ω	0.4182	0.0131
χ^2/dof	1.56	

$0.01(GeV)^2 < |t| < 14(GeV)^2$. The grand total number of 2384 experimental points were used in overall fit. In the calculations we use the following normalization for the dimensionless amplitude:

$$\sigma_{tot} = \frac{4\pi}{s} ImA\,(s, t = 0)\,, \tag{15}$$

$$\frac{d\sigma}{dt} = \frac{\pi}{s^2}[|A_{00}(s,t)|^2 - \frac{t}{4{m_p}^2}\,|A_{01}(s,t)|^2]. \tag{16}$$

The resulting fits for σ_{tot}, ρ, $\frac{d\sigma}{dt}$ are shown in Figs. 1. - 2. with the values of the fitted parameters quoted in Table 1. From these figures we conclude that the multipole Pomeron model corresponding to a sum of gluon ladders up to two rungs complicated with Odderon contribution and spin counting fits the data well in a wide energy and momentum transfer regions. In this paper, we have explored only the simplest phenomenological tripole Pomeron. In fact, the scattering amplitude is much more complicated than just a simple power series in $\ln s$. On the one hand, although we used just a simplified t-dependence in the model, reasonably good results were obtained. Because the slopes of secondary reggeons do not influence the fit sufficiently, we have fixed them at $\alpha'_f = 0.84(GeV)^{-2}$ and $\alpha'_\omega = 0.93(GeV)^{-2}$, which correspond to the values of Chew-Frautschi plot, as well as its slope parameters $b_f = 12.0(GeV)^{-2}$ and $b_\omega = 14.0(GeV)^{-2}$. Additionally we fixed the Pomeron trajectory slope $\alpha'_P = 0.4(GeV)^{-2}$. On the other hand, we included the curvature of the Pomeron trajectory that cannot be negligible. The quality of our fits χ^2/dof=1.56 is comparable with that of the best fit of [25].

4 Summary

We have approved the tripole Pomeron model having each term corresponding to a finite gluon ladder.

This corresponds to the finite sum of gluon ladders with up to two rungs or alternatively up to the tripole Pomeron contribution. We have obtained very good description of pp and $\overline{p}p$ hadron scattering data at intermediate and high energies and all available momentum transfer. We conclude that the nonfactorisable form of the Pomeron and Odderon amplitudes as well as the nonlinearity of its trajectory and the residue function is strongly suggested by data at all available momentum transfer. It should be noted that the addition of spin-flip component of scattering amlitude decisively improves the result of the fit.

Acknowledgments

We are grateful to L.Jenkovszky and E.Martynov for valuable suggestions and A.M.Lapidus for fruitful discussions.

References

[1] E.A.Kuraev, L.N.Lipatov, V.S.Fadin, Zh. Eksp. Teor. Fiz. **72**, 377 (1977) [Sov. Phys. JETP **45**, 199 (1977)].

[2] Ya.Ya.Balitsky, L.N.Lipatov, Sov. J. Nucl. Phys. **28**, 822 (1978).

[3] L.N.Lipatov, Zh. Eksp. Teor. Fiz. **90**, 1536 (1986) [Sov. Phys. JETP **63**, 904 (1986)].

[4] V.S.Fadin, L.N.Lipatov, Phys. Lett. **B429**, 127 (1998) and references therein.

[5] R.Fiore, L.L.Jenkovszky, E.A.Kuraev, A.I.Lengyel, F.Paccanoni and A.Papa, Phys. Rev. **D63**, 056010 (2001).

[6] R.Fiore, L.Jenkovszky, E.Kuraev, A.Lengyel, F.Paccanoni and Z.Tarics, Phys. Rev. **D81**, 056001 (2010).

[7] A.Lengyel, Z.Tarics, Ukr. J. Phys. **58** 703 (2013).

[8] P.Desgrolard, M.Giffon, E.Predazzi, Z.Phys. **C63** 241 (1994).

[9] Yu.Iljin, A.Lengyel and Z.Tarics, Diffraction 2002, ed. R.Fiore et al. 109 (2002).

[10] V.A.Petrov, A.V.Prokudin, Eur. Phys. J. **C23** 135 (2002).

[11] K.J.Kontros, A.I.Lengyel, Z.Z.Tarics, Ukr. J.Phys. **47** 813 (2002); arXiv: 0011398v2 [hep-ph] (2001).

[12] I.M. Dremin, Uspekhi Fizicheskih Nauk **56** 3 (2013).

[13] TOTEM Collaboration G.Antchev, P.Aspell, I.Atanassov, V.Avati, J.Baechler, V.Berardi, M.Berretti et al, Europhys. Lett **95** 41001 (2011).

[14] TOTEM Collaboration G.Antchev, P.Aspell, I.Atanassov, V.Avati, J.Baechler, V.Berardi, M.Berretti et al, Europhys. Lett **101** 21002 (2013).

[15] A.Donnachie and P.V. Landspoff, arXiv: 1309.1292 [hep-ph] (2013).

[16] S.M.Troshin, N.E.Tyurin, Phys. Rev. **D88** 077502 (2013).

[17] L.Frankfurt, M.Strikman, arXiv: 1304.4308v1 [hep-ph] (2013).

[18] A.A.Godizov, arXiv: 1203.6013v3 [hep-ph] (2012).

[19] L.L.Jenkovszky, A.I.Lengyel, D.I.Lontkovskyi, Int. J. Mod. Phys. **A 26** 4755 (2011).

[20] A.I.Lengyel and Z.Z.Tarics, arXiv:1206.5837 [hep-ph](2012).

[21] Jan Kaspar, Vojtech Kundrat, Milos Lokajicek, arXiv:0912.1185 [hep-ph] (2009).

[22] D.A. Fagundes, G.Pancheri, A.Grau, arXiv: 1306.0452v1 [hep-ph] (2013).

[23] V.A.Petrov, A.Prokudin, arXiv: 1212.1924v1 [hep-ph] (2013).

[24] M.J.Menon, P.V.R.G.Silva, arXiv: 1305.2947 [hep-ph] (2013).

[25] E.Martynov, Phys. Rev. **D87**, 114018 (2013).

[26] File with the data "alldata-2.zip" is available at the address: http:/www.theo.phys.ulg.ac.be/alldata-v2.zip.

[27] K.G.Boreskov, A.M.Lapidus, S.T.Sukhorukov, K.A.Ter-Martirosyan, Yad. Fiz.**14** 814 (1971).

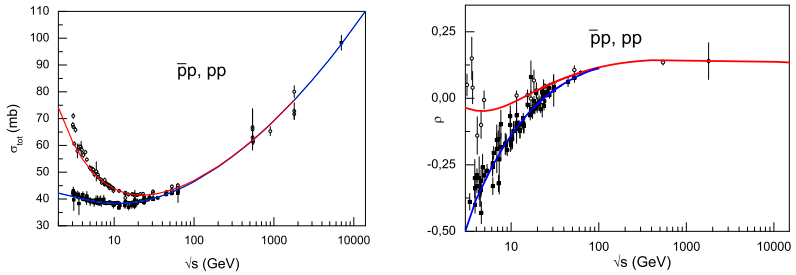

(a) (b)

Figure 1: (a) pp and $\overline{p}p$ total cross sections calculated from the model and fitted to the data in range $\sqrt{s}$ = 5 GeV–7 TeV. (b) Ratio of the real to imaginary part for pp and $\overline{p}p$ scattering amplitude calculated from the same model. Upper curve - presents the $\overline{p}p$ calculation, lower curve - present pp one.

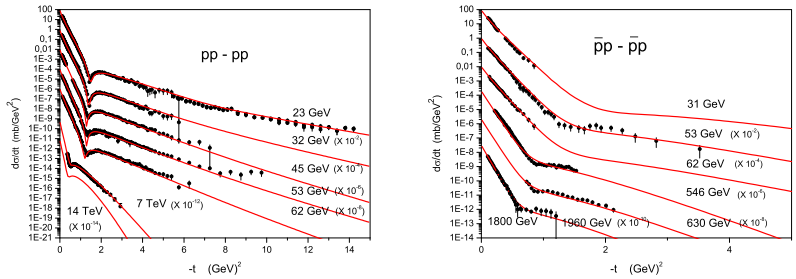

(a) (b)

Figure 2: (a) Differential pp (a) and $\overline{p}p$ (b) cross sections calculated from the model taking into account the spin and fitted to the data in the range $-t$ = 0.1 — 15 GeV^2.

Quark Wars

a particle physics outreach game in the age of Star Wars

T. Csörgő[1,2] and T. Novák[1]

[1]EKE KRC, H - 3200, Gyöngyös, Mátrai út 36, Hungary

[2]Wigner RCP, H-1121 Budapest XII,

Konkoly-Thege Miklós út 29-33, Hungary

December 16, 2016

Abstract:

Quark Wars is an all-new, adventure style game. We recommended playing it outdoors. Quark Wars is modeled upon the outdoor game called Hungarian Number War, with notable influence from Star Wars, the American epic space saga. The players form two opposing teams. Both teams elect their own leader. The team members and their leaders wear particle war bonnets on their foreheads. These headdresses consist of three or four cards indicating combinations of elementary particles. The two teams compete by identifying (reading out loudly) the elementary particle cards on the foreheads of their adversaries. Players are allowed to use the terrain to cover their particle identity on their foreheads and may try to hide, run or band together in a group to win. Quark Wars was tested at a Summer Camp of Berze Science Club in Hungary. Students loved playing Quark Wars, as this game resulted in lots of hilarity and action. In addition, Quark Wars also solidified particle terminology and made the concept of particle identification and discovery more tangible to secondary/middle school students.

1. Long time ago in a small village far, far away…

It is a period of particle war. Rebel student groups, striking from their hidden base, have won their first victory against the evil particle empire.

During the battle, student spies managed to steal secret plans to the Empire's ultimate weapon, the Quark Star, an armored particle accelerator with enough power to destroy an entire Planet.

Pursued by the Empire's sinister agents, Princess Lepton races home, custodian of the stolen plans that can save her people and restore asymptotic freedom to their quarks and to the Early Universe…
/Opening Crawl, with apologies to George Lucas [1]/

It was a roguish and hilarious day with a new game for the students in the Summer Camp of the Berze Secondary School in a small Hungarian village called Visznek. They had just learned about elementary particles and soon their survival depended on their ability to identify them. They were assigned to a difficult mission by their scientist patrons, namely to participate in the test of a new outdoor game called Quark Wars. This required that students develop not only some basic knowledge of elementary particles and focus their mind on some fundamental particle physics, but also tested their endurance, creativity, sneaking skills and fortitude.

The students were already introduced to some of the basic concepts and terminology of elementary particle physics, thanks to their familiarity with certain type of Quark Matter Card Games [2]. In these games, elementary particles like quarks and leptons are represented by particle cards. Csaba Török, a 17-year-old Hungarian secondary school student conceived the idea of a deck of elementary particles, and he created ANTI, the first of the Quark Matter Card Games [3], on the New Year's Eve of 2008/2009. Csaba was a member of the very same Berze Science Club, where the Quark Wars was first tested. Csaba had heard several outreach talks about particle physics in this Science Club before had the idea of representing quarks and leptons of the Standard Model on the faces of a deck of cards. His first game, ANTI was subsequently refined and developed to the so called Quark Matter Card Game [4] with the primary goal of entertainment and secondary goal as a science outreach tool. In this development, Csaba teamed with Judit Csörgő, another 17-year-old member of the Berze Science Club, who realized that these games could be taught even to pre-school 5-years-olds. Tamás Csörgő, Judit's father (and one of the co-authors of this article) also joined the team as a mentor and manager. He is a research physicist who works on experimental as well as theoretical high energy physics problems related to the RHIC accelerator at Brookhaven National Laboratory, USA and the LHC accelerator at CERN. Tamás also acts as the scientist patron of the Berze Science Club.

The Quark Matter Card Game of J. Csörgő, Cs. Török and T. Csörgő [2] provides several opportunities to have fun with elementary particles and anti-particles, in order to model the Big Bang, the formation of the Early Universe in the first few microseconds after its creation, or to play Quark Matter to model and popularize the time evolution of heavy ion collisions at RHIC and at LHC [2], to memorize quarks [5] or to search for your own Higgs boson [6]. Each of these games can be started on the level of laypersons, in an entertaining and delightful manner, in a way that triggers a learning spiral as the

players become more and more enthusiastic and sophisticated participants. The games are designed to scale well with the knowledge level of the participants, as we shall demonstrate here as well on the new game called Quark Wars.

2 Preparations and inventory

In order to be able to play Quark Wars, the students were first of all reminded about some fundamental concepts of elementary particle physics, as realized in the form of the Quark Matter Card Game. They were reminded that in these games two main groups of particles are included: quarks and leptons. Quarks are represented with cards colored red, green or blue, indicating that they participate in the strong interactions. According to Quantum Chromo Dynamics, the theory of the strong interactions, quarks and their anti-particles, called anti-quarks, have certain symmetry properties similar to that of the optical colors. Leptons are charged or neutral particles who do not participate in the strong (or color) interactions, so leptons are represented by black and white cards in the Quark Matter Card Games.

As each particle has an anti-particle, the question arises, how to represent (model) anti-particles on the faces of Quark Matter Cards. We emphasized that for leptons with electric charge, positive and negative signs indicate the electric charge of particle / anti-particle pairs, for example an electron is denoted by " e^- ", so its anti-particle, the positron is denoted by " e^+ ". Obviously, for the quarks with red, green, blue "color charges", and the anti-quarks should be modeled by the corresponding anti-colors.

But what are the anti-red, anti-green and anti-blue colors? In the model applied in the Quark Matter Card Games, anti-color is what makes a given color neutral i.e. white. This way, the anti-red is defined as a green/blue combination, while anti-green is blue/red and anti-blue is red/green. An important rule in the Quark Wars game is that quarks and anti-quarks can appear only in a color neutral or white combination of colors: a red, a green and a blue quarks may form a colorless, white particle called a baryon, a red and anti-red pair of quarks and anti-quarks (or a blue-anti-blue quark – anti-quark pair or a green-anti-green quark – anti-quark pair) forms a meson. The left panel of Figure 1 shows the students participating in this training section. The main idea of the game is indicated on the right panel of Figure 1, where one of their mentors, T. Novák is shown wearing a color neutral combination of quarks on his forehead as a kind of Particle War Bonnet.

Simple tools that are available everywhere can be used to transform the Quark Matter Cards to Particle War Bonnets: a page of a plastic name card holder, elastic rubber bands and cards representing elementary particle will do the job. A valid combination of quarks and anti-quarks or a pair of leptons and anti-leptons are inserted in the same page of the plastic name card holder, the page is cut out and fixed to the forehead of the players as indicated on Figure 2.

Figure 1. Science Club students being introduced to Quark Wars at the Summer Camp (left panel). One of the authors before the screen, wearing Quark Matter Cards as a kind of Particle War Bonnet on his forehead to demonstrate the main idea of this game.

Figure 2. Only a few things are needed to play Quark Wars: elastic rubber bands and a name card holder to keep the cards in position, and a deck of Quark Matter Card Game. The deck is included, for example in the Appendix of the booklet on Quark Matter Card game, shown in Hungarian here. This booklet is available and downloadable in English as well [2], suitable for printing, so that anybody with a color printer can prepare his or her own particle war bonnets for Quark Wars. The two competing teams are recommended to indicate their team, e.g., with the color code of the rubber band (here green or black) that is placed on their foreheads to keep the cards in place.

Figure 3. Two teams are formed, they have a brief (2-3 min) council on how they plan to win the game. Then the players put on their particle war bonnets and hide their team leaders so that members of the other team could not easily find and identify them.

The players form two teams and receive their quark matter war bonnets. The two teams separate and each have a council: team members come together to consult and to make decisions, to develop their plans and strategies on how to play and win the game. Then players put on their Quark Matter Card Game War Bonnets, but in such a way that members of the opposing team could not spy on them as seen on Figure 3, and start the actual Quark Wars.

3 Quark Wars – the goal and the course of the game

The **number of players** is, in principle, arbitrary, but in practice, it is best if both teams have 5 members or more, limited by available number of children in a classroom or in a summer camp.

The **object of the game** is to win, which can be either by identifying all players of the opposing team by leading out loudly the combination of elementary particles on their particle war bonnets, or, by finding and identifying (reading out loudly) the particle identity of the leader of the opposing team.

Due to this mission, during the **course of the game** it is **recommended** that the team leaders wear special particle war bonnets that correspond to Nobel prize winning elementary particles such as the H^0 Higgs boson [7,8] or the Ω^- baryon. When the fundamental theoretical predictions on the existence of these elementary particles were confirmed by experimental observations, Nobel prizes in physics were awarded to Peter W. Higgs and Francois Englert in 2013 [9], and to Murray Gell-Mann in 1969 [10], respectively. So identifying either a H^0 or an Ω^- during the course of Quark Wars identifies one of the team leaders and abruptly ends the Quark Wars game.

This goal also makes the game an interesting strategic game: when one of the teams has only a few members left, they can still try to break into the area of the enemy and to find a weakness in the defense of their opponents. Identifying the particle signs weared by the leader of the opposing team may result in winning the game, similarly how a small squadron of rebels may win the battle against a big army of imperial troops in the epic space opera Star Wars by attacking the Death Star on its weakest point. Due to this reason one of the team leaders can also be named informally as Luke Skywalker and the other as Darth Vader, however, both must wear their particle war bonnet during Quark Wars and can be identified on their particle name only. Identified players become

inactivated, they cannot continue their participation in particle hunting anymore, they become silent observers during the subsequent course of the game.

Note that light-sabers and other toy weapons are not permitted in the Quark Wars style game, not only for safety reasons, but also because we followed the rules of the so called Hungarian Number Wars [11], a game that was familiar to the participants of the Summer Camp of the Berze Science Club in Hungary. In this kind of games, the players are not allowed to cover their war bonnets on their foreheads with their hands. It is also not allowed to “worship the Earth” by lying down and pressing foreheads to the ground: this usually leads to identification by a group from the opposing team, who force the Earth-worshipper to turn up and identify him or her, but this strategy is not only unfair but also makes the game less interesting. The participants are allowed to cover themselves by pressing their foreheads to objects on the terrain such as trees, columns, buildings, and they are allowed to band together in groups of 2-4 to try to win, as indicated in Figure 4.

Figure 4. Players hiding their particle identities on their foreheads. One of the strategies is rushing: running forward while shaking their heads. Another, safer but slower strategy is to band in a group of 2, 3 or 4, pressing foreheads together. This method allows for a slower progress, but it also minimizes the possibility of being identified.

Much of the fun of the Quark Wars comes from the strategies that the players apply to hide their particle identities on their foreheads. One of the possible good strategies is rushing (running forward and shaking head simultaneously) as indicated on Figure 4. Rushing is designed so that reading out the card combination be difficult for the opponents. This allows fast progress but it is risky and physically challenging, needs practice for a good performance. Another, safer strategy is to band in a group of 2, 3 or 4, pressing foreheads together. This method allows for slow progress, and it minimizes the possibility of being identified. The drawback of banding is that it also makes it very difficult to identify anybody from among the opposing team, as the members of the band can hardly see from one another. The best seems to move so that the foreheads are covered with the objects on the terrain as much as possible, to move slowly if covered and to rush through the open areas to reach the terrain of the opponent team.

While the battle is ongoing, our heroes, the leaders of the teams may be just hiding in a safe place, to minimize the risk that they are identified and the other members of the teams try to protect their hiding places, chosen to be difficult to guess or figure out. As an example, during a test Quark War game, one of the team leaders, with particle war bonnet indicating an Ω^- particle was hiding behind the pull-down screen of the instruction room, as shown in the left panel of Figure 5. The other team leader, with a war bonnet representing a Higgs boson, was hiding in the middle of a haystack as indicated on the right photo of Figure 5. Eventually, all the team members of the Emperor's "Higgs boson" team were identified and hence removed from active participation by the Rebel team, the members of the team of Ω^-. Even in this period, it was quite a challenge for the surviving members of the Rebel Alliance or team Ω^- to find the hiding location of commander Darth Vader alias Higgs boson. Probably this was the first time in the history of particle physics outreach, that a symbolic Higgs boson was found and finally identified in a real hay-stack.

Figure 5. One of the team leaders, wearing a particle war bonnet of Ω^-, is hiding behind the pull-down screen, while the other team leader, with particle war bonnet standing for a Higgs boson (H^0) is hiding in a hay-stack.

It is customary that each player keeps a note of his or her own particle identity at hand, so that they could easily cross-check if their identification attempts were successful or not.

Valid combinations on the particle war bonnets include three quark combinations representing baryons (a triplet, combination of a red, a blue, and a green quark) anti-baryons (a combination of three anti-quarks, with anti-red, anti-blue and anti-green colors) as well as four card combinations. These four cards consist of two valid pairs, each of the pairs is a lepton-antilepton pair or a meson consisting of a quark and an anti-quark, where the color of the quark matches the anti-color of the corresponding anti-quark.

The other rules of Quark Wars follow in general the rules of **Hungarian Number War** game, which seems to be well known only in Hungary. For a reasonable English language summary of the rules of this fun outdoor game see ref. [11].

The Quark Wars game can be played on various knowledge levels, so it is a kind of well scalable particle physics outreach game. In this respect, Quark Wars is

similar to the Quark Matter [4], Memory of Quark Matter [5], or Find Your Own Higgs Boson [6] card games.

On a **layperson's or beginner** level, the players can read out only the quark or lepton cards to identify their opponents, for example: red u, green u, blue d! Or red u, anti-red anti-u and an electron-positron pair! They should, however, remember the combinations that identify the team leaders. It is recommended that the war bonnets of the opponent teams be fixed with rubber bands of different colors, e.g. black rubbers for one of the teams and green rubbers for the other team, as indicated on Figure 2.

On an **intermediate level,** the players should be instructed that the Ω^- baryon is a combination of a red s, green s and a blue s quark. The Higgs boson is identified through its leptonic decays, e.g., as two charged lepton-antilepton pairs. The possible Higgs decays that can be used for this purpose are given in Table 1 of [6], that we recapitulate here for completeness:

H^0 decay mode	Final state particles/cards
$H^0 \rightarrow \gamma,\gamma$ or $Z^0Z^0 \rightarrow$	e^+e^- e^+e^-
$\rightarrow$	e^+e^- $\mu^+\mu^-$
$\rightarrow$	$\mu^+\mu^-$ $\mu^+\mu^-$
$H^0 \rightarrow W^+W^- \rightarrow$	$e^+ \nu_e$ $e^- \bar{\nu}_e$
$\rightarrow$	$e^+ \nu_e$ $\mu^- \bar{\nu}_\mu$
$\rightarrow$	$\mu^+ \nu_\mu$ $e^- \bar{\nu}_e$
$\rightarrow$	$\mu^+ \nu_\mu$ $\mu^- \bar{\nu}_\mu$

Table 1. Possible Higgs decays as represented in the Quark Wars outreach game. On the beginner/layperson level, only one of this decays is used to identify one of the team leaders. After gaining more experience with the game, any of the above four particle card combinations can be used to indicate/symbolize one of the team leaders, marking the leader with a Higgs boson decay.

On an **advanced level,** combinations like red u, green u, blue d are not sufficient and acceptable to identify particles consisting of quarks (and/or leptons). Instead, the players should know that a color-neutral (white) combination of uud quarks stands for a proton, udd stands for a neutron, (u,anti-d) stands for a positive pion etc. These intermediate and more advanced levels can be practiced only with a supervisor or referee, who has some basic knowledge of hadrons and other elementary particles, and who can step in to decide if the particle identification was correct or not. Appendix A (Naming the hadrons) of ref. [4] can be used to find the tables that describe the quark contents of various hadrons, as represented by the cards of Quark Matter Card Game. Tables in Appendix A of ref. [4] form a kind of interface from particle physics outreach to the more substantiated e.g. quantum mechanical description of the quark contents of hadrons. These tables are not necessary to play Quark Wars on a beginner or intermediate level, but are useful to play quark wars on an advanced level. Teachers and promoters of Quark Wars should keep in mind that students prefer first of all to play and have fun, so we recommend to start the game on a layperson's level, with as many ordinary students as possible.

The players and in particular their supervisors are also **reminded to check any potential pitfalls and dangers on the terrain**. We recommend to take the children outside to play. It is a wonderful way to spend the day [12]. If no safe outdoor terrain can be secured, this game may also be played or tested indoors, like in a gymnasium or a sports hall of a school. This Quark Wars game is apparently well suited also for a future adaptation as a computer game, but most of the fun of it seems to come from real time

interactions among real players, when not only the intellectual but also the physical abilities like endurance, creativity, sneaking skills and fortitude of the participants are tested and also trained during the course of Quark Wars.

4 Summary

A new particle physics outreach game called Quark Wars has been developed and tested successfully in Hungary. About two dozens of secondary/middle school students (both boys and girls) participated in this test. Quark Wars as a particle physics outreach game brought together ordinary people like secondary and middle school students with teachers and scientists to do extraordinary things, and in doing so, they became part of something greater than themselves. Quark Wars, this new particle physics outreach game, not only resulted in lots of hilarity, hiding, running and yelling outdoors, but participating students also learned a good deal about particle terminology and gained a first-hand experience on how difficult it might be to locate and identify a hiding Higgs boson, and how big a pleasure it is to find and identify it eventually.

Acknowledgments

Thanks and credits are due to Ágota Lang, a physics teacher at the Széchenyi Secondary School in Sopron, Hungary: she had the first idea to create a particle physics outreach game based on the rules of the Hungarian Number Wars game. The authors thank Ildikó Pálinkás and Judit Pető for their careful reading of this manuscript and thank the sponsors of the WPCF 2014 conference in Gyöngyös, Hungary. The presentation of Star Wars at WPCF 2014 was partially supported by the he OTKA NK 101438 grant (Hungary).

References:

[1] Star Wars Opening Crawl, http://www.starwars.com/video/star-wars-episode-iv-a-new-hope-opening-crawl

[2] J. Csörgő, Cs. Török, T. Csörgő, *Quark Matter Card Game - Elementary Particles on Your Own* (2nd English Edition, ISBN 978-963-89242-0-9, 2011).

[3] Introduction to ANTI, a Quark Matter speed card game for two persons (in Hungarian): https://www.youtube.com/watch?v=tEpdTcwZ3xw

[4] Trailer for the Quark Matter Card Game: https://youtu.be/Sn56IEC9VSE

[5] J. Csörgő, Cs. Török, T. Csörgő: *Memory of Quark Matter,* arXiv:1303.2798 [physics.pop-ph] (2013)

[6] T. Csörgő: *Higgs boson – On Your Own*, arXiv:1303.2732 [physics.pop-ph], in Proc. EDS Blois 2013, Saariselka, Finland, September 2013

[7] ATLAS Collaboration: *„Observation of a new particle in the search for the Standard Model Higgs boson with the ATLAS detector at LHC"*, Physics Letters B 716 (2012) 1-29

[8] CMS Collaboration: *„Observation of a new boson at a mass of 125 GeV with the CMS experiment at LHC"*, Physics Letters B 716 (2012) 30-61

[9] The Nobel Prize in Physics 2013 was awarded jointly to François Englert and Peter W. Higgs "*for the theoretical discovery of a mechanism that contributes to our understanding of the origin of mass of subatomic particles, and which recently was confirmed through the discovery of the predicted fundamental particle, by the ATLAS and CMS experiments at CERN's Large Hadron Collider*", http://www.nobelprize.org/nobel_prizes/physics/laureates/2013/

[10] The Nobel Prize in Physics 1969 was awarded to Murray Gell-Mann *"for his contributions and discoveries concerning the classification of elementary particles and their interactions".* http://www.nobelprize.org/nobel_prizes/physics/laureates/1969/

[11] http://hungarykum.blogspot.hu/2015/10/mopdog-monday-capture-hungarian-flag.html

[12] K. Alfano: *The benefits of outdoor play.* http://www.fisher-price.com/en_US/parenting-articles/outdoor-play/the-benefits-of-outdoor-play .

Educational Challenges of Rubik's Cube

Sándor Kiss[1]

[1]Rubik Studio, Városmajor 74., Budapest, Hungary, H-1122

March 31, 2015

Abstract

The first 2x2x2 twisty cube was created as a demonstration tool by Ernő Rubik in 1974 to help his students understand the complexity of space and the movements in 3D. He fabricated a novel 3x3x3 mechanism where the 26 cubies were turning, and twisting independently, without falling apart. The cube was dressed in sophisticated colors which made it a unique puzzle. Even without instruction is the aim of the game was self-explanatory. Its educational value in VSI (Visual-Spatial Intelligence), developing strategy, memorization and logistics, improve concentration and persistence in problem solving is high in every age group. A logical puzzle has outreach far beyond. Those aspects are briefly covered in this article.

1 Introduction

The role of experience in learning has been researched since long. Let us pick up education, mathematics and puzzle. The relations among those 3 factors will or may determine the fate of a puzzle. The relations namely puzzle and education; mathematics and education; mathematics and puzzle; have been showing different behaviors on various puzzle objects. A well balanced mathematical and educational harmony of the puzzle is necessary, but not enough. The puzzle needs brain work and concentration, should give amusement, it should also engage the player and its attractiveness is preferable. In addition the puzzle's usability as educational tool is substantial value. Whether a new puzzle will bring success or will fail

the answer has been occultly determined above relations. The difficult point is how to interpret the message of puzzle-education-mathematics triad for a given puzzle?

Let us talk about the ordinary cube! Even a baby meets with the cube in early age and likes to play with it, without knowing that it is a solid with six congruent square faces, a regular hexahedron which has edges, faces, vertex, face diagonals and space diagonals, just no to go further except one more characteristic the symmetry, the beauty of cube. For a baby, for a young child the cube is fun, a challenging interesting shape. Two or more cubes are more amusing, it gives a rich feeling. Each cube can be personalized by dressing, can be used for construction, and can be moved, turned and thrown. As the toddlers are coming into kindergarten and school age they meet more cubes in various forms like a lump of sugar, a cake, cube cut food, a dice, a cube puzzle for kids, a furniture, a rock salt crystal, plus boxes, frames, ornaments and many cube shaped equipment and utensils. The cubes before everything else are good for toys and perfect for mind teasers. When children go to school and learning art, geometry and mathematics they may meet with variations of cube puzzles: soma, jigsaw cube, secret cubes, folding cubes and during the last four decades also the Rubik's Cube, the originator of family of twisty puzzles.

We can say in the kindergarten the cube is a toy, in elementary school the cube is more an object to study and its playfulness having been pushed into the background. Moreover in junior high schools the math of the cube receives priority. In this learning process familiarity is key factor for the teacher, and this notoriety greatly helps in transmitting the abstract knowledge of cube. This is the way how we did and they acquire the algebra and geometry of the cube, the Platonic object. The teaching comes with learning cube language as well i.e.; 6 cubed is 216, cube root of 27 is 3, the perfect cubes and so on, some day or other follows with more advanced descriptions e.g. octahedron is the dual polyhedron to the cube. However symmetry brings us to highest level, to isometries and group theories of the cube. But the main point is the better you know the more easily you learn. The teacher can also help the deeper understanding by offering choice between scientific approach and heuristic techniques. The steps upward in learning are student, teacher and science.

2 History

After having said that let us talk about Rubik's Cube. It is well known that the first 2x2x2 twisty cube was created as a demonstration tool by Ernő Rubik in 1974 to help his students understand the complexity of space and the movements in 3D. By turns of individual, but interrelated cubes changed their positions and a magical scrambling occurred. A new object was born, but no strategy existed how to put back the little cubes into starting order using. Ernő was both emotionally and intellectually captured by it. There was a structural problem, because the elastic band to keep the cubes together produced a knot and was torn soon. It was the next challenge for Ernő to fabricate a mechanism to overcome that problem. His novel construction gave birth to 3x3x3 cube. Now the cube layers were turning smoothly. The 26 cubies were turning, and twisting independently, without falling apart. Its symmetry implies perfectness.[1] A genuine invention, that

was an object supposed to be impossible before. The patent for his Spatial Logical Toy was granted within a short time on 28th of October, 1976. The cube was dressed in sophisticated colors which turned it into unique puzzle. Even without instruction is the aim of the game was self-explanatory.

The cube was ready, but how to put back the colors was unknown. Here was the next provoking challenge! Experimenting, perhaps better to say a discovery was necessary. Ernő had started the journey on unknown road and after had been into quite a few standoffs and dead ends he has arrived to a safe solution several weeks later. His strategy and his set of algorithms were necessary and enough to solve the cube from any scrambled position.

Of course the potential of his cube had been sensible more and more and gave vigorous reason to get it manufactured as soon as possible. But the cube had been born in a small country existing under communist regime. We "enjoyed" all the drawbacks of state monopolized companies and foreign trade behind the Iron Curtain. However Politechnika, a toy-industrial cooperative after nine months consideration was brave enough to sign a contract with Ernő. Production started and 12,000 pieces *Magic Cube* (Bűvös kocka) were produced in 1977. The official trading companies were not much interested; according to their opinion it was unsolvable, unsalable, unusual piece of junk. The toyshops cautiously placed order for 5000 cubes and without big noise all were sold within short time.

It happened like in the Aladdin fairy tail the lamp had rubbed inadvertently the Genie of the cube has been unleashed. Soon it was in the schools, also seized by teachers during lessons, and as present was given to scientists at conferences outside of Hungary. The Magic Cubes reached the world. The international commercial attempts often ended in vain, but gave a demanding challenge to do it! The scientists loved it and also faced such challenges: What kind of mathematics is hidden in it? Is there any similar function in physics, chemistry or nature? The support and enthusiasm from scientists was important, but it was just observed among buyers but hardly convinced them. Finding a potential business partner was a see-saw situation where one side changed frequently, but in 2 years Ideal Toys, USA went for it. The product as *Rubik's Cube* reached its media boiling point at New York Toy Fair in 1980 and right away took the world by storm.

3 Solution

Those were the exiting days when everyone had to find out the solution by oneself. The solution by manual era arrived next which was followed by the current web tutorial era. Scientifically the first step was the notation of the cube developed by David Singmaster to denote the sequence of moves. The diffusion of the cube among scientists was quick and raised theoretical excitement. Mathematical models and computer programs were developed; analogies in physics and among atomic particles just to name a few were pointed out. The appearance of cube overlapped the peak period in group theory research. Soon Rubik's Cube was selected as illustration of permutation groups. Almost simultaneously the society was shaken by wave of Rubik and cube stories, jokes, songs, cartoons, films, TV series and many more off sides. But definitely it also reached education institutes quite early. Nowadays on the web anyone can select from the plethora of

solutions online, surf the social impacts of the cube, wonder the effects on art, architecture, literature, fashion and competitions, follow the records connected to Rubik's Cube and enjoy scientists' talks about it. A huge collection is waiting for correct categorization and systematic processing.

4 In Education

Scientists who were dealing with Rubik's Cube gave lectures and composed tasks with it for exercise. That was a timely initiative as most of the students were perplexed already by cube. At university level of education each explanation generated request to answer more new queries. It became a compulsory topic in group theory and abstract algebra curriculums. Search for the minimum necessary moves was on high before long. In 2010 utilizing idle time of Google's servers was concluded that God's Number is 20, but it was done by programmed brutal force but the proof is still missing. [2]

Let us proceed to middle and elementary school. Teachers today attracted to the puzzle-solving lesson because it helps to learn mathematics and develops direction-following and memorization plus persistence. But there was a complete different standpoint at the beginning. The Hungarian National Institute of Pedagogy turned down Ernő's initiative to use it in education in 1976 as improper teaching tool. After having the great 1980 success more and more teacher set out to use with good results, but the sales of the cube dropped to negligible level at mid eighties and the speedcubing competitions give a little bust and kept it alive during the nineties. This also downward affected the cube's role in education. Also the torrent of new twisty puzzles drove teacher's intentions into a corner; latest ones might be more attractive than good old cube.

By turn of the century speedcubing was gaining popularity all over the world due to new teenage generation with strong competition spirit supported by wide use of internet. Also it was a decisive factor that the World Cube Association had been established in 1999. WCA laid down standards and rules, governs competitions and keeps records for all puzzles labeled as Rubik.

After celebrating the 30th birthday of Rubik's Cube it became opportune to do something for education. During the past three decades teaching methods have developed and experiments in schools here and there have accumulated a lot of results. Furthermore we have seen new cube like puzzles, for example the void cube without center cubies on all three axes, or giant cubes with as many as 6, 7 or even 10 cubies across cube faces since 2000. Also the family of odd shapes twisty puzzles was grown by dodecahedron, bandaged cubes and so on. Many interesting puzzles, but they have received less and less attention on the market.
Ernő always supported the introduction of the cube to education at all levels. The spatial awareness is still not strong enough in schools worldwide. Most of the spatial teaching tools to meet are of classical unmoving type. It makes a big difference seeing 3D demos versus taking a workable model into own hands. The latter one builds confidence and also helps underachieving students. His initiative and long wish was taken up by Seven Towns, the company behind the world success of the Rubik's Cube. After several year

of preparation the project You CAN do the Rubik's Cube program was launched in 2010. This complex program is to help students across the U.S. and beyond realize their potential while emphasizing teamwork, "outside of the box" thinking, and creativity.[3] Now the Rubik's Cube is in the STEAM (Science, Technology, Engineering, Art, Mathematics) project, which offers the teachers MATH methodology: M – Modify the lesson for understanding; A – Apply the lesson to repeated practice; T– re-Teach the lesson for mastery; H – Higher level learning for enrichment. The need for You CAN do the Rubik's Cube project is justified by 31,000+ implemented packages so far.

5 Summary

The 40th birthday brought the internationally-acclaimed Beyond Rubik's Cube exhibition at Liberty Science Center in New Jersey in 2014 and also we said Happy Returns of the Day to Ernő on his 70th birthday on 13th of July. The BRC exhibition will travel to several cities around the world (Cleveland and Edmonton, Canada in 2105) and hopefully after 5-7 years it will arrive to Budapest. Its interactive content will be monitored, changed and renewed as changes of time would request. We can just repeat Julius Ceasar's famous phrase Alea iacta est, i.e. events have passed a point of no return. The Rubik's Cube now has been living his own life.

One can hardly close this ever developing story, because new developments have been coming since 1974. Instead of closing remark let me quote John von Neumann:

> "By and large it is uniformly true that in mathematics that there is a time lapse between a mathematical discovery and the moment it becomes useful; and that this lapse can be anything from 30 to 100 years, in some cases even more; and that the whole system seems to function without any direction, without any reference to usefulness, and without any desire to do things which are useful." [4]

References

[1] Marcus du Sautoy: *Symmetry, reality's riddle*. TEDGlobal lecture 2009.

[2] Tomas Rokicki, Herbert Kociemba, Morley Davidson, John Dethridge: *God's Number is 20* (2010).

[3] Rohrig, Brian: *Puzzling Science: Using the Rubik's Cube to Teach Problem Solving*. Science Teacher, Volume 77, No. 9 p54-56, Dec 2010. See Rohrig's article.

[4] John von Neumann: Collected Works vol. VI, p. 489.

Qbe: Quark Matter on Rubik's Cube *

T. Csörgő[1,2]

[1]EKE KRC, H-3200 Gyöngyös, Mátrai u. 36, Hungary
[2]Wigner RCP, H-1121 Budapest XII, Konkoly-Thege 29-33, Hungary

February 23, 2017

Abstract

Quarks can be represented on the faces of the 3x3 Rubik's cube with the help of a symbolic representation of quarks and anti-quarks, that was delevoped originally for a deck of elementary particle cards, called Quark Matter Card Game. Cubing the cards leads to a model of the nearly perfect fluid of Quark Matter on Rubik's cube, or Qbe, which can be utilized to provide hands-on experience with the high entropy density, overall color neutrality and net baryon free, nearly perfect fluid nature of Quark Matter.

1 Introduction

In 2011, Cs. Török, a 17 years old secondary school student in studying Gyöngyös, Hungary invented a card game with elementary particles [1]. By 2014, this Quark Matter Card Game became an invention, a patent and a product. Initially, four different kind of games were described in the first edition of a the book "Quark Matter Card Games - Elementary Particles, Playfully" playable with the same deck of 66 cards, representing elementary particles from the Standard Model of particle physics. By now about a dozen of various card games are invented, all based on the same deck of Quark Matter Card Game. Some of these games are described in the public domain, like the memory style quark matter card game [2] (where

*Dedicated to the 10th anniversary of the discovery of the perfect fluid of quarks at RHIC as well as to the 40th anniversary of the invention of Rubik's Cube.

pairs or triplets of particle cards are to be remembered) and its advanced version, called "Find your own Higgs boson" [3] where a Higgs boson is identified from its leptonic decay modes, that requires to remember four cards in an advanced, memory style game. In the so called Quark Matter Card Game, Figure 1, the players can familiarize themselves not only with some of the elementary particles that are the fundamental constituents of matter, but also with the properties of Quark Matter, the recently discovered new phase of matter, that behaves not as a gas but as a perfect fluid of quarks. Such a perfectly flowing Quark Matter filled our Early Universe just a few microseconds after the Big Bang. In 2004, this old-new state of matter was discovered in high energy heavy ion collisions at the RHIC accelerator at BNL, located on Long Island near New York, NY, US. Subsequently, the properties of Quark Matter were confirmed at larger colliding energies at the LHC accelerator, located beneath the France-Switzerland border near Geneva, Switzerland.

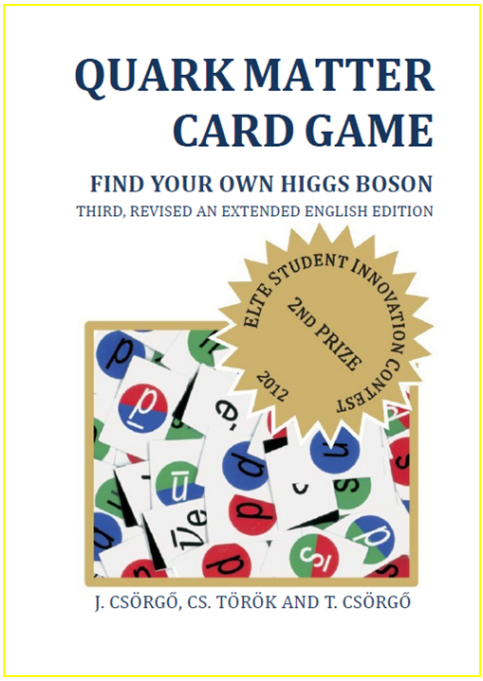

Figure 1: English language edition of Quark Matter Card Gamethat describes games with a deck of elementary particle cards, including a model the Early Universe just a few microseconds after the Big Bang [1]. Pick up a deck of Quark Matter Cards and you can play heavy ion collisions too, for a tiny fraction of the cost of doing an actual experiment at the RHIC or LHC accelerators.

Recently, an outdoor game called "Quark Wars" was also developed and tested, that utilizes the deck of Quark Matter Cards. Quark Wars is modelled on the so called "Hungarian number wars" outdoor game, with notable influence of the American epic space saga "Star wars" [4].

In addition to being a contribution to the proceedings of the WPCF 2014 conference, this manuscript is also an extended and updated version of a handout booklet, distributed by the Guests, Users and Visitors Center of Brookhaven National Laboratory at the 2015 AGS and RHIC Users Meeting, that was dedicated to the 10th anniversary of the publications of the so called RHIC White Papers, announcing the discovery of the prefect fluid of quarks [5, 6, 7, 8].

2 Anniversaries

In 2014, we celebrated several anniversaries:

- 1944, 70 years before: Ernő Rubik was born in Budapest, Hungary [9].
- 1954, 60 years before: CERN, the European Laboratory for Particle and Nuclear Physics was founded [10].
- 1974, 40 years before: Mr. Rubik created the prototype of his cube [9].
- 2004, 10 years before: The perfect fluid of quarks was discovered in gold-gold collisions at BNL's RHIC accelerator [5, 6, 7, 8]

In the followings we present, how one can "dress up" or decorate a 3x3 Rubik's Cube with colored quarks and anti-quarks, using a symbolic notation of quarks and anti-quarks, as developed for the Quark Matter Card Game. This manner, Rubik's Cube becomes Qbe, a model or a symbolic representation of Quark Matter on Rubik's 3x3 Cube, corresponding to a special Cube dedicated to the promotion or popularization of the properties of the Perfect Fluid of Quarks.

The Perfect Fluid of Quarks or Quark Matter is the hottest known form of matter ever made by humans, with temperatures reaching above 5×10^{12} Kelvin in heavy ion collisions at CERN LHC [11]. Such a prefect fluid of quarks has been detected in the debris of high energy heavy ion collisions at BNL's RHIC accelerator and the results were confirmed at larger initial colliding energies at CERN's Large Hadron Collider (LHC). The perfectness of Quark Matter corresponds to its flowing properties: the natural, internal scale of dissipative motion called kinematic viscosity of this fluid is found to have the lowest value from among the known, human-made materials.

This conference contribution was first presented in 2014, at the 10th Workshop on Particle Correlations and Femtoscopy. By now, quite some time has been passed since 2014, but at that time it was natural to dedicate the Quark Matter Cube (in short, Qbe) to the 10th anniversary of the Perfect Fluid of quarks created in gold-gold collisions at BNL's Relativistic Heavy Ion Collider. The artist's view of Qbe is presented on Figure 2 .

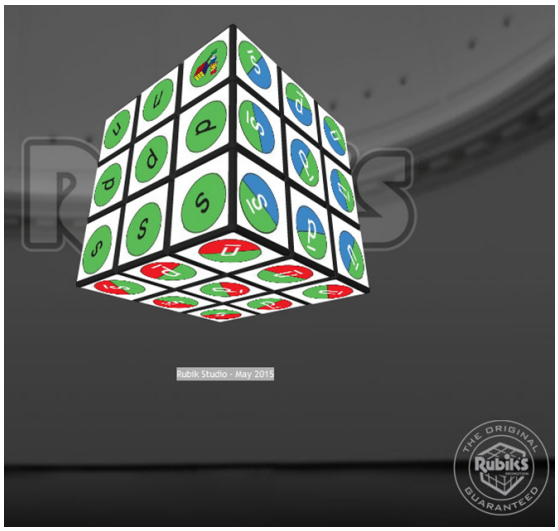

Figure 2: Qbe, the Quark Matter Cube, representing the perfect fluid of quarks that filled the our Universe just a few microsecond after the Big Bang. Image and the corresponding animation of Qbe is the courtesy of Rubik Studio Ltd., [12].

3 Quark Matter on Rubik's Cube - Playfully

Our current knowledge about the fundamental constituents of matter is summarized in the so-called Standard Model of Particle Physics. The elementary particles of the Standard Model can be arranged in the form of a 4x4 table, where the first 3 columns represent the three generations or families of matter-like particles (fermions) and the last column represents the interaction-mediating particles (bosons).

A playful representation of the most frequent matter-like particles was worked out in the year of 2011, in the form of so called Quark Matter Card Games, as illustrated on Figure 3. This representation is detailed in refs. [2, 3].

In 2012, as an extra bonus to this 4x4 table, the last missing piece, the so called Higgs boson of the Standard Model was also discovered experimentally. A card game that popularizes the discovery of the Higgs boson is detailed elsewhere [3]. Here we focus on the gamification and modelling of the properties of Quark Matter, the perfect fluid of quarks discovered at RHIC and confirmed at LHC.

The theory of the strong interactions, Quantum Chromo Dynamics (QCD) has some mathematical properties that are analogous to the properties of the optical colors. Due to this mathematical analogy the quarks can be modelled with cards that have optical colors: quark cards are colored to red, green and blue, the three fundamental colors in the RGB color space. One of the exact laws of QCD is that only those combinations of quarks are experimentally observable, that correspond to a color neutral (white) combination of quarks. One should also emphasize that Color in Quantum Chromo Dynamics is not to be confused with the visible, optical colors, but it can be understood as an optical model or analogy that reflects well the mathematical properties of the physical theory QCD and that analogy is used here to model strongly interacting fundamental particles called quarks and anti-quarks.

For an introduction on the birth of the quark concept that lead the way to the development of QCD as the theory of strong interactions as well as to the first ideas

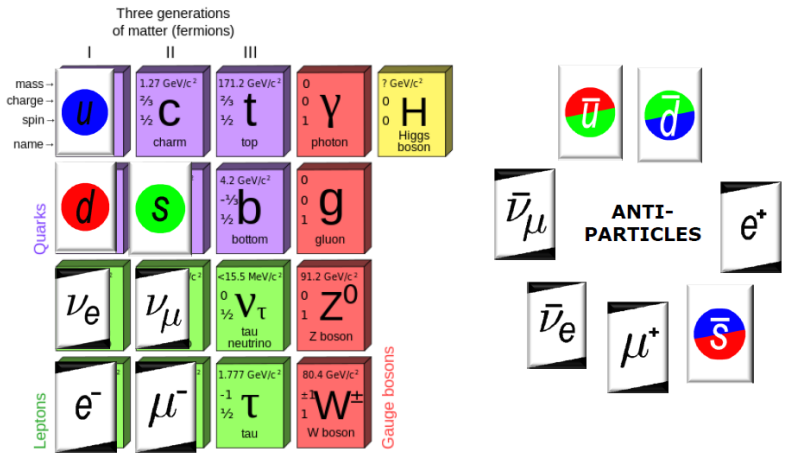

Figure 3: Elementary particles of the Standard Model – playfully, using the representations in the Quark Matter Card Game. Anti-particle representations are also included.

on the analogy of optical colors to model certain symmetry properties of the strong interactions, we recommend two early articles by Zweig and Gell-Mann [13, 14].

Importantly, another exactly satisfied law of elementary particle physics states that for each particle, a there exists a corresponding anti-particle, which is opposite in each properties to the given particle. For example, electron is an elementary particle with negative charge, so its antiparticle, the positron has a positive charge. But what is the opposite color to the red color? In the Quark Matter Card Games, we have chosen a combination of green and blue colors to model (symbolically represent) the anti-red color, because the green and blue combination supplements red to form a neutral, white color. Similarly, anti-green is defined as a combination of blue and red, while anti-blue is a red-green combination. Three major groups of color neutral or white particles can be formed: mesons or quark-antiquark color white bound states, baryons (bound states of red, green and blue quarks) and anti-baryons (bound states of anti-red, anti-green and anti-blue quarks), as indicated on Figure 4.

With the help of the colored quarks and antiquarks, and the six faces of Rubik's cube, one create a customized version of Rubik's cube in the following manner: Three faces that join in a single corner of the cube are selected to have red, green and blue colors. The diagonally opposite corner of the cube is selected to be the place where the anti-colored faces meet. The three most abundantly produced quarks (u, d and s) are also indicated on these little faces. The coloring scheme for the cube is such that quarks with a given color are on opposite faces with anti-quarks with the corresponding anti-color. For example the red quarks are opposite to the green/blue anti-quarks. Thus the opposite faces of Qbe combine to a white color, hence Qbe has an overall white color. This design, or the dressing up of Rubik's cube as Qbe or Quark Matter Cube is laid out on Figure 5.

Such a design can be well compared to the color scheme of the original Rubik's cube. This is illustrated on Figure 6. The Rubik design is dressing up opposite faces with color and color + yellow color: the white face of Rubik's cube is opposite to

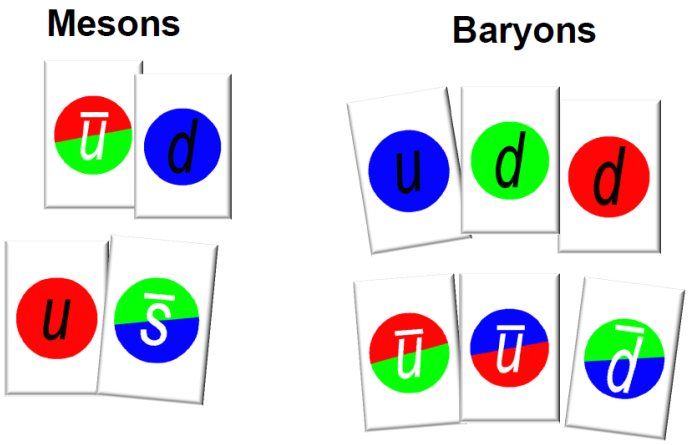

Figure 4: Mesons are colorless (white) combinations of a quark and an antiquark, that is represented in the Quark Matter cards as a red, green or blue quark card matched with an anti-red (green/blue), anti-green (blue/red) or anti-blue (red/green) pair of cards. Baryons are represented by a red, a green and a blue quark card, forming also a colorless (white) combination of three quarks. Anti-baryons are also colorless, they can be formed from an anti-red, anti-green and anti-blue Quark Matter card.

the yellow, red is opposite to orange and the blue face is opposite to the green face. On Qbe, the three faces with the fundamental red, green and blue colored quarks are placed opposite to the three faces with the fundamental anti-colors: anti-red, anti-green and anti-blue. This color scheme of Qbe reflects faithfully the overall color neutrality or whiteness of Quark Matter.

In the Early Universe, just a few microseconds after the Big Bang, Quark Matter is created in a special way, namely the number of quarks and the number of anti-quarks were almost exactly the same at that time. This is property of the Early Universe is faithfully represented: on Qbe the number of quarks is exactly the same as the number of antiquarks, as apparent from Figure 5. In the deck of cards of the Quark Matter Card Game, the number of quarks is larger than the number of anti-quarks, corresponding to the properties of Quark Matter created in high energy heavy ion collisions at man-made accelerators.

The mathematical properties, namely the possible number of color configurations on Rubik's cube are compared to the properties of Qbe on Figure 7. We emphasize that the position of the u, d and s quarks in a heavy ion collision is physically a relevant quantity as the masses and other properties of these quarks vary. So we suggest to distinguish the physical orientations of Qbe, which gives an extra 6x4 $=$ 24 factor for its number of states. In addition, due to the u, d and s letters written on the facelets to represent quarks, the face-center facelets are oriented so the total number of possible configurations of Qbe, the Quark Matter cube is larger than the number of states on Rubik's cube. The logarithm of the number of states corresponds to the entropy content of these cubes. The entropy divided by volume defines their entropy density.

The entropy density of Qbe the perfect fluid of quarks on Rubik's 3x3 cube can

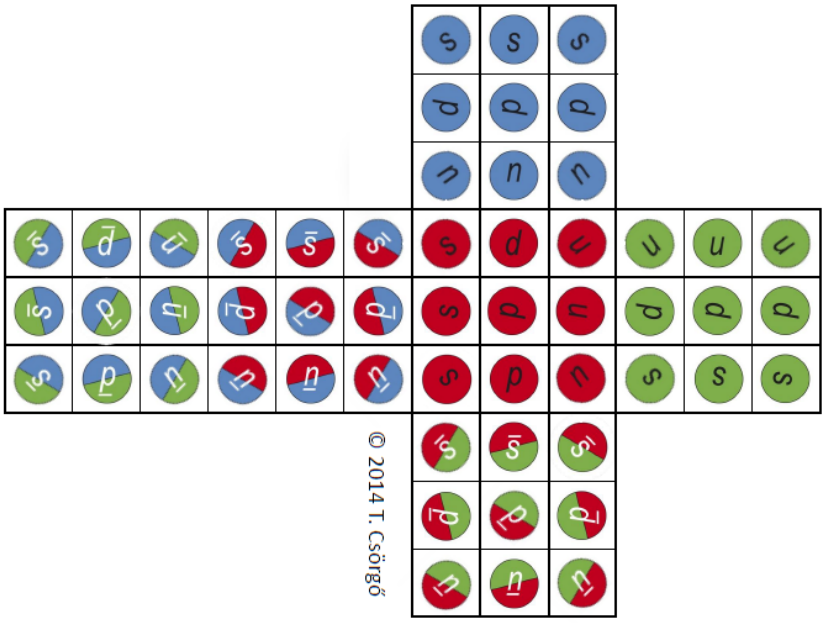

Figure 5: Layout of Qbe, the perfect Fluid of Quarks on Rubik's 3x3 Cube.

be compared to the entropy density of quark matter created in heavy ion collisions at RHIC and LHC accelerators. To have the same entropy density as Quark Matter, Qbe should be scaled down too much, from 57 mm to $2x10^{-12}$ m, but instead of scaling the cube down, we suggest use Qbe as a model of Quark Matter that fits

Original Rubik's Cube	PF Quarks Cube
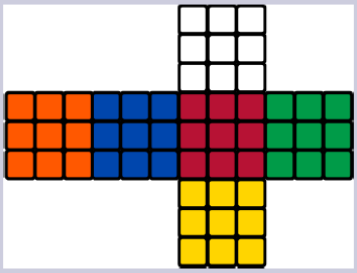	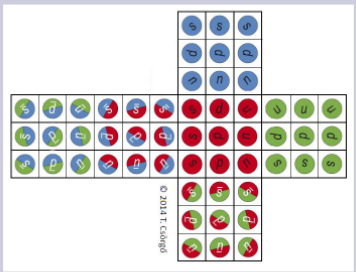
(red, orange)	(red, anti-red)
(white,yellow)	(green, anti-green)
(blue,green)	(blue, anti-blue)

Figure 6: Comparison of the color scheme of Qbe with the color scheme of the original Rubik's 3x3 cube.

suitably the size of our hands. The physical properties of Qbe the Quark Matter Cube can thus be compared also to the physical properties of Quark Matter, as summarized on Figure 8.

Original Rubik's (magic) cube:	**Quark matter (fluid) cube:**
3x3x3 cube, 6 colors 8 corner cubes: 3 colors, 3 positions 12 edge cubes: 2 colors, 2 positions 6 face centers: 1 color, 1 position Even permutations only!	3x3x3, 3 colors+3 anti-colors 8 corner cubes: 3 colors, 3 positions 12 edge cubes: 2 colors, 2 positions 6 face centers: 1 color, 4 positions Even permutations only!
Corner cubes: 8! permutations $3^8/3 = 3^7$ possible orientations Edge cubes: 12! permutations $2^{12}/2 = 2^{11}$ possible orientations Face centers: no orientation Cube: indifferent global orientations	Corner cubes: 8! permutations $3^8/3 = 3^7$ possible orientations Edge cubes: 12! permutations $2^{12}/2 = 2^{11}$ possible orientations Face centers: $4^6/2 = 2^{11}$ orientations Cube: 6x4 different orientations
Number of possible states: $8! \times 3^7 \times 12! \times 2^{11} \times 1 \times 1 / 2$ $\sim 4.3 \times 10^{19}$	Number of possible states: $8! \times 3^7 \times 12! \times 2^{11} \times 2^{11} \times 24 / 2 \sim$ 2.1×10^{24}

Figure 7: Comparison of mathematical properties of Qbe and Rubik's Cube.

	Original Rubik's Cube	**PF Quarks Cube**
Number of states, N	43252003274489856000	21259224694947725402112000
Entropy, S = ln N	~ 45.21	~ 56.02
Length, L [mm]	57	57
Entropy density $\sigma = S/L^3$, [m^{-3}]	~ 2.4×10^5	~3.0×10^5

Comparison to Nature	**Perfect Fluid of Quarks**
Energy density, ε [GeV/fm^3]	15
Speed of sound, c_s^2	0.1
Temperature, T [GeV]	0.22
Entropy density $\sigma = (1+c_s^2)\ \varepsilon /T$, [$m^{-3}$]	7.5×10^{46}

For a perfect model:
$L' = L/ 25^{1/3}/10^{10}$
$L' \sim 2 \times 10^{-12}$ m

Figure 8: Comparison of physical properties of Qbe and Rubik's Cube.

4 Discussion

The connection between the symmetry properties of quarks and Rubik's cube with twisted corner pieces has been noted by Golomb already in 1981 [15]. His article determined the number of color configurations on Rubik's cube as well. Marx and

collaborators considered Rubik's cube as a kind of world model, with conservation laws and transformation rules and they noted how baryons and mesons might be represented with Rubik's cubes with twisted corner or edge cubelets [16]. Hofstadter picked up the idea of Golomb and noted the importance of variations on the same theme as a key element to innovation. His 1982 article made Rubik's Cube with a twisted or "quarked" corner piece to the cover page of Scientific American [17]. However, as far as we know, Quark Matter with colored quarks and anti-quarks was not considered in the context of a Rubik's cube before.

Although the mathematical and engineering aspects of the Rubik's cube were summarized already in 1987 by E. Rubik and collaborators [18], some of the mathematical aspects of the Rubik's cube imposed deep and difficult problems. For example, the minimum number of rotations that are needed to reach any given configuration from a perfectly ordered Rubik's cube (the so called God's number) was proven to be 20 by Rokicki only in 2014 [19]. As far as I know the God's number for Qbe or other generalized Rubik's cubes with oriented face centers is not yet determined.

The educational values of Rubik's cube in visual-spatial intelligence, developing strategy, improving memorization, concentration and persistence in problem solving as well as the marketing values of Rubik's cube in popular Science, Technology, Engineering and Mathematics (STEM) were overviewed recently in ref. [20].

Let us mention, that Rubik's cube was recently envisioned as a model for describing the change of the interiors of black holes while emitting a Hawking particle and thus decreasing the size and corresponding the entropy of a black hole. This processs was conjectured to be analogous with solving the Rubik's cube [21]. This analogy between an evaporating black hole to vacuum and solving the Rubik's cube from a large initial entropy / disorder to a color ordered, zero entropy state may provide further inspiration for follow-up STEM gamification and outreach studies.

To illustrate that quite some time and wisdom might be needed to solve Qbe, let us estimate how many rotations might be needed in every second, if we would try to solve it just by random rotations. Our Universe is about 13.8×10^9 years old and the number of states on Qbe is given in Figure 7 as approximately 2.1×10^{24}. As the lifetime of our Universe converts to about 4.35×10^{17} seconds, one would need to rotate the Qbe a littlebit more than 4.8 million times in every second, for the entire lifetime of our Universe, to be able to solve it just by random rotations. Such a tremendous mindless effort can be contrasted to the various records of solving Rubik's cube using skillful means in speed cubing championships: The current world record for single time on a $3 \times 3 \times 3$ Rubik's Cube was set by Feliks Zemdegs of Australia in December 2016 with a time of 4.73 seconds at the POPS Open 2016 competition in Melbourne, Australia [22].

Let us close this article by noting that what we discussed here was just a toy or a toy model, that does not have to be taken too seriously. In this sense this outreach article is quite similar to many studies in science. A model is just a model, reflecting certain properties of the reality and is best understood with a certain smiling playfulness, similar to the mysterious smile on the face of Mona Lisa. The Road to Reality is often a difficult one but our journey may become much more enjoyable, perspiacious and lightsome if we proceed with a touch of smiling wisdom, as illustrated on Figure 9.

The Appendix of this contribution is organized as a handout booklet, to be distributed with Qbes or Quark Matter Cubes.

Acknowledgments

Inspiring discussions with S. Kiss are greatfully acknowledged. The presentation of Quark Matter on Rubik's 3x3 Cube at the WPCF 2014 conference in Gyöngyös, Hungary has been partially supported by the OTKA NK 101438 grant.

Availability

Limited number of Qbes, Quark Matter on Rubik's Cubes were distributed first as promotional gifts to the participants of the WPCF 2014 conference in Gyöngyös, Hungary. As science outreach gifts, they are also made available at the BERA Shop in the Berkner Hall at Brookhaven National Laboratory, Upton, NY, USA, since June 2015. A limited number Qbes is available just as well in the Iijima Shoten in KEK, Tsukuba, Japan.

References

[1] J. Csörgő, Cs. Török, T. Csörgő: *Quark Matter Card Game - Elementary Particles on Your Own* Lulu Press (2011), ISBN 978-963-89242-0-9.

[2] J. Csörgő, Cs. Török and T. Csörgő, arXiv:1303.2798 [physics.pop-ph].

[3] T. Csörgő, arXiv:1303.2732 [physics.pop-ph].

[4] T. Csörgő and T. Novák, arXiv:1612.05200 [physics.pop-ph].

[5] I. Arsene *et al.* [BRAHMS Collaboration], Nucl. Phys. A **757** (2005) 1

[6] K. Adcox *et al.* [PHENIX Collaboration], Nucl. Phys. A **757** (2005) 184

[7] B. B. Back *et al.* [PHOBOS Collaboration], Nucl. Phys. A **757**, 28 (2005)

[8] J. Adams *et al.* [STAR Collaboration], Nucl. Phys. A **757** (2005) 102

[9] The Cube Story:
`https://eu.rubiks.com/about/the-history-of-the-rubiks-cube/`

[10] 60th anniversary of CERN: `http://cern60.web.cern.ch/en/news`

[11] Highest man-made temperature, a Guinness world record:
`http://www.guinnessworldrecords.com/world-records/highest-man-made-temperature`

[12] Animation of Qbe, the perfect fluid of Quark Matter on Rubik's Cube:
`http://www.rubiksanimations.com/cube/Perfect%20Fluid%20Cube?_lang=en`

[13] G. Zweig, Preprint CERN-TH-401 (unpublished).

[14] M. Gell-Mann, Acta Phys. Austriaca Suppl. **9** (1972) 733.

[15] S. W. Golomb, Am. J. Phys. **49** (1981) 1030.

[16] Gy. Marx, Éva Gajzágó, P. Gnädig, Eur. J. Phys. **3** (1982) 39.

[17] D. R. Hofstadter, Sci. Am. **247**(4) (1982) 14-21.

[18] E. Rubik, T. Varga, G. Kéri, Gy. Marx, T. Vekerdy: *Rubik's cubic compendium.* Oxford University Press (1987), ISBN-10: 0198532024.

[19] T. Rokicki, et al., SIAM Review **56**(4) (2014), 645-670.

[20] S. Kiss, arXiv:1505.00750 [math.HO].

[21] B. Czech, K. Larjo and M. Rozali, JHEP **1108** (2011) 143

[22] Records with Rubik's Cube:
`https://en.wikipedia.org/wiki/Rubik's_Cube#Records`

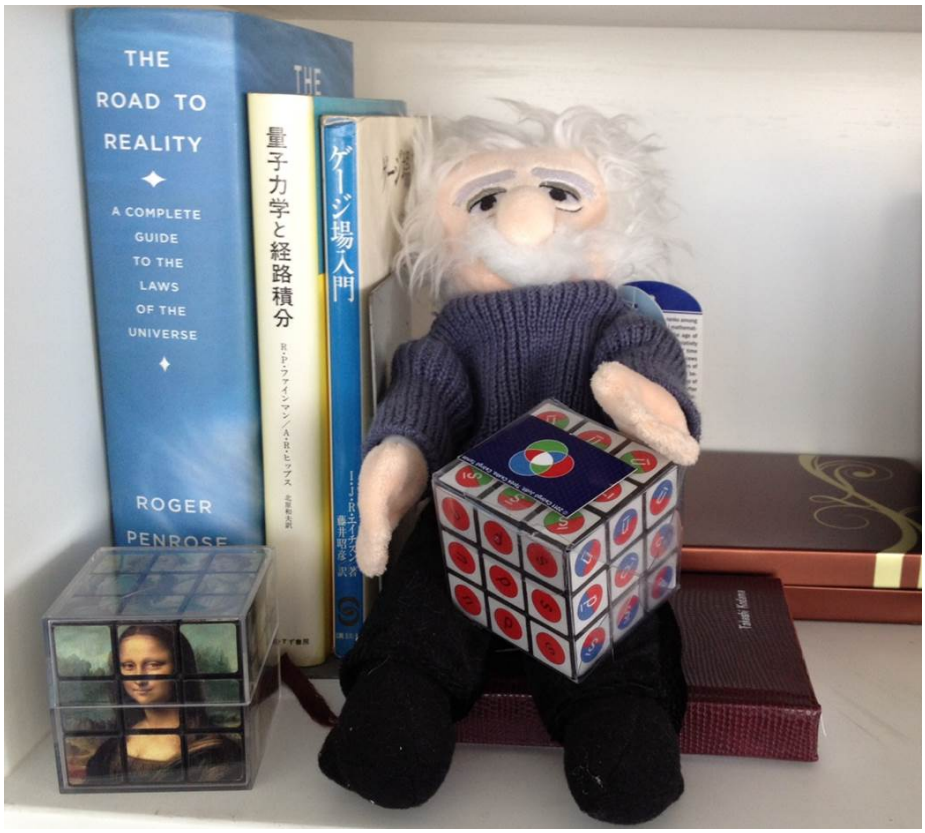

Figure 9: Figure of Albert Einstein, the smile of Mona Lisa and Qbe: Quark Matter on Rubik's 3x3 Cube, next to the Road to Reality: A Complete Guide to the Laws of the Universe. Photo courtesy of prof. T. Kodama, Rio de Janeiro, Brazil.

Legal info and image rights

The "Quark Matter Card Game" and the corresponding deck and representation of elementary particles on cards, commercial and design rights and copyrights are reserved and rest with the Authors.

The RUBIK'S CUBE in its three dimensional form and any graphic or photographic representation of it, in any configuration, colored or uncolored, whether or not it carries the RUBIK'S CUBE name or logo, is protected by intellectual property laws throughout the world. Rubik's Brand Ltd. owns all the international rights in the RUBIK trademarks and in the overall image of the RUBIK'S CUBE. The copyright belongs to Ernő Rubik, the originator of RUBIK'S CUBE who has given Rubik's Brand Ltd. full and exclusive authority to license and administer his rights, and to pursue by whatever legal means necessary any infringement of such rights.

Handout for Qbe: Quark Matter on Rubik's Cube

Perfect Fluid Promotion: Qbe or Quark Matter on Rubik's 3x3 Cube is not only fun but also a promotional tool to introduce and illustrate certain unusual properties of the perfect fluid of quarks. A perfect fluid can flow without internal dissipation. So the perfect fluid of Quark Matter could be modelled faithfully by a perfectly lubricated Rubik's cube, suited perfectly for speed-solving competitions.

Number of players: Typically one person, but speed and memory cubing competitions can be organized.

Object of the game: The goal is to solve a fully scrambled Qbe - Quark Matter on Rubik's 3x3 Cube by reaching its color-flavor-locked ground state. Flavor locking means in this context that the letters representing d flavoured quarks on the face-center facelets should point towards the corner of where the red, green and blue faces meet and the letters $\overline{d}$ that stand for anti-d antiquarks on the face-center facelets of the anti-colored faces should simultaneously be pointing to the opposite corner of Qbe, where faces with anti-red, anti-green and anti-blue colors meet.

The course of the game: The players inspect the thoroughly scrambled Qbe, then place it back to the desk in front of them. They may use any of the agreed methods (both hands, or in extreme cases, single hand, both feet, blindfolded, underwater and so on) to solve Qbe. By rotating the sides of Qbe, they compete to reach the desired (color ordered or color-flavor locked) ground state of Qbe.

Qbe, the Quark Matter on Rubik's 3x3 Cube is a three dimensional combination puzzle that can be solved on beginner, intermediate or advanced levels:

1) *On beginner level,* players do not know the how to solve the standard Rubik's Cube. It is a challenging task to figure it out on your own, but it is worth to try. Physicists or physics students are expected to be able to do the first layer on their own and some may even be able to do the second one without too much effort. Doing all the three layers on his own lasted several weeks even for Mr. Rubik himself, but these days there are several public videos that show how to solve the cube, see for example `https://www.youtube.com/watch?v=rmnSpUgOvyI`. This way the players will be able to solve the colors of Qbe. However, the orientation of the d-quarks on the center facelets on each face may still point to random directions.

2) *On intermediate level,* the goal is to reach the color-flavor locked ground state. In this case, after the faces are color ordered, all the d quarks in the centers should point to the corner where the red, green and blue colors meet, and all the anti-d quarks should point to the opposite corners, where the faces with anti-red, the anti-green and anti-blue colors meet. This means that the players have to change the orientation of the center pieces on the faces of the cube without destroying the color order. This is also an already solved problem, sometimes referred to as solving the Super-Cube, custom-cube or picture-cube. Without significant cubing experience, physicists are not expected to figure this out on their own. To fix the direction of the centers, see e.g. `https://www.youtube.com/watch?v=fk1eCZNCTB4` .

3) *On an advanced level,* the players already know how to solve Qbe. But they can still improve the time they need to do so, they can try to do this blindfolded, by one hand, or may use any other of the several mind-boggling methods that were developed recently for the emerging arts of speed and memory cubing.

Recommended physics talking points are listed as follows:

1. **Color:** Quark Matter is a colorless state, but locally colors are free, deconfined, as most of the cubelets have a net color. Qbe is decorated by colored

quarks and anti-colored anti-quarks to illustrate a state of matter called Quark Matter or Perfect Fluid of Quarks. Quarks come in three different colors: red, green and blue. Antiquarks have anti-colors called anti-red, anti-green and anti-blue, represented by the combination of green/blue, blue/red and red/green colors, following the model developed for the Quark Matter Card Games [1, 2, 3, 3]. In the ground state, the red face of Qbe is opposite to the anti-red, blue face is opposite to anti-blue, green is opposite to anti-green. In a random state of Qbe, locally the colors are not compensating each other to a color neutral, white or red-green-blue combination, however, adding all the colors on Qbe results in an overall, globally white color, that models faithfully the globally color white but locally colored property of the Quark Matter state.

2. **Flavor:** Quarks may have 6 different flavors, denoted as u, d, s, c, t and b. On Qbe, only the first three flavors are utilized: u, d and s. These flavors correspond to the flavors of the most abundantly produced quarks at RHIC and LHC. Can you order the faces of Qbe by the flavor?

3. **Baryon number:** The net baryon number of any system of quarks is defined as the number of quarks minus the number of anti-quarks, divided by 3. What is the net baryon number of Qbe in its ground (ordered) state? Do rotations (that mix the quarks and antiquarks of Qbe) modify its net baryon number?

4. **Entropy density:** Quark Matter has a huge entropy density, $\sigma \approx 7.5 \times 10^{45}/\mathrm{m}^3$. This can be compared to the huge number of physically different states of Qbe. When the 24 possible orientation of a given cube in space as well as all the possible orientation of the center pieces are also taken into account, the possible number of states of Qbe becomes a huge number: 2,125,922,464,947,725,402,112,000 ($\approx 2.12 \times 10^{24}$), a bit larger than Avogadro's number, 6.02×10^{23}. Derive the entropy density of Qbe, given that an edge of Qbe is 57 mm.

5. **Perfect Fluidity:** A fluid is perfect if it has no internal dissipation. The resistence of a fluid to internal friction/shearing motion is characterized by the so called kinematic viscosity, denoted by η/σ. This is somewhat analogous to the resistance of the faces of Rubik's cube to rotation: in a perfect model of a perfect fluid, a rotating outer third of the cube could keep on rotating forever, without resistance. Due to dissipative forces, this rotation is coming to an end shortly on a physical model like a Qbe. Use this analogy to estimate the kinematic viscosity η/σ of Qbe, the Quark Matter on Rubik's 3x3 Cube, if the torque needed to rotate an outer third layer of Qbe is of the order of 0.1 Nm and σ is the entropy density of Qbe evaluated in item 4 above. How far Qbe is from the conjectured quantum limit for a perfect fluid, $\eta/\sigma = \hbar/(4\pi)$?